Platinum stable isotope fractionation and adsorption on marine ferromanganese oxide substrates

Loretta Corcoran

A thesis submitted to the Victoria University of Wellington
in fulfilment of the requirements for the degree of
Doctor of Philosophy (Geology)

Victoria University of Wellington, 2016

Abstract

In the modern oxic ocean, ferromanganese sediments in the form of crusts and nodules precipitate directly from seawater over geological timescales. These slow growing ferromanganese sediments incorporate many trace elements, recording changes in ocean chemistry such as variations in the sources of metals to the marine environment and redox changes linked to ocean circulation and atmosphere conditions at the time of precipitation. Ferromanganese sediments are the primary sink for platinum (Pt) in the modern marine environment, with Pt concentrations two orders of magnitude higher than in average upper continental crust. With five stable isotopes and several oxidation states in nature, the Pt stable isotope system has potential to add to the existing suite of stable isotope tracers of ocean environment and processes. This is the first study to evaluate the Pt stable isotope system in a low temperature environment.

To investigate Pt in the marine environment and its potential as (paleo)environmental tracer, chemical separation and a double spike multi-collector inductively coupled plasma mass spectrometry method was developed to measure the platinum isotopic composition of ferromanganese sediments. Measured $^{198}Pt/^{194}Pt$ are reported as $\delta^{198}Pt$ values, representing permil variations relative to the IRMM-010 Pt standard. The external reproducibility in natural, bulk, ferromanganese nodule samples is ca. ± 0.089 ‰ (2 sd), likely limited by sample homogeneity.

The incorporation of Pt into the ferromanganese sediments is expected to impart a stable isotopic fractionation, such that the Pt isotopic composition recorded in the sediments will be offset from seawater. To constrain the incorporation mechanism of Pt onto ferromanganese sediments, a series of adsorption experiments were conducted to evaluate the oxidation state, coordination chemistry and speciation of the platinum adsorbed onto the surface of iron oxyhydroxide and manganese oxide substrates using X-ray absorption spectrometry. The experiments show Pt adsorbs to goethite, ferrihydrite, and δ-MnO_2 as Pt^{4+} at variable pH (pH = 2, 4, 6, and 8), with δ-MnO_2 significantly more effective than the Fe hydroxyoxides at adsorbing Pt, by a factor of > 19 at pH = 8. The presence of Pt^{4+} suggests a chemisorptive redox mechanism in

which Pt^{2+} from seawater is adsorbed and oxidised to Pt^{4+} on the mineral surface. The lighter isotopes of Pt are preferentially adsorbed during this process resulting in an isotopically heavy solution, with an average offset of ca. 0.4 ‰ between the solid and the solution ($\alpha^{198}Pt_{li\text{-}so}$ ~ 1.0006, for δ-MnO_2 at pH = 8). By analogy to the ocean, this suggests that the platinum in seawater will be isotopically heavier than the platinum sequestered into marine ferromanganese sediments.

A globally-distributed suite of modern ferromanganese crusts and nodules was measured to investigate the Pt isotopic composition of natural ferromanganese sediments. Both hydrogenetic and diagenetic crusts and nodules are isotopically heavier than any other natural materials measured to date; up to ca 0.8 ‰ heavier than IRMM-010 and up to ca. 1.0 ‰ than terrestrial mantle and crustal samples. Suspected hydrothermal inputs to ferromanganese deposits result in wide range of isotopic compositions, suggesting hydrothermal processes may introduce both heavier and lighter Pt on a local scale. Given that ferromanganese sediments adsorb lighter Pt, this indicates that seawater will have a heavy Pt isotopic composition.

The Pt concentration in seawater is too low for direct Pt isotopic measurement, as is the concentration in the primary source of Pt to the marine environment, river waters. However, the Pt isotopic character of riverine input was evaluated through a series of leaching experiments as a simplified analogy for oxidative weathering of terrestrial sources. Leaching of three Pt-bearing crustal samples (standard reference materials SARM-76, WPR-1, and PTA-1) indicate that the most mobile platinum, most likely dominated by sulphide minerals, is isotopically heavy relative to the bulk platinum isotopic signature of the samples, with an isotopic offset of up to 5.3 ‰ with respect to the residue, which is consistent with an isotopically heavy seawater composition.

A first order model of the marine Pt isotopic system has been developed, with a predicted seawater composition of $\delta^{198}Pt$ = 0.6 – 1.5 ‰. The measureable isotopic differences among the components of the marine and crustal cycle indicate that Pt shows promise as a new non-traditional stable isotopic tracer of low temperature processes.

Acknowledgements

Firstly, I would like to thank my supervisors Monica Handler and Terry Seward for your valuable insight and support throughout this study. I would also like to thank Martin Bizzarro for allowing me the opportunity to work at the University of Copenhagen. I wish to thank John Creech and Sabrina Lange for your unyielding support and help in all things related to the geochemistry lab, irrespective of the time of day.

I would like to acknowledge the Royal Society of New Zealand Marsden Fund for funding all laboratory work undertaken at Victoria University and for my PhD scholarship. I would also like to thank Victoria University for providing the additional funding for laboratory work undertaken at the University of Copenhagen and a Victoria University submission scholarship and faculty strategic research grant for additional financial support.

I would like to thank the many people who have made my time at Victoria University so enjoyable – Ben, Calum, Celine, Chris, Denise, Elliot, Emily, Jess, John, Juliet, Matt, Rich, and Shaun. I am also very grateful to Terry and Di for those long chats, on a wide range of topics, standing at your office door. Thank you Sabrina and Stewart for those early morning coffees and laughs, it was a fantastic way to start the day. For the many hours spent in the lab I would like to thank Connie and Sabrina for keeping a smile on my face. To Jenni, the best office buddy in the world, thank you for your friendship and support throughout my time at Victoria University – thanks for keeping me sane.

To Alex, Cassie, Gemma, and Kathleen thanks for your kind friendship and the many laughs over the past few years. Finally, to my family, thank you for your continued support, throughout all my endeavours. It was always a welcome distraction to skype home for a while.

Table of Contents

Chapter 1

Introduction 1

1.1 Introduction 2

1.2 Platinum and platinum group element chemistry 3

1.3 Platinum in the marine environment 8

1.31 Sources of platinum to the marine environment 8

1.32 Platinum behaviour in seawater 13

1.33 Platinum sinks in the marine environment 18

1.331 Fe-Mn sediment formation and description 20

1.332 Concentration and incorporation mechanisms of platinum onto Fe-Mn sediments 25

1.333 Global platinum concentration in Fe-Mn sediments 29

1.4 Non-traditional stable isotopes in the marine environment 30

1.41 Iron stable isotopes in the oceans 33

1.42 Molybdenum stable isotope in the oceans 35

1.43 Nickel isotope in the oceans 37

1.5 Objectives and structure of this thesis 39

Chapter 2

Method development 41

2.1 Introduction 42

2.2 Digestion method 44

2.2.1 Bulk digestion methods 45

2.1.1.1 Nickel sulphide fire assay 45

2.1.1.2 Aqua regia digestion 48

2.1.1.3 Hydrofluoric and nitric acid digestion 48

2.2.2 Authigenic digestion methods 49

2.2.3 Preparation of solution samples 49

2.3 Platinum separation..... 50

2.3.1 Anion exchange chemistry..... 51

2.3.2 Multi element concentration analysis by ICP-MS 53

2.3.3 Evaluation of the elution profiles and Pt yields 54

2.3.3.1 Comparison of authigenic and bulk digestion methods.....56

2.4 Platinum isotope analysis by MC-ICP-MS..... 59

2.4.1 MC-ICP-MS standards and double spike 60

2.4.2 Isotopic notation and standard reproducibility and precision 61

2.5 Data reduction..... 63

Chapter 3

Platinum adsorption onto ferromanganese substrates: experimental constraints on mechanisms and associated platinum isotopic fractionation..... 65

Preface

3.1 Introduction..... 66

3.2 Experimental Methods 67

3.2.1 Synthesis of the Fe oxyhydroxides and Mn oxide 67

3.2.1.1 Goethite.....69

3.2.1.2 Ferrihydrite 69

3.2.1.3 δ-MnO_2 70

3.2.1.4 XRD of the synthesised Fe oxyhydroxides and Mn oxide 70

3.2.2 Platinum containing solutions..... 72

3.2.3 Adsorption equilibria 74

3.2.4 Analytical methods and procedures 76

3.2.4.1 Preparation of adsorption samples for ICP-MS and MC-ICP-MS analysis 76

3.2.4.2 Preparation of adsorption samples for Synchrotron X-ray absorption spectroscopy 77

3.3 Results of adsorption experiment, XAS analysis and the associated isotopic fractionation 79

3.3.1 Platinum adsorbed onto the oxyhydroxide and oxide surfaces..... 79

3.3.1.1 Platinum adsorption onto goethite 79

3.3.1.2 Platinum adsorption onto ferrihydrite 81

3.3.1.3 Platinum adsorption onto δ-MnO_2 83

3.3.1.4 Platinum adsorption onto samples prepared for synchrotron x-ray absorption spectroscopy 85

3.3.2 Synchrotron X-ray absorption spectroscopy..... 86

3.3.2.1 X-ray absorption near edge (XANES) structure of the platinum adsorbed onto the surface of the oxyhydroxides and oxides 86

3.3.2.2 X-ray absorption fine structure (EXAFS) of the platinum adsorbed onto the surface of the oxyhydroxides and oxides 92

3.3.3 Platinum isotopic composition of adsorption experiments..... 95

3.3.3.1 Platinum isotopic composition of the platinum containing solution ..95

3.3.5.2 Isotopic composition of Pt adsorbed onto the goethite surface 96

3.3.5.3 Isotopic composition of Pt adsorbed onto the ferrihydrite surface 98

3.3.5.4 Isotopic composition of Pt adsorbed onto the δ-MnO_2 surface 101

3.4 Discussion 103

3.4.1 Platinum adsorption and bonding environment 103

3.4.2 Platinum stable isotope fractionation..... 107

3.5 Summary 109

Chapter 4

Effects of leaching on the platinum isotopic composition: approximating weathering in an oxic environment 110

Preface

4.1 Introduction 111

4.2 Samples 112

4.3 Methodology 115

4.4 Results 116

4.4.1 Concentration of leached platinum 116

4.4.2 Platinum isotopic composition 120

4.5 Discussion 122

4.5.1 Implications for riverine platinum input into seawater 125

4.5 Summary 127

Chapter 5

Stable platinum isotopic composition of modern ferromanganese crusts and nodules 128

Preface

5.1 Introduction 129

5.2 Ferromanganese crust and nodule samples 130

5.2.1 Ferromanganese nodules (FMN) 130

5.2.2 Ferromanganese Crusts (FMC) 133

5.3 Ferromanganese crust and nodule sample preparation and analysis 140

5.4 Platinum concentration and isotopic composition of the natural samples 142

5.5 Discussion 147

5.5.1 Platinum heterogeneity in Nod-A-1 147

5.5.2 Platinum concentrations 150

5.5.3 Platinum isotopic variations 157

5.5.3 Implications for the marine Pt cycle 161

5.6 Summary 164

Chapter 6

Conclusions and future directions 165

6.1 Summary and Conclusions 166

6.1.1 How is platinum incorporated into the sediment record, and what effect has the incorporation mechanism on the platinum stable isotope composition? 167

6.1.2 What variations are observed in platinum stable isotope chemistry in the modern oxic oceans? 168

6.1.3 Do platinum stable isotopes have potential as a marine geochemical tracer? 169

6.2 Future Directions 171

6.21 Temporal variations in platinum concentration and δ^{198}Pt 172

References 173

List of figures

Chapter 1

Introduction

Figure 1.1 Periodic table of elements 4
Figure 1.2 Global distribution map of major platinum deposits 6
Figure 1.3 Platinum concentration and marine profile 14
Figure 1.4 Marine pH with depth profile and Pt species distribution with varying pH and Cl concentration periodic table of elements 17
Figure 1.5 Global distribution of ferromanganese crusts and nodules 19
Figure 1.6 Illustration of hydrogenetic and hydrothermal ferromanganese crust and nodule formation locations 20
Figure 1.7 Simplified electrochemical adsorption mechanism for cations and anions on manganese oxides and iron oxyhydroxides 22
Figure 1.8 Chrondrite normalised PGE and REE diagram for ferromanganese sediments 26
Figure 1.9 Equilibrium and kinetic isotope fractionation 31
Figure 1.10 Modern marine cycle of Fe stable isotope system 34
Figure 1.11 Modern marine cycle of Mo stable isotope system 36
Figure 1.12 Modern marine cycle of Ni stable isotope system 38

Chapter 2

Method Development

Figure 2.1 Photographs of various stages of nickel sulphide digestion elements 47
Figure 2.2 Schematic of resin cleaning and elution sequence of anion exchange chemistry 52
Figure 2.3 Platinum elution profile demonstrating the 'double peak' in natural sample 55
Figure 2.4 Platinum elution profiles of various digestion methods 57
Figure 2.5 Platinum and major matrix elution profile after nickel sulphide digestion 58
Figure 2.6 δ^{198}Pt IRMM – 010 and Baker standard reproducibility 62

Chapter 3

Platinum adsorption onto ferromanganese substrates: experimental constraints on mechanisms and associated platinum isotopic fractionation

Figure 3.1 XRD profiles of the three synthetic minerals 71
Figure 3.2 Percent of Pt^{2+} species in Pt-Cl-OH system 73
Figure 3.3 pH equilibrium of incorporation suspensions 75
Figure 3.4 Concentration of Pt adsorbed onto goethite surface..... 79
Figure 3.5 Concentration of Pt adsorbed onto goethite surface..... 80
Figure 3.6 Concentration of Pt adsorbed onto ferrihydrite surface 81
Figure 3.7 Percent of Pt remaining in solution after adsorption onto ferrihydrite.... 82
Figure 3.8 Concentration of Pt adsorbed onto δ-MnO_2 surface..... 83
Figure 3.9 Percent of Pt remaining in solution after adsorption onto δ-MnO_2..... 84
Figure 3.10 Platinum adsorbed onto goethite, ferrihydrite, and δ-MnO2 for XAS analysis 85
Figure 3.11 XANES spectra of Pt L_3-edge for $PtCl_2$ and $PtCl_4$..... 87
Figure 3.12 XANES spectra for Pt L_3-edge for platinum standards..... 88
Figure 3.13 XANES LCF for XAS synthetic samples 91
Figure 3.14 EXAFS of Pt adsorbed onto synthetic samples..... 94
Figure 3.15 δ^{198}Pt of the platinum containing solution (controls) 95
Figure 3.16 δ^{198}Pt of the platinum adsorbed onto the goethite surface..... 96
Figure 3.17 Δ^{198}Pt for goethite adsorption pairs as a function of pH 98
Figure 3.18 δ^{198}Pt of the platinum adsorbed onto the ferrihydrite surface 100
Figure 3.19 Δ^{198}Pt of the platinum adsorbed onto the ferrihydrite surface..... 100
Figure 3.20 δ^{198}Pt of the platinum adsorbed onto the δ-MnO_2 surface 101
Figure 3.21 Δ^{198}Pt for goethite adsorption pairs as a function of pH 102
Figure 3.22 Platinum (μg/g) adsorbed onto the surface as a function of pH..... 103
Figure 3.23 Percent of Pt^{2+} species in Pt-Cl-OH system 105
Figure 3.24 δ^{198}Pt of adsorbed and remaining Pt as a function of Pt adsorbed 108

Chapter 4

Effects of leaching on the platinum isotopic composition: approximating weathering in an oxic environment

Figure 4.1 Percent of platinum leached based on ID calculations 120
Figure 4.2 Leaching pairs for pseudo digest samples 121
Figure 4.3 Percent platinum leached against the α^{198}Pt of leached samples..... 122
Figure 4.4 Eh – pH diagrams for Pt-H_2O-Cl and Pt-S-H_2O 124
Figure 4.5 Percent platinum leached against the Δ^{198}Pt of leached samples 125
Figure 4.6 Δ^{198}Pt for the pseudo digest and the adsorption experiments leachates 127

Chapter 5

Stable platinum isotopic composition of modern ferromanganese crusts and nodules

Figure 5.1 Location map and coordinates of FMN and FMC samples..... 131
Figure 5.2 Fe, Mn, and Cu+Ni+Co (x10) discrimination plot of the FMN and FMC samples..... 133
Figure 5.3 Sample photographs of FMC samples from USGS..... 135
Figure 5.4 Sample photographs of the Colville FMC samples..... 136
Figure 5.5 Fe, Mn, and Cu+Ni+Co (x10) discrimination plot of the Colville FMC samples..... 137
Figure 5.6 REE spider diagram of the Colville FMC samples 138
Figure 5.7 Photograph of typical thickness of the Colville FMC samples 141
Figure 5.8 δ^{198}Pt of the FMN and FMC grouped by ocean basin 144
Figure 5.9 δ^{198}Pt and platinum concentration of the FMN and FMC grouped by sediment type and ocean basins 146
Figure 5.10 δ^{198}Pt and Pt concentration heterogeneity of USGS Nod-A-1 147
Figure 5.11 Comparision of platinum concentration to Mn/Fe ratio and sample depth 152
Figure 5.12 Crossplot of redox indices and platinum versus Ce anomaly..... 154
Figure 5.13 Dissolved oxygen profiles from the modern Atlantic, Pacific, and Indian Ocean 156

Figure 5.14 δ^{198}Pt of FMS and other terrestrial and extraterrestrial samples 157
Figure 5.15 δ^{198}Pt versus Pt concentration, depth, Ce anomaly, and Mn/Fe ratio.. 159
Figure 5.16 Range of δ^{198}Pt and Ce anomaly of Colville samples 160
Figure 5.17 Range of δ^{198}Pt in the modern marine environment..... 163

Chapter 6
Conclusions and future directions
Figure 6.1 Range of δ^{198}Pt and sources of Platinum in the modern marine environment 170

List of tables

Chapter 1

Introduction

Table 1.1 General chemical properties of PGE 5

Table 1.2 Range of estimated platinum flux to the marine environment 12

Table 1.3 Mean platinum concentration of previously studied FMS 29

Chapter 2

Method Development

Table 2.1 Location and platinum concentration of nodule standard reference materials 44

Table 2.2 Fluxing agents for nickel sulphide fire assay technique 46

Table 2.3 Typical running parameters of ICP-MS (Agilent and Element2) 53

Table 2.4 Typical running parameters of MC-ICP-MS (Neptune and Nu-Plasma) . 59

Chapter 3

Platinum adsorption onto ferromanganese substrates: experimental constraints on mechanisms and associated platinum isotopic fractionation

Table 3.1 Mineral characteristics of the iron and manganese oxides and oxy-hydroxides that were synthesised 68

Table 3.2 Platinum concentration of the six samples that were measured using synchrotron x-ray absorption spectroscopy 86

Table 3.3 Linear combination fitting of the XANES for the adsorbed Pt..... 90

Table 3.4 EXAFS derived first shell distances form the CCDC for the model compounds 92

Table 3.5 EXAFS derived first shell distances for the adsorbed Pt 93

Table 3.6 δ^{198}Pt of the platinum remaining in solution and the platinum adsorbed onto the surface of goethite 97

Table 3.7 δ^{198}Pt of the platinum remaining in solution and the platinum adsorbed onto the surface of ferrihydrite 99

Table 3.8 δ^{198}Pt of the platinum remaining in solution and the platinum adsorbed onto the surface of δ-MnO_2 102

Chapter 4

Effects of leaching on the platinum isotopic composition: approximating weathering in an oxic environment

Table 4.1 Details of pseudo digest experiment samples (SRM) 113

Table 4.2 Sample details and results of pseudo digest experiments 117

Chapter 5

Stable platinum isotopic composition of modern ferromanganese crusts and nodules

Table 5.1 Platinum concentration and δ^{198}Pt of the natural ferromanganese crust and nodules 143

List of Abbreviations

2 sd	Second standard deviation
2 se	Two standard error
ca.	Circa, from Latin meaning approximately
CCDC	Cambridge Crystallographic Data Centre
CFA	Carbonate fluorapatite
CN	Coordination number
CRM	Certified reference materials
FMC	Fe-Mn crusts
FMN	Fe-Mn nodules
FMS	Fe-Mn sediments (crust and nodules)
GeoRem	Geological and Environmental Reference Materials
GNS	Institute of Geological and Nuclear Science
GSJ	Geological Survey of Japan
HREE	Heavy rare earth elements
ICDD	International Centre for Diffraction Data
ICP-MS	Inductively coupled plasma mass spectrometer
ID	Isotope dilution
IRMM	Institute for Reference Materials and Measurements
JCPDS	Joint Committee on Powder Diffraction Standards
K	Kelvin, temperature
keV	kiloelectron volt
LCF	Linear combinatorial fit
mbsl	Meters below sea level
MC-ICP-MS	Multi-collector inductively coupled plasma mass spectrometer
Milli Q water	Ultra-pure water (>18.2 MΩ, TOC < 5 ng/g)
NIWA	National Institute of Water and Atmospheric Research
NOAA	National Oceanic and Atmospheric Administration
OMZ	Oxygen minimum zone
PAAS	Post Archean Australian Shale
PCZ	Prime crust zone

PDF #	Powder diffraction file number
PGE	Platinum group elements
PGM	Platinum group metals
PGN	Platinum group nugget
ppb	part per billion
ppm	Parts per million
ppt	Parts per trillion
Pt_D	Dissolved platinum
Pt_S	Suspended platinum
REE	Rare earth elements
RSD	Relative standard deviation (%)
rpm	Revolutions per minute
SRM	Standard reference materials
TOC	Total organic content
UCC	Upper continental crust
UMGC	Ultramafic-gabbro complex
UoC	Centre for Star and Planet Formation, Natural History Museum of Denmark, University of Copenhagen, Denmark
USGS	United States Geological Survey
VUW	Geochemistry laboratory facilities, SGEES, Victoria University of Wellington
WOCE	World Ocean Circulation Experiments
wt%	Weight per cent
XANES	X-ray absorption near edge structure
EXAFS	Extended X-ray absorption fine structure
XAS	X-ray absorption spectroscopy
XPS	X-ray photoelectron spectroscopy
XRD	X-ray powder diffraction
ZPC	Zero point of charge

Chapter 1

Introduction

1.1 Introduction

Non-traditional stable isotope systems are being increasingly utilised to investigate a diverse range of high- and low-temperature planetary processes, such as planetary formation, and changing ocean chemistry. Mass-dependent changes in the stable isotope ratios of an element can be produced by a wide range of physiochemical and biological processes, however in heavier elements, these variations are typically on a sub permil level. The development of new analytical technologies, specifically multiple-collector inductively coupled plasma mass spectrometry (MC-ICP-MS), now makes it possible to measure the small mass-dependent differences in isotope systems of heavier elements such as iron, molybdenum, cerium, nickel, thallium, copper, and zinc. (Anbar and Rouxel, 2007, Beard et al., 2003, Gall et al., 2013, Goldberg et al., 2009, Nakada et al., 2016, Rehkämper et al., 2004, Severmann et al., 2008, Zhu et al., 2000). Applied to the marine realm, these non-traditional stable isotope systems can be used to trace changes in ocean chemistry through Earth's history, for example through measuring the subtle isotopic fractionation associated with changes in marine redox conditions that may not be preserved in concentration data alone (Anbar and Rouxel, 2007, Barling and Anbar, 2004, Beard et al., 2003, Rehkämper et al., 2004).

The platinum stable isotope system has potential to be applied to both high- and low-temperature processes due to the highly siderophile nature, chalcophile tendencies, and redox sensitivity of platinum. The only reported Pt stable isotope data for terrestrial samples to date, has documented measureable isotopic variations (up to 0.4‰, with a reproducibility of 0.08‰) for a range of crustal and mantle samples (Creech et al., 2014). The redox sensitive nature of platinum and high concentration of platinum in authigenic marine sediments suggest it has potential to provide insights into changes in ocean chemistry, and ocean-atmosphere interaction. However, samples from the marine environment have not yet been explored.

This thesis presents the first study of the platinum stable isotopic system for a low-temperature environment with the aim of evaluating Pt stable isotopic fractionation in the marine environment. The platinum cycle in the modern oxic oceans is investigated

as first step toward evaluating this isotopic system as a potential tracer of changing ocean chemistry. Similar to previous studies on various metals in the oceans (Fe, Mo, Tl, Ni, Cu), ferromanganese crusts and nodules were the primary focus of this study. Ferromanganese crusts and nodules act as an archive of ocean chemistry due to their slow growing nature and how they accumulate metals from the water column (chapter 1.33; Beard et al., 2003, Cameron and Vance, 2014, Goldberg et al., 2009, Rehkämper et al., 2004, Severmann et al., 2008, Zhu et al., 2000). In addition to ferromanganese crusts and nodules recording ocean chemistry they are also enriched in platinum relative to other sediments (table 1.1) allowing for ease of measurement of platinum concentration and stable isotope composition.

This introduction chapter briefly reviews the current understanding of platinum geochemistry in general, and in the marine environment in particular, as well as the application of metal non-traditional stable isotope systems to the marine environment.

1.2 Platinum and platinum group element chemistry

Platinum is a non-bio-essential metal with six naturally occurring isotopes, ^{190}Pt, ^{192}Pt, ^{194}Pt, ^{195}Pt, ^{196}Pt and ^{198}Pt, with relative abundances of ca. 0.01 %, 0.78 %, 32.86 %, 33.78 %, 25.21 %, and 7.36 %, respectively. All of the naturally occurring platinum isotopes are stable with the exception of ^{190}Pt, which is radioactive, with a long half-life of $t_{1/2} \sim 10^{11}$ years (^{190}Pt – ^{186}Os decay system; Walker et al., 1995). Platinum occurs in several oxidation states in nature, Pt^0, Pt^{2+} and Pt^{4+} (table 1.1). The dominant oxidation state and most mobile platinum in the superficial environment is Pt^{2+} in the form of chlorides and hydroxides depending on the availability of chlorides (Elding, 1978, Fuchs and Rose, 1974, Goldberg et al., 1986, Halbach et al., 1989, Hein et al., 1988). Pt^{4+} may also be present to a lesser extent, however, it is predicted to only dominant in highly oxidizing, acidic environments (Colombo et al., 2008).

Pt forms part of the platinum group elements (PGE), ruthenium, rhodium, palladium, osmium, iridium, and platinum, which are second and third row transition elements (figure 1.1) that exhibit similar chemical properties, distinctive from their neighbours.

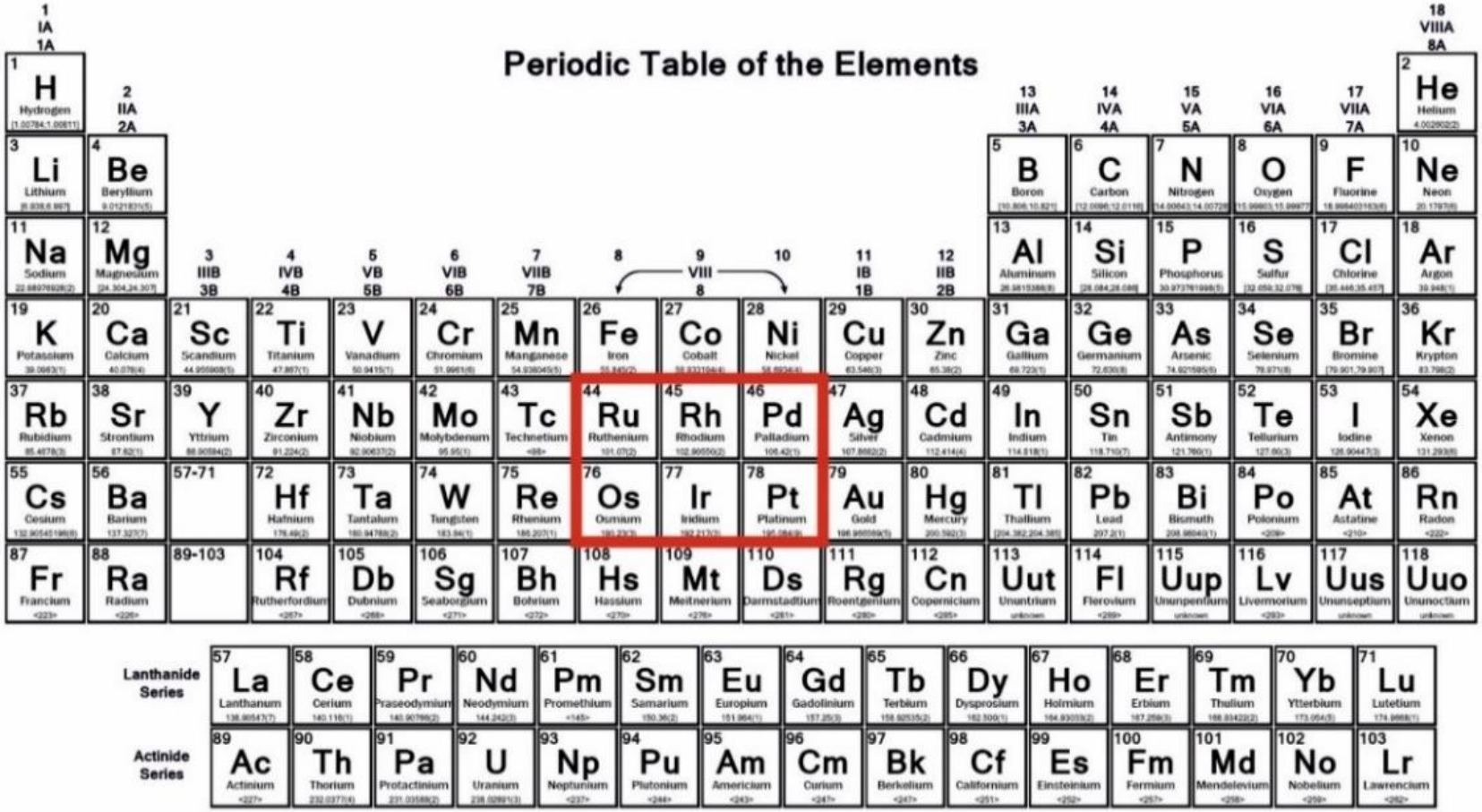

Figure 1.1: Periodic table of the elements with the platinum group elements (PGE): Ru, Rh, Pd, Os, Ir, and Pt, highlighted in red. Modified from Helmenstine, 2015.

Table 1.1 Platinum group element (Ru, Rh, Pd, Os, Ir, and Pt) general chemical properties and concentrations from different planetary environments, modified from Creech, 2014.

Element	**Ru**	**Rh**	**Pd**	**Os**	**Ir**	**Pt**
Atomic number	44	45	46	76	77	78
Atomic weight (g/mol)	101.07	102.91	106.42	190.23	192.22	195.08
Electron configuration	[Kr] $4d^7 5s^1$	[Kr] $4d^8 5s^1$	[Kr] $4d^{10}$	[Xe] $4f^{14} 5d^6 6s^2$	[Xe] $4f^{14} 5d^7 6s^2$	[Xe] $4f^{14} 5d^9 6s^1$
Naturally occurring isotope(s)	7	1	6	7	2	6
Principal oxidation states	0, 2, 3, 4	0, 3	0, 1, 2, 4	0, 2, 3, 4, 8	0, 3, 4	0, 2, 4
Primary minerals phases[a]	RuS_2	RhAsS	PdTe, (Pt,Pd)S, $PdTe_2$	OsS_2	IrAsS	PtS, (Pt,Pd)S, $PtAs_2$, $PtTe_2$
Iron meteorites (ng/g)[b]	10600	2200	4000	15400	10400	14700
Bulk earth (ng/g)[c]	1310	242	1015	900	835	1866
Core (ng/g)[c]	4000	740	3100	2750	2550	5700
Primitive upper mantle (ng/g)[c]	4.97	0.91	3.85	3.43	3.19	7.07
Continental crust (ng/g)[d]	0.1	0.06	0.4	0.05	0.05	0.4
Pelagic sediments (ng/g)[e]	0.2	0.4	6	0.1	0.4	5
Manganese crusts (ng/g)[f]	17	15	4	2	6	268
Ocean (pmol/kg)[g]	< 0.50	0.8	0.6	< 0.50	< 0.001	< 1

Data sources: [a] Mondal (2011), [b] Creech (2014), [c] McDonogh et al. (2003), [d] Wedopohl et al. (1995), [e] Li (1991), [f] mean global crust concentrations, Hein et al. (2005), [g] mean global ocean concentrations, Bruland and Lohan (2006).

The PGE are highly siderophile metals that prefer to form metallic bonds with iron over bonds with oxygen and silicon (Becker, et. al., 2006, Righter, 2003). Due to the siderophile nature of the PGE they are preferentially sequestered into the metallic core during planetary differentiation leading to a relative depletion of the PGE in the mantle and crust compared to the core, 0.05 – 0.4 ng/g and 740 – 5700 ng/g, respectively (table 1.1; Creech, 2014, McDonough et al., 2003, Wedepohl et al., 1995). In reducing environments in the presence of sulphur the PGE may exhibit chalcophile behavior. In the crust the PGE are most commonly associated, together, with sulphides in mafic-ultramafic rocks in a variety of settings (table 1.1, figure 1.2; Maier, 2005, Mondal, 2011).

Figure 1.2 Global distribution of the largest platinum deposits with countries with two or more deposits are named. Modified from Reith et al., 2014.

PGE crustal deposits are divided into three primary deposits types (ophilites and zoned Alaskan-Ural types, layered intrusions, and komatiites) and a number of secondary deposit types (Economou-Eliopoulos, 2010, Reith et al, 2014). The primary deposits are associated with mafic and ultramafic deposits with several sub-types described depending on their location within the mafic/ultramafic intrusion (Eckstrand and Hulbert, 2007, Maier, 2005, Reith et al., 2014). For example, PGE enrichments occur in a number of settings: 1) along the base or sidewall of intrusions (Platreef of the Bushveld Complex and Portimo, Finland), 2) within ultramafic silicate cumulates

(peridotites and pyroxenites) 100 – 1000 m above the base of the intrusion (Kapalagulu Intrusion, 3) western Tanzania and the main sulphide zone of the Great Dyke, Zimbabwe), and 4) in the central portion of intrusions (Merensky Reef of the Bushveld Complex and J-M reef of the Stillwater Complex, Montana; Eckstrand and Hulbert, 2007, Maier, 2005, Reith et al., 2014). Other enrichments are related to late magmatic and hydrothermal fluids, for example Lac des Iles, Ontario and may be primary or secondary. PGE can be enriched as by-products in some magmatic Ni–Cu sulphide deposits and occurrences. These are formed in a number of ways, such as sulphide melts being entrained by silicate magma or precipitation and concentration of sulphide melt in areas such as widening sections of lava channels. Secondary deposits include laterites (Yilgarn Craton, western Australia) and eluvial – alluvial placers (Kamchatka, Russia; Reith et al., 2014). These secondary deposits form due to the weathering of primary deposited PGE and redeposition elsewhere. For example, the leaching of PGE from the Merensky Reef of the Bushveld Complex and redeposition in the anorthositic norite footwall (Fuchs and Rose, 1974).

Currently, the Bushveld Complex in South Africa is the largest mine of platinum producing ~ 70 % of the world's supply (Wilburn and Bleiwas, 2004). Over the past several decades the requirement for platinum has increased with the introduction of automobile catalytic converters along with its use in anti-cancer treatments, jewellery and the petrochemical industry (Barbante et al., 2001, Ek et al., 2004, Hein et al., 2013, Reith et al., 2014). This increase in usage has resulted in the examination of Fe–Mn sediments (Fe-Mn crust and nodules), hereafter referred to as FMS, as a potential economic Pt source as a by-product of Ni and Cu mining.

The behaviour of platinum in the marine environment is poorly constrained, however, it has long been recognised that in the modern oxic marine environment the largest sink for platinum is FMS, with platinum enrichments of up to 1100 times over upper continental crust concentrations (Halbach et al. 1989, Hein et al., 2005, Hodge et al., 1985). FMS precipitate directly from hydrogenetic and hydrothermal metal sources in the marine environment, which results in the FMS recording the ocean chemistry at the time of the sediment formation (chapter 1.33).

1.3 Platinum in the marine environment

The behaviour of platinum in the marine environment is dependent on an interplay between: source, sinks and solubility, with ocean pH and redox state affecting stability. In the following section the currently available information on the marine cycle of platinum is discussed.

1.31 Sources of platinum to the marine environment

The overall sources of platinum in the marine environment are not well constrained. However, there are four main sources: 1) the prominent source is riverine, 2) hydrothermal inputs a lesser and more localised source, 3) aeolian and 4) cosmic dust contributions (table 1.2; Soyol-Erdene and Huh, 2012). Both riverine and aeolian fluxes are currently affected by anthropogenic contributions due to the use of platinum in many modern technologies, such as automobile exhaust catalysts and the electronics industry. It has been estimated that currently up to 85 % of the mobile platinum in the modern environment at the earth's surface is derived from an anthropogenic source (Sen and Peucker-Ehrenbrink, 2012) A few recent studies have focused on the impact of the catalytic converter on local platinum concentrations by comparing river water samples collected in a sparsely populated areas before the introduction of catalytic converters to river and estuary water samples collected in Tokyo Bay, with average concentrations almost two orders of magnitude lower in the regions unaffected by anthropogenic inputs (Obata et al., 2006, Soyol-Erdene and Huh, 2012). However, the influence of anthropogenic platinum extends beyond local sources as, for example, platinum concentrations in ancient ice (7 ka) from Greenland are ca**.** 0.01 pg/g, which is six times lower than in modern snow precipitation from the same location (Barbante et al., 2001).

The flux of platinum to the marine environment from river sources is poorly constrained. A range of 0.36 – 0.84 pM for the dissolved platinum concentration (Pt_D) of rivers is based on eleven large river systems in East Asia and the Gironde Estuary in SW France (Cobelo-Garcia, 2014, Soyol-Erdene and Huh, 2012). This Pt_D

concentration represents an average of 200 samples draining various lithologies, with no appreciable variation in platinum concentration observed with runoff over different lithologies. Based on the estimated global river runoff (discharge to the marine environment) of 3.74 x 10^{13} m^3/yr this would result in a Pt_D concentration influx of 2,600 – 6,100 kg/yr (13,500 – 31,000 mol/yr) to the marine environment (table 1.2; Cobelo-Garcia, 2014, Palmer and Edmond, 1989, Soyol-Erdene and Huh, 2012).

The suspended platinum (particulate matter) concentration (Pt_S) present in rivers may affect the concentration of Pt_D discharged by ± 50% to the marine environment due to thermodynamically and kinetically driven desorption and adsorption of platinum during estuary mixing (Cobelo-Garcia, 2014, Soyol-Erdene and Huh, 2012). Cobelo-Garcia (2014) examined the Gironde Estuary under different discharge conditions and noted that the Pt_D varied with the amount of Pt_S present, the species of platinum on the particle and the flushing time of the estuary. When the flushing time of the estuary increased so did the Pt_D due to the remobilization of platinum from suspended particles. The Pt_D decreases as a result of adsorption and flocculation primarily due to increases in salinity. Soyol-Erdene and Huh (2012) suggested that the Pt_D may also decrease through interaction with organic matter in estuarine waters. A conservative estimate on the effect of estuary mixing on the riverine Pt_D input would place a range of 1,300 – 12,250 kg/yr (6,700 – 62,000 mol/yr) to the oceans from river input.

To date, there have been limited studies evaluating the concentration of platinum from aeolian-derived (terrestrial only) input to the marine environment. Most studies focus on the platinum concentration of urban roadside dust samples to constrain the input of anthropogenically sourced platinum for evaluating metal toxicity issues. The platinum concentration for roadside dust has a range of 14–700 ng/g, with the lowest concentration measured being more than 25 times the upper continental crust (UCC) concentration of platinum, 0.510 ng/g (Hodge and Stallard, 1986, Mukai et al., 1990, Peucker-Ehrenbrink and Jahn, 2001, Schutyser et al., 1977). The best estimates of platinum concentration in non-urban aeolian sources are indirect, and use the UCC concentration of platinum for airborne dust. The UCC platinum concentration for aeolian dust is consistent with most major and trace elements in loess having similar

concentrations to those of UCC (Peucker-Ehrenbrink and Jahn, 2001). Considering the slow growth rate of authigenic marine sediments, which are the subject of this study, contamination of platinum from anthropogenic sources is not relevant over the timescales investigated. Thus, estimates of non-urban aeolian sources will be used to characterize the contribution of airborne dust to the oceans.

The overall contribution of airborne dust to the oceans is 4.5 x 10^{11} kg/yr with the impact of the dust diminishing further away from continental sources (Jickells et al., 2005). Based on the UCC platinum concentration the platinum discharged to the marine environment from aeolian sources would be 230 kg/yr (Jickells et al., 2005, Peucker-Ehrenbrink and Jahn, 2001). However, not all of this platinum will be soluble, published data indicating a range of 3 – 43 % (Alt et al., 1993, Hill and Mayer, 1977, Soyol-Erdene and Huh, 2012). Alt et al. (1993) determined by HCl leaching experiments the total soluble proportion of platinum of airborne dust samples collected in Dortmund was 30 – 43 %, whereas, samples collected in a car tunnel in Austria had a soluble fraction of 2.5 – 6.9 %. The difference in the platinum solubility between the Dortmund and the car tunnel samples being attributed to the different origins of the platinum, environmentally derived versus traffic. However, Soyol-Erdene and Huh (2012) used the solubility of aerosol-borne gold, determined by mass balance of Au in the ocean, of 3% by Falkner and Edmond (1990) due to the similarities between gold and platinum. Taking into account the solubility of aeolian derived platinum (3 – 43 %), the estimated global Pt_D influx from aeolian source would be 7 – 100 kg/yr (35 – 500 mol/yr), which is an order of magnitude lower than the estimated riverine source of platinum to the marine environment (Soyol-Erdene and Huh, 2012).

The cosmic dust flux of platinum into the marine environment has yet to be quantified. Soyol-Erdene and Huh (2012) estimated a cosmic flux of platinum of 150 mol/yr based on the average chondritic platinum concentration of 990 ng/g in meteorites and the global meteorite flux of 3 ± 1.5 10^7 kg/yr (Anders and Grevesse, 1989, Peucker-Ehrenbrink and Ravizza, 2000). As is the case for the aeolian flux, there is uncertainty concerning the soluble fraction of cosmic-derived platinum, which is estimated to be in the range of 20–100%, using the soluble fraction of osmium in cosmic dust as an

analogue (Colodner, 1991, Esser and Turekian, 1988, Soyol-Erdene and Huh, 2012). Therefore, the global influx of cosmic-derived platinum to the marine environment is likely to be 6 – 30 kg/yr (30 – 150 mol/yr), comparable to slightly less than the aeolian flux.

The cosmic flux also includes spherules, which typically comprise a Fe–Ni metal core. However, more than half of reported spherules analysed, ≥ 300 μm in size, have a platinum group nugget (PGN) instead of a Fe–Ni core, and are believed to have formed by the oxidation of molten meteoritic metal during atmospheric entry (Brownlee et al., 1984). Due to the insolubility of these spherules, they exert a negligible influence on dissolved platinum concentrations, but could affect concentrations observed in Fe–Mn crusts and nodules if they are directly incorporated into the sediment (Halbach et al., 1989).

The fourth source of platinum to the marine environment is hydrothermal systems. It is thought that hydrothermal systems will only have a localised effect on marine platinum concentrations, due to the formation of sulphides close to the hydrothermal vents and oxy-hydroxides close to the ridge axis that act as sinks for platinum (Soyol-Erdene and Huh, 2012). However, elements with similar ocean residence times to Pt (16 kyr – 1 Myr; chapter 1.32) have been observed to travel > 200 km from hydrothermal source (e.g. Cu, Zn, Ni; Barrett et al., 1987; Li, 1982; 1991). Colodner (1991) measured hydrothermal fluid samples from the Mid-Atlantic Ridge, and determined a platinum concentration of 5×10^{-13} M ± 2×10^{-13} M for the largest sample, with all the other samples having concentrations below detection limits. McKibben et al. (1990) found that geothermal brines of the Salton Sea yielded a maximum platinum concentration of 2.5×10^{-9} M. Given the limited information available on the hydrothermal flux of platinum to the oceans, an estimate of 195 kg/yr (1000 mol/yr), based on measurement of sediments from under the Rainbow hydrothermal plume on the Mid-Atlantic Ridge, is adopted for the purposes of this discussion (Soyol-Erdene and Huh, 2012).

Table 1.2 Range of estimated platinum flux to the marine environment in kg/yr and the calculated input percentage (references within text).

Source	kg/yr		% input	
	Min	Max	Min	Max
Rivers (& estuary)	1300	12250	99	97
Aeolian	7	100	0.5	0.8
Cosmic	6	30	0.5	0.2
Hydrothermal	0	195	0.0	1.6
Total	1313	12575		

The global flux of river discharge and the global dust flux are not constant over geological time, for example significant variations between glaciated and interglacial periods. During a glaciated period, there is a decrease in the amount of chemical weathering but this is offset by an increase in physical weathering due to increased mechanical break-down of rocks (Foster and Vance, 2006, Oxburgh, 1998). Consequently, glaciated periods see an increase in global dust flux; analysis of an ice core from the Antarctic suggests an increase of 25 times that of typical interglacial periods (Kohfeld and Harrison, 2001, Lambert et al., 2008). The affect these variations have on the platinum flux to the marine environment and therefore on the isotopic composition in authigenic marine sediments over the long time scale of accumulation of these sediments is unknown. However, a variation in the δ^{56}Fe of a FMC from the North Atlantic has been used to infer the Northern hemisphere glaciation with a lighter δ^{56}Fe composition as a result of an increase in detrital load (Beard et al., 2003). A study measuring the ^{187}Os/^{186}Os ratio of a core from the flanks of the East Pacific Rise, which represents 200,000 years of sediment accumulation, has shown an offset of 0.5 in the ^{187}Os/^{186}Os from interglacial to the late stage of the past two glacial periods, ^{187}Os/^{186}Os ~ 8.5 and 8.1, respectively (Oxburgh, 1998). This offset was attributed to the osmium composition of seawater having less radiogenic signature due to a reduction in continental chemical weathering, the main source of radiogenic osmium to seawater. Changes in the osmium isotopic signature however, would be expected to

be significantly larger than for Pt isotopes. This reflects a radiogenic isotope system where evolved crustal rocks have evolved to ratios higher than hydrothermal (mantle) inputs at a percent level, compared to the sub-permil level typical of variations in heavier non-traditional stable isotopes.

1.32 Platinum behaviour in seawater

The concentration and depth profiles of platinum in deep-water ocean basins is not well constrained, with three previous studies providing very different profile types (figure 1.3): (1) nutrient-type profile was determined by single beam atomic absorption spectrometer following preconcentration by anion exchange chemistry from sample collected in the east Pacific (Goldberg et al., 1986); (2) a scavenged-type profile was determined by cathodic stripping voltammetry following sample irradiation with UV for samples collected in the Indian Ocean (Jacinto and Van Den Berg, 1989); (3) a conservative profile was determined by isotope dilution based on an investigation of Atlantic and western Pacific waters (Colodner, 1991).

A nutrient-type profile is controlled by biological cycles within the upper ~ 100 m (photic zone) of the water column. An element with a nutrient-type profile is depleted in the photic zone by uptake by organisms and biogenic particles. The organisms and biogenic particles undergo decomposition or dissolution as they descend through the water column releasing the element back into the water column at depth e.g. zinc (Bruland and Lohan, 2006). A scavenged-type profile is controlled by the reactive nature of the element in the water column. The highest concentration of a scavenged-type element is located proximal to its source. If the source is riverine or aeolian, such as aluminum, the highest concentration is in surface waters and decreases through the water column as the element interacts with particles (Bruland and Lohan, 2006). A conservative profile shows little variation with depth as the conservative-type element has weak interactions with particles and biological cycles, resulting in a long residence time (> 10 Kyr; Bruland and Lohan, 2006).

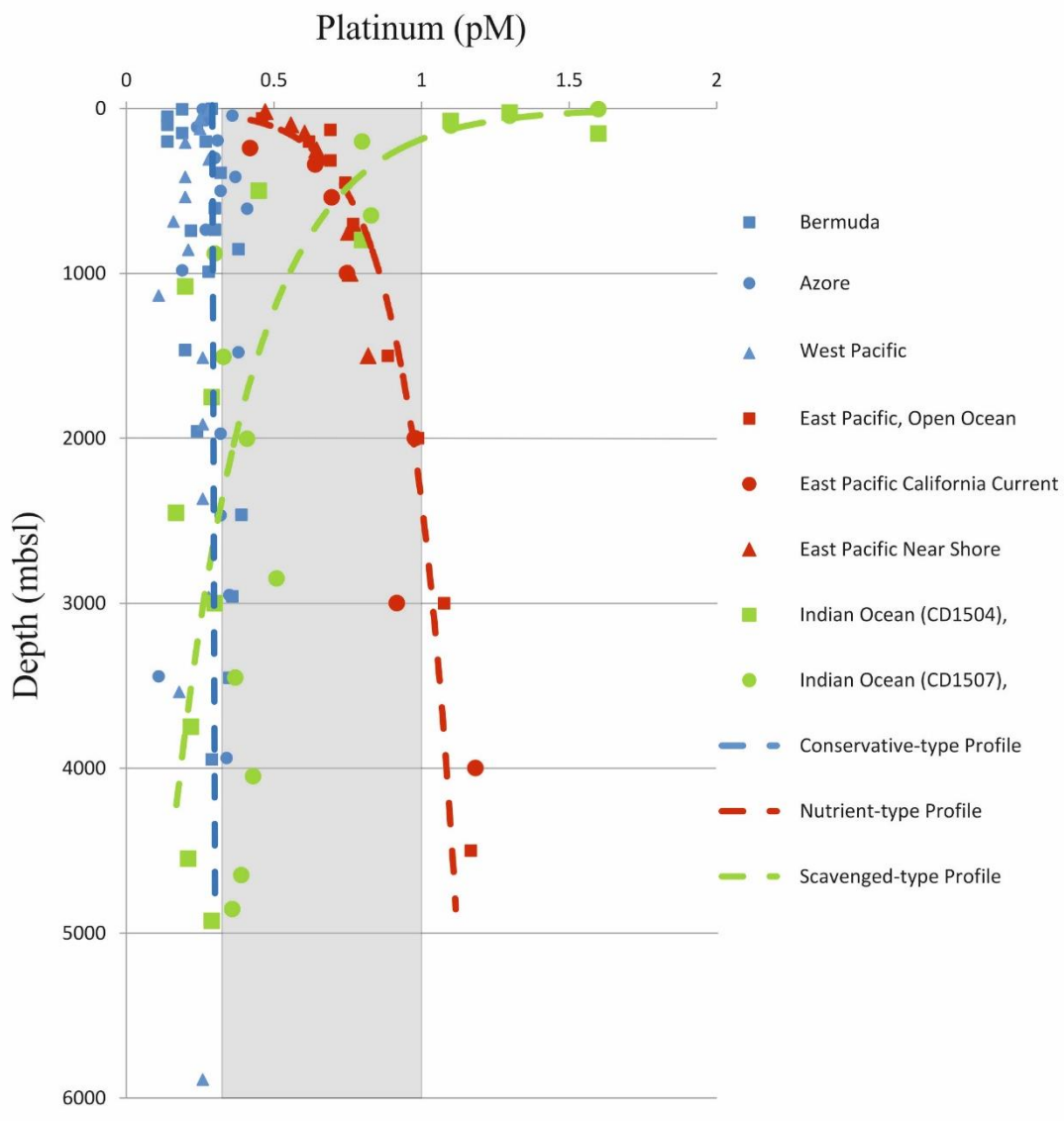

Figure 1.3 Mean platinum concentration (picomolar) and profile of the two locations from the Atlantic; Bermuda profile, W Atlantic, and Azores profile, E Atlantic (Colodner, 1991), four locations from the Pacific; Western Pacific (Colodner, 1991), open ocean, E Pacific, near shore, E Pacific, and California Current, E Pacific (Goldberg et al., 1986) and two locations from the Indian Ocean; CD1507, west Indian, and CD1504, south west Indian (Jacinto and Van Den Berg, 1989). The grey shaded area represents the range of mean platinum concentration for the three ocean basins. Modified from Colodner (1991).

Platinum concentrations appear to vary significantly from basin to basin, particularly in the upper 1,000 m with a range of 0.2 – 1.5 pM, whereas the Atlantic and Indian Ocean platinum concentrations at > 1000 m depth are similar at ca. 0.3 pM (Colodner, 1991, Goldberg et al., 1986, Jacinto and Van Den Berg, 1989). The disparity in profiles could be the result of the Indian Ocean receiving a larger aeolian flux relative to the other basins, however, this is unlikely based on global flux models, which show that the northern Atlantic Ocean receives nearly double the aeolian flux of the Indian (Jickells et al., 2005). Ravizza et al. (2001) and Colodner (1991) suggested that the large range in concentration and the variation in profiles could be a result of analytical artefacts rather than natural variation as all three studies used different analytical methodologies. However, as the studies do not have any localities in common, it is not possible to make a direct comparison of the methodologies and the variations may be real.

As with most aspects of platinum in the marine environment the residence time of platinum in the ocean is also not well constrained, with estimates ranging from 16 kyr to 1 Myr (Goldberg et al., 1986, Soyol-Erdene and Huh, 2012). The lowest residence time is based on calculations of source input fluxes, whilst calculations based on platinum sinks give intermediate residence times of 33–100 kyr. The longest estimated residence time of 1 Myr was based on the perceived stability of platinum in the marine environment (Colodner, 1991, Goldberg et al., 1986, Soyol-Erdene and Huh, 2012). Although there is a large range of proposed residence times (16 kyr to 1 Myr) they are all significantly longer than the ocean mixing time, as full homogeneity of elemental concentration, and isotope ratios, in the deep ocean is thought to be achieved in 1.6 kyr (Bruland, 1980).

The speciation of platinum in seawater has not been measured directly but has been derived experimentally and modeled (estimated) from thermodynamic data for various chlorine concentrations at 25° C (figure 1.4). The predominant oxidation state of dissolved platinum in seawater is thought to be Pt^{2+}, based on experimentally derived stability constants (Elding, 1978, Goldberg et al., 1986, Halbach et al., 1989, Hein et al., 1988, Koschinsky et al., 2005, Wood, 1991, Wood et al., 1992). Elding (1978) and others have suggested that the dominant species are halide complexes, in particular $PtCl_4^{2-}$, based on its high stability constant relative to other complexes and the availability of Cl^- in seawater (Elding, 1978, Goldberg et al., 1986, Halbach et al., 1989). The high stability constant of $PtCl_4^{2-}$ has been used to calculate the long residence time of 1 Myr suggested by Goldberg et al. (1986). More recent studies have suggested the importance of the hydroxyl complex, $Pt(OH)_{2(aq)}$, at pH values greater than 7.5, $\Sigma Cl^- \approx 0.6$ M (figure 1.4; Sassani and Stock, 1998, Wood et al., 1992). Given the current thermodynamic data, this would suggest that at depth in the modern marine environment at pH ≈ 7.8, platinum may be available as $PtCl_4^{2-}$ and $Pt(OH)_2$ (figure 1.4).

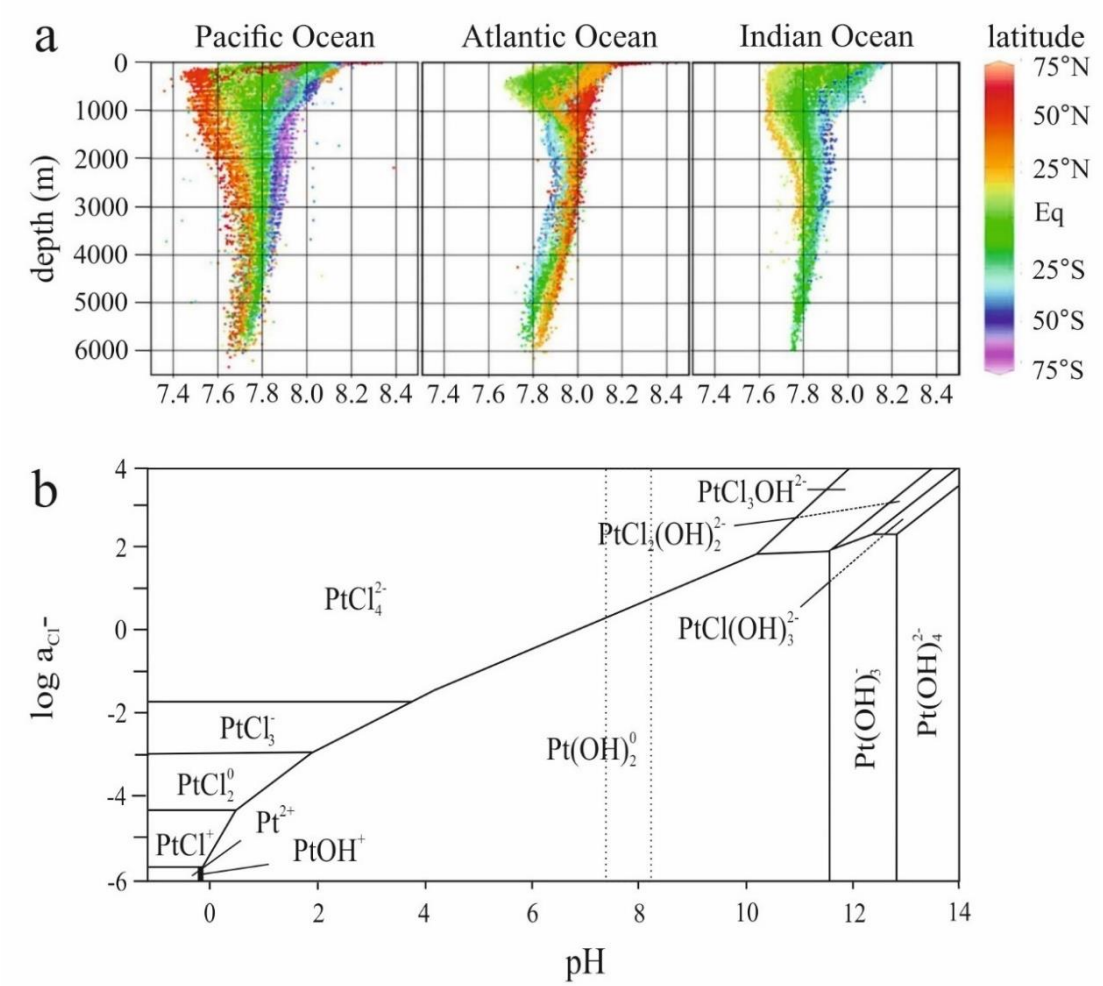

Figure 1.4 (a) pH profile with depth (m) for the Pacific, Atlantic, and Indian Ocean. The colours represent the different pH observed at various latitudes, modified from Pelejero et al., 2010. **(b)** Plot of log a_{Cl^-} versus pH for the Pt-Cl-O-H system showing the stability fields of the various chloride, hydroxide and mixed hydroxychloride complexes. The dashed lines represent the range of pH values found in the modern oceans. The dominant oxidation state of Pt at or near neutral pH is divalent with both $PtCl_4^{2-}$ and $Pt(OH)_2$ present in the marine environment at the pH of seawater and ΣCl^- (ca. 0.6 M). Modified from Wood et al. (1992).

1.33 Platinum sinks in the marine environment

In the modern oxic marine environment, the largest sink for platinum are FMS, which precipitate directly from seawater and are found throughout all ocean basins (figure 1.5; Hein et al., 2014). Platinum is enriched in these authigenic sediments (6–940 ng/g; average = 245 ng/g) compared to pelagic sediments (0.6–21.9 ng/g, average = 3 ng/g; Goldberg et al., 1986). FMS that are older or formed in shallow water depths tend to have higher platinum concentrations than modern FMS, or those that formed in deeper waters (Halbach et al., 1989).

As well as platinum, other trace metals are concentrated in FMS relative to UCC, for example, Te, Ce, and Tl are 10, 50, and 1700 times more enriched in FMS than UCC, respectively (Goldberg et al., 1986, Hein et al., 2012). The combination of the slow growth, direct precipitation from seawater and enrichment in trace metals, drives interest and research on FMS as both potential resources of economic value and long-lived archives of ocean chemistry (e.g. Goldberg et al., 2009, Hein et al., 2014, Rehkämper et al., 2002).

Many metals, for example, Fe, Mo, Tl, and Ni, have been investigated in ferromanganese sediments due to their potential to record variations in metal concentration and isotopic signature over geological time. The variations are recorded in ferromanganese sediments due to their slow growing nature and the incorporation of metals directly from the water column, which allows them to act as an archive of ocean chemistry (chapter 1.331). Therefore, if there is a decrease in the source of metal to the ocean, for example, during glaciation or if the redox condition of the ocean changes, this can be recorded in ferromanganese sediments.

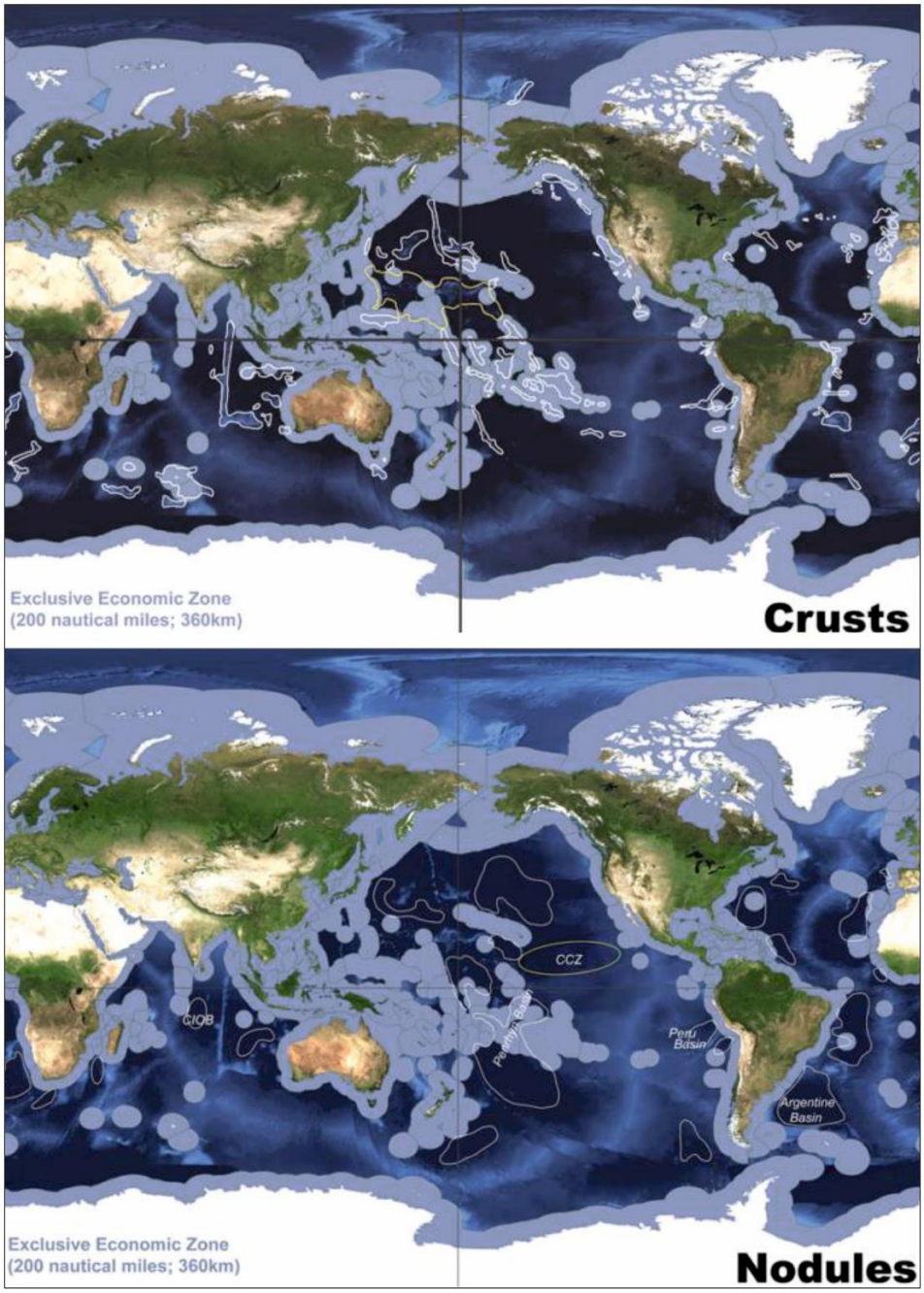

Figure 1.5 Global distribution of the main areas of ferromanganese crusts and nodules. The grey shaded area represents exclusive economic zones. FMC and FMN are found throughout the world's oceans, however, the white lines enclose areas rich in FMC and FMN. The areas enclosed by a yellow line represent the areas of highest economic potential; Prime Crust Zone (PCZ) for FMC and Clarion-Clipperton Zone (CCZ) the largest FMN field. Modified from Hein (2014).

1.331 Fe-Mn sediment formation and description

There are five key morphological types of FMS: 1) crusts (FMC), 2) nodules (FMN), 3) sediment-hosted stratabound layers and lenses, 4) cements, and 5) mounds and chimneys (Hein et al., 1997). However, for the purpose of this study only crusts and nodules are discussed. FMC and FMN are classified based on the source of the elements that form the deposit: hydrogenetic precipitation of metals from cold ambient bottom seawater; precipitation from hydrothermal fluids from ca. 89,000 km of oceanic spreading centers and volcanic arcs; and diagenetic i.e. precipitation from sediment pore water, however a combination of metal sources can contribute to the accumulation of an FMS (figure 1.6; Hein et al., 1997, Hein et al., 2013). The dominant formation process will dictate the FMS growth rate and the primary mineralogy observed and therefore the relative abundance of the various elements adsorbed onto FMS due to differing surface charges of the various colloidal phases (figure 1.7; Hein et al., 2012).

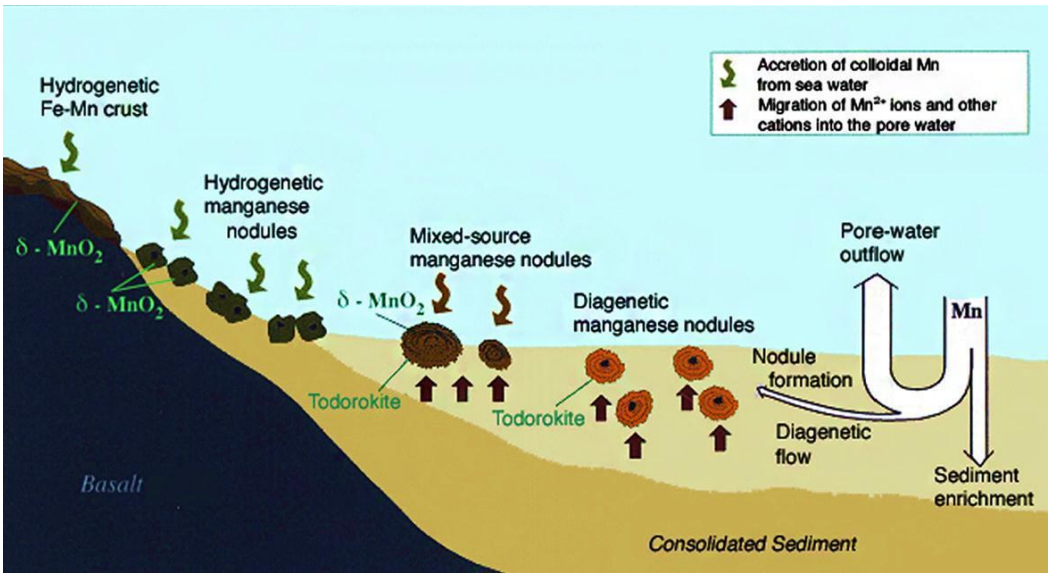

Figure 1.6 Formation of hydrogenetic, hydrothermal, and mixed origin FMS and the dominant mineral phase associated with the various forms of FMS, modified from Hein et al. (2013). Pure hydrogenetic FMS are located proximal to the seamount/abyssal slope with diagenetic influence increasing with distance away from the seamount to the diagenetic endmember.

The growth rate of the FMS increases from hydrogenetic, 1 – 5 mm/Myr, to diagenetic, which is up to 250 mm/Myr. The fastest growing FMS are hydrothermally sourced deposits due to the abundance of Fe and Mn (Hein et al., 1997). The primary mineral phase associated with hydrogenetic FMC and FMN is Fe–vernadite (δ-MnO_2), with lesser amounts of Mn–feroxyhyte, (δ-FeO(OH)), whereas 10 Å manganite (todorokite) and minor amounts of 7 Å manganite (birnessite) and δ-MnO_2 are associated with hydrothermal FMC and FMN. The primary phase associated with diagenetic deposits is todorokite. In addition to the primary mineral phases, both FMC and FMN contain varying amounts of goethite and detritial grains such as quartz and feldspar. Deposits > 10 Myr have a secondary mineral, carbonate fluorapatite (CFA), which is attributed to a more pronounced paleo-oxygen minimum zone (OMZ) from increased surface water bio-productivity (Halbach et al., 1984, Halbach et al., 1989, Hein et al., 1997, Lyle, 1978). The OMZ refers to zones in the ocean where the water column is depleted in oxygen. The exact depth can vary spatially but it typically occurs between 200 m to 2000 m water depth (Hein, 2014, Takahashi et al., 2014). The oxygen depletion is caused by plankton and other organic matter descending through the water column from the photic zone and being oxidized, which removes oxygen.

The enrichment of various elements in FMS is dependent both on the different accumulation rates and on the origin of the metal; hydrogenetic, diagenetic or hydrothermal i.e. the mechanism of ferromanganese growth (Hein et al., 1997, Hein et al., 2013). In general, the slower the accumulation rate, the more trace elements will be removed from the water column and onto the FMS. Figure 1.7 illustrates a simplified electrochemical model to illustrate how various hydrogenetic and hydrothermal sourced elements are scavenged from the water column. As dissolved Mn and Fe migrate from oxygen – poor environments, e.g. OMZ, to oxygen – rich zones, they become oxidized and forms solid phases (colloidal particles), primarily MnO_2 and FeOOH, which slowly settles out of the water column (Glasby, 2000, Hein et al., 1997, Hein et al., 2013). As the solid phases descend through the water column, cations adsorb onto the negatively charged MnO_2, while anions, neutral elements and large complexes adsorb onto the slightly positive FeOOH (Koschinsky and Hein, 2003). Diagenetic FMS form through the remobilization of Mn and other elements

from the surrounding sediment pore fluid rather than directly from seawater. Elements and complexes incorporated onto FMS from a diagenetic source do not directly show the seawater chemistry as the diagenetic elements undergo chemical reactions with the enclosing sediments.

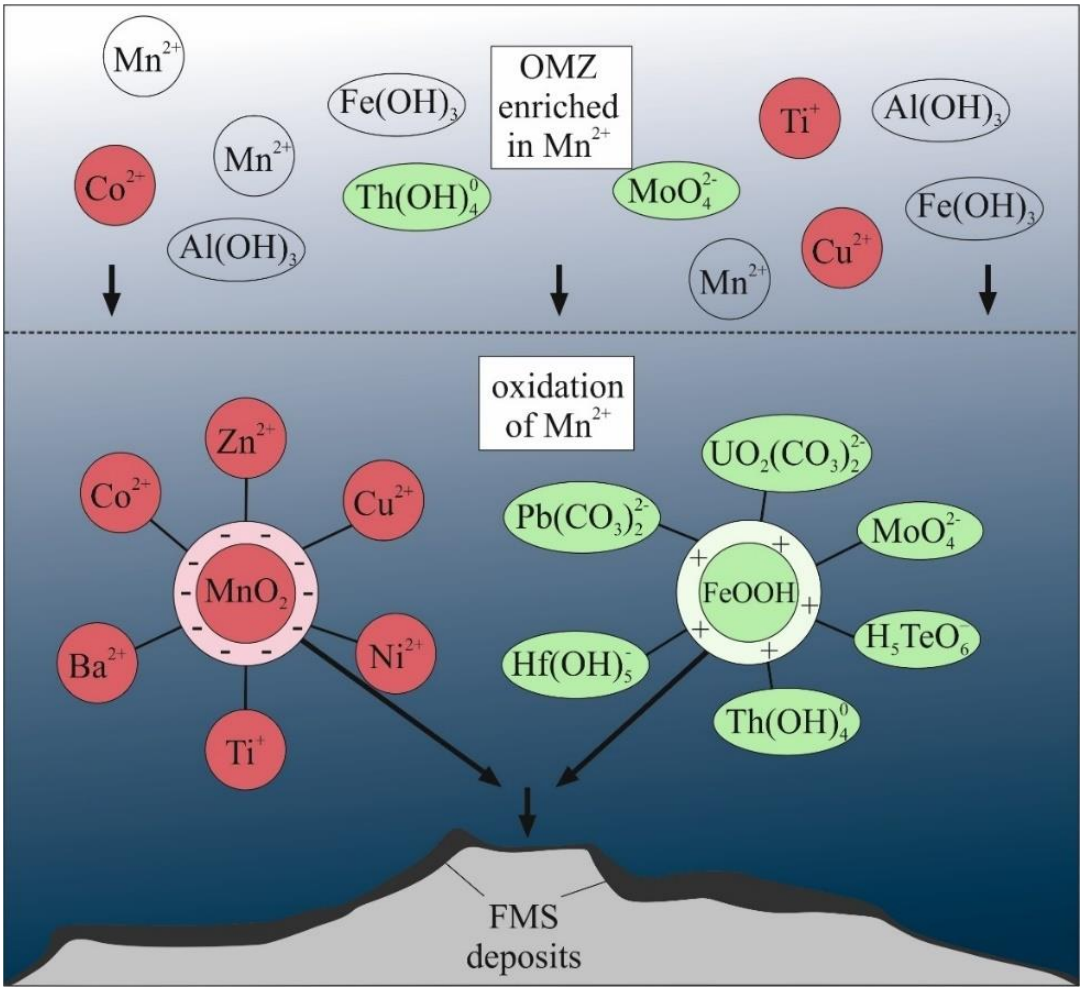

Figure 1.7 Simplified electrochemical adsorption of various elements and complexes onto MnO_2 and FeOOH. The dashed line represents the transition zone from OMZ and oxygen rich deep ocean, where Mn^{2+} is oxidized and colloidal phases form and precipitate onto the substrate. Modified from Koschinsky and Halbach (1995).

Hydrogenetic crusts and nodules are typically enriched in Bi, Mo, Nb, Pt, REE, Te, Th, Ti, W, Y and Zr, whereas diagenetic nodules are relatively enriched in Ni, Cu and Li (Hein et al., 2012, Hein et al., 2013). The abundance of trace metals in hydrothermal crusts is dictated by the composition and abundance of metals in the hydrothermal waters: a consequence of the leaching and composition of the country rock surrounding the hydrothermal vent system, rather than sorption of metals from the water column (Hein et al., 1997).

Fe-Mn crusts are found throughout the world's oceans at water depths of 400 – 7,000 m, with the most metal rich FMC, in particular Ni, Co and Mo, found between 800 – 2,500 m (figure 1.5; Hein, 2014). FMC range in thickness from < 1 to 260 mm, with thicker FMC typically found on older substrates, which have had a longer time to accumulate (Hein et al., 2013, Usui and Someya, 1997). FMC grow on a solid substrate in areas of low to nil sedimentation, allowing the slow accumulation of the FMC over time. The Pacific Ocean has a larger occurrence of FMC relative to the Indian and Atlantic Oceans due to abundance of suitable areas of accumulation i.e. seamounts, ridges, and plateaus (Hein et al., 2013). Hydrogenetic FMC from different ocean basins tend to have different Fe/Mn ratios, with higher manganese concentrations seen in the open Pacific Ocean, Fe/Mn ≈ 0.73 (n = 368), and higher iron concentrations in the Pacific continental-margins and the Atlantic and Indian Oceans, with Fe/Mn ratios of 0.83 (n = 286), 1.44 (n = 43), and 1.32 (n = 23), respectively (Hein et al., 1997). Hydrothermal deposits can range from nearly pure Fe hydroxide to Mn oxide endmembers near the vents, however, these deposits generally form stratabound deposits rather than FMC. The more distal hydrothermal waters are from the vent system, the more mixing with seawater that occurs, resulting in crusts of mixed origin (Lyle, 1978, Hein and Koschinsky, 2013). The FMCs with the highest economical potential are found in an area known as the Prime Crust Zone (PCZ) in the central and western equatorial Pacific (figure 1.5). These have relatively high concentrations of trace metals as a result of their distance from sources of contamination, such as, detrital material from a continental source and hydrothermal input, which would increase the growth rate and therefore not allow adequate time for the adsorption of REE and other trace metals (Hein et al., 1997, Hein et al., 2013, Usui and Someya, 1997).

FMN are found throughout the world's oceans predominately at water depths of 3,500 – 6,500 m, however, they can occur at shallower depths (figure 1.5). FMN form on any sediment covered substrate/consolidated ground with sedimentation rates lower than < 10 cm/kyr (Hein et al., 1997, Hein et al., 2012). FMN accumulate in a similar manner to FMC, however FMN require a nucleus, which can be a rock fragments, calcareous or siliceous tests, shell, shark teeth, coral and glass, all of which have been observed (Burns, 1975, Hein, 2014, Stoffers et al., 1984). It has been proposed that a layer of hydrated iron oxide precipitates onto the nucleus as a result of a localized increase in pH due to the dissolution and hydrolysis of the carbonate, silicate, and phosphate anions surrounding the nucleus. This hydrated iron oxide layer then accumulates MnO_2 and FeOOH similar to the FMC (Burns, 1975).

FMN are classified based on both the origin of the metals, similar to FMC, and the size of the nodule; FMN are defined as nodules with a diameter greater than 10 mm, whereas micronodules have a diameter < 10 mm. Hydrogenetic FMN typically grow on seamount slopes and commonly have a large rock fragment as the nucleus (figure 1.6), whereas diagenetic FMN generally form on the well oxygenated abyssal plains and have a relatively small nucleus compared to the thickness of the authigenic deposit, with mixed origin FMN located between these two endmembers (Hein, 2014, Lyle, 1978). FMN have the ability to move relative to the substrate, however most FMN are buried either partially or completely. FMN exhibit variable Fe/Mn values with three to six times more Mn than Fe due to the diagenetic influence observed in most FMN. The FMN with the highest economical potential and largest nodule field are found in an area known as the Clarion-Clipperton Zone (CCZ) in central Pacific Ocean (figure 1.5).

Micronodules have similar characteristics to FMN, and are typically found in deep water settings with low sedimentation rates (Banerjee and Iyer, 1991, Lyle, 1978). Micronodules form solely due to diagenetic processes within the sediment column and the abundance of micronodules decreases with increasing depth within the sediment column (Banerjee and Iyer, 1991). The Fe/Mn ratio of micronodules are related to the depth within the sediment column at which the micronodules grew, with the upper ca. 15 cm being Mn-rich, whereas, deeper micronodules are Fe-rich (Banerjee and Iyer,

1991. Banerjee and Iyer (1991) proposed that dissolution of Mn at depth followed by upward diffusion results in the abundance of Mn-rich micronodules in the upper sediment column and relative enrichment of Fe with depth. Considering micronodules grow within the sediment column from diagenetically sourced metals and therefore do not directly represent the seawater chemistry at the time of accretion, they will not be discussed further in this study.

1.332 Concentration and incorporation mechanisms of platinum onto Fe-Mn sediments

Platinum is enriched in FMS as compared with other PGE, for example, the Pt/Pd ratio in seawater is 4.5, whereas analysis of an FMC from the western Pacific Ocean yielded a Pt/Pd ratio of up to 1300 (Hodge et al., 1985). This enrichment of platinum relative to other PGE has been coined the 'platinum anomaly' (Hodge et al., 1985). The platinum anomaly is similar to the cerium anomaly where cerium is also enriched relative to adjacent light REE (figure 1.8; Takahashi et al., 2000). In the case of Ce, this is attributed to it being the only REE that can be adsorbed onto the surface of MnO_2 through the surface oxidation of Ce^{3+} to Ce^{4+}.

Assuming Pt^{2+} ion is the dominant species in seawater, two mechanisms have been proposed for the incorporation of platinum onto FMS: 1) reduction of Pt^{2+} and co-precipitation with MnO_2 or oxidation and 2) surface adsorption of Pt onto MnO_2, similar to the mechanism proposed for Ce (Halbach et al., 1984, Halbach et al., 1986, Halbach et al., 1989, Hein et al., 1988, Hein et al., 1997, Hodge et al., 1985)

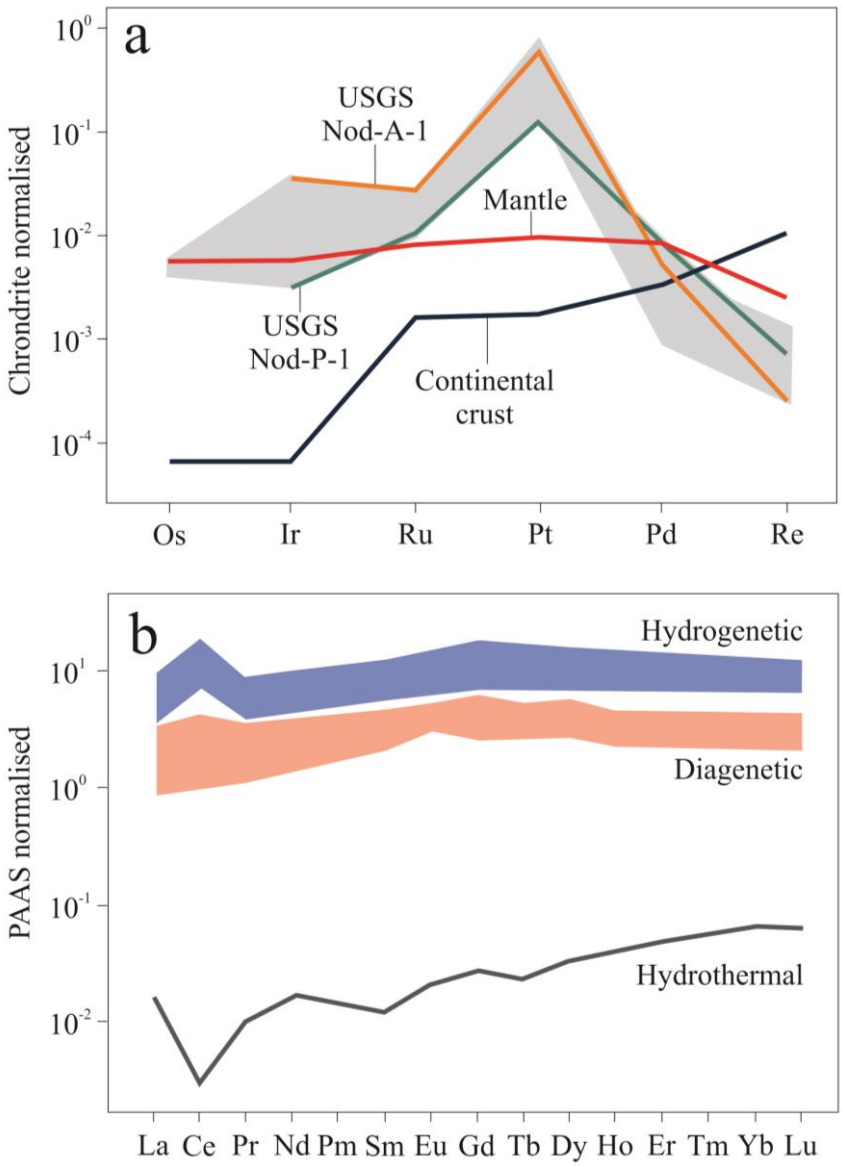

Figure 1.8 (a) Chondrite normalised PGE and Re data for mantle, continental crust, and nodule standards, USGS Nod-A-1 and USGS Nod-P-1. The grey shaded area represents the field of concentrations of PGE and Re of FMS from the Bollons nodule field, and Marshall Islands region of the Pacific Ocean. It shows the enrichment of platinum relative to the other PGE elements, known as the platinum anomaly. Modified from Baker et al. (2004). **(b)** PAAS normalised REE diagram for hydrogenetic, hydrothermal, and diagenetic FMS. A field of concentrations is given for both hydrogenetic (blue) and diagenetic (orange) FMS collected from the Central and NW Pacific Ocean. Modified from Takahashi et al. (2007).

The first proposed mechanism involving the reduction of Pt^{2+} to Pt^0 (Halbach et al., 1989) is based on combining two half-reactions: the reduction of Pt^{2+} in seawater to Pt^0 (equation 1.1) and the oxidation of Mn^{2+} to MnO_2 (equation 1.2) resulting in MnO_2 and Pt^0 co-precipitating from the water column (equation 1.3; Halbach et al., 1984, Halbach et al., 1986, Halbach et al., 1989, Hodge et al., 1985).

$$PtCl_4^{2-} + 2e^- \rightarrow Pt^0 + 4\,Cl^- \qquad (1.1)$$

$$Mn^{2+} + 2H_2O \rightarrow MnO_2 + 2e^- + 4H^+ \qquad (1.2)$$

$$Mn^{2+} + PtCl_4^{2-} + 2H_2O \rightarrow MnO_{2(s)} + Pt^0_{(s)} + 4Cl^- + 4H^+ \qquad (1.3)$$

For these half-reactions to take place there has to be a substantial amount of Mn^{2+} available and an oxygen-poor environment to hinder the oxidation of Mn^{2+}, such as in an OMZ. The concentration of Mn^{2+} in the modern OMZ is < 5 nmol/kg, which has been shown to be insufficient in Mn^{2+} for the required half reactions to occur (Halbach et al., 1989). Consequently, this mechanism does not explain the enrichment of platinum in FMS in the current ocean or over a large portion of the growth history of FMS (Halbach et al., 1989, Hein, 1999). However, this mechanism may be responsible for the higher platinum concentration identified in older generations of FMC. For example, Halbach et al. (1989) observed ~ 2 times more platinum in the older generation of FMC from the central Pacific Ocean, > 10 Myr, relative to the younger generation of FMC from the same location, 0.65 µg/g and 0.36 µg/g, respectively. This has been attributed to a more pronounced paleo-OMZ, resulting in higher Mn^{2+} concentrations and thus allowing the half-reactions to proceed (Halbach et al., 1989). This interpretation is supported by the impregnation of the older generation of FMC by carbonate fluoroapatite (CFA). CFA alteration has been suggested to be related to a more pronounced paleo-OMZ and an increase in phosphorus, derived from intense continental chemical weathering due to prolonged warm climatic conditions, and accumulated in the OMZ (Halbach et al., 1989, Hein, 1999, Hein et al., 2003, Koschinsky et al, 1997).

The second and most widely cited mechanism is through the surface oxidation of Pt^{2+} to Pt^{4+} on MnO_2 (Hein et al., 1988, Hein et al., 1997, Hodge et al., 1985, Koschinsky et al., 2005). This calls on a similar mechanism to that producing the Ce anomaly (Hodge et al., 1985, Ohta and Kawabe, 2001). In this scenario, platinum in its dissolved form, Pt^{2+}, undergoes oxidization on the MnO_2 surface to Pt^{4+} with Mn^{4+} in the MnO_2 being reduced to Mn^{2+}. Equation 1.4 expresses a simplified reduction of MnO_2.

$$MnO_2 + 4H^+ + 2e^- \rightarrow Mn^{2+} + 2H_2O \qquad (1.4)$$

Equations 1.5 and 1.6 show the simplified oxidation of $PtCl_4^{2-}$ and $Pt(OH)_2$, respectively.

$$PtCl_4^{2-} + 2H_2O \rightarrow PtO_2 + 4Cl^- + 4H^+ + 2e^- \qquad (1.5)$$

$$Pt(OH)_2 \rightarrow PtO_2 + 2H^+ + 2e^- \qquad (1.6)$$

By combining equations 1.4 and 1.5 a simplified expression of the coupled redox reaction can be described for the surface adsorption of $PtCl_4^{2-}$ (equation 1.7).

$$PtCl_4^{2-} + MnO_2 \rightarrow PtO_2 + Mn^{2+} + 4Cl^- \qquad (1.7)$$

And by combining equation 1.4 with equation 1.6 a simplified expression of the coupled redox reaction can be described for the surface adsorption of $Pt(OH)_2$ (equation 1.8).

$$Pt(OH)_2 + MnO_2 + 2H^+ \rightarrow PtO_2 + Mn^{2+} + 2H_2O \qquad (1.8)$$

The mechanism of incorporation of platinum onto FMS will be discussed further in chapter 3.

1.333 Global platinum concentration in Fe-Mn sediments

There have been a number of studies undertaken to measure the platinum concentration of FMS, primarily focusing on the Pacific Ocean where the Prime Crust Zone (PCZ) and Clarion-Clipperton Zone (CCZ), which have the greatest economic potential, are located (Table 1.5). Hein et al. (1997, 2000, 2003, 2013) suggested that the average global Pt concentration in FMC is 0.7 µg/g with a basinal variation observed. The platinum concentration is higher in the west Pacific (2.6 µg/g for an individual sample), that decrease towards both the North American margin and proximal to the west Pacific Arc (Hein et al., 1997). The decrease in Pt observed along the North American margin is attributed to the influence of detrital material from the continental shelf, whereas, the decrease seen proximal to the Pacific Arc is related to hydrothermal influences i.e. the growth rate of the hydrothermally influenced FMC outpaces the incorporation of platinum onto the surface (Banakar et al., 2007). Halbach et al. (1984) undertook a study on FMN from the Central Pacific, and reported a mean Pt concentration of .42 µg/g, with both Pt and Ni showing a positive correlation with Mn, suggesting that Pt and Ni are incorporated in the Mn oxide fraction. It was also noted that crusts from shallow water depths and older generation FMC (> 10 Myr) have a higher concentration of platinum, 0.63 µg/g, than younger generation FMC, 0.39 µg/g (Halbach et al., 1984, Halbach et al., 1989).

Table 1.3 Mean platinum concentration complied by Hein et al., 2013

Atlantic	Indian	N. Pacific PCZ	N. Pacific Non-PCZ	South Pacific	Calf margin	Pacific CCZ	Peru Basin
µg/g (n)	µg/g (n)	µg/g (n)	µg/g (n)	µg/g (n)	µg/g (n)	µg/g (n)	µg/g
0.57 (2)	0.21 (6)	0.48 (66)	0.23 (24)	0.46 (15)	0.07 (23)	0.13 (12)	0.04

The number of analysis (n) for each sample location is given in the parentheses after the concentration data.

1.4 Non-traditional stable isotopes in the marine environment

The slow growth rate of FMS along with the ability to date individual layers within the FMS using ^{10}Be, results in the FMS being ideal hydrogenetic metal records of ocean chemistry spanning several tens of millions of years. Following advances in analytical instruments, in particular MC-ICP-MS, over the past two decades, measurements of the stable isotopes of 'non-traditional' elements such as Fe, Ni, Cu, Zn, Mo, and Tl have become possible (Anbar, 2004, Barling and Anbar, 2004, Beard et al., 2003, Bermin et al., 2006, Cameron and Vance, 2014, Gall et al, 2013, Levasseur et al 2004, Marechal et al., 2000, Mathur, 2005, Rekamper et al., 2002, Rekamper et al., 2004, Siebert et al., 2003, Zhu et al 2000, Zhu et al., 2002).

Physicochemical reactions in nature can lead to fractionations in the relative ratios of stable isotopes of an element in coexisting phases, with one phase favouring lighter isotopes and another favouring heavier isotopes. At low temperatures isotope distributions are primarily due to equilibrium and kinetic fractionation (figure 1.9).

Equilibrium fractionation occur in a reversible reaction, where the forward and backward reaction rates of the isotopes in the system are the same i.e. equilibrium constant. Equilibrium fractionation relates directly to the mass differences among different isotopes of an element. Variations in the vibration of different isotopes with mass (zero-point energy) leads heavier isotopes to form stronger bonds than lighter isotopes in compounds (lower energy; Bigeleisen, 1965, Urey, 1947). Therefore, fractionation is associated with the substitution (exchange) of heavier isotopes for lighter isotopes to lower the energy of the system i.e. lighter isotopes are more volatile. As temperature increases equilibrium fractionation effect decreases due to the difference in the zero-point energies decreasing. An example of equilibrium fractionation occurs during the condensation of water. Liquid water in equilibrium with water vapour in a closed system will result in the water vapour becoming isotopically lighter in $\delta^{18}O$ than the liquid water. The enrichment of one phase relative to another can be expressed as the fractionation factor, α (equation 1.9).

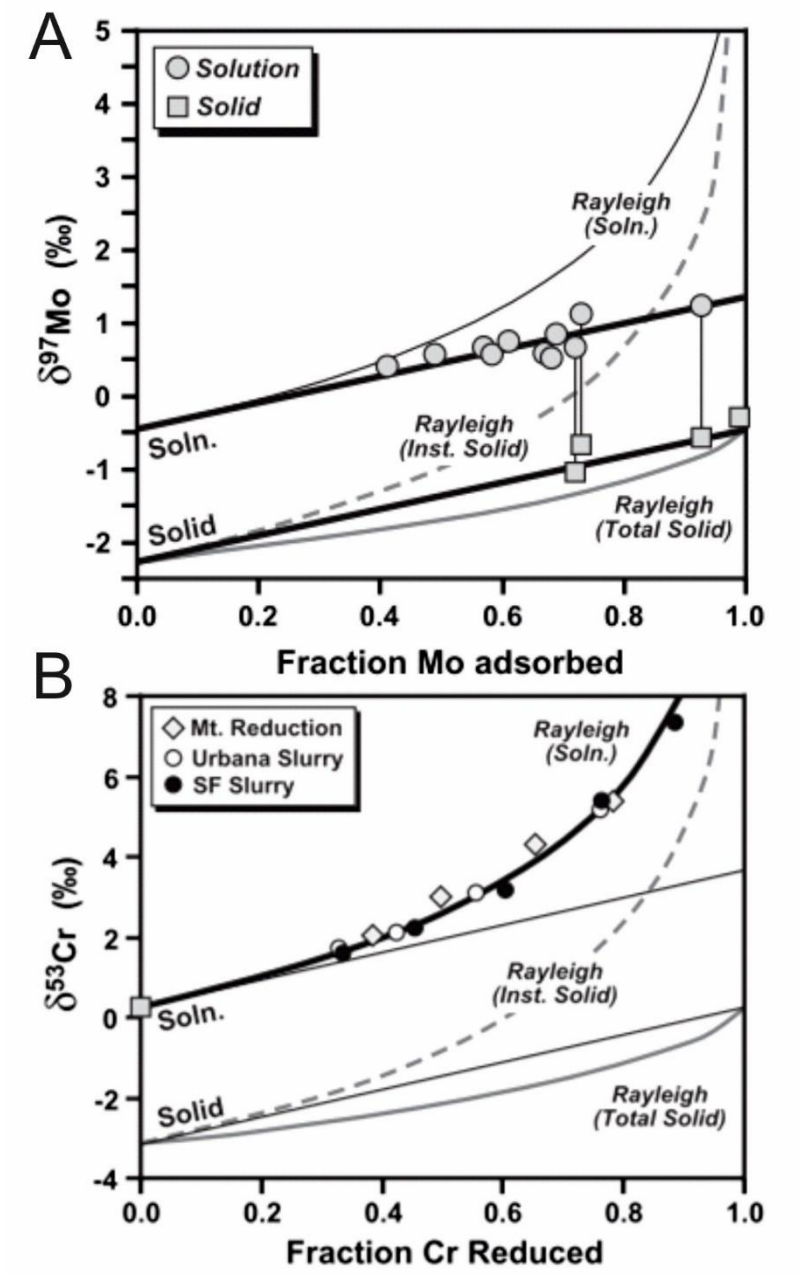

Figure 1.9 A) δ^{97}Mo of Mo adsorbed onto MnO_2 surface as a function of Mo adsorbed. The solution and solid samples follow a linear trend (solid black lines) indicating the isotopic equilibrium is continuously maintained between the solution and solids i.e. equilibrium fractionation. Modified from Barling and Anbar (2004). B) the kinetic fractionation observed in the δ^{53}Cr of solutions remaining as a function of Cr reduced. The samples plot along the exponential curve of the Rayleigh solution line due to isolation of the reduced Cr^{3+} to limit isotopic exchange. Modified from Ellis et al. (2002).

$$\alpha = (\delta_A + 1) / (\delta_B + 1) \quad (1.9)$$

If δ_A represents $\delta^{18}O_{(l)}$ and δ_B represents $\delta^{18}O_{(v)}$ then an $\alpha > 1$ implies $\delta^{18}O_{(l)}$ is enriched in the heavier isotope, whereas, an $\alpha < 1$ implies $\delta^{18}O_{(v)}$ is enriched in the heavier isotope. An $\alpha = 1$ means no fractionation was observed.

Kinetic fractionation is associated with varying rates of forward and backword reactions (i.e. unidirectional reactions), such as biologically mediated uptake of elements. The lighter isotope is preferentially utilised as lighter isotopes diffuse quicker. In addition, lower energy is required to break the bond relative to the heavier isotope bond (i.e. due to weaker bonds). For example, Zhu et al. (2002) have shown the preferential biological uptake of lighter Fe and Cu isotopes relative to heavier isotopes, with a -1.5 ‰ fractionation observed in Cu. Ellis et al. (2002) describes the kinetic fractionation associated with the reduction of Cr^{5+} to Cr^{3+} and precipitation (figure 1.9). When the Cr^{3+} precipitates it ceases to isotopically exchange with the aqueous Cr^{5+}, resulting in the remaining Cr^{5+} solution becoming exponentially heavier than the solid (Cr^{3+}).

This study represents the first examination of platinum stable isotopes applied to ferromanganese sediments. However, the stable isotopes of other transition metals have been applied to FMS as tracers of changing ocean chemistry and processes. In the following section, three of these systems, Fe, Mo, and Ni, will be discussed. The Fe, Mo, and Ni isotopic systems have received considerable attention as paleoceanography proxies, however all these systems are still relatively new and require significant additional information to complete the marine cycle of each element. The following sections are not an in-depth review of these systems, but rather a brief discussion to provide insight into what information can be gained from examining ferromanganese crust and nodules through both concentration and stable isotope data.

1.41 Iron stable isotopes in the oceans

The primary sources of iron to the ocean are rivers, aeolian (primary source to the open ocean), oceanic crust alteration, and diagenetic pore fluids from shelf sediments. It has been suggested that hydrothermally sourced iron is an important source and could account for up to 22 % of the deep oceans Fe budget and up to 30 % locally (Bennet et al., 2008, Tagliabue et al., 2010). The primary sink of Fe is hydrogenetic ferromanganese oxides (Beard et al., 2003, Severmann et al., 2008). The Fe isotope system consists of four stable isotopes; ^{54}Fe, ^{56}Fe, ^{57}Fe, and ^{58}Fe with the isotope composition normally expressed as δ^{56}Fe (equation 1.10).

$$\delta^{56}\mathrm{Fe} = [\ \frac{56}{54}\mathrm{Fe}_{(\mathrm{sample})} / \frac{56}{54}\mathrm{Fe}_{(\mathrm{IRMM\text{-}14})} - 1] \times 10^3 \qquad (1.10)$$

Fe isotopes can be fractionated in a number of ways including biotic and abiotic redox processes, such as abiotic Fe^{2+} oxidation and precipitation of ferric hydroxides, and sorption of aqueous Fe^{2+} onto ferric hydroxide. Fractionation can also be caused due to non-redox processes such as the mineral precipitation of Fe oxides. However, due to the quantitative removal of Fe (i.e. short residence time) from the water column, the isotopic composition of the Fe sinks are dictated by the δ^{56}Fe of the sources (figure 1.9; Anbar and Rouxel, 2007). Therefore, the temporal variation of δ^{56}Fe in ferromanganese crusts should indicate variations in Fe source to the marine environment. The δ^{56}Fe of igneous rocks and aeolian derived flux is ca. 0.1 ‰, whereas, rivers and groundwater compositions are isotopically lighter, -1 – 0 ‰ and < -1 ‰, respectively. The primary sinks are identical to the source (Anbar and Rouxel, 2007).

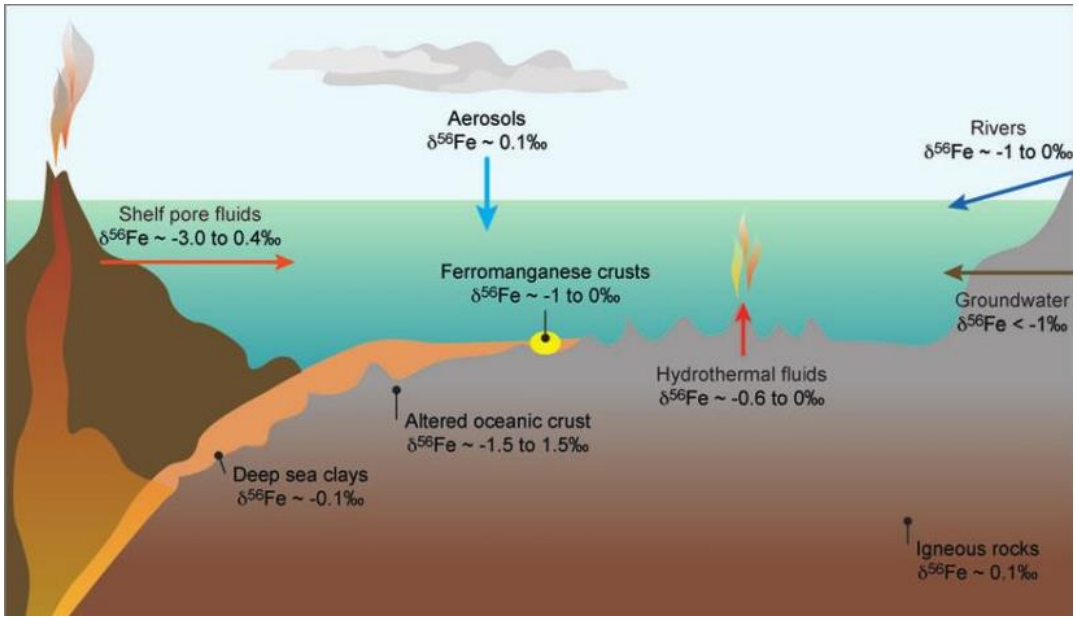

Figure 1.10 Marine cycle of the modern Fe stable isotope system. Modified from Anbar and Rouxel, 2007.

A number of studies investigating the δ^{56}Fe of ferromanganese crusts have shown a correlation between δ^{56}Fe and Pb isotopes (^{206}Pb/^{204}Pb), which has been used to trace sources of continental weathering, in particular over the past 2 Myr (Beard et al., 2003, Zhu et al., 2000). Zhu et al. (2000) examined a ferromanganese crust representing 6 Myr of accumulation from the North Atlantic Ocean and interrupted a decrease in both δ^{56}Fe and ^{206}Pb/^{204}Pb as a change in proportion of two continental sources of Fe and Pb to the marine environment. However, Beard et al. (2003) have suggested that this lighter δ^{56}Fe is a result of an increase in detrital load due to the Northern Hemisphere glaciation (i.e. increase in mechanical weathering and therefore riverine and atmospheric fluxes). A ferromanganese crust from the Pacific Ocean has shown a decrease in δ^{56}Fe with an increase in Mn, Mg, Ni, and Cu, suggesting the variation in δ^{56}Fe is due to an increase in hydrothermal input rather than continental flux (Chu et al., 2006). This is suggested to be a localised effect rather than basinal as it was not observed in ferromanganese crusts located 100 km away.

1.42 Molybdenum stable isotope in the oceans

In the modern oxic marine environment Mo is primarily available as molybdate, MoO_4^{2-}, with a concentration of 10.3 ± 0.48 (2σ) µg/L and a long residence time of 800 kyr (Anbar and Rouxel, 2007, Barling et al., 2001, Siebert et al., 2003). Due to the long residence time (800 Kyr), the oceans are suggested to be homogeneous for Mo (Barling and Anbar, 2004). The largest source of Mo to the marine environment is rivers with sulphide (anoxic) deposits and ferromanganese crust and nodules being the largest sinks.

The Mo isotope system consists of seven stable isotopes; ^{92}Mo, ^{94}Mo, ^{95}Mo, ^{96}Mo, ^{97}Mo, ^{98}Mo, and ^{100}Mo. The Mo isotopic composition is commonly reported as either ^{97}Mo/^{95}Mo (equation 1.11) or ^{98}Mo/^{95}Mo (equation 1.12), in delta notation with respect to in-house laboratory standards (Barling et al., 2001, Barling et al., 2004). For the purpose of this discussion the δ^{97}Mo notation will be used.

$$\delta^{97}\text{Mo} = [\ \frac{97}{95}\text{Mo}_{(\text{sample})} / \frac{97}{95}\text{Mo}_{(\text{standard})} - 1] \times 10^3 \qquad (1.11)$$

$$\delta^{98}\text{Mo} = [\ \frac{98}{95}\text{Mo}_{(\text{sample})} / \frac{98}{95}\text{Mo}_{(\text{standard})} - 1] \times 10^3 \qquad (1.12)$$

The mean δ^{97}Mo of sources and sink of Mo are shown in figure 1.11 with rivers showing a similar δ^{97}Mo to that of crustal values, ~ 0 ‰, suggesting generally there is no fractionation associated with continental weathering (Siebert et al., 2003). However, various Mo-rich minerals may not be isotopically uniform, therefore the mobile Mo may not be uniform (Anbar and Rouxel, 2007). The largest isotopic fractionation is associated with the incorporation of Mo onto MnO_2 in ferromanganese crust and nodules and suboxic sediments, with up to 2 ‰ offset from seawater (Barling and Anbar, 2004, and McManus et al., 2006). Both oxic and suboxic sediments are isotopically light sinks relative to seawater, whereas the fractionation associated with anoxic and euxinic sediments is not apparent due to the quantitative removal of Mo from seawater under these conditions. The suggested mechanism for the observed

fractionation is related to bonding environment rather than an oxidation change; where isotopically light Mo bonds are more readily broken, facilitating partitioning into the solid phase (Barling et al., 2004, Siebert et al., 2003).

An investigation of a suite of ferromanganese crusts from the Atlantic, Pacific, and Indian Oceans revealed that the Mo isotopic composition over the past ~ 60 Myr has been uniform with an offset of 0.5 ‰ (lighter) from seawater with a range of < 0.25 ‰ (Anbar and Rouxel, 2007, Siebert et al., 2003). This has been suggested to reflect a uniform seawater composition during the Cenozoic with ocean oxygenation varying less than 10 % over the 60 Myr time scale of the analysed ferromanganese crust and nodules (Siebert et al., 2003).

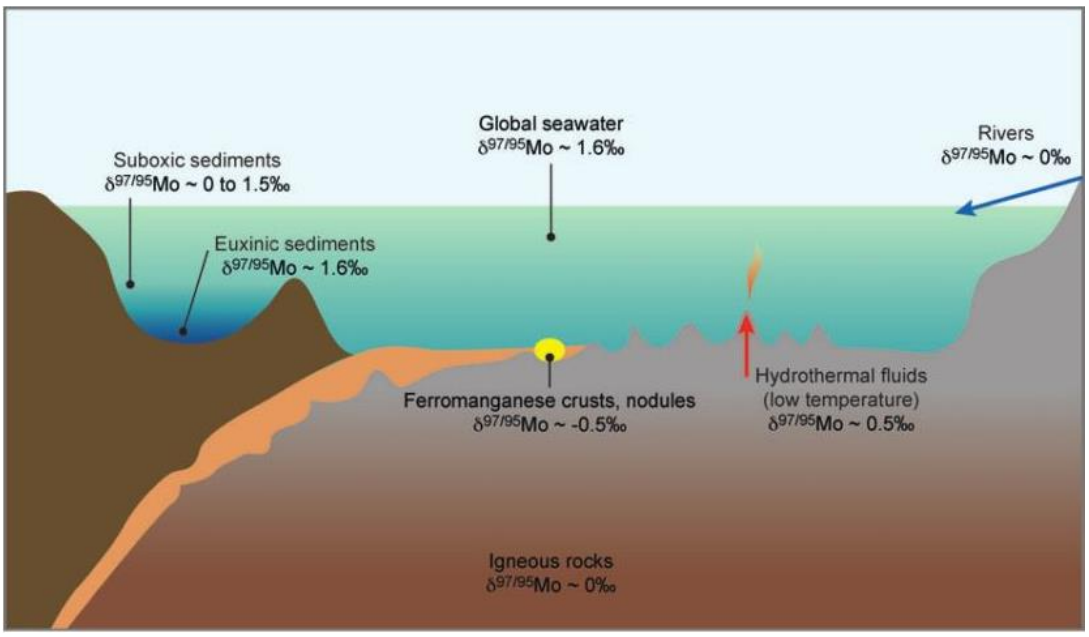

Figure 1.11 Marine cycle of the modern Mo stable isotope system. Modified from Anbar and Rouxel, 2007.

In anoxic to euxinic conditions molybdenum is more readily scavenged from seawater through the intermediary oxothimolybdate ion, which aids in the co-precipitation of Mo with insoluble sulphides. The removal of Mo in anoxic to euxinic environments would be (near) quantitative, and therefore no fractionation between seawater composition and that of anoxic and euxinic sediements should exist (Algeo and Lyons, 2006, Barling et al., 2001). Consequentially, temporal variations in Mo stable isotopes may reflect changes in oxygenation (redox conditions) of seawater at the time the sediment was deposited.

1.43 Nickel isotope in the oceans

In the modern oxic marine environment, Ni has a residence time of 4 – 10 kyr and displays a range of concentrations from 2 to 12 nmol/kg with a nutrient profile i.e. depletion in the photic zone due to biological uptake. Bottom water concentrations vary from 12 mnol/kg in the northeast Pacific to 5 nmol/kg in the Atlantic (Gall et al., 2013). The largest sources of Ni to the marine environment are rivers and aoelian input, approximately 40 % of the Ni budget each, with the remainder being supplied from hydrothermal sources. The largest sinks are ferromanganese crusts and pelagic sediments, with Ni associated with the MnO_2 in ferromanganese crusts and nodules through the adsorption of the hydrated Ni ion (Ni^{2+}) onto the negatively charged MnO_2 (Koschinsky and Halbach, 1995). However, recent studies have suggested $NiCO_3^0$ and $NiCl^+$ may play an important role, with these species accounting for over 50% of Ni in seawater (Glasby and Schulz, 1999).

The Ni isotope system consists of five stable isotopes; ^{58}Ni, ^{60}Ni, ^{61}Ni, ^{62}Ni, and ^{64}Ni. The Ni isotopic composition is commonly reported as $^{60}Ni/^{58}Ni$ (equation 1.13), in delta notation with respect to NIST standard reference material (SRM) 986:

$$\delta^{60}Ni = [\ \frac{60}{58}Ni_{(sample)} / \frac{60}{58}Ni_{(SRM\ 986)} - 1] \times 10^3 \qquad (1.13)$$

The riverine source of Ni to the marine environment is isotopically heavier than that of bulk continental crust, by up to 1 ‰, with the mean seawater composition being heavier again by ~ 0.5 ‰ (Cameron and Vance, 2014) The composition of modern ferromanganese crusts i.e. surface scrapings, is similar to that of seawater, with a mean δ^{60}Ni of 1.6 ‰ and a large range, 0.9 – 2.5 ‰. No intra-basin variation has been identified to date however (figure 1.12). A measured hydrothermal ferromanganese crust also has a Ni composition similar to seawater, suggesting that the hydrothermal flux to the marine environment is the same as seawater (Gall et al., 2013). All the ferromanganese crusts measured to date (hydrogenetic and hydrothermal) are similar to seawater suggesting no fractionation is observed during incorporation of Ni onto MnO_2 (Cameron et al., 2009, Cameron and Vance, 2014, Gall et al., 2012).

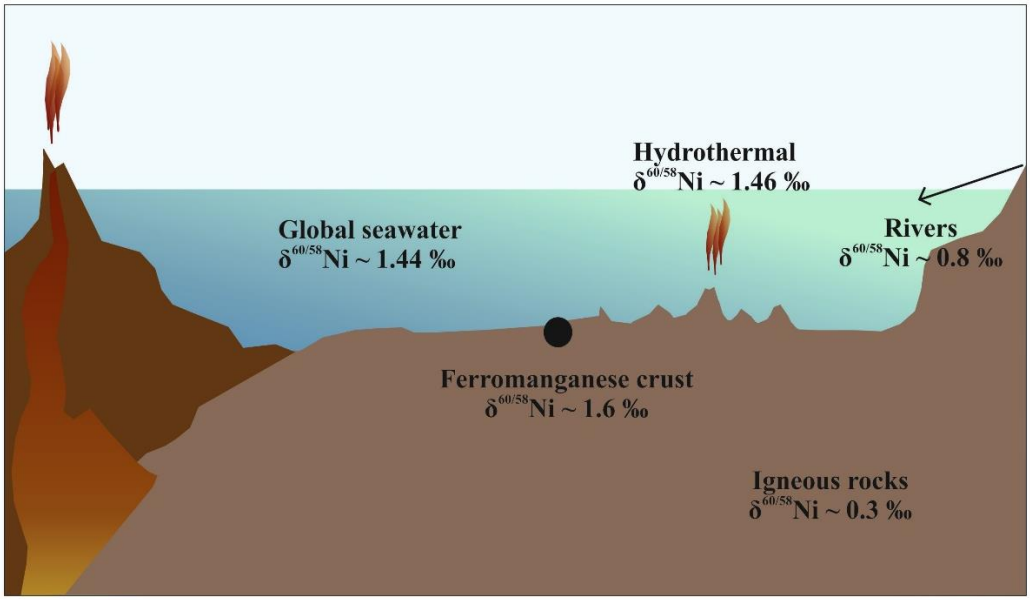

Figure 1.12 Marine cycle of the modern Ni stable isotope system. Modified from Anbar and Rouxel, 2007.

The large range of δ^{60}Ni identified for the ferromanganese crusts has been attributed to a number of possible mechanisms; preferential uptake of lighter Ni isotopes by biotic processes resulting in a localised heavier compositions in seawater. Alternatively, equilibrium fractionation between Ni species in seawater has been suggested, where the heaviest isotopes have been modelled to be associated with

carbonates, followed by sulphates, and hydroxide complexes associated with lighter isotopes (Fujii et al., 2011, Gall et al., 2013). Gall et al. (2013) have suggested that the most likely mechanism is source variation in isotopic composition (rivers and hydrothermal) and a recent study has reported a suite of global river samples with a wide range of δ^{60}Ni composition, 0.29 – 1.34 ‰ (Cameron and Vance, 2014), supporting this mechanism.

An investigation of a Pacific crust that represents accretion over the Cenozoic has shown that the mean Ni isotope composition through the crust is the same as in the surface scraping samples, suggesting that there has been no long term variation in Ni input into the Pacific Ocean. However, there is a correlation between MnO_2 content and δ^{60}Ni, with an increase of MnO_2 resulting in a heavier δ^{60}Ni. The increase in MnO_2 is interpreted to reflect an increase in hydrothermal activity, suggesting δ^{60}Ni can record fluctuations in hydrothermal fluxes to the marine environment.

1.5 Objectives and structure of this thesis

The primary aims of this study are to enhance our understanding of platinum in the marine environment and to develop a new isotopic proxy with which to track changes in ocean chemistry. This was approached through three separate but related questions:

1. *How is platinum incorporated into the sediment record, and what effect has the incorporation mechanism on the platinum stable isotope composition?*

2. *What variations are observed in platinum stable isotope chemistry in the modern oxic oceans?*

3. *Do platinum stable isotopes have potential as a marine geochemical tracer?*

To address the above questions, the following approach was undertaken;

A matrix-appropriate analytical technique was developed to isolate platinum from ferromanganese sediments with Pt yields of sufficient purity for analytical needs (chapter 2).

The mechanism of platinum adsorption onto ferromanganese sediments was investigated through laboratory adsorption experiments on synthesised iron oxy-hydroxides and manganese oxides. The platinum adsorption onto these synthesised sediments was evaluated using X-ray absorption techniques to determine the oxidation state, coordination chemistry and speciation of platinum. The platinum isotopic composition for the synthesised sediments was then analysed to determine the effect the adsorption has on the isotopic signature. (chapter 3).

To translate these results into the natural environment an estimate of the platinum isotopic composition of modern seawater is required, however the very low Pt concentration of seawater precludes direct measurement of seawater. Therefore, a first order evaluation of the input into the oceans was tackled via leaching experiments conducted on terrestrial rock samples to constrain the platinum isotopic composition of sources e.g. continental weathering (chapter 4).

Finally, a globally distributed suite of modern ferromanganese sediments was analysed to evaluate the spatial variations in Pt stable isotopes present in the modern ocean environment and the primary factors controlling this (chapter 5). In addition, a first order estimate of the platinum isotopic composition of seawater has been calculated based on the results from the experimental and natural sample analysis.

A summary of the findings of this study is given in chapter 6, with proposed areas of further investigation needed to better constrain the platinum marine cycle.

Chapter 2

Method development

2.1 Introduction

The need for high yield and purity in non-traditional stable isotope measurement is required as analytical artefacts can cause isotopic mass bias that can be larger than the small natural isotopic fractionation associated with these heavy systems (Johnson et al., 2004, Rehkämper et al., 1997). The separation and purification method itself can cause mass dependent fractionation due to non-quantitative yield during ion exchange chemistry or isobaric interferences during MC-ICP-MS analysis resulting in a bias in the measured isotopic ratio (Anbar, 2004, Cameron and Vance, 2014, Hoefs, 2008, Horner et al., 2010, Rehkämper et al., 1997). Thus, a balance is needed between sufficiently high purity to avoid analytical matrix effects and sufficiently high yields to avoid fractionation on the columns. The use of a double spike can mitigate these effects as it can correct for non-quantitative yield through chemistry and correct for instrumental mass bias (Cameron and Vance, 2014, Creech et al., 2013, Little et al., 2014, Millet et al., 2012, Rudge et al., 2009, Siebert et al., 2005). In addition, the double spike analyses can be reformulated to produce isotope dilution concentrations (Albarede et al., 2004, Cameron and Vance, 2014, Colodner et al., 1993, Millet et al., 2012).

A method for the separation, purification, and stable isotope analysis of platinum by MC-ICP-MS for extraterrestrial and terrestrial mantle-derived samples was first established by Creech et al. (2013). This method involves a combination of double-spike, nickel sulphide (NiS) fire assay, anion exchange chemistry and MC-ICPMS analysis. NiS fire assay digestion is a widely applied technique for the analysis of platinum-group elements. It has the advantage over other bulk digestion methods as it sequesters the PGE into a metallic bead (nickel sulphide beads) due to the siderophilic nature of the PGE (chapter 1), with the majority of other matrix elements in the sample removed in the silicate slag (Balaram et al., 2006, Balcerzak, 2002, Creech et al., 2013, Gros et al., 2002, Morcelli et al., 2004). The NiS beads are physically removed from the silicate slag that forms during the NiS fire assay method, and the NiS beads dissolved using multiple acid attacks. Thus it also acts as a pre-concentration step for the PGE. In the method developed by Creech et al. (2013) the pre-concentrated and

dissolved extraterrestrial and terrestrial mantle-derived samples were processed through anion exchange chemistry to separate platinum from other elements to sufficient purity to allow isotopic analysis by MC-ICPMS. A ^{196}Pt – ^{198}Pt double spike was added to the samples at a ratio of 0.55:0.45, double spike to natural platinum, prior to digestion by NiS fire assay to allow the sample and double spike to fully equilibrate (Creech et al., 2013, Creech et al., 2014).

In contrast to the silicate and metallic samples studied by Creech (Creech et al., 2013, Creech et al., 2014), FMS samples have both a very different matrix, and significantly lower Pt concentrations (0.01 – 15 ppm vs 0.1 – 0.5 ppm, respectively). In addition, the FMS samples are two component samples with a mixture of an authigenic component, representing the bulk platinum concentration derived directly from the water column (hydrogenetic) and therefore the seawater composition at that time and a detrital component. Consequently, it was necessary to evaluate the method described by Creech (Creech et al., 2013, Creech et al., 2014) and other various digestion methods.

A series of tests were undertaken to ensure adequate separation and purity of platinum is achieved for this different sample matrix using three commercially available standard reference materials (SRM); US Geological Survey Manganese Nodule, USGS Nod-A-1, and USGS Nod-P-1, and Geological Survey of Japan (GSJ) Manganese Nodule, JMn-1 (table 2.1). These three nodule standards represent homogenised ferromanganese deposits that closely approximate the samples targeted in this study.

In addition to the nodule standards, a synthetic nodule composition was prepared in the laboratory, based on the average concentrations of the major constituents of USGS Nod-A-1 and USGS Nod-P-1: Fe, Mn, Mg, Ca, Ni, Co, Cu and Pt (appendix A).

Table 2.1 Standard reference materials: USGS Nodule standards: USGS Nod-A-1, and USGS Nod-P-1, and GSJ Manganese Nodule, JMn-1 standard, dredge location and platinum concentration

Standard	Type	Locality	Depth (mbsl)	Pt conc. (µg/g)
USGS Nod-A-1	Mn nodule	Blake Plateau, Atlantic Ocean (31° 02' N, 78° 22' W)	788	0.52
USGS Nod-P-1	Mn nodule	Pacific Ocean (14° 50' N, 124° 28' W)	4300	0.12
GSJ JMn-1	Mn nodule	Southern Central Pacific (0° 47.2' S, 166° 07.1' W)	5200	0.11

Data source: GeoReM database (Jochum et al., 2005).

All sample preparation and digestions were undertaken in the geochemistry laboratory facilities at School for Geography, Environment, and Earth Sciences, Victoria University of Wellington (VUW). All platinum separation work was conducted in class 10 laminar flow hoods situated in the class 100 clean laboratory at VUW, unless stated otherwise. The reagents used were 1 x sub-boiled analytical reagent grade nitric (HNO_3) and 1 x sub-boiled analytical hydrochloric (HCl) acids, unless otherwise stated. Details of acid distillation and grades are given in appendix A

2.2 Digestion method

A number of different digestion methods were trialled, including both bulk digestion methods and authigenic component digestion methods. Authigenic-only digestion would solely reflect the seawater contribution of the samples and limit the possible dilution affect presented by the detrital components (Axelsson et al., 2002, Bayon et al., 2002, Plant, 2015).

2.2.1 Bulk digestion methods

Three bulk digestion methods were evaluated in this study; nickel sulphide fire assay digestion, aqua regia digestion and hydrofluoric and nitric acid digestion. NiS fire assay is a well-documented method for digestion and pre-concentration of PGE's from a number of different matrixes (Balaram et al., 2006, Balcerzak, 2002, Creech et al., 2013, Gros et al., 2002, Morcelli et al., 2004) but this method can result in high blank levels (Rehkämper and Halliday, 1997). The advantage of an acid digest such as aqua regia or hydrofluoric acid and nitric acid digest is that the blank levels are low. Conversely, the PGE are not pre-concentrated as none of the major rock matrix elements (except Si in an HF/HNO_3 digest) are removed.

2.1.1.1 Nickel sulphide fire assay

The method used in this study follows Creech et al (2013) with some minor alteration, briefly described here. Powdered sample is weighed directly into a cleaned 50 mL ceramic crucible (appendix A) and the appropriate amount of double spike added to each powder sample and allowed to air dry overnight. Once dry, the double spike will have formed a cake within the powder sample, this is gently broken with a methanol cleaned Teflon coated spatula to distribute the spike evenly. The fluxing agents; sodium carbonate, sodium tetraborate, nickel, and sulfur are added to the double spiked powder sample and mixed thoroughly (table 2.2). Pure silica is also added for samples weighing less than 7.5g, to bring a total of sample + SiO_2 to 7.5g. The powder sample is ready for fusion in the furnace.

For tests of the full method, the Pt isotopic standard IRMM-010, which is the natural isotopic composition of Pt, was also processed through full chemistry, including NiS fire assay. In these cases, 7.5 g of silica was weighed directly into a crucible. To this the standard solution was added, plus the double spike if not already spiked. The solution is allowed to air dry at room temperature. Once dried the standard will have formed a cake within the silica. This was gently broken with a methanol cleaned Teflon coated spatula and the standard treated the same as powdered samples and standards.

Table 2.2 Fluxing agents for nickel sulphide fire assay technique.

Fluxing agent	Formula	Supplier	Purity	Mass (g)
Sodium carbonate	Na_2CO_3	Acròs organics	99.95%	5.000
Sodium tetraborate	$Na_2B_4O_7$	Acròs organics	98.00%	10.000
Nickel	Ni	Acròs organics	99.90%	0.500
Sulfur	S	Fisher Scientific	99.90%	0.375
Silica (Silicic acid)	H_4O_4Si	Merck KGaA	99.00%	7.50-sample

The mass of the fluxing agents and the sample charge has been halved in this study to what was used in Creech et al, 2013, due to the concentration of platinum present and the availability of sufficient sample mass of ferromanganese samples. The different fluxing agents have a specific purpose within the charge; sodium carbonate will react with silicates to form a silica slag. Sodium tetraborate acts to lower the fusing point of the NiS fire assay charge. The nickel and sulphur act as the collector and form the nickel sulphide beads which sequester the PGE. Silica is added to prevent attack on the ceramic crucible when there is limited silica or other lithophile oxides present in the sample, due to sample size or composition. Silica is also used in this study as the NiS fire assay blank component to allow a full chemistry blank to be determined.

The mixed sample (or standard) and flux was placed in a S.E.M. (SA) PTY Ltd. muffle furnace at 950 °C for 30 minutes. The temperature is then increased to 1050 °C for a further 60 minutes. The sample is removed from the furnace and allowed to cool at room temperature. Once cooled the sample (including the crucible) is broken with a hammer (wrapped in parafilm and kimwipes) to allow access to the NiS beads embedded in the silicate slag (figure 2.1). The NiS beads are removed using methanol cleaned tweezers and placed into a cleaned 60 mL Savillex® beaker (appendix A). The NiS beads typically consisted of one large bead and three to five smaller beads. The NiS beads for each sample were weighed, with an average weight of 0.65g. The NiS beads were initially dissolved in 20 mL of 11 M HCl and the sample evaporated to dryness on a hotplate at 120 °C. H_2S is released from the NiS beads as they dissolve. A further 20 mL of 11 M HCl was added and then evaporated on the hotplate for 2 – 3 hours, until the volume had decreased by ca. 5 mL. The sample was topped up with

5 mL 15 M HNO_3 to produce aqua regia in the beaker (aqua regia = 3:1 HCl: HNO_3). The beaker was then tightly capped and placed on the hotplate at 120 °C overnight. This was usually sufficient time for the NiS beads to fully dissolve, however in some cases up to an additional 12 hours was required.

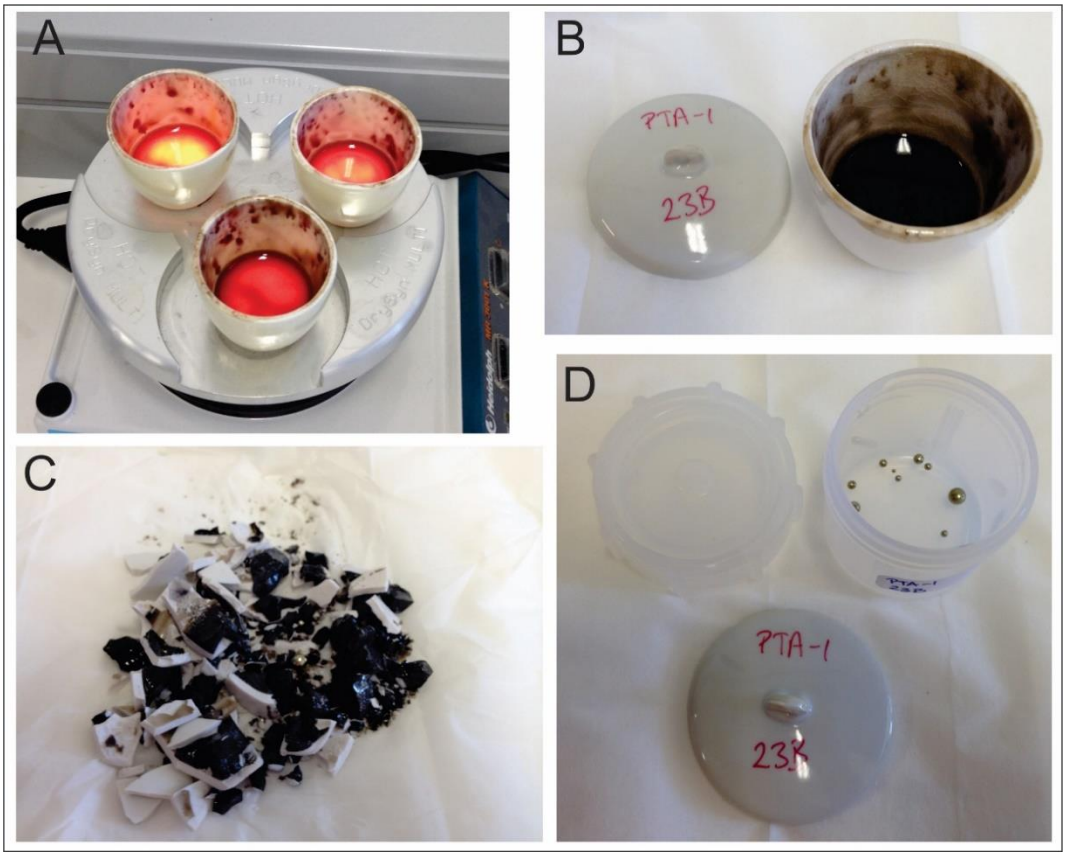

Figure 2.1 Pictures of various steps through the nickel sulphide fire assay digestion method. **A)** 50 mL ceramic crucibles with melted sample and fluxing reagents immediately after removal from the furnace (temperature of furnace 1050 °C), **B)** example of a sample after the charge has cooled after fusion, the silicate slag is all that is visible from the top of the samples as the beads, generally, will density settle to the base of the crucible. **C)** The crucible and contents are broken with a hammer to allow access to the metallic beads within the silicate slag. **D)** The metallic beads are placed in a cleaned 60 mL Savillex® beakers awaiting acid digestion. The average weight of the metallic beads removed from the silicate slag is 0.65 g, equivalent to the weights of the NiS fire assay fluxing agents listed in table 2.2.

The dissolved sample was then evaporated to incipient dryness on a hotplate at 120 °C, 5 – 10 mL of 11 M HCl added to convert the sample to chloride form, and evaporated again. The addition of 5 – 10 mL of 11 M HCl and evaporation was repeated. The sample was then taken up in 5 – 10 mL of 0.5 M HCl and evaporated and finally taken up in 10 mL of 0.5 M HCl, ready for anion exchange chemistry.

2.1.1.2 Aqua regia digestion

For aqua regia digestion tests, 0.05 – 0.5g of sample was weighed into a pre-cleaned Savillex® vial. The appropriate amount of double spike was added at this point, if required. Eight mL of aqua regia was added and the sample tightly capped and refluxed on a hotplate at 120 °C for 48 hours. The sample was allowed to cool and then evaporated on the hotplate until dry. The sample was then taken up in 8 mL of aqua regia again and allowed to reflux overnight. The samples were fully digested at this point. In preparation for anion exchange chemistry the sample was dried down and 5 – 10 mL of 11 M HCl is added to convert the sample to chloride form, and evaporated again. This step was repeated and then 2 mL of 0.5 M HCl added and evaporated before it was finally taken up in 10 mL of 0.5 M HCl, ready for anion exchange chemistry.

2.1.1.3 Hydrofluoric and nitric acid digestion

For the HF-HNO_3 digestion tests, 0.05 – 0.5g of sample was weighed into a pre-cleaned Savillex® vial. The appropriate amount of double spike was added, if required. The sample is taken up in 65 drops of 29 M optima HF and 25 drops of 15 M HNO_3 (volume of acids required increase with increasing sample size). The sample was tightly capped and put on a hotplate at 120 °C for 72 hours until fully digested. The sample is removed from the hotplate and allowed to cool, then evaporated on the hotplate until dry. The sample was then taken up in 2 mL 15 M HNO_3 and evaporated to remove any fluorides that may have formed. This step was repeated. Two mL of 11 M HCl was added to convert to chloride form and then dried down, with this step repeated once. Two mL of 0.5 M HCl was added and evaporated and the sample finally taken up in 10 mL of 0.5 M HCl, ready for anion exchange chemistry.

2.2.2 Authigenic digestion methods

This involves an acid dissolution of the Fe-Mn (hydroxy)oxide components, leaving any silicate (detrital) material undissolved. A small proportion of the detrital material may be dissolved under an acid attack. However, Plant (2015) evaluated the appropriate time needed to limit the proportion of detrital material dissolved while allowing the authigenic component to be fully dissolved. Platinum is associated with Fe-Mn (hydroxyl)oxide component rather than the detrital material, therefore a minor amount of detrital material dissolving should not impact the platinum composition.

0.5-1.0 g powder sample is weighed into a pre-cleaned Savillex® vial (appendix A). The powder sample is then placed in the drying oven at 110 ˚C for 24 hours to eliminate the possibility of hydroxide alteration, ferromanganese nodules are able to absorb up to 10 % by weight of moisture (Flanagan and Gottfried, 1980, Plant, 2015). If the powder sample was to be used for isotopic analysis the double spike was added at this stage.

To digest the authigenic component 5 mL of 11 M HCl was added to the dried sample and allowed to react for 30 minutes at room temperature with the cap left loose, followed by refluxing for 30 minutes on a hotplate at 120 ˚C. The authigenic component of the powder sample is fully digested after these two steps (Plant, 2015). The sample was removed from the hotplate and allowed to cool. The sample residue and solution were transferred to a pre-cleaned 10 mL centrifuge tubes and centrifuged for five minutes at 2,000 revolutions per minute (rpm). This separates the supernatant (dissolved authigenic component) from the aluminosilicate residue (detrital component) allowing for the two components to be successfully separated. The supernatant was pipetted into the original Savillex® beaker (that was used to dissolve the sample) which was rinsed three times with ultra-pure water (>18.2 MΩ), hereafter referred to as Milli Q water. The aluminosilicate residue was discarded. The authigenic component of the sample was then evaporated to dryness, before it being re-dissolved in 11 M HCl. This procedure of evaporation and re-dissolving was repeated two more times (for a total of three times in 11 M HCl). A small volume of 0.5 M HCl was added

to the sample and dried down, a further 10 mL added and the beakers closed tightly and refluxed on the hotplate for 24 hours. The sample was then ready for loading onto the anion exchange column for platinum separation.

2.2.3 Preparation of solution samples

For solution samples (e.g. IRMM-010) a known aliquot of the solution was pipetted into a clean Savillex® beaker and the appropriate amount of double spike added. The sample was placed on the hotplate at 120 °C and then evaporated to dryness and re-dissolved in 5 mL 11 M HCl. This was repeated three times in total to ensure solution sample and double spike equilibrate. A small volume of 0.5 M HCl was added, ensuring all the sample is covered, and evaporated to dryness. 10 mL of 0.5 M HCl was then added and the sample refluxed on the hotplate at 120 °C overnight. The sample was ready for loading onto anion exchange columns.

2.3 Platinum separation

For accurate stable isotope measurements, it is necessary to purify the element of interest to reduce the risk of isobaric interferences and the possibility of matrix effects when the sample is analysed using multiple collector inductively coupled plasma mass spectrometry (MC-ICP-MS; Creech et al., 2014, Pearson and Woodland, 2000, Rehkämper and Halliday, 1997, Strelow and Toerien, 1966). Resin exchange chemistry is commonly used to separate a specific element or a group of elements from matrix and other elements in the sample, and has the advantage over alternate methods, such as co-precipitation, of having lower blank levels. An anion exchange chemistry has been developed to separate Pt from silicate (perioditic and basaltic compositions) and metal (iron meteorite) samples (Creech et al., 2014), and was the basis for the method applied to the ferromanganese sediments here. Bio-Rad® AG1-8X, 100 – 200 µm dry mesh, chloride form resin, was used throughout this study. The anion exchange resin allows for the successful separation of the PGE from other elements and from each other due to the strongly retained anionic PGE chloro-complexes in HCl (Pearson and Woodland, 2000).

2.3.1 Anion exchange chemistry

The resin was cleaned prior to use by rinsing and then decanting with the following reagents in sequence; Milli Q water, 6 M HCl, Milli Q water, 4 M HNO_3. The resin is stored in slurry form with Milli Q water. Fresh resin was used for each column i.e. resin was not reused. The ion exchange columns used in this study, unless otherwise stated, were Eichrom® 0.8 cm internal diameter, 2 mL polypropylene columns with a polypropylene frit, with a 25 mL reservoir fitted. The columns and column racks were cleaned carefully with Milli Q water between samples.

1 mL of clean resin was loaded into the columns and cleaned using the following sequence of reagents ; 5 mL Milli Q water, 20 mL 0.8 M HNO_3, 5 mL Milli Q water, 10 mL 11 M HCl, 5 mL Milli Q water, 25 mL 15 M HNO_3, 5 mL Milli Q water, 40 mL 6 M HCl, 5 mL Milli Q water (figure 2.2). If columns were not to be used immediately, approximately 10 mL Milli Q water was added and the top of the column was sealed with parafilm. The columns drip ca. 2 mL of Milli Q water before the pressure decreases sufficiently in the upper reservoir to hold the Milli Q water in the column, thus preventing the resin from drying out. Before use the Milli Q water was eluted and 40 mL 0.5 M HCl was loaded to condition the resin before sample loading. Samples were always introduced to the column in a 0.5 M HCl solution. 10 mL of sample was loaded onto the column and washed sequentially with (figure 2.2). Platinum was eluted in 40 mL 15 M HNO_3 (the platinum cut). During method testing all elution cuts were collected to monitor major and trace element elution profiles. At all other times just the platinum cut was collected.

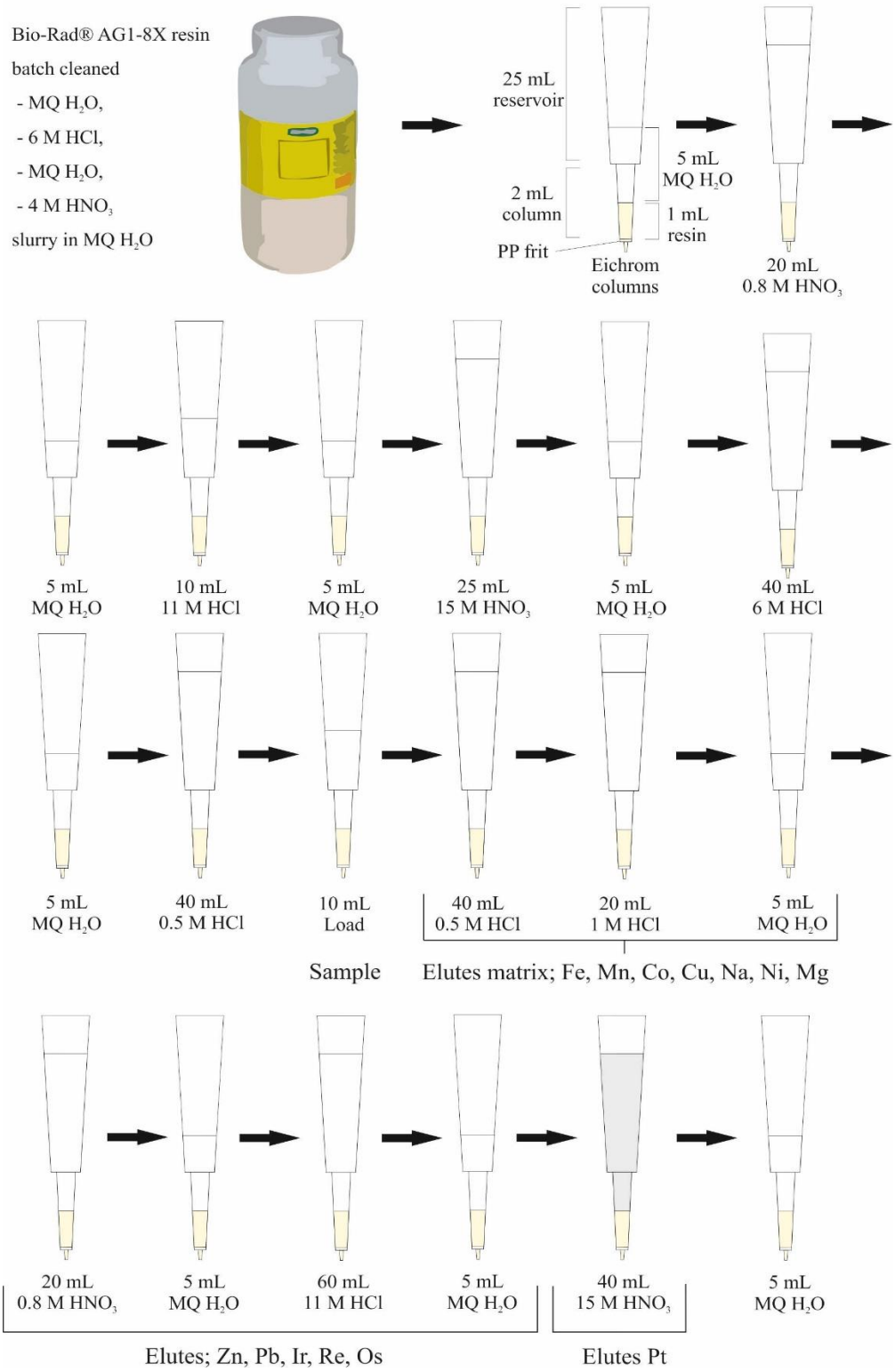

Figure 2.2 Resin batch cleaning and elution sequence of standard columns for platinum separation.

2.3.2 Multi element concentration analysis by ICP-MS

All platinum and multi-trace element concentration analyses were undertaken using either an Agilent 7500CS ICP-MS or a Thermo Scientific Element2 sector-field ICP-MS, both housed at VUW. ICP-MS analysis was undertaken for elution cuts during method testing to monitor major and trace element elution profiles, as well as the yield and purity of platinum achieved in the platinum cut. For samples where the Pt concentration was unknown, e.g. most natural and experimental samples, a small subsample was digested using aqua regia digestion and analysed for Pt concentration. The typical analytical conditions for the Agilent 7500CS ICP-MS and the Thermo Scientific Element2 ICP-MS are summarised in table 2.3. Due to the stability, solubility and efficiency of wash-out from the ICP-MS all PGE analysis were conducted in 0.5 M optima HCl, rather than in dilute HNO_3.

Table 2.3 Typical running parameters of the two ICP-MS instruments used in this study. Both tuning standards were prepared in 0.5 M HCl, as were all samples.

ICP-MS	Agilent 7500CS Octopole	Thermo Element2
Acquisition mode	Peak hopping	Peak hopping
Detection mode	Pulse and analogue	Pulse and analogue
Aspiration	Free	Free
Nebuliser	Glass 0.2mL/min	Glass 0.2mL/min
Running acid	0.5 M HCl	0.5 M HCl
Tuning standard	Agilent 10 ng/g standard (Li, Co, Y, Ce, Tl)	Thermo 1 ng/g standard (Li, B, Na, K, Sc, Fe, Co, Ga, Y, Ru, Rh, Pd, In, Ba, Lu, Re, Os, Ir, Pt, Au, Tl, U)
Monitored isotopes and oxides during tuning	^{7}Li, ^{59}Co, ^{89}Y, ^{140}Ce, ^{205}Tl, $^{156}CeO^{+}/^{140}Ce$ (RSD < 5%)	^{7}Li, ^{39}K, ^{56}Fe, ^{115}In, ^{238}U, $^{254}UO^{+}/^{238}U$ (RSD < 2%)
RF Power	1500 W	1715 W
Carrier/sample gas (Ar)	0.82 L/min	1.045 L/min
Makeup/auxillary gas (Ar)	0.38 L/min	0.85 L/min
Peristatlic pump speed	10 - 12 rpm	12 rpm

A precious metals ICPMS standard solution (100 ng/mL diluted from Specpure® Precious Metals, plasma standard solution; Au, Ir, Os, Pd, Pt, Re, Rh, Ru at 100 µg/mL in 20% HCl) was used to quantitatively monitor the PGE elution profile from anion exchange chemistry on the Agilent 7500CS ICP-MS. The major matrix elements were measured qualitatively, and counts per second (CPS) for each column cut were normalised to 100% for that element across the elution profile.

A multi element standard comprising 17 elements (Mn, Fe, Co, Ni, Cu, Zn, Mo, V, Cr, Ba, Ce, Zr, Pb, Ta, Hf, W, Gd) and the Specpure® Precious Metals plasma standard solution was prepared in 0.5 M HCl and used to concentration analyses on the Element2 ICPMS. A calibration method was used on the Element2 ICP-MS, where three dilutions of the multi-element standard, typically 1, 2.5, and 5 ng/mL, were run at the start of each analytical session. A 1 ng/mL multi-element standard was run regularly throughout the analytical session as an unknown to monitor the instrument over time (appendix E).

2.3.3 Evaluation of the elution profiles and Pt yields

As the ferromanganese sample matrix is very different from those materials analysed by Creech et al. (2014) the column exchange chemistry was tested using a combination of FeMn SRMs dissolved using different methods, as well as a synthetic FeMn sample. Initial elution profiles collected on the HCl digested nodule standards, synthetic standard and IRMM-010 were performed on the Agilent 7500CS ICP-MS. The total platinum yields were ≥ 90%, however it appeared that not all of the platinum in the nodule SRMs was present in the platinum cut, with up to 25% being eluted in the 11 M HCl elution cut. This double peak platinum elution behavior was only observed with the natural nodule standards not in the synthetic or IRMM-010 standards (figure 2.3).

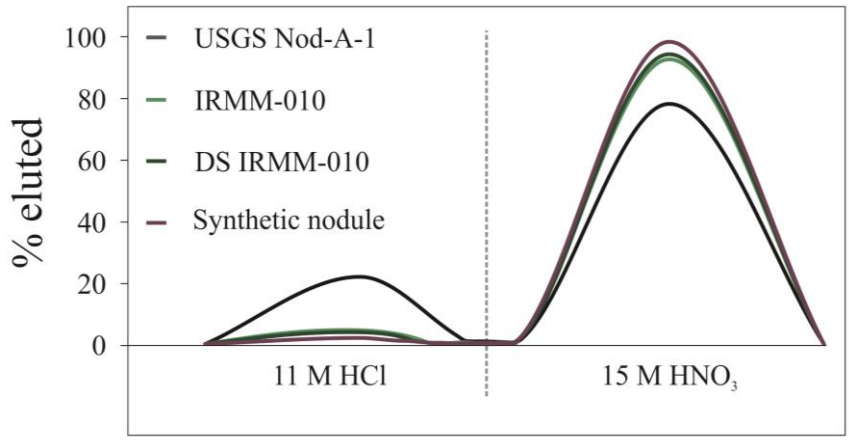

Figure 2.3 Platinum elution curve in USGS Nod-A-1, IRMM-010, DS – IRMM, and synthetic nodule with concentrated acids (i.e. 11 M HCl and 15 M HNO_3).

The early peak may be the result of different behavior of Pt in the natural FeMn samples (e.g. more than one species present) or an unaccounted for isobaric interference on the Pt mass analysed. The presence of potential isobaric interferences was checked in the 11M HCl cut, for example Hf ($^{179}Hf^{16}O$) and Gd ($^{155}Gd^{40}Ar$), but could not explain the second peak. The possibility of two species of Pt, such as the divalent and tetravalent species, being present was explored. Like the synthetic solution samples, natural nodule standards digested using NiS fire assay did not produce the double elution peak (figure 2.4 b). A number of oxidation and reduction steps were tested with the HCl digestion method (appendix A and E) to ensure all the platinum was present in a single oxidation state, either Pt^{2+} or Pt^{4+}, prior to loading on the columns. The additional oxidation and reduction steps changed the relative proportions of when the platinum was apparently eluted but did not completely remove the double peak effect (figure 2.4 a).

Subsequent analysis of elution cuts using the Element2 ICP-MS did not produce the double elution peak (figure 2.4 c), suggesting that the platinum double elution peak was an analytical artifact caused by an unknown interference on the Agilent 7500CS ICP-MS, which was resolvable by low resolution, 300 ΔM, on the Element2. To continue to monitor any possible effects of interferences each platinum analysis was also measured at medium resolution (4000 ΔM) on the Element2.

2.3.3.1 Comparison of authigenic and bulk digestion methods

A number of criteria were evaluated to determine which digestion method (authigenic or bulk digestion) was most suited for use to separate platinum from the FMS sample matrix, such as the platinum blanks, purity and yield.

A concern with bulk digestion using NiS fire assay is the potential for large procedural blanks relative to acid digestion methods due to the impurities in the fluxing agents (table 2.2; Balaram et al., 2006, Meisel et al., 2001, Pearson and Woodland, 2000, Ravizza and Pyle, 1997). Therefore, full procedural blanks were conducted with each batch of digestions for both authigenic and bulk digestion methods. The mean NiS fire assay procedural blank was 2 ng/g with a maximum of 4 ng/g. The acid digestion methods procedural blanks had a maximum value of 0.1 ng/g. These blank concentrations would contribute 0.7 – 3.6 % and 0.02 to 0.1 %, respectively, based on the three SRM (USGS Nod-A-1, USGS Nod-P-1, and GSJ JMn-1) used for method development

Both authigenic and bulk digests resulted in > 90 % yield, however, the purity (total separation from matrix) of platinum was not sufficient for the acid digestion relative to the bulk digestion (figure 24 d). The HCl digestion resulted in elements, such as Hf and Tl, remaining in the solution which may cause both isobaric and matric interferences during analysis on the MC-ICP-MS and would require an additional purification step. However, undertaking an additional separation step would increase the risk of fractionation due compounding loss of yields.

The NiS fire assay digestion method effectively preconcentrated the platinum and removed sufficient REE and other possible interferences prior to anion exchange chemistry. The remainder of elements were successfully removed with anion exchange chemistry (figure 2.5). Therefore, the bulk digestion method was utilised in sample preparation for MC-ICP-MS.

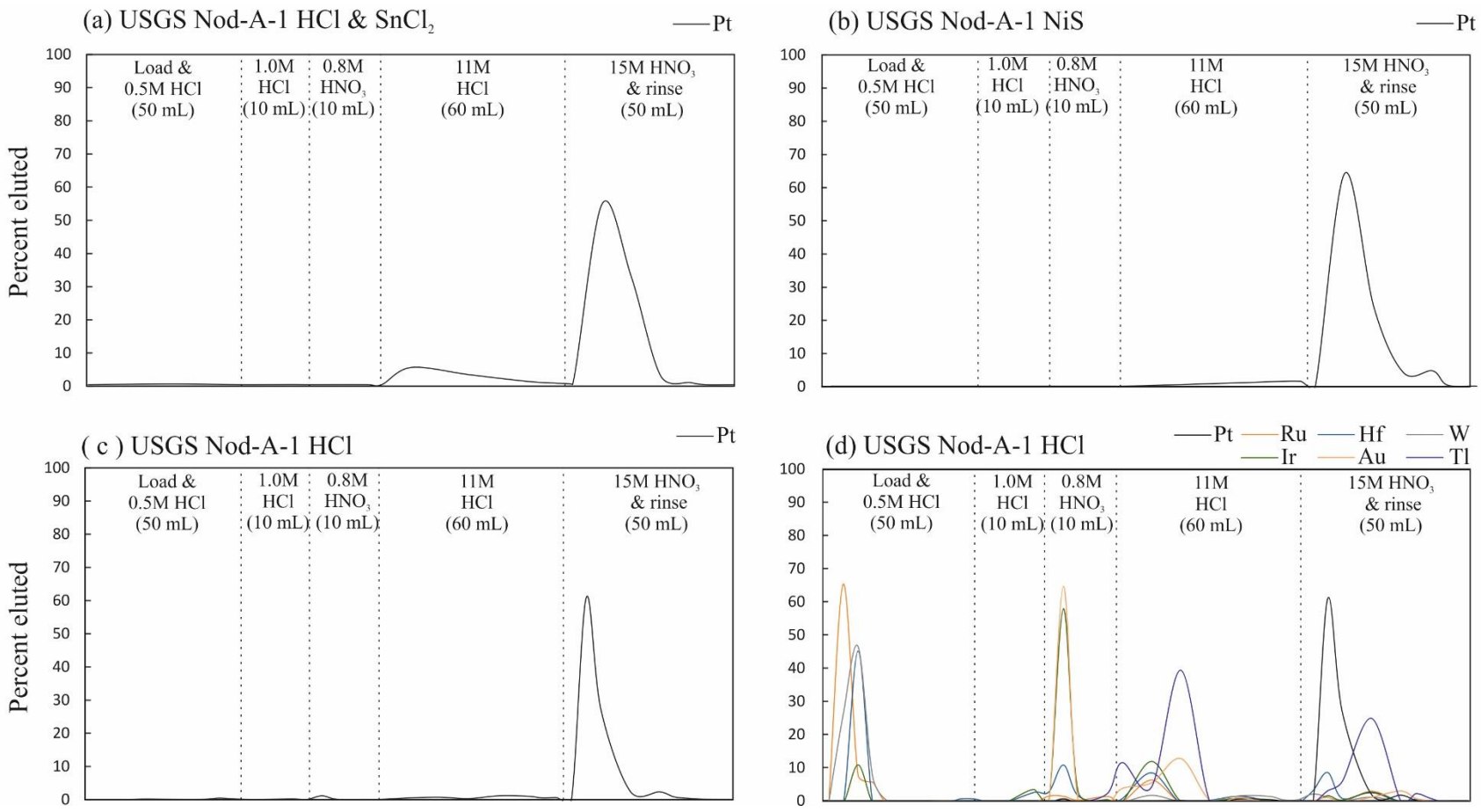

Figure 2.4 (a) Pt elution following digestion with HCl and SnCl2 analysed on the Agilent. **(b)** Pt elution curve following digestion with NiS. **(c)** Pt elution curve following digestion with HCl analysed on the Element2. **(d)** Pt and other elements that elute in the 'platinum cut' in a HCl digest. ICP-MS data is given in appendix E.

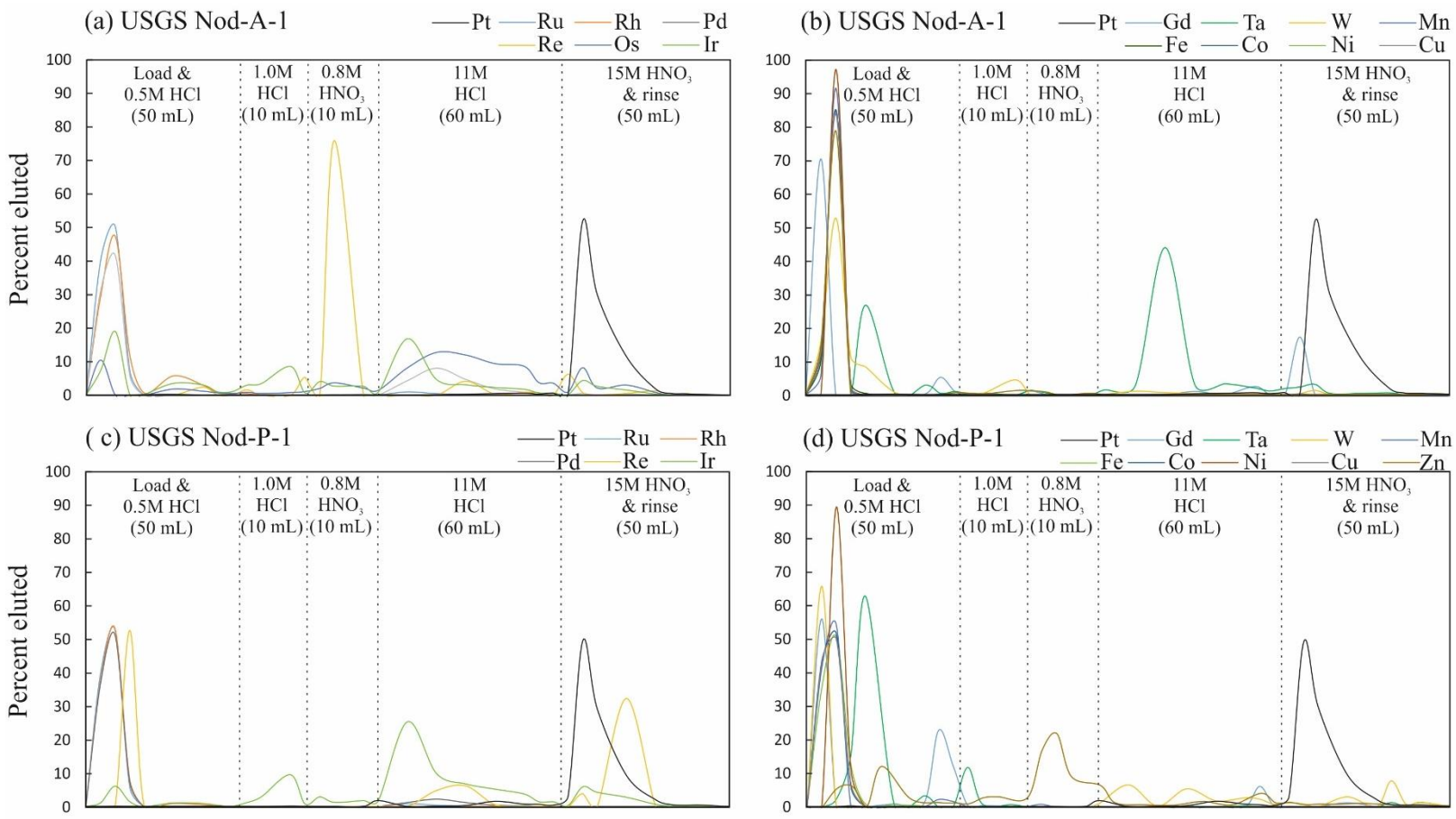

Figure 2.5 (a) PGE and Re elution profile for USGS Nod-A-1. **(b)** Major matrix and interference elements elution profile for USGS Nod-A-1. **(c)** PGE and Re elution profile for USGS Nod-P-1. **(d)** Major matrix and interference elements elution profile for USGS Nod-P-1. ICP-MS data is given in appendix E.

2.4 Platinum isotope analysis by MC-ICP-MS

The platinum isotope analyses were primarily conducted on a ThermoFisher Neptune MC-ICP-MS at Centre for Star and Planet Formation, Natural History Museum of Denmark, University of Copenhagen, Denmark (UoC) and also on the Nu-Plasma HR MC-ICP-MS at VUW, with typical analytical conditions summarised in table 2.4.

Table 2.4 Typical running parameters of the two MC-ICP-MS used in this study.

MC-ICP-MS	ThermoFisher Neptune	Nu-Plasma HR
RF power	1200 W	1300 W
Plasma gas flow rate	15 L/min	14 L/min
Acceleration voltage	10 kV	6 kV
Instrument resolution	~ 1600	~ 1840
Mass analyser pressure	~ 8 x 10^{-9} mbar	~ 7.5 x 10^{-9} mbar
Detector	9 Faraday detectors	9 Faraday detectors
Sample introduction system	ESI Apex IR w/ACM	Nu instruments DSN-100
Sample uptake rate	~ 30 µL/min	~ 75 µL/min
Running acid	0.5 M HCl	0.5 M HCl

The Neptune MC-ICP-MS was operated in low-resolution with a mass resolution of 1600 (M/ΔM is derived from the peak slope of the rising edge measured at 5% and 95% relative peak height). The samples were introduced with an ESI Apex IR desolvation nebuliser introduction system. The sample uptake rate was approximately 30 µL/min with typical sensitivity of ~ 100 V/ppm total Pt on a 100 ng/mL natural platinum solution that was double spiked (^{196}Pt – ^{198}Pt). The masses that were monitored (Faraday cups) included the six platinum isotopes; ^{190}Pt, ^{192}Pt, ^{194}Pt, ^{195}Pt, ^{196}Pt, and ^{198}Pt, plus three possible interferences; ^{188}Os, ^{191}Ir, ^{200}Hg. Each platinum isotope measurement consisted of one block of 100 x 8.3 s integrations, ca. 14 minutes of acquisition time. A washout of 0.5M HCl for 30 minutes generally resulted in an on-peak baseline of < 2 mV. Peak centering was performed at the start of each analysis.

2.4.1 MC-ICP-MS standards and double spike

Stable isotope data are reported relative to a standard reference material (e.g. IRMM-14 for Fe). The Pt isotope standard solution IRMM-010 was selected for the reference standard for Pt isotope measurements. IRMM-010 is provided in the form of a platinum wire segment and prepared as a stock solution by John B. Creech (Creech, 2014), described briefly here. The platinum wire segment was weighed and cleaned in Milli Q water, analytical grade methanol and 5% optima HNO_3. The cleaned platinum wire segment was then digested in optima aqua regia in a cleaned Savillex® Teflon beaker. The IRMM-010 solution (digested platinum wire solution) was then converted to chloride form by evaporating and dissolving in concentrated optima grade HCl, twice, and then brought up in 20% optima HCl. From this concentrated platinum solution, a 100 ng/mL solution of IRMM-010 in 0.5M HCl was prepared and a double spike added.

The J.T. Baker® Atomic Absorption Standards 1000 µg/mL refined platinum metal SRM was used as a secondary standard. A 100 ng/mL solution of the Baker standard was prepared using optima grade HCl and optimally double spiked.

The double spike used in this study was designed and calibrated by John B. Creech at VUW (Creech et al., 2013) and briefly described here. The double spike consists of two single isotope spikes, ^{196}Pt and ^{198}Pt, which were purchased from Oak Ridge National Laboratory as fine-grained metallic powders. The two single isotopic spikes were digested in optima aqua regia and dried down. The two isotopic spikes were then re-dissolved in 11 M optima HCl and evaporated to dryness, to convert to chloride form. The two spikes were then re-dissolved in 20% optima HCl for use. The two spikes solutions were measured using IRMM-010 for standard bracketing on the MC-ICP-MS to determine their concentration and were then mixed in the proportion of 27.7 % and 72.3 %, respectively, based on the theoretical ideal double spike composition (Rudge et al., 2009). This double spike solution was evaporated and taken up in a small volume of 11 M optima HCl and evaporated to dryness. The double spike was then re-dissolved in 6 M optima HCl for calibration.

A combination of both double spike and standard bracketing techniques were utilised as both techniques can correct for different possible effects. The use of the double spike will allow for the correction of potential instrumental mass bias due to higher masses being preferentially detected in MC-ICP-MS and incomplete yield through chemistry. The double spike technique involves a known double spike (^{196}Pt – ^{198}Pt) added to the unknown sample resulting in an unnatural isotopic ratio for ^{196}Pt – ^{198}Pt. The variation in the measured ratio of ^{196}Pt – ^{198}Pt relative to the initial double spike ratio is used to determine the instrumental mass bias during the analysis. The measured composition of the double spike-sample mixture can then be corrected for instrumental mass bias. The double spike component is mathematically subtracted from the instrumental mass bias corrected double spike-sample mixture for the natural fractionation to be calculated. The standard bracketing technique allows for the correction of any instrument drift with time due to loss of sensitivity or mass calibration.

2.4.2 Isotopic notation and standard reproducibility and precision

Following convention (Johnson et al., 2004), the platinum isotopic composition is reported as a heavy over light ratio, ^{198}Pt/^{194}Pt, in delta notation with respect to IRMM-010 (equation 2.1; Barling et al., 2001, Creech et al., 2013, Rehkämper et al., 2002, Siebert et al., 2005).

$$\delta^{198}\mathrm{Pt} = [\ \frac{198}{194}\mathrm{Pt}_{(\mathrm{sample})} / \frac{198}{194}\mathrm{Pt}_{(\mathrm{IRMM\text{-}010})} - 1] \times 10^3 \qquad (2.1)$$

The optimally spiked IRMM-010 (DS IRMM-010) was run as the bracketing standard for all platinum isotopic analysis and is the isotope reference material used to normalise all the isotopic data. The external reproducibility of the double spike corrected δ^{198}Pt for DS IRMM-010 based on six sessions at UoC is δ^{198}Pt ± 0.022 ‰ (2sd) and ± 0.036 ‰ (2sd) based on four analytical sessions at VUW (figure 2.6). The internal precision, two standard error (2 se) on the double spike corrected DS IRMM-010 is δ^{198}Pt ± 0.018 ‰ for UoC and ± 0.062 ‰ for VUW (figure 2.6).

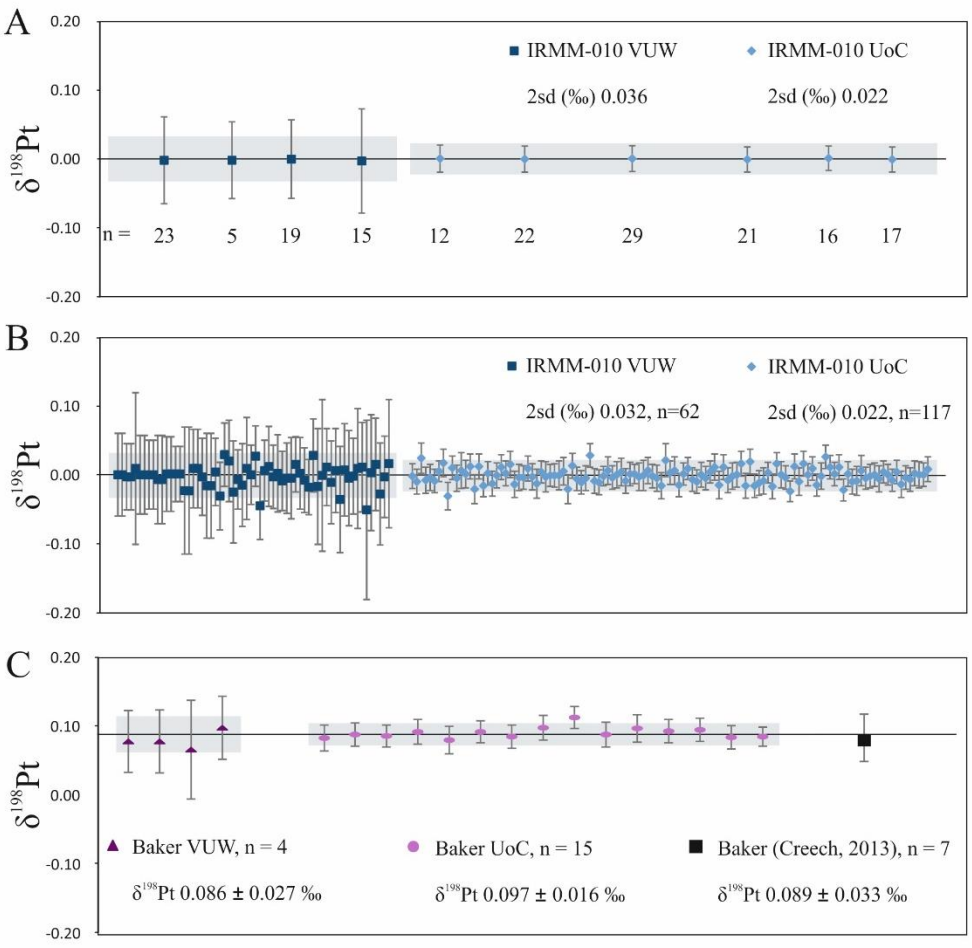

Figure 2.6 (A) Mean double spike corrected δ^{198}Pt DS IRMM-010 based on 6 analytical sessions at UoC is δ^{198}Pt ± 0.022 ‰ (mean 2sd) and 4 analytical sessions at VUW is δ^{198}Pt ± 0.036 ‰ (mean 2sd), represented by the grey hatched box. The error bars are the mean 2 sd for the individual analytical session. **(B)** Individual analysis of double spike corrected δ^{198}Pt for DS IRMM-010 VUW and UoC. The error bars on each analysis represent the 2 se for each, with the grey hatched box representing the mean 2 sd of all analysis at UoC and VUW, δ^{198}Pt ± 0.022 ‰ and δ^{198}Pt ± 0.032 ‰, respectively. The average 2 se for all analysis is δ^{198}Pt ± 0.018 ‰ and δ^{198}Pt ± 0.062 ‰, for UoC and VUW, respectively. **(C)** Individual analysis of double spike corrected δ^{198}Pt Baker standard analysed at VUW and UoC. The grey box representing the mean 2 sd of all analysis at VUW (0.027 ‰) and UoC (0.016 ‰). The mean δ^{198}Pt 0.089 ± 0.033 ‰ (mean 2sd) as determined by Creech et al., 2013 is also presented.

The Baker standard has a measureable offset from the IRMM-010 (δ^{198}Pt = 0.089 ± 0.033 ‰ (mean 2sd); Creech et al., 2013). During every analytical session, a Baker standard was run as a secondary standard. The mean δ^{198}Pt for Baker standards measured in this study are 0.086 ± 0.033 ‰ (mean 2sd, n = 4) and 0.097 ± 0.016 ‰ (mean 2sd, n = 15) for VUW and UoC, respectively (figure 2.6).

Potential fractionation due to the separation and purification of Pt was monitored by processing IRMM-010 through chemistry. The δ^{198}Pt was -0.038 ± 0.042 (2sd), which is comparable to the chemistry processed IRMM-010 samples of Creech et al. (2014), -0.039 ± 0.060 (2sd). Creech et al. (2013) undertook a number of doping tests on various matrix and isobaric interference elements (Mg, Al, Ca, Ti, Cr, Mn, Fe, Ni, Cu, Mo, W, Rh, Pd, Ir, Au, and Os) up to 10% of the Pt concentration in IRMM-010. All δ^{198}Pt were within analytical error of undoped IRMM-010 except for Au. However, due to the low concentration of Au in FMS (SRM < 10 ng/g) and the effectiveness of the anion exchange chemistry Au should not be present in the final solution.

2.5 Data reduction

All concentration and isotopic data collected on the Agilent ICP-MS-MS, Nu-Plasma HR MC-ICP-MS and Neptune MC-ICP-MS were reduced offline using Iolite, a package that runs within the Wavemetrics Igor Pro software. The double spike inversion and isotope dilution calculations were also determined offline within Iolite.

The double spike reduction add-on, IsoSpike, is discussed in detail in Creech et al., 2015. The double spike reduction in IsoSpike consists of three simultaneous non-linear algebraic equations based on the mixing relationship of the sample and the double spike and a combination of instrumental and natural isotopic fractionation exponential mass bias laws (equation 2.2; Creech et al., 2015, Rudge et al., 2009).

$$F_i(\lambda, \alpha, \beta, n, m, T) = \lambda T_i + (1-\lambda)n_i e^{-\alpha P_i} - m_i e^{-\beta P_i} = 0 \qquad (2.2)$$

where i refers to the ith isotopic ratio of the sample, P is the natural log of the ratio of atomic masses, m is the measured compositions of the sample-spike mixture and n is the measured composition of the unspiked samples, respectively. T represents the isotopic composition of the double spike. λ is related to the proportion in which the sample and double spike are mixed, α and β are the natural and instrumental mass fractionation factors, respectively. The IsoSpike add-on allows for the rapid and consist evaluation of each integration within an analysis. The isotope dilution (ID) calculation was based on the Albarede et al. (2004) and Colonder et al. (1993) equations using ^{198}Pt as the spiked isotope and ^{194}Pt as the unspiked isotope (Creech et al., 2014).

All concentration data collected on the Element2 ICP-MS were reduced using the Thermo Scientific software suite. As a means of quality control on the results from this reduction package, a selection of random data files were reduced using both Iolite and Microsoft excel to determine any variations due to different reduction procedures. The concentration data determined using the Element2 ICP-MS software was within 5 % of Iolite reduced data.

Chapter 3

Platinum adsorption onto ferromanganese substrates: experimental constraints on mechanisms and associated platinum isotopic fractionation.

Preface

This chapter addresses the first of the research questions posed in chapter 1:

"How is platinum incorporated into the sediment record, and what effect has the incorporation mechanism on the platinum stable isotope composition?"

This chapter details experiments in which platinum with a known isotopic composition was adsorbed onto synthetic Fe and Mn oxyhydroxides and oxides at various pH as a function of time. The relative abundance at which the platinum is adsorbed onto these different substrates as a function of pH provides insight into the mechanism of adsorption of platinum onto the surface. Direct measurement of the bonding environment of the platinum adsorbed onto the surfaces was investigated using synchrotron X-ray absorption spectroscopy (XAS), allowing the redox state of the adsorbed platinum to be determined, as well as the first shell nearest neighbours and their distances from the central platinum atom. Following the determination of the adsorption mechanism of platinum onto the Fe and Mn oxyhydroxide and oxide surfaces, the platinum isotopic composition of experimental charges was examined to determine the effect adsorption has on the isotopic signature.

3.1 Introduction

Iron-manganese sediments (FMS) are the primary sink for platinum in the marine environment, yet the mechanism of platinum incorporation remains speculative at best with both reduction and oxidation of platinum onto the surface of the FMS being suggested (chapter 1.32; Halbach et al., 1984, Halbach9 et al., 1989, Hodge et al., 1985). An understanding of the mechanism of platinum sequestration by Fe-Mn oxide and oxyhydroxides is fundamental for deciphering the marine platinum cycle and key to evaluating the isotopic fractionation associated with the mechanism of incorporation.

Due to the low concentration of platinum (< 1 µg/g) in natural FMS, it is not possible to investigate the oxidation state, coordination chemistry and speciation of platinum adsorbed onto them directly with current analytical techniques. Therefore, a series of adsorption experiments were designed to increase the concentration of platinum that is adsorbed onto synthetic Fe-Mn oxide and oxyhydroxides to allow direct measurements to be undertaken with synchrotron X-ray absorption spectroscopy (XAS), similar to studies conducted on molybdenum and cerium (Barling et al., 2004, Goldberg et al., 2009, Takahashi et al., 2007). XAS allows the redox state and bonding environment of the platinum adsorbed onto the surface of the synthetic Fe-Mn oxide and oxyhydroxides to be investigated directly.

Similar XAS experiments have been undertaken on the naturally available cerium and cobalt in ferromanganese oxide surfaces and have successfully shown that cerium is present as Ce^{4+} and cobalt as Co^{3+} and associated with δ-MnO_2 in ferromanganese oxides (Takahashi et al., 2007). Previous XAS studies of platinum adsorbed onto various substrates have focused on the oxidation state of platinum for anticancer treatments and for automobile catalysts (Hall et al., 2003, Hyde and Sankar, 2015, Matthew and Russell, 2000, Yoshida et al., 2005). However, two recent studies have examined the adsorption of platinum onto both δ - MnO_2 and Fe oxyhydroxides (Koschinsky et al., 2005, and Maeno et al., 2015). Koschinsky et al. (2005) using X-ray photoelectron spectroscopy (XPS) suggest that Pt^{2+} is preferentially oxidised to

Pt^{4+} by the Mn oxide surfaces relative to Fe oxyhydroxides substrates. Maeno et al. (2015) further support this finding with an XPS and XAS study of Pt^{2+} sorbed onto δ-MnO_2. Maeno et al. (2015) proposed that the platinum is adsorbed via a redox mediated isomorphous substitution between Pt^{4+} and Mn^{4+}.

In this study, the concentration of platinum adsorbed onto the oxide and oxyhydroxide surfaces as well as the isotopic fractionation associated with the adsorption process have been determined using ICP-MS and MC-ICP-MS analysis. Combining the XAS data with platinum stable isotopic measurements permits an evaluation of the platinum oxidation state, bonding environment, and incorporation onto these chemical sediments as well as the resulting platinum isotopic fractionation.

3.2 Experimental Methods

3.2.1 Synthesis of the Fe oxyhydroxides and Mn oxide

Three Fe-Mn minerals were synthesised at VUW for the purpose of the adsorption experiments, i.e. two iron oxyhydroxides, goethite (α-FeOOH), and ferrihydrite (approximately $5Fe^{3+}{}_2O_3 \cdot 9H_2O$) and one manganese oxide, birnessite (δ-MnO_2). These three minerals, goethite, ferrihydrite, and δ-MnO_2, were chosen due to their presence in many natural FMS (chapter 1.331; Hein et al., 2013, Koschinsky et al., 2005). The general characteristics of these three minerals are listed in table 3.1.

Goethite is a common iron oxy-hydroxide in natural environments and normally forms under oxidizing conditions as a weathering product of iron minerals (e.g. pyrite and magnetite) and may precipitate from aqueous media at conditions ranging from ambient to hydrothermal (Cornell and Schwertmann, 2003, Jaiswai et al., 2013). Goethite is a polymorph of ferroxyhyte and lepidocrocite and has been utilised as an adsorbent in many studies, due to its prevalence in nature, to study the sequestration of many metals such as copper, germanium, molybdenum, strontium, and vanadium (Carroll et al., 2008, Goldberg et al., 2009, Jaiswal et al., 2013, Peacock and Sherman, 2004, Pokrovsky et al., 2006).

Ferrihydrite is metastable iron oxy-hydroxide precursor to goethite and hematite (Michel et al., 2007). It can precipitate directly as nanocrystals (<10 nm size) from iron containing waters depending on the pH and has been utilised as an adsorbent in many studies (e.g. cerium, lead, molybdenum, and zinc; Goldberg et al., 2009, Little et al., 2014, Takahashi, 2007).

Birnessite (δ-MnO_2) is a manganese oxide polymorph and precipitates directly from seawater under ambient conditions (Barling et al., 2004). δ-MnO_2 has been used to study the incorporation mechanism of many metals (e.g. cobalt, copper, lead, molybdenum, nickel, and REE) onto FMS as it is likely to be the dominant form of manganese oxide in the sediments (Barling et al., 2004, Ohta and Kawabe, 2001, Parida et al., 1996).

Table 3.1 Mineral characteristics of the iron and manganese oxides and oxy-hydroxides that were synthesised for the incorporation experiments.

	Goethite	Ferrihydrite	Birnessite
Empirical Formula	$Fe^{3+}O(OH)$	$5Fe^{3+}{}_2O_3 \cdot 9(H_2O)$	δ MnO_2
Colour	Yellow-brown	Dark brown	Dark brown/blac
Crystal structure	Orthorhombic	Trigonal	Monoclinic
Density	3.8 g/cm^3	3.8 g/cm^3	3.0 g/cm^3
Surface area	30 – 90 m^2/g	100 m^2/g	300 m^2/g
ZPC	7.5	8	2.4

The zero point of charge (ZPC) and other data are from the webmineral database and the references therein, as well as from Cornell and Schwertmann (2003), Kosmulski (2002).

3.2.1.1 Goethite

Goethite was synthesised following the methodology of Cornell and Schwertmann (2003). It was precipitated by adding 180 mL of 5 M potassium hydroxide (KOH) to 100 mL of freshly prepared 1.0 mol/dm^3 ferric nitrate ($Fe(NO_3)_3$), which forms a brown ferrihydrite suspension. This suspension was then diluted to 2 L with ultra-pure water (Milli Q water, >18.2MΩ) and heated at 70 °C in an oven for 60 hours. This transforms the ferrihydrite suspension to a yellow goethite precipitate that settles at the base of the reaction flask.

The excess solution was decanted with the goethite and remaining solution transferred to 50 mL Labcon centrifuge tubes (appendix A) and centrifuged for 20 minutes at 2,500 rpm with the solution then decanted. The goethite was then washed by re-suspending the solid in Milli-Q water, centrifuging and decanting again. This washing process was repeated until the goethite had been washed with the equivalent of three times the volume of the preparation solution (i.e. 6 litres). The goethite was transferred to cleaned petri-dishes and dried in an oven at 50 °C and then fully disaggregated in a cleaned agate mortar and pestle until it was visually homogeneous, before storage (Teflon container; appendix A).

3.2.1.2 Ferrihydrite

Ferrihydrite was also synthesised according to Cornell and Schwertmann (2003). A 200 mL solution of 1.0 mol/dm^3 KOH was added to 500 mL of freshly prepared 0.1 mol/dm^3 $Fe(NO_3)_3$, while continuously stirring. An additional 150 mL of 1.0 mol/dm^3 KOH was added dropwise to adjust the pH to ca. 7.5, thus producing a dark brown/black precipitate. The ferrihydrite slurry was centrifuged for 20 minutes at 5,000 rpm and the solution decanted. The ferrihydrite was then washed as described above for goethite and stored in a damp condition.

3.2.1.3 δ-MnO_2

Hexagonal δ-MnO_2 was synthesised (see Barling et al., 2004) by addition of 3.5 mL of 11 mol/dm^3 HCl to a 0.14 mol/dm^3 $KMnO_4$ solution and left to react for 3 hours and then diluted to 1 L with Milli Q water. The pH was adjusted from 2 to 7 with the addition of 1 mol/dm^3 or 5 mol/dm^3 KOH. The δ-MnO_2 was then filtered using a vacuum filtering system fitted with a Milli Q water dampened SPI-Pore™ polycarbonate 0.4 µm membrane filter and then stored as a suspension at 5° C.

3.2.1.4 XRD of the synthesised Fe oxyhydroxides and Mn oxide

The identity of the synthesised minerals was confirmed by X-ray powder diffraction (XRD). The XRD analysis were performed using an X'PERT PRO PANalytical X-Ray Diffractometer equipped with a Cu anode, with a wavelength of 1.54060 Å, as a radiation source, which is supplied with 45 kV and a current of 40 mA. The X'PERT PRO PANalytical X-Ray Diffractometer is located in the School of Chemical and Physical Sciences, Victoria University of Wellington. All data was collected over a range of 10.0066 – 80.9866 °2θ with a step size of 0.0130 °2θ and with 86.8526 s (time) per step.

Prior to analysis, the ferrihydrite and δ-MnO_2 were centrifuged and decanted and then the suspensions placed in a desiccator with the ferrihydrite being dried completely and the δ-MnO_2 left damp.

The XRD profiles for the three synthetic minerals are shown in figure 3.1. The patterns for both goethite and δ-MnO_2 show good correlation with the peak positions and intensities of XRD standards from the International Centre for Diffraction Data (ICDD); ICDD powder diffraction file number (PDF#) 29-0713 and ICDD Joint Committee on Powder Diffraction Standards (JCPDS) 13-0105 for goethite and δ-MnO_2, respectively. The XRD profile for the δ-MnO_2 sample is considerably noisier than that of goethite due to the δ-MnO_2 being less well crystallised.

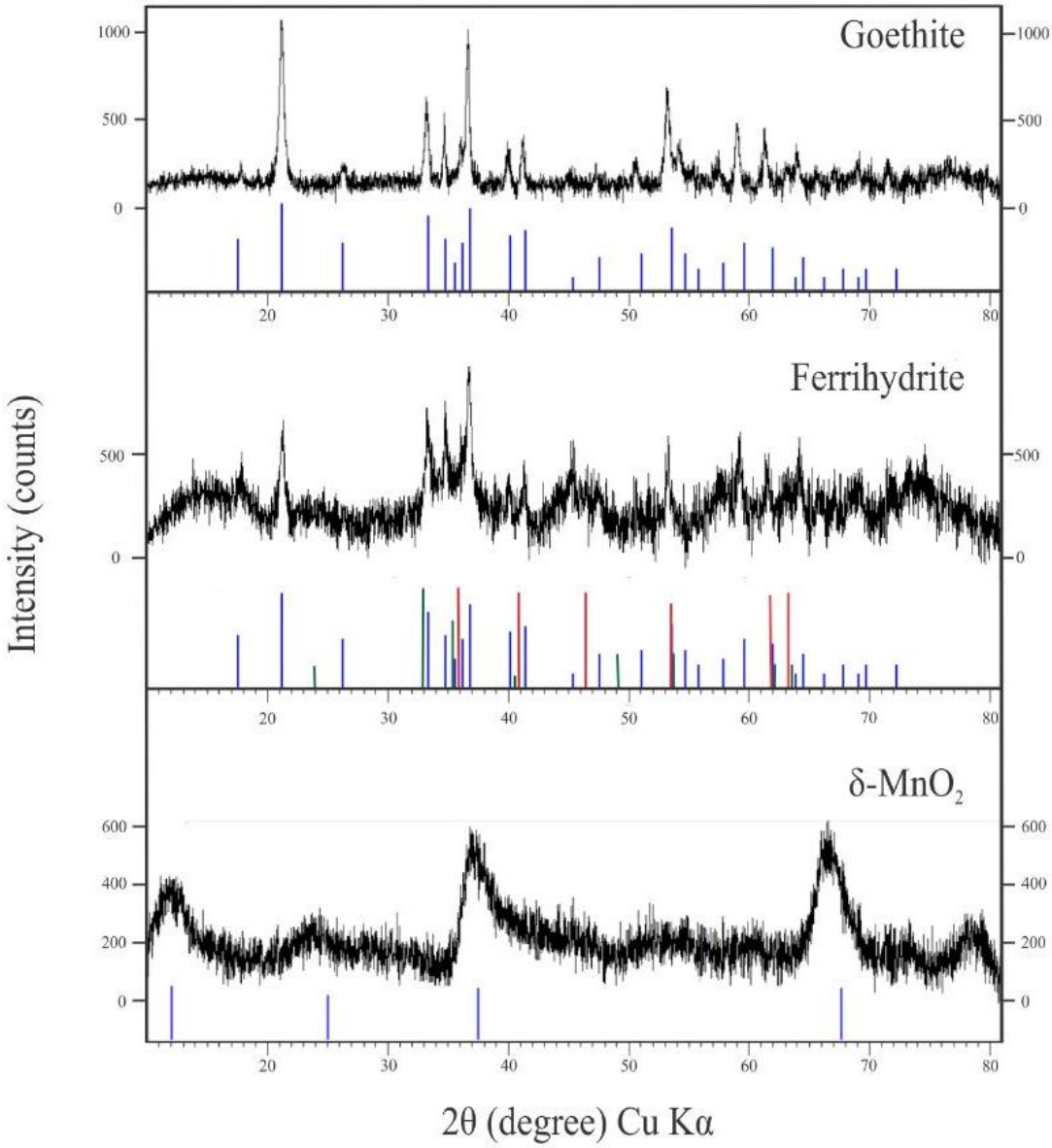

Figure 3.1 XRD profiles of the three synthetic minerals; goethite, ferrihydrite, and δ-MnO_2. A) goethite XRD pattern with the blue rods representing the peak locations of a goethite standard. B) ferrihydrite XRD pattern with the blue lines representing the peak locations of a goethite standard, green shows the peak location of a hematite standard, and the red lines represent the peak locations of a ferrihydrite standard. C) δ-MnO_2 XRD pattern with the blue rods representing the peak locations of a δ-MnO_2 standard.

The XRD pattern of the ferrihydrite showed peaks for goethite and hematite indicating that it had at least partially transformed to goethite and hematite. Ferrihydrite is not as thermodynamically stable as goethite or hematite and is a precursor for both, given the correct conditions (Michel et al., 2007). The presence of goethite and hematite is likely due to the pH of the ferrihydrite suspension not being fully equilibrated prior to drying for analysis. To minimise any transformation, the ferrihydrite was therefore prepared just prior to conducting the adsorption experiments (Raven et al., 1998).

3.2.2 Platinum containing solutions

Platinum occurs in seawater at concentrations ≤ 1 pmol/dm^3 (Colodner, 1991, Goldberg et al., 1986, Jacinto et al., 1989) which gives rise to iron and manganese oxides/oxyhydroxides (i.e. natural nodules and crusts) containing levels of adsorbed platinum on the order of 0.7 µg/g as noted in chapter 1 (Halbach et al. 1984, Halbach et al., 1989, Hein et al, 2013). To study the adsorption of platinum onto goethite, ferrihydrite and δ-MnO_2 surfaces, synthetic solutions were prepared such that platinum was available for adsorption onto the oxide and oxyhydroxide substrates in concentrations sufficient for reliable analytical detection by X-ray absorption spectroscopy and measurement of the isotopic composition. Therefore, starting solutions were prepared containing 50 µmol/dm^3 of platinum by the addition of a standard platinum solution (CRM SPEX CertiPrep 5 mmol/dm^3 platinum ICP standard in 10% HCl, hereafter referred to as the SPEX standard) to a 0.5 mol/dm^3 HCl, 0.6 mol/dm^3 NaCl (ΣCl^- = 1.1 mol/dm^3) solution.

The platinum in the SPEX standard is present as $PtCl_4^{2-}$, with this remaining the dominant species in the pH adjusted platinum containing solution at pH = 2, 4, and 6 (figure 3.2). The pH of the solution was adjusted to the required pH = 2, 4, 6, and 8, with the addition of 1 and 5 mol/dm^3 NaOH, such that the final concentration of ΣCl^- = 0.97 mol/dm^3 and platinum = 44 µmol/dm^3. The solutions were allowed to equilibrate before adsorption started for at least 48 hours with the pH being monitored and adjusted to the starting pH value (e.g. pH = 2, 4, 6, and 8). The concentration of dissolved platinum in the solutions was periodically checked using ICP-MS (Thermo

Scientific Element2). Both experimental and modeled (estimated) thermodynamic data compiled by Sassani and Stock (1998) from Sanders and Martin (1961) and Yamamoto et al. (1964), suggests that as the pH of the platinum containing solution approaches that of the natural marine environment (pH ≈ 7.4 - 8), the hydroxyl neutral species, $Pt(OH)_{2(aq)}$, becomes dominant at pH > 7.5 (figure 3.2).

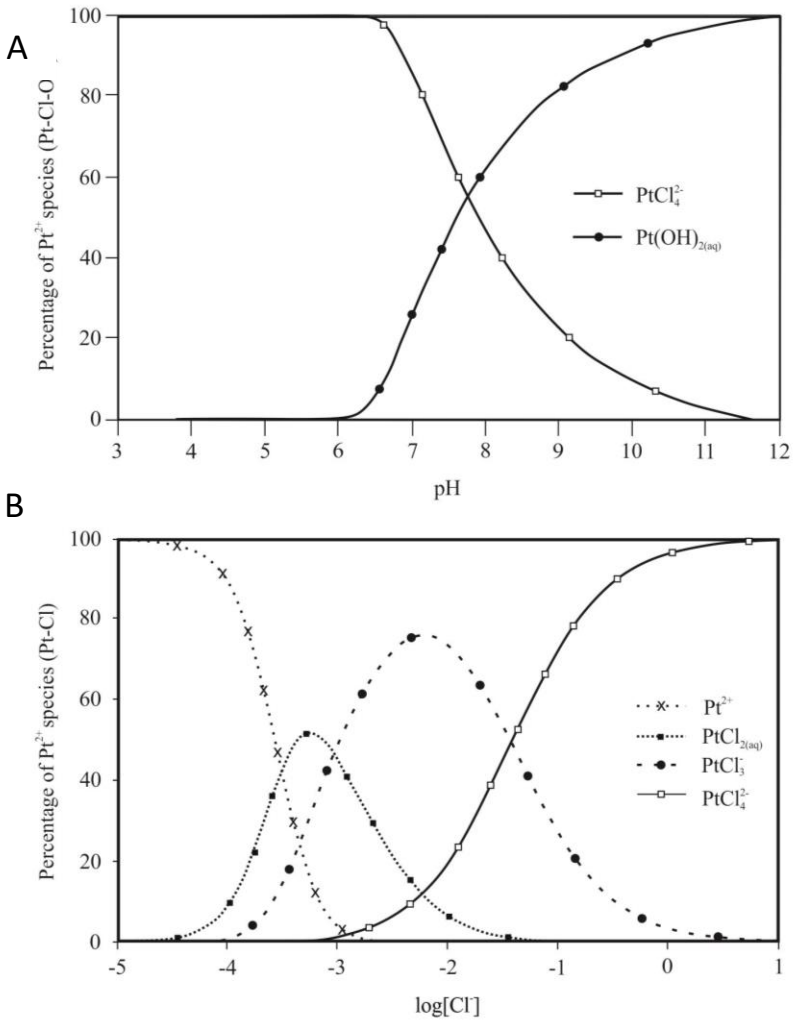

Figure 3.2 A) The percent of Pt^{2+} species present in solution as a function of pH at 25 ° C and ΣCl^{-} = 1 mol/dm^3 for ΣPt^{2+} = 8.6 x 10^{-19} mol/dm^3. The thermodynamic data were compiled by Sassani and Shock, 1998 using data derived by Brown and Sylva (1987), Sanders and Martin (1961), and Yamamoto et al. (1964). **B)** The percent of Pt^{2+} chloride species present as a function of $[Cl^{-}]$ concentration at 25 ° C, and ΣPt^{2+} = 1 x 10^{-9} mol/dm^3. This model was proposed by Colombo et al., 2008 using thermodynamic data from the NBS tables (Wagman et. al, 1982).

3.2.3 Adsorption equilibria

A series of experiments were conducted at each pH as a function of time to examine the adsorption of platinum, present as $PtCl_4^{2-}$ and $Pt(OH)_{2(aq)}$ in the platinum containing solutions, onto the oxyhydroxide and oxide substrates to determine the time required for adsorption equilibrium to be reached.

Four 0.50 g samples of goethite and ferrihydrite and four 25 mL aliquots of the δ-MnO_2 suspension were weighed into 50 mL centrifuge tubes (appendix B). A 25 mL aliquot of each pH adjusted platinum containing solution was added to one of each of the weighed synthesised oxyhydroxides and oxide. Each adsorption experiment (i.e. sealed 50 mL centrifuge tube) was placed onto a Heidolph Promax 1020 platform shaker set to 100 rpm, at laboratory temperatures (21 ± 1° C). A Scichem Tech SCT BEN-pH-01 meter with a standardised glass electrode was used to monitor the pH of the samples at intervals of 1, 3, 5, 7, 9, 12, 24, 30, 36, 48 hours, after the commencement of each experiment (appendix B).

All goethite and δ-MnO_2 suspensions achieved pH equilibrium within 12 hours, however, the ferrihydrite equilibration required up to 24 hours (figure 3.3). The adsorption experiments were therefore allowed to run for at least 24 hours before solid and liquid aliquots were taken for bulk Pt concentration and Pt isotopic analysis. The pH evolved with time as adsorption proceeded during the first 48 hour period and these values are shown in figure 3.3.

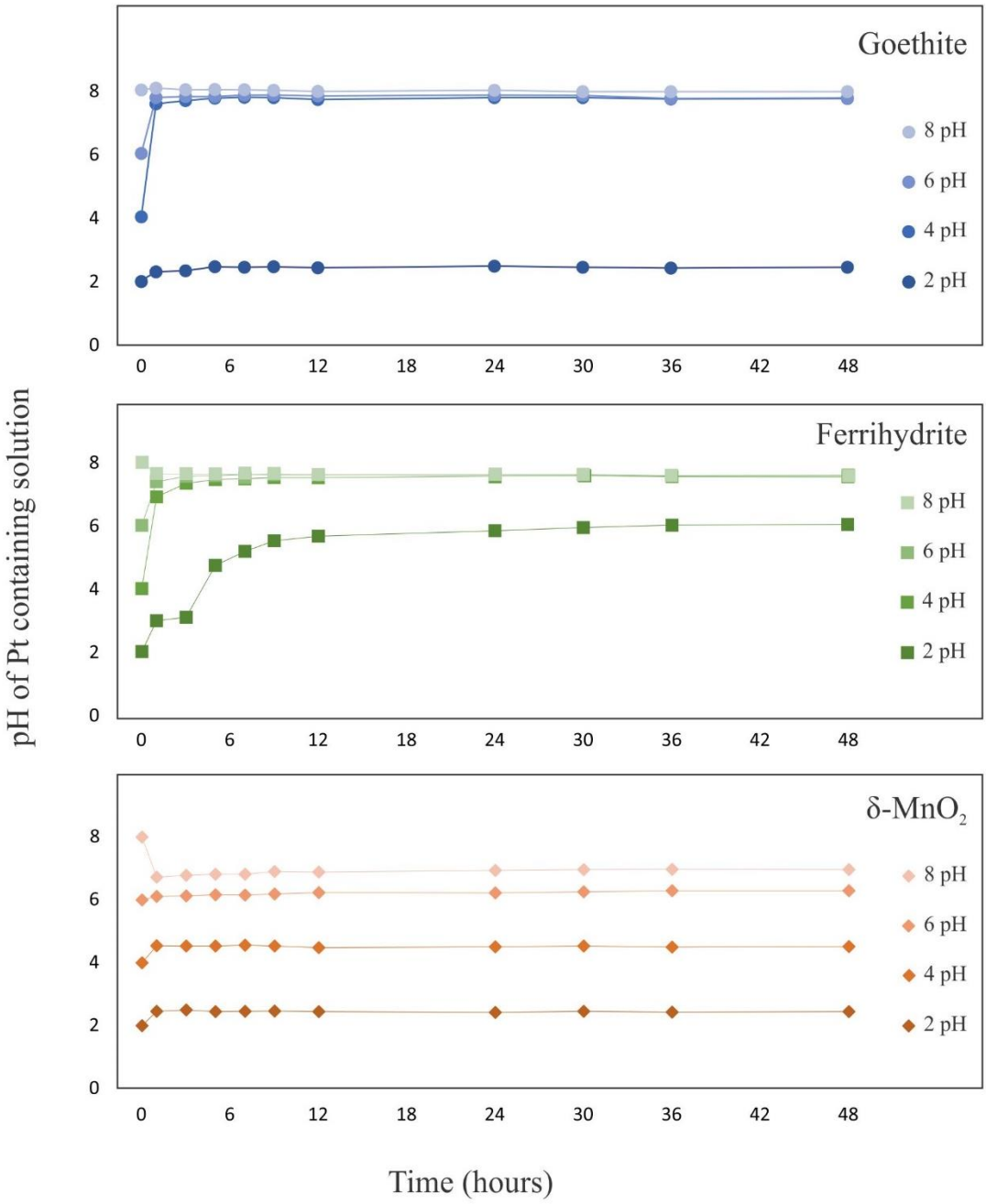

Figure 3.3 pH equilibrium of incorporation suspensions. Time required for solutions having initial pH = 2, 4, 6, and 8, to reach an equilibrium during the platinum adsorption experiments. The starting pH is given as the pH value of the platinum containing solution that was used for each sample. The pH equilibrium was reached for goethite and δ-MnO_2 within 12 hours, whereas, the ferrihydrite suspension with an initial pH = 8 took up to 24 hours to reach full equilibrium.

3.2.4 Analytical methods and procedures

3.2.4.1 Preparation of adsorption samples for ICP-MS and MC-ICP-MS analysis

The adsorption experiments were conducted at intervals of 24, 48, 96, 168, 336, and 504 hours and at four values of pH = 2, 4, 6 and 8. Approximately 0.50 g of goethite and ferrihydrite and 25 mL aliquot of the δ-MnO_2 suspension were weighed into 50 mL reaction tubes with 24 individual samples for each synthesised mineral (six time steps at four pH values). A 25 mL aliquot of each of the four pH adjusted platinum containing solutions was added to each synthesised mineral sample (appendix B). All suspensions were then placed onto the platform shaker at 100 rpm at laboratory temperatures.

The pH was not adjusted for the 24 and 48 hour samples, however, for samples that formed part of the longer time series (i.e. 96, 168, 336, and 504 hours) the pH was monitored and adjusted with HCl or NaOH. The pH was measured and adjusted at 48 hours for the 96 hour series, at 48 and 96 hours for the 168 and 336 times series, and at 48 hours and 240 hours for the 504 hour series (appendix B).

At the end of each experiment, the suspension was centrifuged at 2,000 rpm for 15 minutes. The solution sample, the supernatant, was decanted and filtered using a Luer lock syringe fitted with a Whatman® Swin-lok filter holder with a 0.45 µM cellulose filter membrane, hereafter referred to as the filter system (appendix B). To condition the filter system, a small volume of Milli-Q water was pushed through the filter system followed by a small volume of the solution sample, which was discarded. The sample solution was then filtered into a 50 mL centrifuge tube. The solid that was isolated on the filter membrane was washed back into the original centrifuge tube with the solid sample. The solid sample was washed (Milli-Q water), centrifuged and filtered, with the supernatant being discarded after filtering. This process was repeated three times and the sample then dried in a Teflon beaker.

All solid samples were digested in 11 mol/dm^3 HCl and an aliquot removed for concentration analysis using the Element2 ICP-MS instrument. An aliquot removed from each of the aqueous solution samples was also analysed to the determine the platinum concentration.

Solid and solution adsorption samples for the three oxyhydroxides and oxides at 24, 168, and 504 hours at each pH, comprising 72 samples in total, were prepared for isotopic analysis on the Neptune MC-ICP-MS at UoC. Sample preparation is described in detail in chapter 2 and briefly here. An aliquot of both the digested solid sample and solution sample were double spiked (^{196}Pt-^{198}Pt) based on the concentration determined from the Element2 ICP-MS and allowed to equilibrate by evaporating the double spiked sample to dryness and re-dissolved in 5 mL 11 M HCl three times in total prior to the final re-dissolving in 0.5 M HCl (chapter 2). A double spike methodology was utilised to allow for rigorous correction of instrumental mass fractionation and also to correct for incomplete yield of platinum through chemistry. The samples were then processed using anion exchange chromatography to separate platinum from the matrix elements, thus ensuring a more robust measurement on the MC-ICP-MS. Isotope dilution calculations were used to determine the concentration of platinum in the samples (chapter 2).

3.2.4.2 Preparation of adsorption samples for Synchrotron X-ray absorption spectroscopy

The sample size required for XAS analysis is larger than that required for ICP-MS-MS and MC-ICP-MS based on the calculated mass required using the XAFSmass freeware (Klementiev, 2012). Therefore, the mass of the oxyhydroxide and oxides and the volume of platinum containing solution were increased for the adsorption samples prepared for the synchrotron. Three pH values (2, 4, and 6) and single time interval were used for the synchrotron samples (appendix b).

All analyses were conducted at the Australian Synchrotron (Melbourne, Australia) in hutch B on the X-ray absorption spectroscopy beamline, employing a cryostat at 12 kelvin (K), to minimise radiation damage to the samples. The Pt-L_3 edge (11.6 KeV) was measured in the optimal energy range of 8.5 – 18 keV using Si (111) crystal recorded with a 36 element fluorescence detector by scanning the incident X-ray energy at three different steps depending on which part of the spectrum was being examined; 11.440 – 11.544 KeV at 0.003 KeV steps, 11.544 – 11.614 at 0.00025 KeV steps, and 11.614 –14 KeV steps at 0.035 KeV steps.

Both the X-ray absorption near edge structure (XANES) and X-ray absorption fine structure (EXAFS), were used to determine the average oxidation state and the local coordination environment of platinum adsorbed onto the oxyhydroxide and oxide surfaces. The XANES and EXAFS of a number of platinum model compounds were also measured; i.e. platinum foil (Pt^0), anhydrous platinum(II) chloride ($PtCl_2$), anhydrous platinum(IV) oxide monohydrate ($PtO_2 \cdot H_20$), platinum(IV) chloride ($PtCl_4$), and sodium hexachloroplatinate(IV) hexahydrate ($Na_2PtCl_6 \cdot 6H_2O$). The model compounds and oxyhydroxide and oxide samples were diluted (mixed), as required, with cellulose and then mounted as a pellet onto the sample holder with adhesive tape.

Due to the relatively low concentration of platinum in the samples, aluminium foil was used to mask the effects of iron and manganese on the signal. In addition to the aluminium foil, a solar slit was used for the analysis of the goethite samples. The solar slit was also utilised when analysing the $PtCl_4$ and $Na_2PtCl_6 \cdot 6H_2O$ standards.

All data collected at the Australian synchrotron were initially viewed with the Australian Synchrotron VeRSI computer program, Sakura, which converts the files from.mda to ascii and allows the XAS data to be explored (Sakura, 2013). The ascii files were then reduced using IFEFFIT package; i.e. Athena for XANES followed by Artemis for XAFS (Newville, 2001, Ravel and Newville, 2005).

3.3 Results of adsorption experiment, XAS analysis and the associated isotopic fractionation

3.3.1 Platinum adsorbed onto the oxyhydroxide and oxide surfaces

3.3.1.1 Platinum adsorption onto goethite

Platinum adsorption onto the surface of goethite showed an increase with increasing pH; the mean platinum concentration at pH = 2, 4, 6, and 8 was 11 µg/g, 37 µg/g, 79 µg/g, and 142 µg/g, respectively (figure 3.4). The adsorption at pH = 2, 4 and 8 remains moderately constant after the initial 24 hours, whereas the series of experiments at pH = 6 exhibits a monatomic increase in adsorbed platinum with increasing time (figures 3.4 and 3.5).

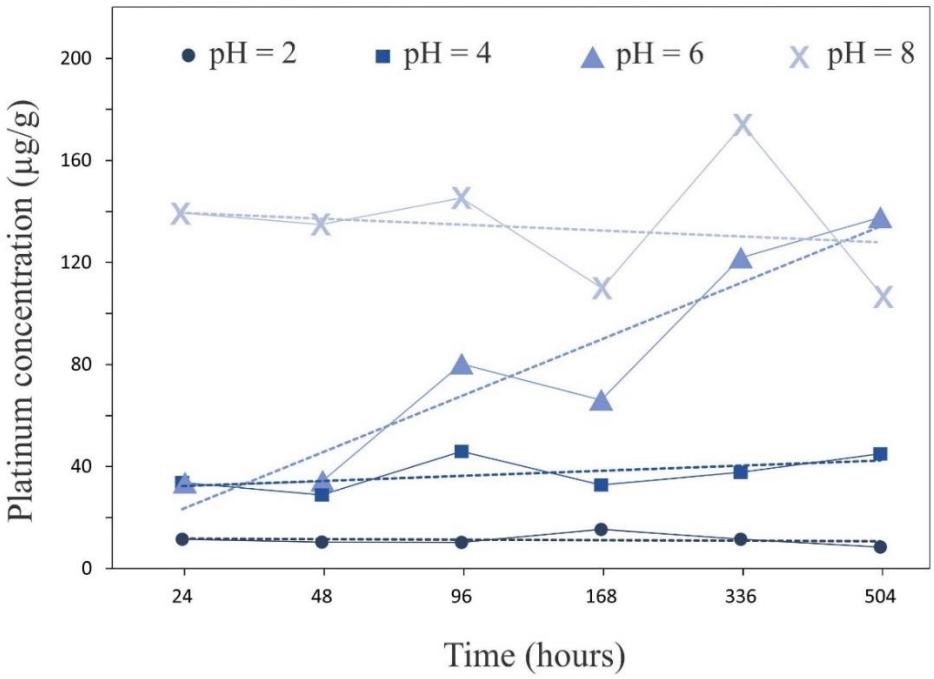

Figure 3.4 Concentration (µg/g) of platinum that adsorbed onto the surface of the goethite at pH = 2, 4, 6, and 8 over time. The dashed lines are the best fit lines showing the general trends of each pH series of adsorption experiment.

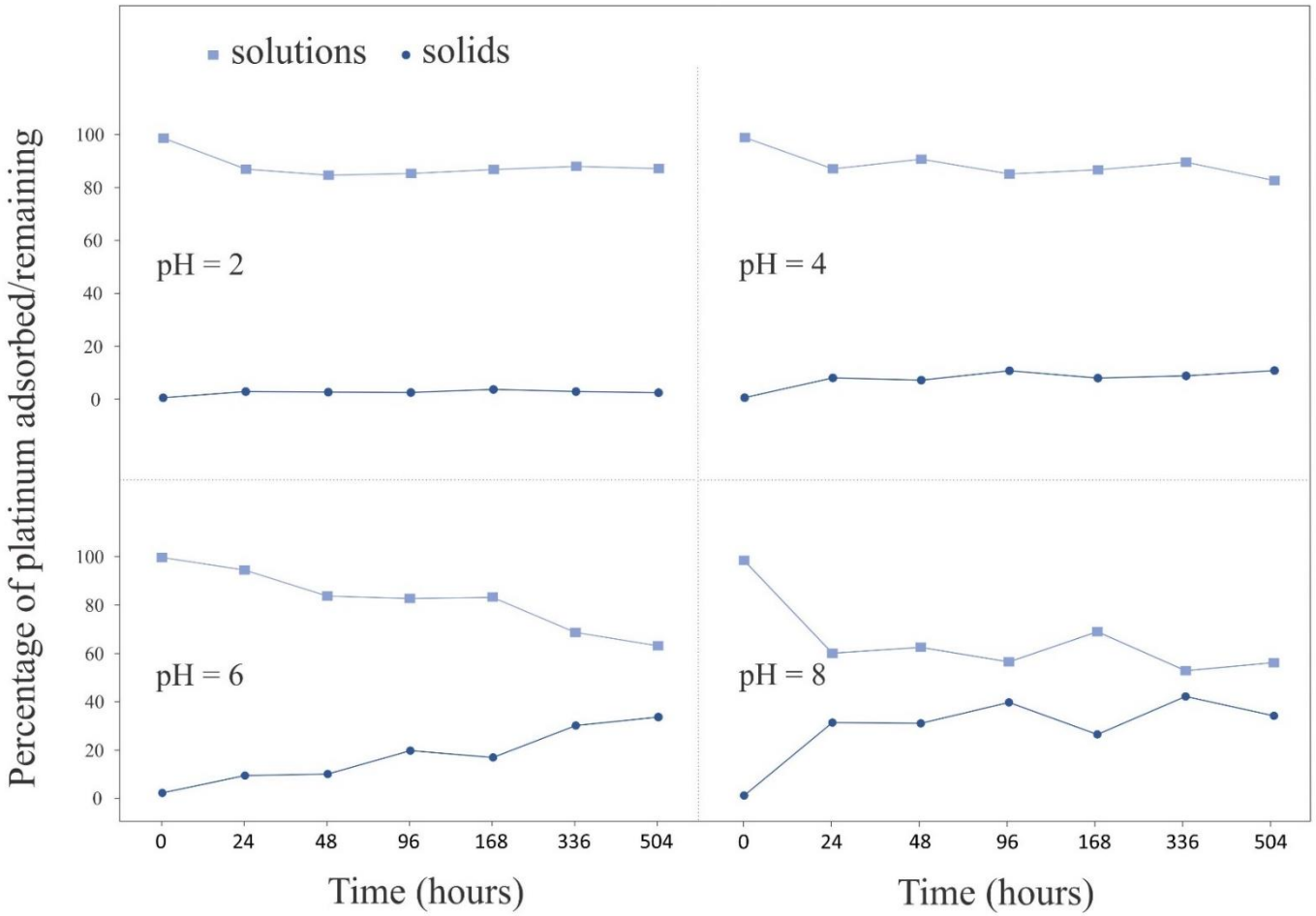

Figure 3.5 The percentage of platinum remaining in solution (squares) and the percentage of platinum adsorbed onto the surface of goethite (circles) as a function of time at pH = 2, 4, 6, and 8.

3.3.1.2 Platinum adsorption onto ferrihydrite

Platinum adsorption onto the surface of ferrihydrite increased with increasing pH; the mean platinum concentration at each given pH = 2, 4, 6 and 8 was 86 µg/g, 197 µg/g, 214 µg/g, and 347 µg/g, respectively (figure 3.6). At pH = 4, 6, and 8, the adsorption, in general, increases with increasing time that the solid is in contact with the platinum containing solution. However, the pH = 2 series deviated from the pattern with a decrease of platinum adsorption after 96 hours (figure 3.7). The adsorption of platinum over the first 96 hours for pH = 2, 4, 6 is similar in concentration and shows an increase with increasing time, whereas, pH = 8 samples show a higher platinum concentration at each time interval (figure 3.7).

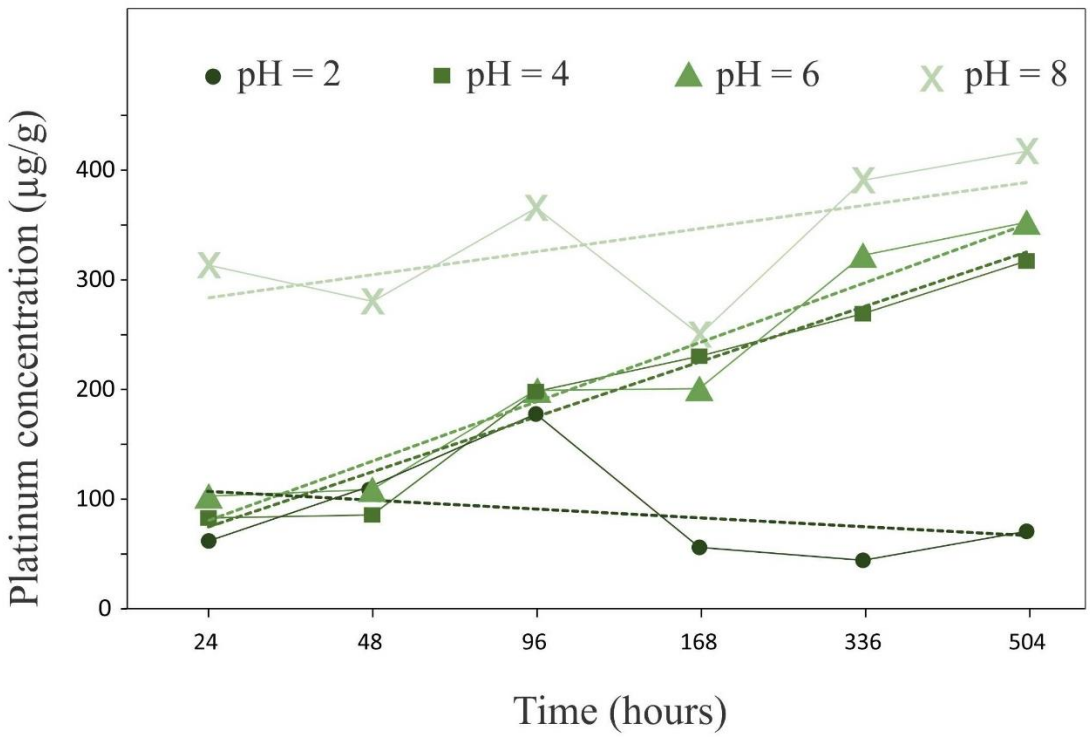

Figure 3.6 Concentration (µg/g) of platinum adsorbed onto the surface of the ferrihydrite at pH = 2, 4, 6, and 8 as a function of time; the dashed lines are the best fit lines showing the general trends of each pH series of adsorption experiment.

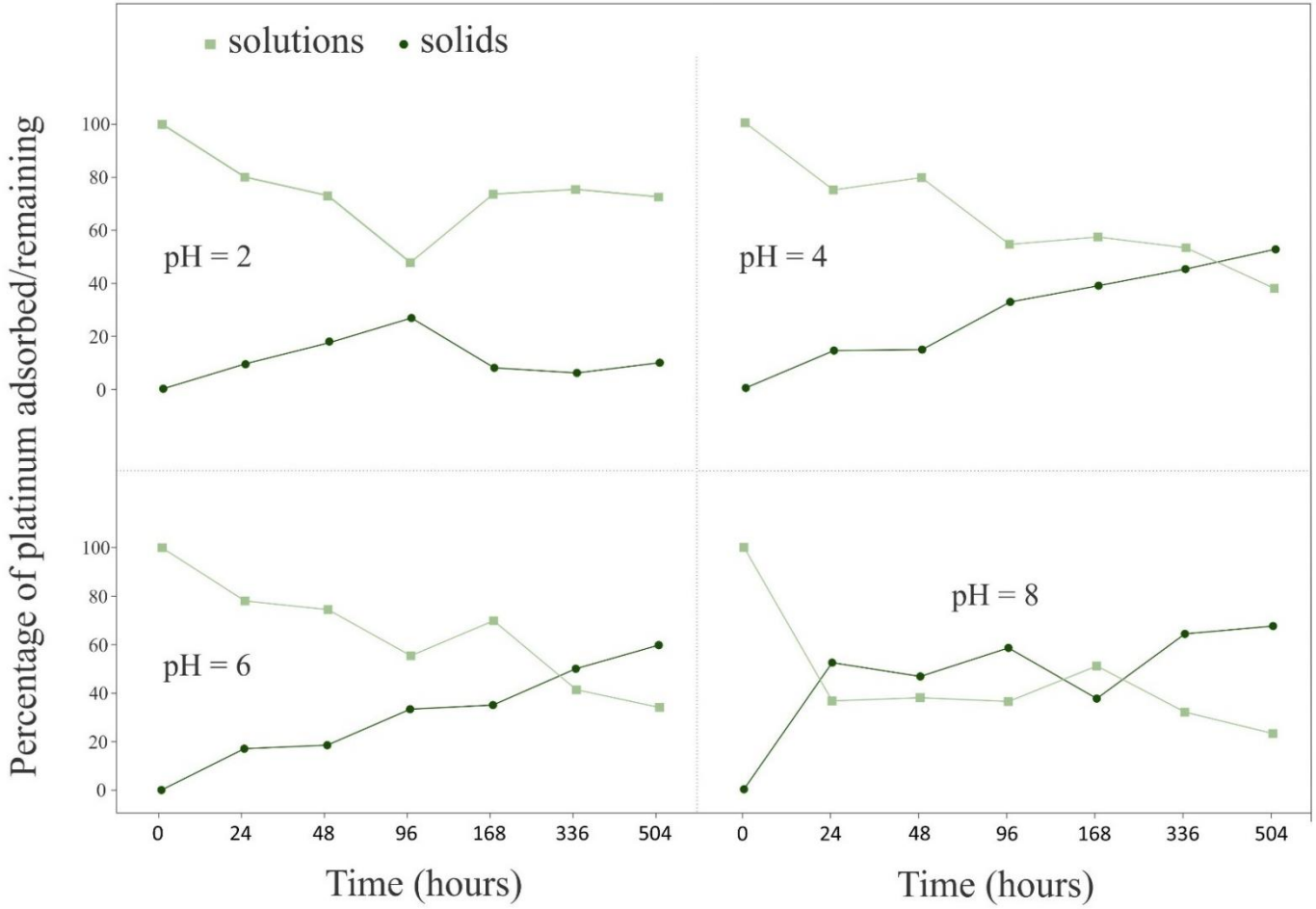

Figure 3.7 The percentage of platinum remaining in solution (squares) and the percentage of platinum adsorbed onto the surface of ferrihydrite (circles) as a function of time at pH = 2, 4, 6, and 8.

3.3.1.3 Platinum adsorption onto δ-MnO_2

Platinum adsorption onto the surface of δ-MnO_2 shows an increase with increasing pH with the pH = 8 samples having a mean concentration of 8 times that of the pH = 6 samples (figure 3.8). The mean platinum concentration adsorbed onto the surface of δ-MnO_2 at pH = 2, 4, 6, and 8 was 27 µg/g, 104 µg/g, 448 µg/g, and 3502 µg/g, respectively. Adsorption remains relatively constant for the pH = 2 and 4 series as a function of time. However, the pH = 6 and 8 series show an increase for both 24 and 48 hour samples prior to the first pH adjustment (figure 3.9). The samples for the time intervals > 96 hours for pH = 6 and 8 are relatively constant thereafter (figure 3.9).

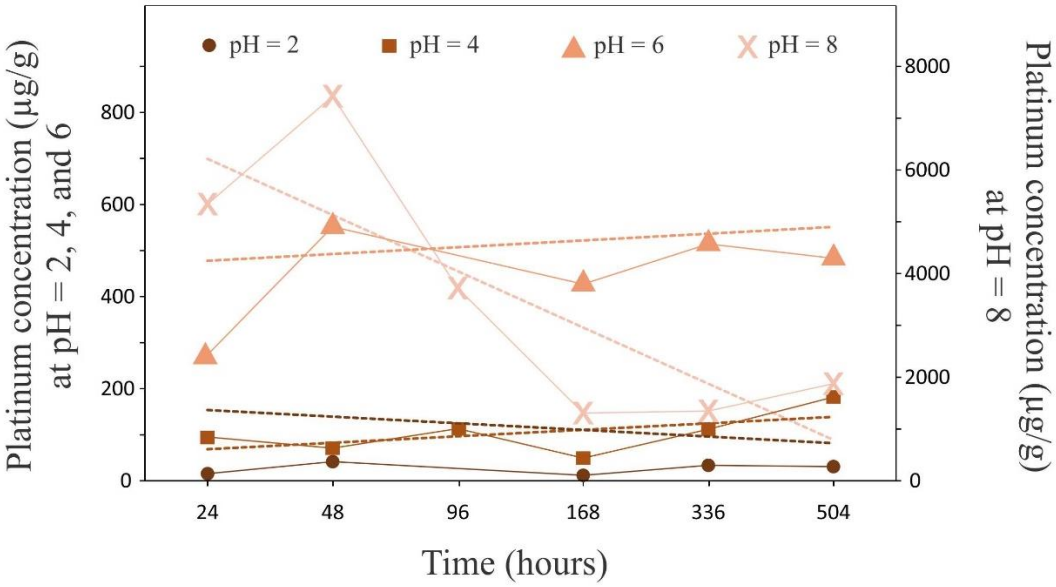

Figure 3.8 Concentration (µg/g) of platinum adsorbed onto the surface of the δ-MnO_2 at pH = 2, 4, 6, and 8 as a function of time. The dashed lines are the best-fit lines showing the general trends of each pH series of adsorption experiment. Note the differing scales: due to the variation of platinum adsorbed, the concentrations are given on the two vertical axis (i.e. samples from pH = 2, 4, and 6 are given on the primary vertical axis and samples from pH = 8 are given on the secondary vertical axis).

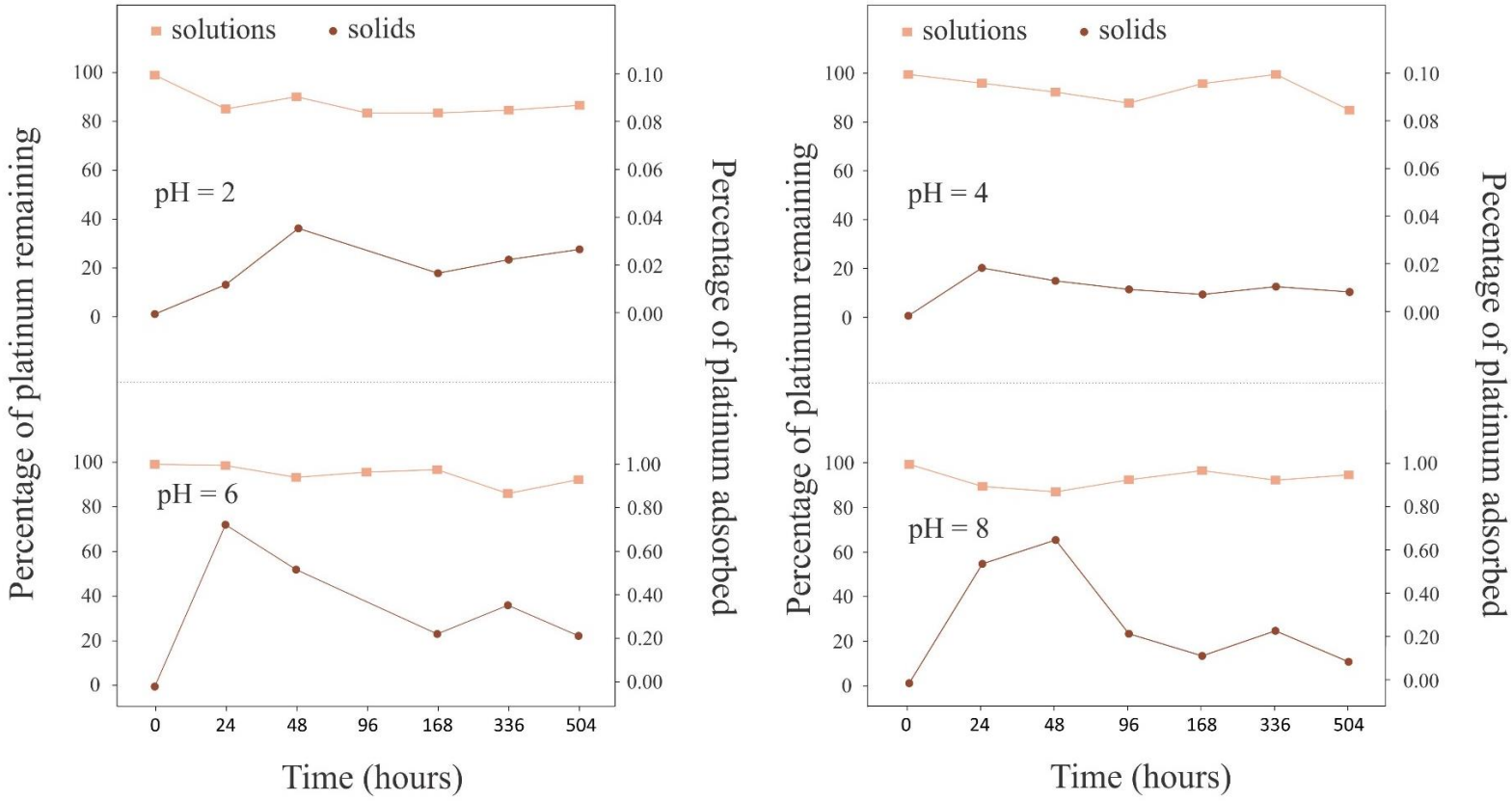

Figure 3.9 The percentage of platinum remaining in solution (squares) and the percentage of platinum adsorbed onto the surface of δ-MnO_2 (circles) as a function of time at each given pH = 2, 4, 6, and 8. The percentage remaining in solution is given on the primary vertical axis and the percentage adsorbed onto the δ-MnO_2 surface is given on the secondary vertical axis. The scale for the platinum adsorbed at pH = 6 and 8 is an order of magnitude larger than that of the pH = 2 and 4.

3.3.1.4 Platinum adsorption onto samples prepared for synchrotron x-ray absorption spectroscopy

The 1 g goethite samples prepared for XAS adsorbed less platinum than the 0.5 g goethite samples (figure 3.10). A slight increase in the platinum adsorbed onto the surface is also observed with increasing pH from pH = 2 to pH = 6 (figure 3.10). However, the pH = 4 samples for both masses show the highest concentration of platinum adsorbed.

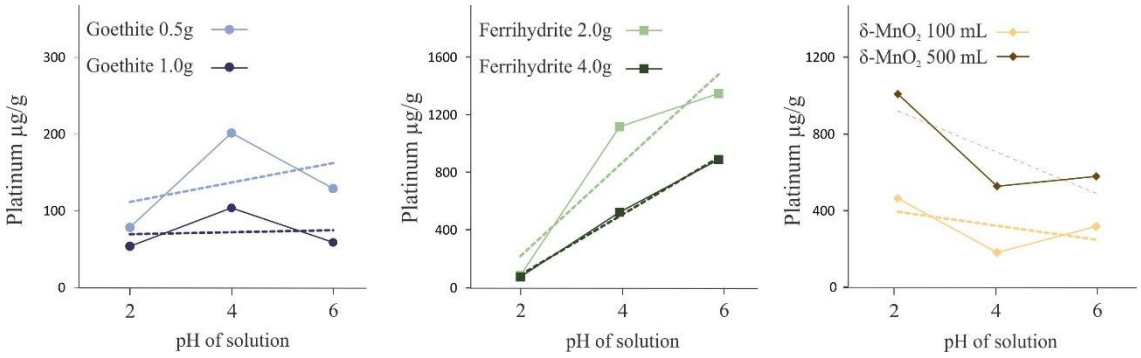

Figure 3.10 Platinum concentration (µg/g) adsorbed onto the surface of the synthetic oxyhydroxide and oxide surfaces at varying mass as a function of pH. The dashed lines represent the general trend observed for each sample over the pH series (2, 4, and 6).

The larger sample size for ferrihydrite, 4 g, also resulted in lower adsorption of platinum than the smaller sample size, 2 g, as seen with goethite (figure 3.10). The platinum adsorption increases with increasing pH with both masses. Platinum is 1.1, 2.1, and 1.5 times more concentrated in the 2.0g samples than the 4.0g samples at pH values of 2, 4, and 6, respectively.

δ-MnO_2 shows an increase in platinum concentration with increasing δ-MnO_2 sample mass; however, the amount of platinum in the solution was five times higher for the 500mL samples compared to the 100mL samples. Unlike the δ-MnO_2 adsorption experiments (chapter 3.3.1.3), there is an inverse relationship between the amount of platinum adsorbed and the pH.

3.3.2 Synchrotron X-ray absorption spectroscopy

Six samples were analysed by synchrotron X-ray absorption spectroscopy: goethite (0.5 g) pH = 6; ferrihydrite (4.0 g) pH = 4 and 6; and δ-MnO_2 (500 mL) pH = 2, 4, and 6 (table 3.2). These samples were chosen due to the amount of sample remaining to allow for adequate scans to be performed and the platinum concentration. The higher the platinum concentration, the less the masking effect from Fe and Mn.

Table 3.2 The six samples that were measured using synchrotron x-ray absorption spectroscopy. The concentration of the platinum adsorbed onto the oxyhydroxide and oxide surfaces was determined by ICP-MS analysis on the Element2 ICPMS. The percent platinum adsorbed is calculated based on the initial platinum in solution less the platinum adsorbed onto the solid, as determined by ICP-MS.

Synthetic mineral and mass used	pH	Pt adsorbed (μg/g)	Pt adsorbed (%)
Goethite 0.5g	6	129	13
Ferrihydrite 4.0g	4	1120	20
Ferrihydrite 4.0g	6	1350	34
δ-MnO_2 500mL	2	1010	2
δ-MnO_2 500mL	4	530	2
δ-MnO_2 500mL	6	581	1

3.3.2.1 X-ray absorption near edge (XANES) structure of the platinum adsorbed onto the surface of the oxyhydroxides and oxides

All spectra were normalised in Athena, including background removal, pre- and post-edge jumps and Fourier transforms over a k-range of 3 to 10.5 Å and an r-range of 1.3 to 3 Å. The normalised Pt L_3-edge XANES spectra of the platinum standards, $PtCl_2$, $PtCl_4$, $PtO_2 \cdot H_20$, and $Na_2PtCl_6 \cdot 6H_2O$ and the XANES spectra of Pt adsorbed onto oxyhydroxide and oxide surfaces (table 3.2) are given in figure 3.11. The white lines (i.e. the main absorption peak) of the standards examined show variations in their intensities with platinum foil having the lowest intensity and $Na_2PtCl_6 \cdot 6H_2O$ showing

the highest, that is, 1.25 and 2.24 times the normalised adsorption, respectively. The white line intensity of the Pt L_3-edge is associated with the electron transition from $2p_{3/2}$ to $5d_{3/2}$ and $5d_{5/2}$ transitions. If the platinum is oxidised, a larger white line intensity is seen compared to a metallic platinum due to the vacancy in the d-orbital in the oxidised platinum versus no electron vacancy in a Pt^0, the intensity increasing with increasing platinum oxidation state. Other factors also contribute to the white line intensity including the nearest neighbour distance and bonding environment with compounds in which platinum is bound to oxygen generally having higher intensities than those in which platinum is bound to chlorine (Hall et al., 2003, Hyde et al, 2011, Matthew and Russell, 2000, Yoshida et al., 2005).

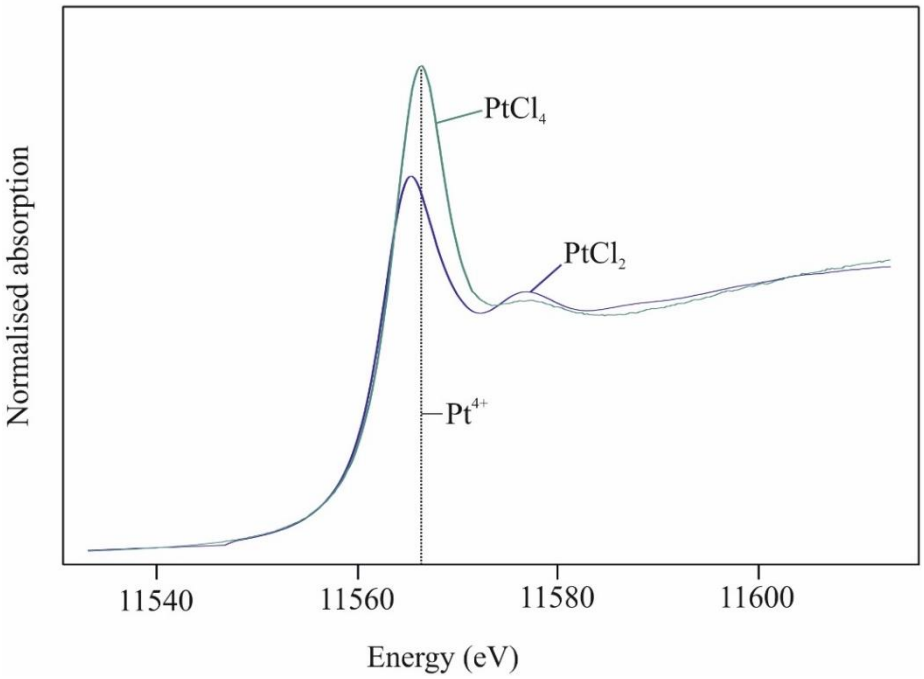

Figure 3.11 XANES spectra of Pt L_3-edge for $PtCl_2$ and $PtCl_4$, with a fit range of 20 eV below and 30 eV above the white line (dashed line represents the Pt^{4+} white line). The plot shows the difference in peak height between two oxidation states of platinum, Pt^{2+} and Pt^{4+}, with Pt^{4+} being higher than Pt^{2+}. This is similar to studies conducted by Hall et al. (2003) on different platinum complexes, namely cis-$[Pt^{(II)}Cl_2(NH_3)_2]$ and cis,trans,cis-$[Pt^{(IV)}Cl_2(OH)_2(NH_3)_2]$.

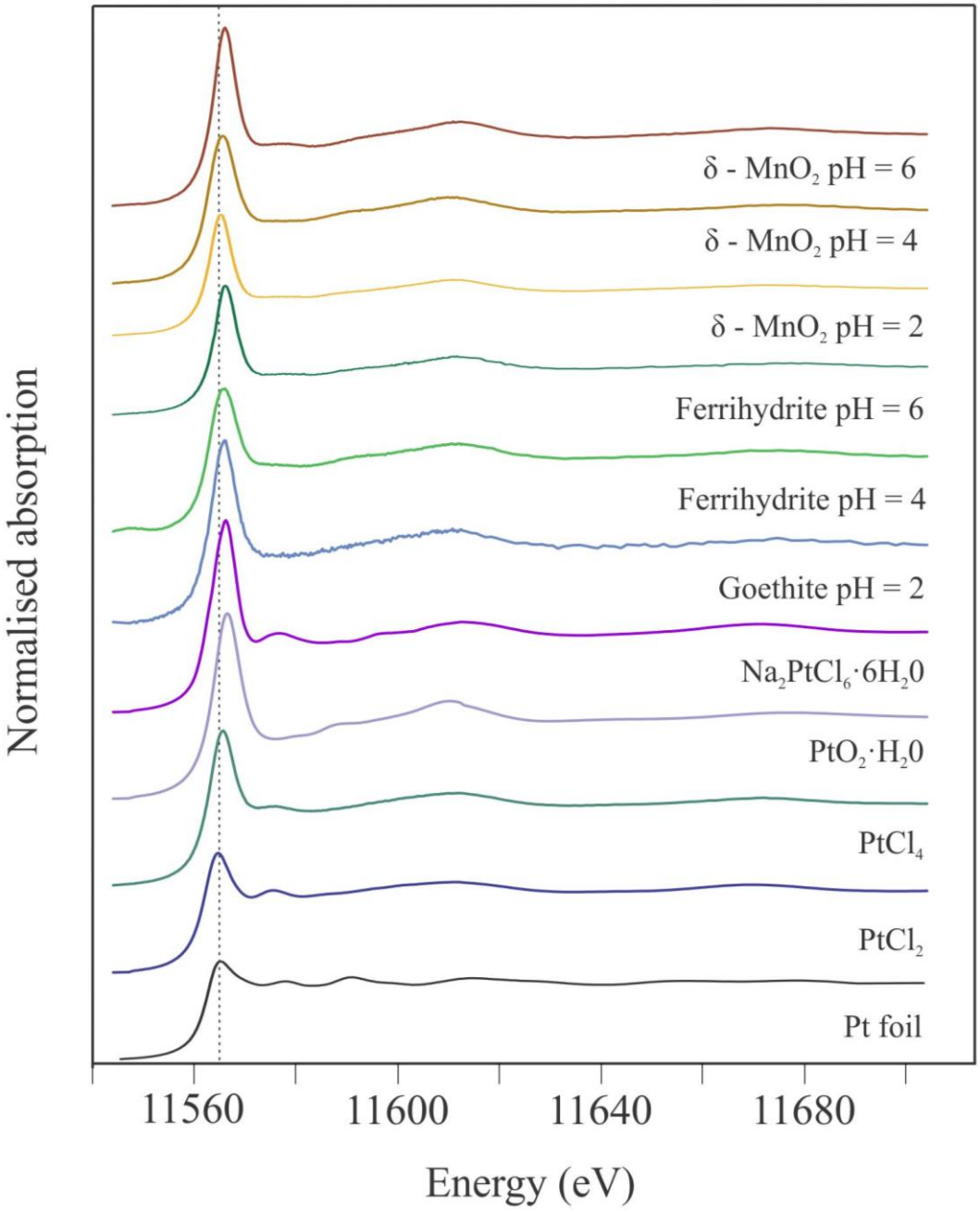

Figure 3.12 Normalised absorption XANES spectra of Pt L_3-edge for the various platinum standards which include Pt foil, $PtCl_2$, $PtCl_4$, $PtO_2 \cdot H_20$, and $Na_2PtCl_6 \cdot 6H_20$ as well as the XANES spectra of Pt L_3-edge of the platinum adsorbed onto the samples, with a range of 20 eV below and 140 eV above the white line. The dashed line represents the white line of the Pt foil.

The difference in the white line intensity along with a slight energy shift, < 5 eV, between the three oxidation states of Pt^0, Pt^{2+} and Pt^{4+} is clearly evident with the offset in the $PtCl_2$ spectrum compared to that of $PtCl_4$ plotted in figure 3.11. This shift of energy and variation in white line intensity are visibly noticeable in the six spectra of the oxyhydroxide and oxides with the energy increasing by up to 2 eV as the valency changes from Pt^{2+} to Pt^{4+}. The white line intensities are also greater than that of platinum foil and $PtCl_2$, 1.25 and 1.41, respectively (figure 3.12).

The structure at 11575 eV located just above the white line in $PtCl_2$, $PtCl_4$, and $Na_2PtCl_6{\cdot}6H_2O$ has been associated with the presence of a Cl^- in the system (Maeno et al., 2015). This is supported by the lack of this structure in $PtO_2{\cdot}H_2O$. This structure is not as obvious in the oxyhydroxide and oxide samples used for platinum adsorption, but nevertheless, it is observed in each spectrum, suggesting the presence of chloride in the system. Others have suggested that the occurrence of this structure is insufficient evidence alone to support the presence of Cl^- in the system (Hyde et al., 2011, Hyde and Sankar, 2015).

A linear combination fit (LCF) was applied to the normalised XANES spectra of the platinum adsorbed onto the oxyhydroxide and oxide samples using the four platinum standard model compounds analysed at the time of data collection (table 3.3). The LCF technique was employed to further examine the redox state of the platinum adsorbed and to suggest but not confirm the possible nearest neighbours. The first six best fitted LCF for each oxyhydroxide and oxide samples are given in appendix b. The 'goodness of fit' is determined mathematically by Athena and expressed as the R-factor (equation 3.1), which is the fractional misfit between the measured data and the fit.

$$\text{R-factor} = \Sigma(\text{data-fit})^2 \text{ x number of point} / \Sigma\text{data}^2 \qquad (3.\ 1)$$

The first generated LCF fitting was used to describe the XANES spectra for three of the samples (goethite at pH = 6, ferrihydrite at pH = 4, and ferrihydrite at pH = 6). The other three oxyhydroxide and oxide samples do not use the first suggested LCF fitting as some fittings included negative proportions of the modal standards. The LCF shows

Pt^{4+} to be the dominant oxidation state of the platinum adsorbed from the aqueous solution onto the oxyhydroxide and oxide surfaces. The LCF analysis indicates that up to 5% Pt^{2+} is present on the ferrihydrite surface with the proportion of Pt^{2+} decreasing from 4.7% to 0.7% with increasing pH from 4 to 6. The δ-MnO_2 at pH = 4 shows a minor amount of Pt^{2+} = 0.27 %, whereas no Pt^{2+} was noted in the δ-MnO_2 samples at other pH values and the goethite sample (table 3.3 and appendix b).

Table 3.3 Linear combination fitting (LCF) of the XANES for platinum adsorbed onto the oxyhydroxide and oxide surfaces using the XANES of the standard compounds ($PtCl_2$, $PtCl_4$, $PtO_2 \cdot H_20$, and $Na_2PtCl_6 \cdot 6H_2O$) for the fittings. The predominant oxidation state of platinum present on the surface of the samples is Pt^{4+} with minor amounts of Pt^{2+} as indicated (appendix b).

	R factor	Pt^{2+} species (%)	Pt^{4+} species (%)
Goethite, pH = 6	0.0028	-	100.00
Ferrihydrite, pH = 4	0.0009	4.67	95.33
Ferrihydrite, pH = 6	0.0005	0.73	99.27
δ-MnO_2, pH = 2	0.0240	-	100.00
δ-MnO_2, pH = 4	0.0039	0.27	99.73
δ-MnO_2, pH = 6	0.0091	-	100.00

Figure 3.13 shows the best fit LCF plotted against the spectrum of each synthetic mineral. The correlation between the best fit LCF and the goethite and ferrihydrite samples is good; R-factor < 0.003 and reduced X^2 < 0.003. The correlation between the δ-MnO_2 samples and the best fit has some discrepancies, in particular, the intensity of the white line especially for δ-MnO_2 pH = 2; R < 0.024 and reduced X^2 < 0.009.

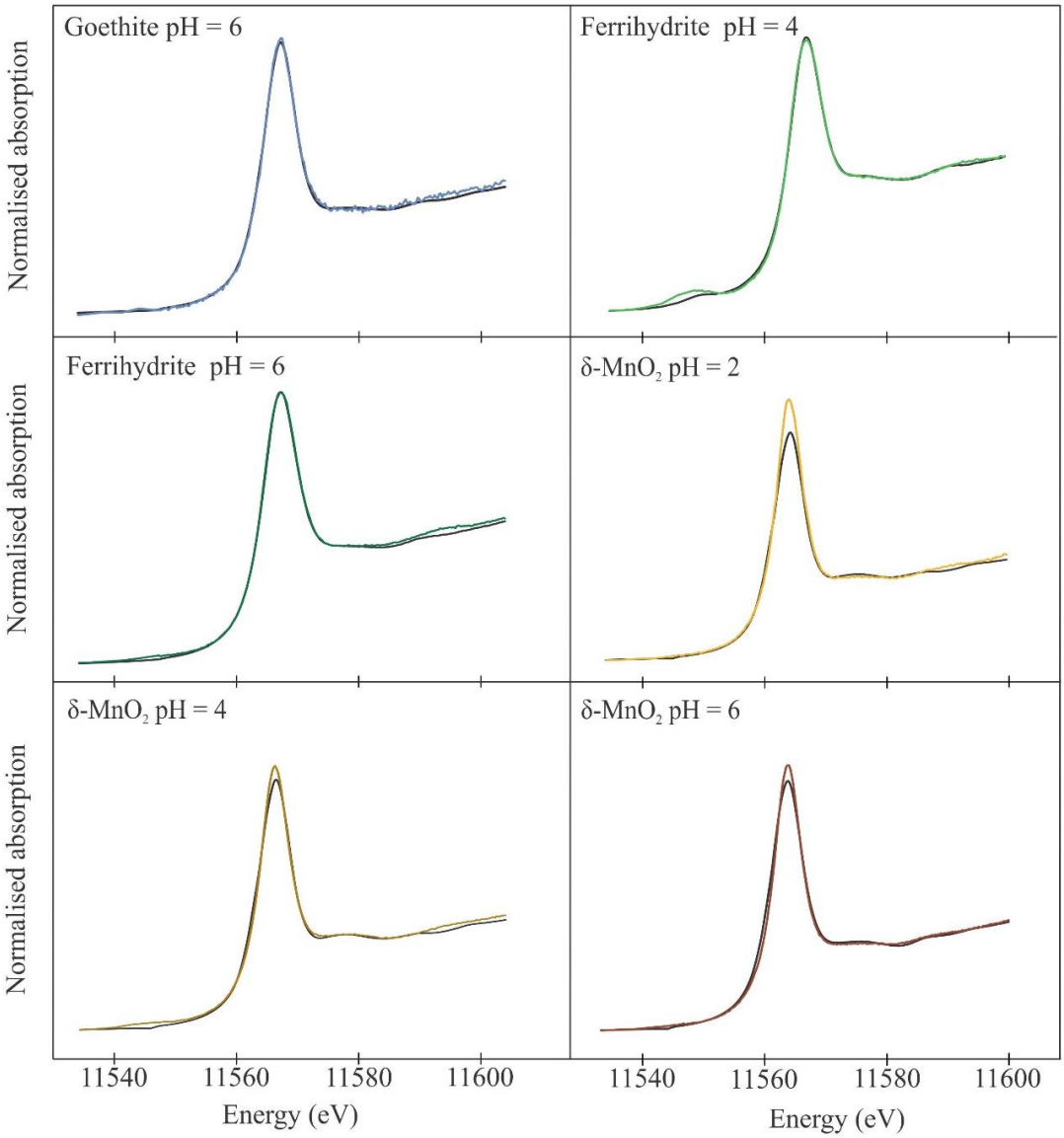

Figure 3.13 Normalised XANES LCF best fit (black line) for the XANES spectra (Pt L_3-edge) of platinum adsorbed onto the oxyhydroxide and oxide samples, within the range from -20 eV below to +30 eV above the white line.

3.3.2.2 X-ray absorption fine structure (EXAFS) of the platinum adsorbed onto the surface of the oxyhydroxides and oxides

The EXAFS for the five model compounds were background subtracted and Fourier transforms obtained. The resulting first shell distances (R/Å) were then compared with crystal structure data from the Cambridge Crystallographic Data Centre (CCDC) as shown in table 3.4.

Table 3.4 EXAFS derived first shell distances (R/Å) and coordination numbers (CN) and the associated Debye Waller factor (σ^2) as well as the crystallographic distances from the CCDC for the model compounds. The R-factor is the mathematically derived 'goodness of fit' based on the fractional misfit between the measured data and the fit. The Debye Waller factor (σ^2) is defined within Artemis as the mean square displacement of interatomic distance i.e. bond distance variation within coordination shell due to thermal or structural disorder.

	Atom-pair	**CN**	**R-factor**	**σ^2**	**R/Å**	
					This study	**CCDC**
$Pt^{(0)}$ foil	Pt-Pt	12.00	0.00	0.004	2.76	2.789
$Pt^{(II)}Cl_2$	Pt-Cl	4.00	0.03	0.001	2.30	2.314
$Pt^{(IV)}Cl_4$	Pt-Cl	4.00	0.05	0.004	2.29	2.300
$Pt^{(IV)}O_2 \cdot H_2O$	Pt-O	5.74	0.02	0.002	2.01	2.085
$Na_2Pt^{(IV)}Cl_6 \cdot 6H_2O$	Pt-Cl	6.00	0.03	0.002	2.31	2.314

To determine the coordination number of the experimental samples, the amplitude reduction factor, S_0^2, which is the parameter used to account for the shake-up/shake-off processes of the absorbing (central) atom i.e. the loss of amplitude due to multi-electron excitation of the inner shell was first deduced. This was achieved by setting the coordination number for each of the platinum model compounds to the measured crystallographic value from the CCDC database within the parameters of Artemis and thus allowing the S_0^2 to be estimated, 0.850. The S_0^2 was then set and the coordination number was set as a 'guess parameter' for all the oxyhydroxide and oxide samples.

The coordination number are listed in table 3.5 and the Fourier transformed Pt-L_3 edge EXAFS data of platinum adsorbed onto the oxyhydroxide and oxide surfaces are shown in Figure 3.14. Both oxygen and chlorine were considered in the fitting of the first shell scatterers. The EXAFS derived coordination number (CN) and the Pt^{4+} – O and Pt^{4+} – Cl distances (R/A) are given in table 3.5. The first shell distances are similar to those given for pure compounds obtained from the CCDC database table 3.4. In the case of goethite at pH = 6, for example, the $Pt^{(4+)}$ is bound to 4 first shell neighbours i.e. 2 oxygen and 2 chlorines at a length of 1.98 Å and 2.27 Å, respectively, whereas the CCDC bonding lengths are 1.998 Å and 2.300 Å.

Two of the six samples show a 4-fold coordination (goethite at pH = 6 and ferrihydrite at pH = 4) with the other four samples showing a 6-fold coordination (ferrihydrite at pH = 6, and δ-MnO_2 at pH = 2, 4, and 6).

Table 3.5 EXAFS derived first shell distances (R/Å) of Pt^{4+} - O and Pt^{4+} - Cl and coordination numbers (CN) and the associated Debye Waller factors (σ^2) for the platinum adsorbed onto the oxyhydroxide and oxide surfaces. The R-factor is the mathematically derived 'goodness of fit' based on the fractional misfit between the measured data and the fit. The Debye Waller factor (σ^2) is defined within Artemis as 'the mean square displacement about the half path length of the path'.

	Atom-pair	CN	R-factor	σ^2	R/Å
Goethite 6pH	Pt^{4+}- O	2.47	0.05	0.001	1.98
	Pt^{4+}- Cl	1.83	0.05	0.003	2.27
Ferrihydrite 4pH	Pt^{4+}- O	2.83	0.03	0.005	2.03
	Pt^{4+}- Cl	1.46	0.03	0.005	2.31
Ferrihydrite 6pH	Pt^{4+}- O	5.10	0.05	0.005	2.01
	Pt^{4+}- Cl	0.55	0.05	0.009	2.28
δ-MnO_2 2pH	Pt^{4+}- O	5.18	0.08	0.003	2.03
	Pt^{4+}- Cl	1.28	0.08	0.003	2.31
δ-MnO_2 4pH	Pt^{4+}- O	4.45	0.05	0.003	2.05
	Pt^{4+}- Cl	1.30	0.05	0.003	2.33
δ-MnO_2 6pH	Pt^{4+}- O	5.95	0.07	0.006	2.05
	Pt^{4+}- Cl	0.96	0.07	0.008	2.33

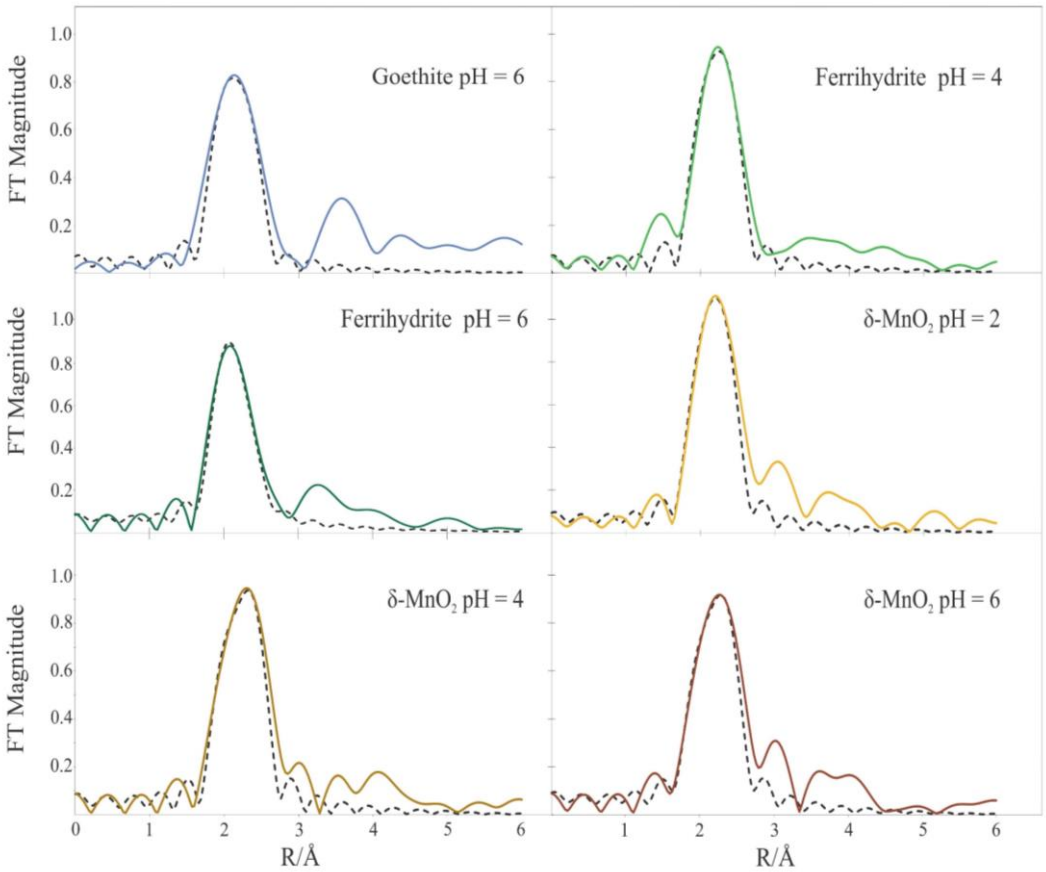

Figure 3.14 Fourier transformed EXAFS data of Pt adsorbed onto synthetic iron and manganese oxides and the calculated best-fit data. The calculated EXAFS is shown with the black dashed line with the measured values shown with the coloured solid lines. The fitting was preformed over an R-range of 1.5 – 3 Å

3.3.3 Platinum isotopic composition of adsorption experiments

3.3.3.1 Platinum isotopic composition of the platinum containing solution

The platinum isotopic composition is reported as δ^{198}Pt (equation 3.2).

$$\delta^{198}\text{Pt} = [\ \frac{198}{194}\text{Pt}_{(\text{sample})} / \frac{198}{194}\text{Pt}_{(\text{IRMM-010})} - 1] \times 10^3 \qquad (3.2)$$

The initial δ^{198}Pt composition of the platinum containing solution (SPEX standard) for the four different pH experiments was δ^{198}Pt = 0.035 ± 0.023 ‰, analysed on a Thermo Fisher Neptune MC-ICP-MS at the University of Copenhagen (chapter 2.4). This mean δ^{198}Pt value will be used as the δ^{198}Pt starting composition for all adsorption pairs discussed in the following sections.

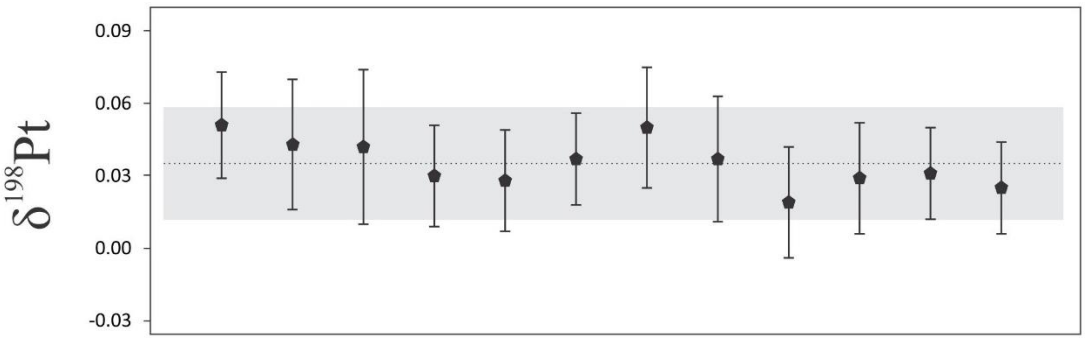

Figure 3.15 The δ^{198}Pt of the platinum containing solution (SPEX standard). The mean δ^{198}Pt is 0.035 ± 0.023 ‰ (2sd), n = 12. The individual error on each analysis is 2se with the grey shaded area representing the mean 2sd from all analysis of the SPEX solution and the dashed black line showing the mean.

3.3.5.2 Isotopic composition of Pt adsorbed onto the goethite surface

The δ^{198}Pt of the adsorption pairs (platinum adsorbed onto the solid and platinum remaining in solution) for goethite over all pH and time intervals is shown in figure 3.16. For all adsorption pairs at pH = 4, 6, and 8, the solutions were isotopically heavier than the original platinum containing solution, whereas, the solids exhibited a lighter platinum isotopic composition indicating that the lighter isotopes are preferentially adsorbed onto the goethite surface during the experiments. The δ^{198}Pt composition of the solids at pH = 2 are all similar to the initial platinum isotopic composition of the Pt-containing solution although a small fractionation of lighter platinum is observed at 504 hours. It should also be noted that <3% of the total platinum was adsorbed from the solution onto the goethite surface at pH = 2, whereas at pH = 4, 6 and 8, a minimum of 7% platinum was adsorbed from solution (appendix b).

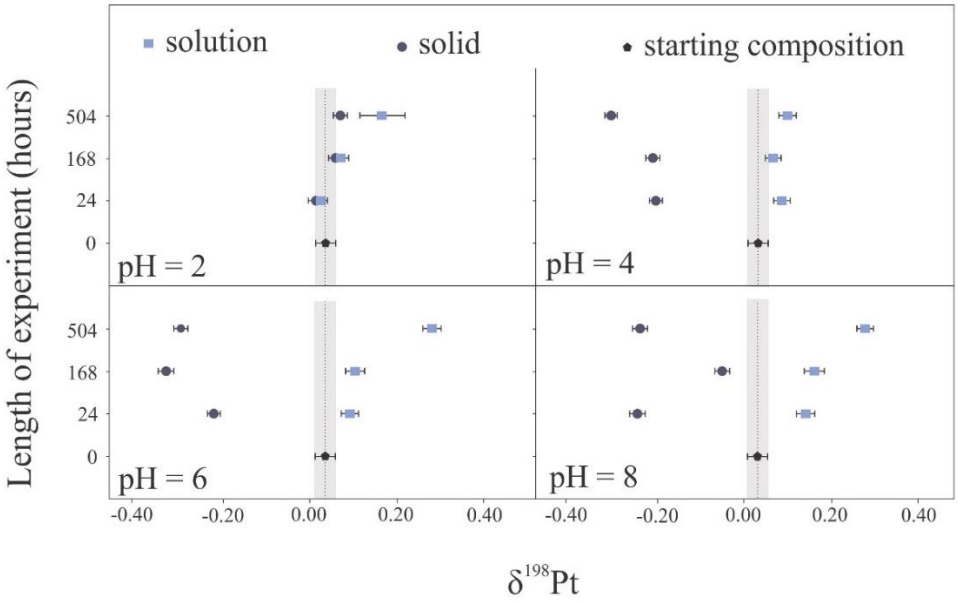

Figure 3.16 The isotopic composition of platinum (as δ^{198}Pt) adsorbed onto goethite surface and the corresponding composition of the platinum remaining in the platinum containing solution. The error bars are the 2se associated with the individual analyses. The grey perpendicular box is the 2sd of the starting platinum containing solution and the vertical line indicates the mean value (figure 3.15).

The isotopic fractionation, $\Delta^{198}Pt$, between the platinum remaining in solution and the platinum adsorbed onto the goethite surface is defined by equation 3.3

$$\Delta^{198}Pt = \delta^{198}Pt_{(solution)} - \delta^{198}Pt_{(solid)} \quad (3.3)$$

and the fractionation factor, $\alpha^{198}Pt$, the ratio of the platinum remaining in solution and platinum adsorbed onto the goethite surface is defined by equation 3.4

$$\alpha^{198}Pt = [1 + \delta^{198}Pt_{(solution)}/1000] / [1+ \delta^{198}Pt_{(solid)}/1000] \quad (3.4)$$

Table 3.6 Platinum isotopic composition (as $\delta^{198}Pt$) of the platinum remaining in solution and the platinum adsorbed onto the surface of goethite as well as the calculated $\Delta^{198}Pt$ and $\alpha^{198}Pt$. The 2se are the standard errors associated with the individual analyses.

Sample	Hours	Solution		Solid		$\Delta^{198}Pt$	$\Delta^{198}Pt$ 2se	$\alpha^{198}Pt$
		$\delta^{198}Pt$	$\delta^{198}Pt$ 2se	$\delta^{198}Pt$	$\delta^{198}Pt$ 2se			
Goethite pH = 2								
	24	0.024	0.015	0.013	0.018	0.011	0.033	1.00001
	168	0.070	0.018	0.058	0.016	0.012	0.034	1.00001
	504	0.166	0.052	0.069	0.016	0.097	0.068	1.00010
Goethite pH = 4								
	24	0.090	0.019	-0.200	0.015	0.290	0.034	1.00029
	168	0.070	0.018	-0.207	0.016	0.277	0.034	1.00028
	504	0.103	0.020	-0.303	0.014	0.406	0.034	1.00041
Goethite pH = 6								
	24	0.092	0.020	-0.221	0.015	0.313	0.035	1.00031
	168	0.104	0.022	-0.331	0.018	0.435	0.040	1.00044
	504	0.281	0.021	-0.297	0.016	0.578	0.037	1.00058
Goethite pH = 8								
	24	0.146	0.021	-0.241	0.018	0.387	0.039	1.00039
	504	0.283	0.019	-0.235	0.017	0.518	0.036	1.00052

All goethite series show an increase of Δ^{198}Pt with both increasing pH and increasing time with the values ranging from 0.01 ‰ to 0.58 ‰ (table 3.6 and figure 3.17). The fractionation factor, α^{198}Pt, across all pH and time steps is > 1, showing that the solution is heavier than the resulting solid within the range of 1.00001 ‰ to 1.00058 ‰.

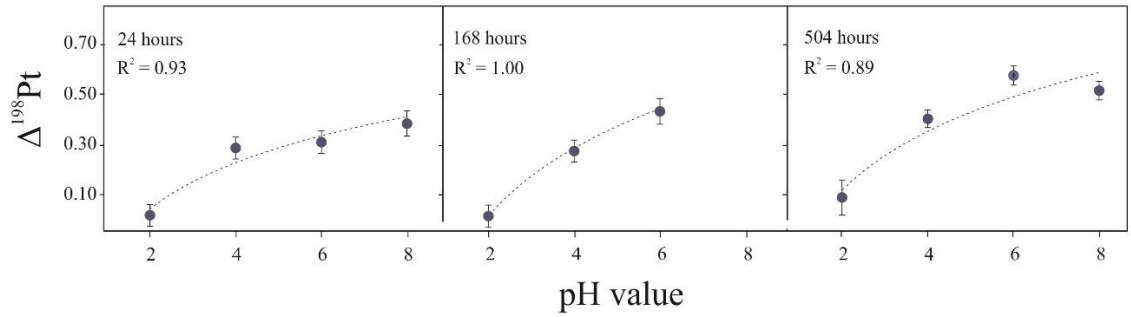

Figure 3.17 The Δ^{198}Pt for goethite as a function of pH at the three time steps (24, 168, and 504 hours). The dashed lines are the statistically derived logarithmic best fit trend lines and associated R^2.

3.3.5.3 Isotopic composition of Pt adsorbed onto the ferrihydrite surface

The δ^{198}Pt of the adsorption pairs for ferrihydrite over all pH values and time intervals are listed in table 3.7. For all adsorption pairs the solutions were heavier than the original platinum containing solution with the exception of the pH = 2 at 24 hour samples, which are lighter than the initial solution. The solids all show a lighter δ^{198}Pt composition indicating that the lighter platinum isotopes are preferentially adsorbed onto the solid over the heavier isotopes, which remain in the solution.

The ferrihydrite series shows an increase of Δ^{198}Pt with both increasing pH and increasing time with a range from 0.23 ‰ to 0.68 ‰ (table 3.7 and figure 3.19). The fractionation factor (α^{198}Pt) is > 1 and shows an increase with increasing pH, with a range of 1.00024 ‰ to 1.00068 ‰.

Table 3.7 δ^{198}Pt of the platinum remaining in solution and the platinum adsorbed onto the surface of ferrihydrite as well as the calculated Δ^{198}Pt and α^{198}Pt. The 2se are the standard error values associated with the individual analysis.

Sample	Hours	Solution		Solid		Δ^{198}Pt	Δ^{198}Pt 2se	α^{198}Pt
		δ^{198}Pt	δ^{198}Pt 2se	δ^{198}Pt	δ^{198}Pt 2se			
Ferrihydrite pH = 2								
	24	-0.029	0.016	-0.321	0.016	0.292	0.032	1.00029
	168	0.041	0.017	-0.304	0.019	0.345	0.036	1.00035
	504	0.060	0.020	-0.268	0.016	0.328	0.036	1.00033
Ferrihydrite pH = 4								
	24	0.034	0.019	-0.274	0.018	0.308	0.037	1.00031
	168	0.163	0.017	-0.262	0.015	0.425	0.032	1.00043
	504	0.343	0.021	-0.221	0.018	0.564	0.039	1.00056
Ferrihydrite pH = 6								
	24	0.084	0.015	-0.364	0.018	0.448	0.033	1.00045
	168	0.146	0.022	-0.314	0.019	0.460	0.041	1.00046
	504	0.421	0.018	-0.212	0.017	0.633	0.035	1.00063
Ferrihydrite pH = 8								
	24	0.143	0.021	-0.092	0.025	0.235	0.046	1.00024
	168	0.219	0.023	-0.256	0.019	0.475	0.042	1.00048
	504	0.510	0.016	-0.170	0.019	0.680	0.035	1.00068

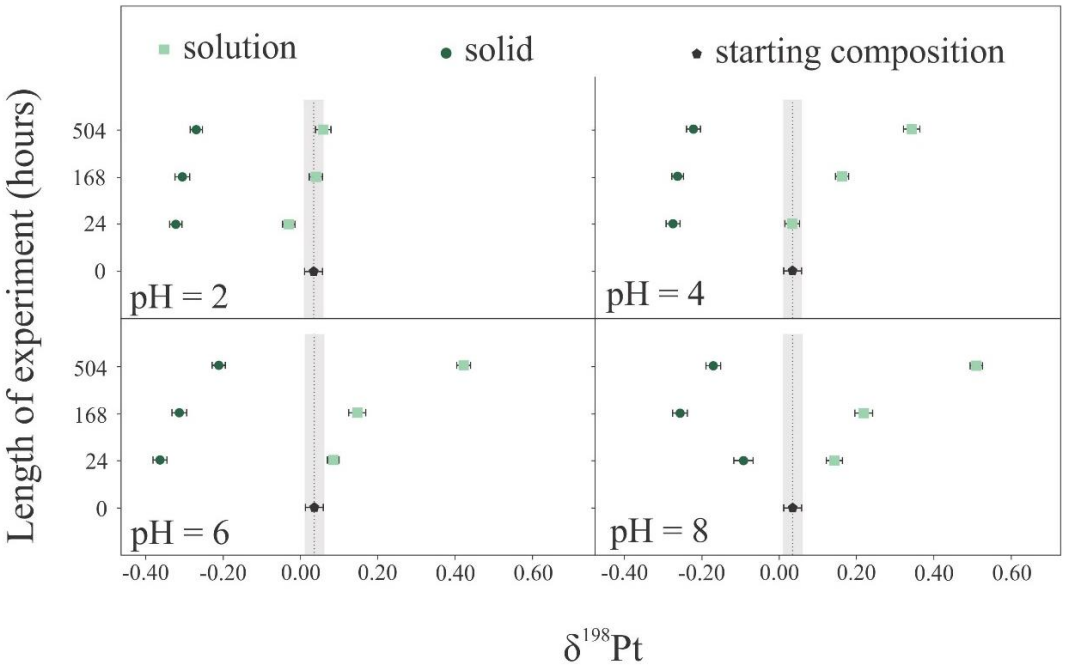

Figure 3.18 δ^{198}Pt of platinum adsorbed onto the ferrihydrite surface and the corresponding δ^{198}Pt of the platinum remaining the solution. The error bars are the 2se associated with the individual analysis. The grey box is the 2sd with the black line indicating the mean δ^{198}Pt of the starting platinum containing solution (figure 3.15)

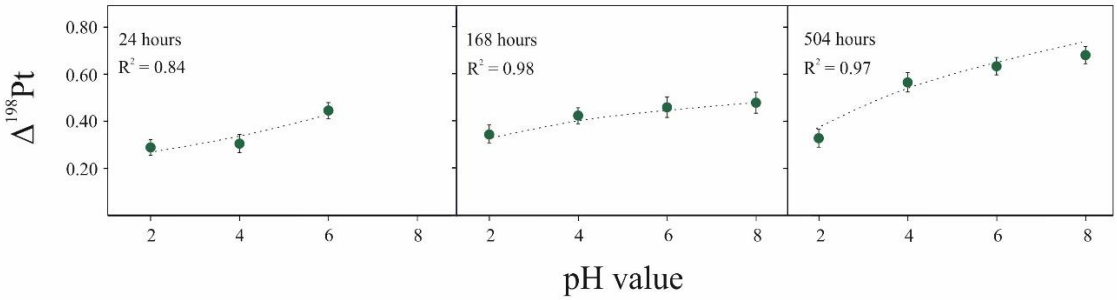

Figure 3.19 The Δ^{198}Pt for ferrihydrite as a function of pH at the three time steps (24, 168, and 504 hours). The dashed lines are the statistically derived exponential trend line for 24 hours and logarithmic trend lines for 168 and 504 hours and associated R^2.

3.3.5.4 Isotopic composition of Pt adsorbed onto the δ-MnO_2 surface

The δ^{198}Pt of the adsorption pairs for δ-MnO_2 over all pH values (pH = 4, 6, and 8) and time intervals are shown in figure 3.20. The δ^{198}Pt of the platinum remaining in the solutions does not deviate from the initial platinum containing solution due to the low amount of platinum that was removed from the platinum containing solution onto the δ-MnO_2 solids, < 1 % (figure 3.9). However, the platinum adsorbed onto the surface show a lighter composition than the initial δ^{198}Pt composition indicating that the lighter platinum isotopes are preferentially adsorbed relative to the heavier isotopes.

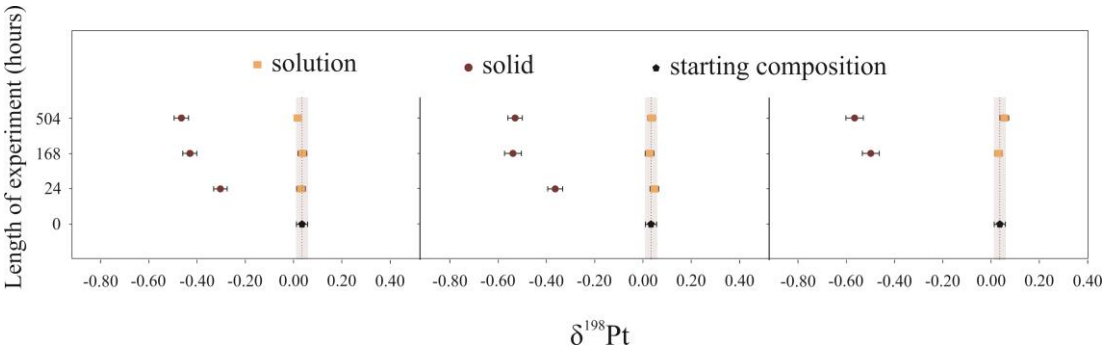

Figure 3.20 δ^{198}Pt of platinum adsorbed onto the δ-MnO_2 surface and the corresponding δ^{198}Pt of the platinum remaining the solution. The 2se are the individual standard error associated with the individual analysis. The grey box is the 2sd with the black line indicating the mean δ^{198}Pt of the starting platinum containing solution (figure 3.15)

The Δ^{198}Pt for the δ-MnO_2 adsorption shows an increase of Δ^{198}Pt with increasing pH with a range of 0.334 ‰ to 0.620 ‰. The α^{198}Pt values for all pH and time intervals are > 1 with a range of 1.00033 ‰ to 1.00062 ‰.

Table 3.8 Platinum isotopic composition (as δ^{198}Pt) of the platinum remaining in solution and the platinum adsorbed onto the δ-MnO_2 surface as well as the calculated Δ^{198}Pt and α^{198}Pt. The 2se are the standard error values associated with the individual analysis.

Sample	Hours	Solution		Solid		Δ^{198}Pt	Δ^{198}Pt 2se	α^{198}Pt
		δ^{198}Pt	δ^{198}Pt 2se	δ^{198}Pt	δ^{198}Pt 2se			
δ - MnO_2 pH = 4								
	24	0.031	0.018	-0.303	0.028	0.334	0.046	1.00033
	168	0.037	0.018	-0.430	0.029	0.467	0.047	1.00047
	504	0.017	0.014	-0.465	0.030	0.482	0.044	1.00048
δ - MnO_2 pH = 6								
	24	0.049	0.018	-0.362	0.031	0.411	0.049	1.00041
	168	0.029	0.018	-0.537	0.035	0.566	0.043	1.00057
	504	0.038	0.016	-0.528	0.030	0.566	0.046	1.00057
δ - MnO_2 pH = 8								
	168	0.030	0.016	-0.499	0.035	0.529	0.051	1.00053
	504	0.054	0.018	-0.566	0.036	0.620	0.054	1.00062

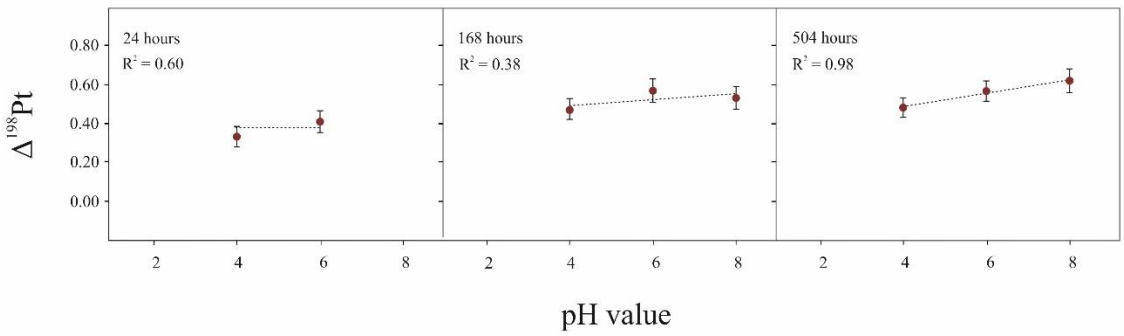

Figure 3.21 The Δ^{198}Pt for δ-MnO_2 as a function of pH at the three time steps (24, 168, and 504 hours). The dashed lines are the statistically derived best fit trend lines and associated R^2 given.

3.4 Discussion

3.4.1 Platinum adsorption and bonding environment

The overall trends observed in the platinum adsorption onto the oxyhydroxide and oxides was an increase of platinum adsorption with increasing pH (figure 3.4, 3.6, and 3.8). As the pH approaches that of the modern marine environment, ca. pH = 7.4 – 8 at depths greater than 1000 m depth (Palmer et al., 1998, Pelejero et al., 2010), platinum adsorbs onto δ-MnO_2 more readily than onto goethite or ferrihydrite (figure 3.22). The concentration of platinum adsorbed onto the δ-MnO_2 surface is ca. 19 times that of goethite and 6 times that of ferrihydrite at pH = 8 (appendix b).

The observed preference of the phase associated with platinum adsorption under the experimental conditions described in this chapter was ferrihydrite > δ-MnO_2 > goethite at pH = 2, ferrihydrite > δ-MnO_2 > goethite at pH = 4, δ-MnO_2 > ferrihydrite > goethite at pH = 6, and δ-MnO_2 > ferrihydrite > goethite at pH = 8.

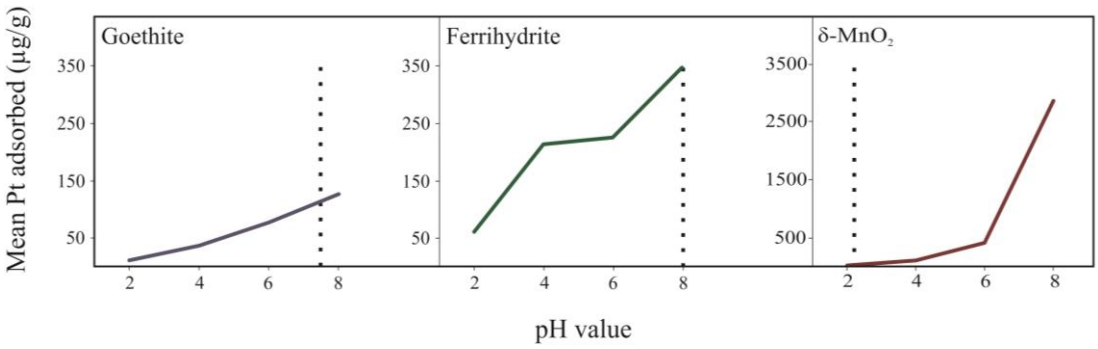

Figure 3.22 Mean platinum (µg/g) adsorbed onto the three oxyhydroxide and oxide surfaces as a function of pH. The scale of the δ-MnO_2 is 10 times that of goethite and ferrihydrite. The dashed vertical line is the zero point of charge (zpc) for each oxyhydroxide and oxide (i.e. goethite zpc = 7.5, ferrihydrite zpc = 8, and δ-MnO_2 zpc = 2.4 (see table 3.1).

All goethite and ferrihydrite experiments (with the exception of the data at pH = 8 for ferrihydrite) were conducted below the zero point of charge (ZPC) of both compounds (i.e. pH = 7.5, and pH = 8 for goethite and ferrihydrite, respectively; table 3.1) which would result in both the oxyhydroxides having a positive surface charge at the conditions of these experiments. The platinum is present in solution as the negatively charged $PtCl_4^{2-}$ species at pH = 2, 4, and 6 with the addition of the neutral species of $Pt(OH)_{2(aq)}$ at pH ≅ 6.3, which becomes the dominant species at and above pH = 7.5 (figure 3.23). It might be expected that the positive surface charge of goethite and ferrihydrite would attract the negatively charged $PtCl_4^{2-}$ species, giving rise to an enhanced adsorption at low pH. This is not observed however, indicating that the equated, tetrachloride Pt^{2+} species is more stable than the possible surface complex in which Pt^{4+} (from XANES) is bound to 2 to 5 oxygen electron donors and 1 to 2 chlorides (from EXAFS, table 3.5). In contrast, when $Pt(OH)_{2(aq)}$ species become available in the pH = 8 series the proportion of platinum increases as the more stable $PtCl_4^{2-}$ is no longer the dominant species.

The ZPC of δ-MnO_2 is pH = 2.4, therefore the surface charge of δ-MnO_2 is positive for experiments undertaken at pH = 2 and negative for the experiments conducted at pH = 4, 6, and 8 (Kosmulski et al, 2002). The adsorption of platinum by the δ-MnO_2 becomes more pronounced at pH > 6 when the neutral species of $Pt(OH)_{2(aq)}$ becomes more important. The EXAFS data suggest that at least some tetrachloride(Pt^{2+}) is initially adsorbed and that during the redox mediated surface reaction of Pt^{2+} to Pt^{4+}, one first shell chloride is retained and remains bound to the Pt^{4+} surface moiety (i.e. the functional group).

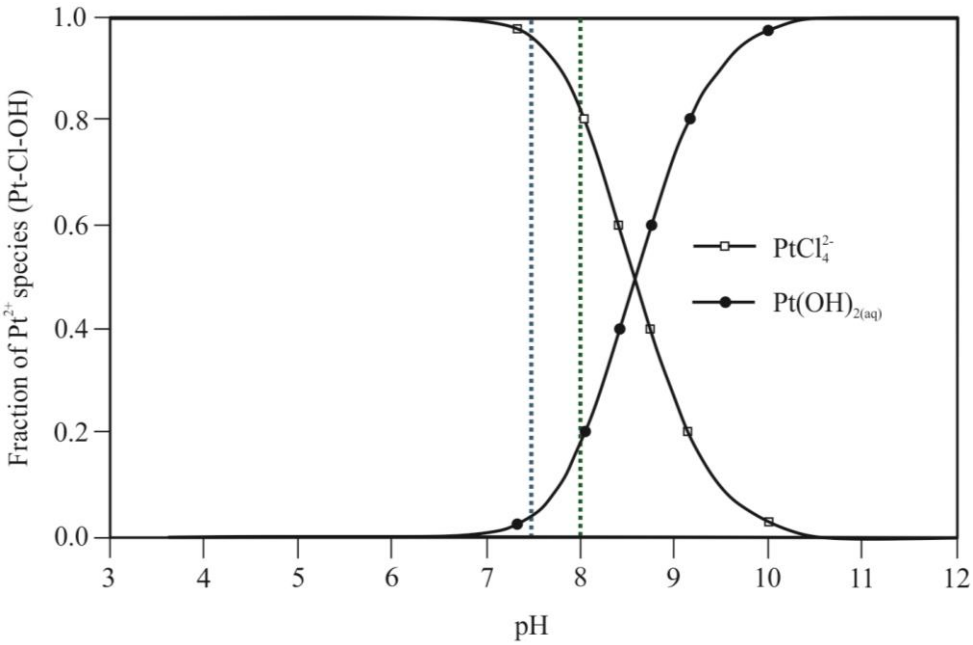

Figure 3.23 shows the percent of Pt^{2+} species present in aqueous chloride solution as a function of pH at 25 ° C, ΣCl^- = 1 mol/dm^3, ΣPt^{2+} = 8.6 x 10^{-19} mol/dm^3. The thermodynamic data were compiled by Sassani and Shock, 1998 using data derived by Brown and Sylva, 1987, Sanders and Martin, 1961, and Yamamoto et al., 1964. The ZPC for goethite is shown with the blue vertical line (pH = 7.5) and ferrihydrite with the green vertical line (pH = 8). δ-MnO_2 ZPC is off the graph at pH = 2.4.

The observation that platinum preferentially adsorbed onto the δ-MnO_2 supports the hypothesis that in the natural environment, the 'platinum anomaly' observed in FeMn crust and nodules is due to a chemisorptive redox mechanism in which Pt^{2+} is adsorbed from seawater and oxidised to Pt^{4+} on the MnO_2 surface (i.e. reduction of Mn^{4+} to Mn^{2+}), as has been observed for cerium in which Ce^{3+} is oxidised to Ce^{4+} on the δ-MnO_2 surface (equation 3.5 and 3.6; Hein et al., 2012, Hodge et al., 1985, Nakada et al., 2016, Ohta and Kawaba, 2001, Takahashi et al., 2000).

$$Ce^{3+} + MnO_2 + 2H_2O = CeO_2 + MnO(OH) + 4H^+ \quad (3.5)$$

$$2Ce^{3+} + MnO_2 + 2H_2O = 2CeO_2 + Mn^{2+} + 4H^+ \quad (3.6)$$

The XANES linear combination fitting (LCF) and the observed intensities and offset of the white line indicate that the majority of the platinum adsorbed onto the surface of all three oxyhydroxide and oxides surfaces is Pt^{4+} with a minor amount of Pt^{2+} being present in the ferrihydrite samples. This indicates that platinum is oxidised from the Pt^{2+} state (present in solution as $PtCl_4^{2-}$ and $Pt(OH)_{2(aq)}$) to Pt^{4+} during the redox mediated adsorption reaction on the solid.

The EXAFS data show that the coordination number of platinum adsorbed from the platinum containing solution changes from 4-fold coordination (4 chlorides) of Pt^{2+} in a square planar complex or by 2 hydroxyls and 2 waters in the case of $Pt(OH)_{2(aq)}$, to a 6-fold coordination environment of Pt^{4+} on the surface of δ-MnO_2 with the coordinating atoms being oxygen and chlorine (see table 3.5). Maeno et al. (2015) has suggested that the incorporation mechanism of Pt onto δ-MnO_2 is the isomorphous substitution of Pt^{4+} and Mn^{4+}, after the surface oxidation of Pt^{2+} to Pt^{4+} by the reduction to Mn^{4+} to Mn^{2+}. A similar mechanism was suggested for incorporation of cobalt into ferromanganese sediments with the substitution of Co^{3+} for Mn^{4+} after the cobalt is oxidised from Co^{2+} to Co^{3+} (Hein et al., 1988, Hein et al., 2003). The observations made in this study would support the surface oxidation.

The adsorbed platinum on both goethite at pH = 6 and ferrihydrite at pH = 4 surfaces exhibit a 4- fold coordination whereas the platinum adsorbed onto ferrihydrite surface at pH = 6 exhibits a 6- fold coordination. Zinc exhibits different coordination geometries when adsorbed by different hydrous ferric oxides (HFO) with both 4 and 6- fold coordination observed possibly due to the crystallographic surface (i.e. 110 or 021) onto which the zinc was adsorbed (Ponthieu et al., 2006). With the data collected in this current study it was not possible to obtain the second shell distances required to evaluate the Pt-Fe distances. More XANES analysis of samples with higher platinum concentration would be needed to mask the effect of Fe on the signal. This would suggest the number of oxygens shared between Pt and Fe and allow the degree of sorption to be evaluated i.e. outer or inner sphere sorption (Nakada et al., 2013).

Similar to the adsorption of Pt onto δ-MnO_2 the Pt adsorbed onto iron oxyhydroxides was oxidised to Pt^{4+}. Therefore, the mechanism is suggested to be similar to that of Pt onto δ-MnO_2 and tellurium oxidation on the surface of iron oxyhdroxides (Hein et al., 2003).

3.4.2 Platinum stable isotope fractionation

The δ^{198}Pt measured for the three synthetic minerals show that the lighter platinum isotopes are preferentially adsorbed over the heavy, resulting in a heavier composition in the residual platinum containing solution (figure 3.24). The α^{198}Pt increases with increasing pH across all three (oxyhydr)oxides showing that the source (i.e. the platinum containing aqueous solution) becomes isotopically heavier in all cases. This is consistent with Pt^{2+} being more tightly bound in the aqueous $PtCl_4^{2-}$ moiety than by Pt^{4+} bound predominantly to oxygen (i.e. just 1 chloride, except for goethite at pH = 6) on the oxide mineral surfaces. Heavier isotopes are typically associated with stronger bonds than lighter isotopes (Bigeleisen, 1965, Urey, 1947). This results in the lighter isotopes bonds being more readily broken relative to heavier isotopes. If the stronger bond is found in the aqueous species ($PtCl_4^{2-}$) the heavier isotopes will preferentially remain in solution over the solid.

The change in the fractionation ratio seen at different pH and on the different minerals could represent the fractionation associated with the adsorption of platinum on more than one type of surface adsorption site on the oxide and oxyhydroxides. The variation in coordination numbers and interatomic distances observed using EXAFS suggests that this is possible. The heavier, tightly bound platinum remains in the aqueous, resulting in the preferential incorporation of the lighter isotopes onto the surface of the minerals.

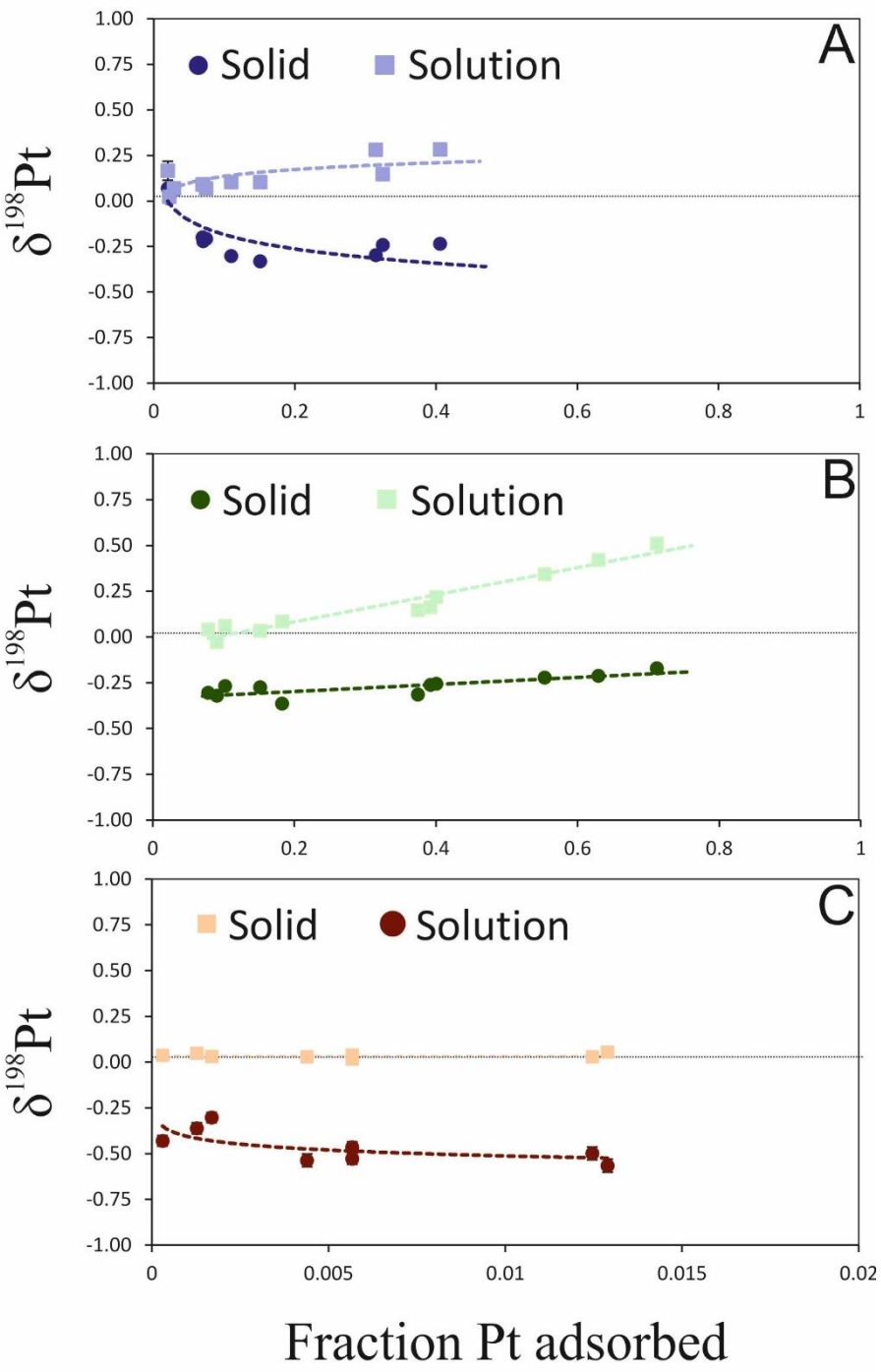

Figure 3.24 δ^{198}Pt of the Pt adsorbed onto the surface of the solid and the δ^{198}Pt of the Pt remaining in solution after adsorption for the three minerals; A) goethite, B) ferrihydrite, and C) MnO_2 as a function of the proportion of Pt adsorbed. The relationship between the solid and solution for both ferrihydrite (B) and MnO2 (C) appears to be linear in relation to fraction of Pt adsorbed, whereas, (A) shows a possible exponential relationship.

The observations made in this study suggests that in the marine environment the incorporation of Pt onto FMS is due to the surface oxidation of Pt on both manganese oxide and iron oxyhydroxide surfaces with manganese oxide being the dominant associated phase at pH > 6. The findings in this study supports the proposed surface oxidation mechanism (Hein et al., 1988, Hein et al., 1997, Hodge et al., 1985, Koschinsky et al., 2005) rather than the reduction mechanism (Halbach et al., 1989, Hodge et al., 1985). In addition, the platinum isotopic composition of the manganese oxides and iron oxyhdyroxies samples are systematically lighter than the starting solution. This would suggest that in the marine environment the FMS are isotopically lighter than seawater i.e. the FMS preferentially adsorb lighter isotopes resulting in a heavier isotopic composition in seawater.

3.5 Summary

The results of the experiments show that the primary redox state of Pt adsorbed onto all mineral phases used in this current study was Pt^{4+}, which indicates that the Pt undergoes oxidation from Pt^{2+} present in the aqueous solution to Pt^{4+} on the solid surfaces. This observation from XANES measurements that Pt is adsorbed onto the δ-MnO_2 surface via a chemi-sorptive redox process involving the oxidation of Pt^{2+} to Pt^{4+} is in agreement with the X-ray photoelectron spectroscopic measurements (XPS) reported recently by Maeno et al (2015). The platinum adsorbed onto the surface of goethite and ferrihydrite shows both a 4- and 6-fold coordination depending on the pH at which the adsorption experiment was conducted, whereas a 6-fold coordination is associated with the MnO_2 phase, irrespective of pH. Pt is adsorbed onto both the manganese oxides and the iron oxyhydroxides at all pH. At pH < 6 ferrihydrite is the dominant phase, whereas, at pH great than six δ-MnO_2 becomes the dominant phase.

The platinum isotope analyses show that the solids preferentially adsorbed the lighter platinum isotopes resulting in a relatively heavier platinum isotopic composition in the corresponding aqueous solution. By analogy with our experimental results, it would suggest that seawater would also be isotopically heavier with respect to its platinum isotopic composition than marine ferromanganese crusts and nodules.

Chapter 4

Effects of leaching on the platinum isotopic composition: approximating weathering in an oxic environment

Preface

The marine platinum isotopic composition is a balance of sources and sinks. The largest source of platinum to the marine environment is thought to be the riverine input (chapter 1.3), with the platinum riverine load derived from weathering of continental rocks. A series of leaching experiments was undertaken on several bulk rock powders to evaluate the platinum isotopic composition of the most readily leached platinum in an oxidising environment, and thus place first order constraints on the platinum isotopic composition of terrestrial weathered (riverine) input to the marine environment.

4.1 Introduction

The riverine input into the oceans is an important source of platinum with rivers apparently accounting for ~ 97 % of the overall available platinum in the oceans (chapter 1.3). This chapter attempts to place constraints on the platinum isotopic composition of riverine platinum. As for seawater, the concentration of platinum in the world's river systems is too low to measure the platinum isotopic composition directly by MC-ICP-MS (i.e. 0.36 pM; Soyol-Erdene et al., 2012). Additional preconcentration methods would be required prior to analysis on natural samples to allow direct isotopic analysis, such as chelating resin. The hydrothermal input is currently unknown. Therefore, a series of reconnaissance experiments was performed to mimic a simplistic oxidative weathering system on three standard reference materials, with the leachate analysed for both platinum concentration and isotopic composition. This allows the broad platinum isotopic composition of the mobile fraction of platinum to be evaluated.

Sequential leaching to release variously bound metal fractions from sediments and rocks can be used to mimic weathering processes. Leaching of sediments and rocks to determine the mobility and speciation of heavy metals has been undertaken for a wide range of metals, such as, the speciation of barium and chromium in drilling fluid wastes, iron speciation within hydrothermal and soil environments etc. (Chapman et al., 2009, Ghode et al., 1995, Rauret, G., 1997, Yacoub et al., 2014). These studies typically implement a sequential leaching process, commonly following the methodology of Tessier et al. (1979). In an oxidative weathering system such as in the typical supergene and subaerial environment, it has been suggested that heavy metals are bound in five basic fractions: cation exchangeable sites, carbonates, Fe-Mn oxides, organic bound/oxidisable, and the residual metals (Tessier et al., 1979). Each fraction can be sequentially leached using a sequence of different solvents: 1) The exchangeable fraction is leached by changing the ionic composition to affect sorption-desorption processes using magnesium chloride or sodium acetate solution. 2) Carbonate bound metals are leached by changing the pH using a solution of sodium acetate and acetic acid. 3) Metals bound to iron and manganese oxides, which are

leached by reducing the Eh of the system (increasing anoxia) with a solution of sodium dithionite and sodium citrate. 4) Metals bound to organic matter/sulphide (the oxidisable) fraction are leached by oxidizing with a solution of nitric acid and hydrogen peroxide (Kersten and Forstner, 1987, Mäkelä et al., 2011, Peng et al., 2009). 5) Residue metals are contained in the crystal structure of primary and secondary minerals that remain after the previous four leaching steps. Tessier et al. (1979) proposed that that the trace metals remaining in the residue at this point would only be removed by full digestion, such as heating in hydrofluoric and perchloric acid.

In crustal rocks, platinum group elements (PGE) are most commonly associated with sulphides, metal alloys and arsenides in mafic-ultramafic rocks (Mondal, 2011). Consequently, the experiments undertaken here focused on the fourth component of Tessier et al. (1979), the organic matter/sulphide oxidisable fraction utilising nitric acid as the solvent. Whilst this does not cover all the possible platinum phases within potential source sediments and rocks, it provides a first order exploration of platinum by targeting the dominant phase associated with the PGE, sulphides. Nitric acid was used to target the sulphide bound platinum, similar to previous studies that have used a single acid leaching technique (nitric acid) to investigate the mobility of various heavy metals, including; As, Cd, Pb, and Mo (Ghode et al., 1995, Mäkelä et al., 2011, Yacoub et al., 2014). Nitric acid leaching will not completely remove all the platinum in the material, which was not the aim of the experiment, but it will allow for the most mobile fraction to be liberated, thus allowing the platinum isotopic composition to be determined of the most readily oxidised proportion, which is likely to be representative of the platinum dominantly liberated during oxidative weathering.

4.2 Samples

A key requirement in selecting samples for these reconnaissance experiments is a relatively high platinum concentration to provide a higher likelihood that leaching will release sufficient platinum to precisely measure the platinum isotopic composition in the leachate. Three samples were selected: SARM-76, a platinum-group mineral (PGM) ore standard reference material (SRM); PTA-1, a platiniferous black sand

SRM, and WPR-1, an altered ultramafic igneous rock SRM (table 4.1). As SRMs, these samples have the further advantage of being well characterised in composition, including mineralogy and platinum concentrations, and having sufficient homogenised material available for multiple experiments. These samples host platinum primarily in sulphides, arsenides and alloys, with bulk platinum concentrations ranging from 0.3 – 3.6 ppm (detail below).

Table 4.1 Leaching experiment samples detailing the primary platinum phase(s), platinum concentration (SRM reference concentration and Creech et. al., 2014 platinum concentration determined by isotope dilution), and the δ^{198}Pt for each sample.

Standard	SARM-76	PTA-1	WPR-1
Type	PGM ore	Planitifereous blank sand	Altered ultramafic igneous rock
Pt mineralisation	Sulphide[1]	Iron[2]	Arsenic, iron, (sulphide)[3]
Pt conc (µg/g)[4]	3.59	3.05	0.29
Pt conc (µg/g)[5]	3.87	2.72	0.26
δ^{198}Pt[5]	0.027 ± 0.023 (2)	-	-0.003 ± 0.051 (2)
δ^{198}Pt[6]	-0.052 ± 0.013 (9)	0.057 ± 0.03 (15)	-0.061 ± 0.067 (23)

[1] Barnes et al., 2002, Godel et al., 2006, [2] Cook and Fletcher, 1992, Findlay, 1969, [3] Barkov et al., 2002, [4] from Jochum et al., 2005, [5] this study, and [6] Creech et al., 2014. The δ^{198}Pt is reported with the mean 2sd and the number of analysis in parentheses.

SARM-76 is from the Merensky Reef Ore of the Bushveld Igneous Complex in South Africa, purchased from MINTEK. The Bushveld Igneous Complex is the largest known layered intrusion with an emplacement age of 2054 Ma and one of the largest reserves of PGE in the world (Scoates and Friedman, 2008). The Merensky Reef is generally 30 cm in thickness. The PGE are primarily associated with sulphide minerals, which comprise 1 – 5 % of the Merensky Reef (Barnes et al., 2002). The dominant sulphide minerals found are cooperite (PtS), pyrrhotite (Fe_xS), pentlandite ($(Fe,Ni)_9S_8$), and chalcopyrite ($CuFeS_2$) with platinum concentration in the Merensky Reef Ore being approximately 280 ppm (Barnes et al., 2002, Godel et al., 2006, Naldrett et al., 1987).

PTA-1 is a concentrate of platinum rich alluvial material collected from the Tulameen River area of British Columbia, Canada, purchased from CANMET (Canadian Certified Reference Materials Project; CCRMP). The Tulameen River basin discharge runs over the Tulameen ultramafic-gabbro complex (UMGC). The Tulameen UMGC is an Alaskan-type intrusive complex with an emplacement age of ca. 186 Ma (Findlay, 1969). It consists of an approximately 6 km^2 dunite core composed of forsteritic olivine with accessory chromite, which is surrounded by concentric shells of olivine and hornblende clinopyroxenites and gabbroic rocks (Cook and Fletcher, 1992, Findlay, 1969). The PGE mineralization is associated with massive chromite segregations within the dunite core, with the most common platinum group minerals being platinum-iron alloys; tetraferroplatinum (PtFe), isoferroplatinum ($(Pt,Pd)_3(Fe,Cu)$), and tulameenite (Pt_2FeCu) (Cook and Fletcher, 1992, Findlay, 1969). The platinum concentration within the massive chromite segregated zone is up to 16 ppm (Fletcher et al., 1995)

WPR-1 is an altered ultramafic igneous rock from the Wellgreen Complex, Yukon, Canada, purchased from CANMET-CCRMP. The Wellgreen Complex is part of the Kluane Mafic-Ultramafic belt, which is located along the lower margin of the greater Quill Creek ultramafic complex. The emplacement age of Quill Creek ultramafic complex is ca. 232 Ma (Marcantonio et al., 1994). The ultramafic is dominantly antigorite and chlorite, with magnetite, chromite, pyrrhotite, pentlandite and chalcopyrite present as accessory phases. The most common platinum group minerals are sperrylite ($PtAs_2$), geversite ($Pt(Sb,Bi)_2$), Pt–Pd–Fe–(Cu) alloys, tetraferroplatinum, and native platinum or isoferroplatinum, however, it is likely that platinum will be associated with the accessary sulphide phases present, for example, pyrrhotite, pentlandite and chalcopyrite (Barkov et al., 2002).

4.3 Methodology

Thirty-nine parallel experiments were conducted with 13 x 1 g aliquots of each sample material, treated with various nitric acid molarities over different time intervals; 1, 5, and 10 % HNO_3 at 96, 168, 336, 504, and 5760 hours (table 4.2). Each sample was weighed directly into pre-cleaned 50 mL centrifuge tubes and 25 mL of the appropriate acid was added. The centrifuge tubes were sealed and placed on a shaking table at 250 rpm for the required time. Following removal from the shaking table, the samples were centrifuged for 5 minutes at 2,000 rpm to separate the residue from the supernatant. The supernatant (leachate) was decanted and filtered using a Luer lock syringe fitted with disposable 30 mm PTFE syringe filters with a sealed 0.20 µM filter membrane. Prior to filtering the leachate, the filters were equilibrated by filtering a small volume of Milli Q water followed by a small volume of the leachate, which was discarded. The leachate was then filtered into a clean 50 mL centrifuge tube. An aliquot of the leachate was removed for platinum concentration determination using the VUW Thermo Scientific Element2 ICP-MS. Based on the determined concentration of platinum, the remainder of the leachate was double spiked to facilitate Pt isotope analysis (chapter 2).

The residue was washed three times using Milli Q water, centrifuging and discarding Milli Q water supernatant after each wash. The residue was transferred to a Teflon beaker, dried and weighed (table 4.2). An appropriate amount of double spike was added to the residue based on the initial platinum concentration of the individual sample (SRM Pt concentration data x mass of sample used) less the amount of platinum that was leached from the solid into the leachate as determined by the Element2 ICPMS. The residue was then digested using the NiS fire assay method (chapter 2). Both leachate and dissolved residue were purified for platinum isotopic measurement using anion exchange chemistry (chapter 2).

4.4 Results

4.4.1 Concentration of leached platinum

Platinum concentration and isotopic data for the full suite of experiments is presented in Table 4.2.

All 1% HNO_3 leaches had insufficient platinum present in the leachate to measure the platinum concentration on the Element2 ICP-MS, and therefore none of these samples (i.e. 1% HNO_3) were processed for isotopic analysis. In addition, all leaching preformed on the PTA-1 material, which primarily hosts Pt in platinum-iron alloys, failed to release sufficient platinum for isotopic analysis to be conducted (i.e. < 5 ng/g Pt; table 4.2). The remaining samples, 5% and 10% HNO_3 leaches of WPR-1 and SARM-76, ranged from 1 – 300 ng Pt in the leachate (Table 4.2). The SARM-76 leachates were all greater than ~ 30 ng Pt and all but the lowest (5% HNO_3, 336 hours) were processed for Pt isotopic composition. Of the WPR-1 leachates, only the longest leach (240 days) in 10% HNO_3 produced > 10 ng Pt and was processed for Pt isotopic composition.

The leaching experiments proved to be most successful for the SARM-76 samples with sufficient platinum for isotopic analysis being found in all 5% and 10% HNO_3 samples (table 4.2, figure 5.1). The SARM-76 in 5% HNO_3 and 10% HNO_3 samples show a slight decrease of platinum liberated with increasing time. The 10% HNO_3 liberated 2 to 3 times more platinum than the 5% HNO_3 leaching process.

Table 4.2 Mass of samples used for the pseudo digest experiments with the platinum concentration determined using Element2 ICP-MS and isotope dilution (ID) for the samples that were analysed for platinum stable isotope composition. All errors associated with each analysis are given in appendix c.

Time (hours)	Starting sample (g)	Pt conc. initial SRM (ng)	Pt leachate ng (E2)	Pt residue ng (SRM)	Pt leachate ng (ID)	Pt residue ng (ID)	Pt leachate ID (%)	Leachate δ^{198}Pt	Leachate δ^{198}Pt 2se	Residue δ^{198}Pt	Residue δ^{198}Pt 2se	Δ^{198}Pt	Δ^{198}Pt 2se	α^{198}Pt
SARM-76 1% HNO_3														
96	1.029	3696	-											
168	1.005	3608	-											
336	1.029	3694	-											
504	1.009	3622	< 5											
SARM-76 5% HNO_3														
96	1.035	3716	78	3638	119	2994	4.0	1.936	0.094	-0.011	0.022	1.947	0.116	0.99806
168	1.065	3825	63	3762	89	2813	3.1	2.800	0.100	0.109	0.027	2.691	0.127	0.99732
336	1.020	3661	28	3633										
504	1.007	3616	38	3578	33	3915	0.9	1.940	0.210	-1.628	0.050	3.568	0.26	0.99644
SARM-76 10% HNO_3														
96	1.058	3797	204	3594										
168	1.010	3625	266	3359	271	2814	9.6	0.961	0.080	0.058	0.026	0.903	0.106	0.99910
336	1.016	3647	226	3420	306	2270	13.5	1.368	0.084	-0.110	0.022	1.478	0.106	0.99852
504	1.014	3640	145	3495	181	3768	4.8	0.959	0.069	0.084	0.054	0.875	0.123	0.99913
5760	1.020	3662	214	3448	231	2093	11.0	1.478	0.051	0.006	0.029	1.472	0.080	0.99853

Time (hours)	Starting sample (g)	Pt conc. initial SRM (ng)	Pt leachate ng (E2)	Pt residue ng (SRM)	Pt leachate ng (ID)	Pt residue ng (ID)	Pt leachate ID (%)	Leachate δ^{198}Pt	Leachate δ^{198}Pt 2se	Residue δ^{198}Pt	Residue δ^{198}Pt 2se	Δ^{198}Pt	Δ^{198}Pt 2se	α^{198}Pt
PTA-1 1% HNO_3														
96	1.038	3166	-											
168	1.265	3860	-											
336	1.010	3079	-											
504	1.019	3109	-											
PTA-1 5% HNO_3														
3	1.026	3129	-											
168	1.042	3179	< 5											
336	1.012	3086	< 5											
504	1.011	3083	< 5											
PTA-1 10% HNO_3														
96	1.073	3273	-											
168	1.053	3211	< 5											
336	1.046	3190	< 5											
504	1.040	3173	< 5											
5760	1.012	3088	< 5											
WPR-1 1% HNO_3														
96	1.021	291	-											
168	1.025	292	-											
336	1.009	288	-											
504	1.042	297	-											

Time (hours)	Starting sample (g)	Pt conc. initial SRM (ng)	Pt leachate ng (E2)	Pt residue ng (SRM)	Pt leachate ng (ID)	Pt residue ng (ID)	Pt leachate ID (%)	Leachate δ^{198}Pt	Leachate δ^{198}Pt 2se	Residue δ^{198}Pt	Residue δ^{198}Pt 2se	Δ^{198}Pt	Δ^{198}Pt 2se	α^{198}Pt
WPR-1 5% HNO_3														
96	1.044	298	< 5											
168	1.072	305	< 5											
336	1.028	293	< 5											
504	1.078	307	< 5											
WPR-1 10% HNO_3														
96	1.041	297	< 5											
168	1.024	292	< 5											
336	1.017	290	< 5											
504	1.059	302	< 5											
5760	1.003	286	21	265	31	162	19.2	5.440	0.120	0.118	0.063	5.322	0.183	0.99471

Initial platinum leachate concentrations determined using the Element2 with the initial platinum remaining in the residue calculated by subtracting the platinum in the leachate from the SRM determined Pt value, which was used to determine the double spiked addition.

Δ^{198}Pt and α^{198}Pt are calculated as follows: $\Delta^{198}Pt = \delta^{198}Pt_{(residue)} - \delta^{198}Pt_{(leachate)}$: $\alpha^{198}Pt = [1 + \delta^{198}Pt_{(residue)}/1000] / [1+ \delta^{198}Pt_{(leachate)}/1000]$.

- indicates that the platinum concentration was below detection limit and a blank signifies no measurement were undertaken.

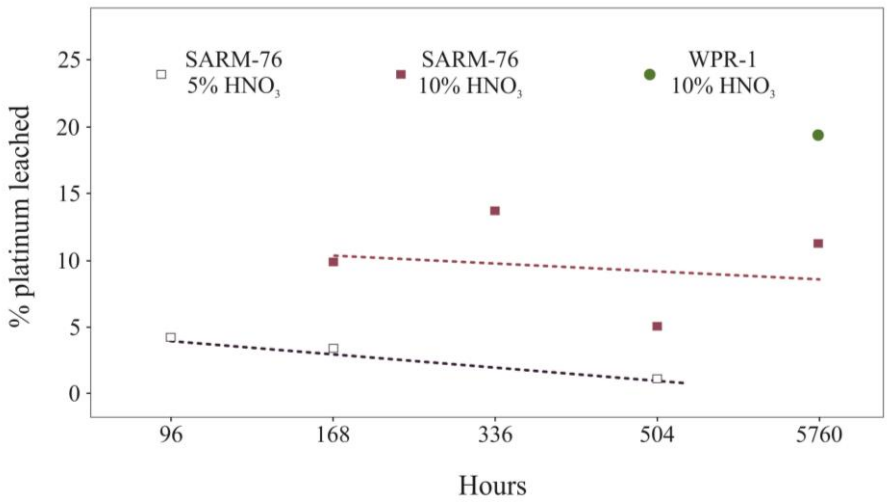

Figure 4.1 Percent of platinum leached based on isotope dilution calculations for SARM-76 5% and 10% HNO_3 and WPR-1 10% HNO_3. The two dashed lines represent the best fit trend line of the SARM-76 5% and 10%.

4.4.2 Platinum isotopic composition

In total, 8 samples were analysed for platinum isotope composition; SARM-76 5% HNO_3 96, 168, and 504 hours, SARM-76 10% HNO_3 168, 336, 504, and 5760 hours, and WPR-1 10% 5760 hours. All leachates (supernatant) have a heavier platinum isotopic composition than the starting solid composition (SRM bulk platinum composition this study and Creech et al., 2014) and composition of the residue (figure 4.2). The difference between the residue and leachate is shown in table 4.2 as $\Delta^{198}Pt$ (equation 4.1).

$$\Delta^{198}Pt = \delta^{198}Pt_{(residue)} - \delta^{198}Pt_{(leachate)} \quad (4.1)$$

The WPR-1 leachate has a $\Delta^{198}Pt$ = 5.3 ‰ offset, and the SARM-76 samples show an offset of $\Delta^{198}Pt$ = 0.9 – 3.5 ‰ (figure 4.2, table 4.2).

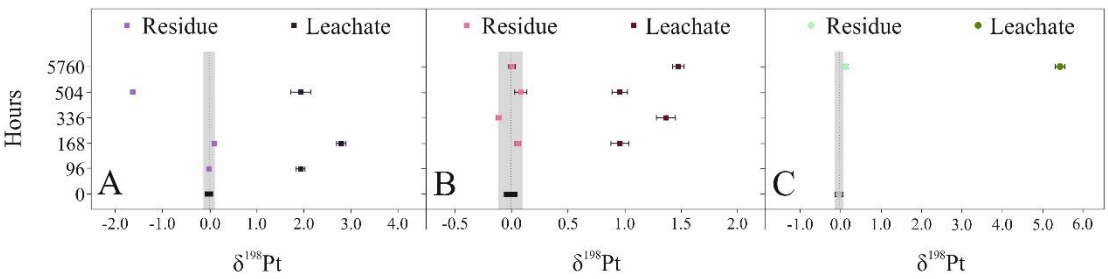

Figure 4.2 Leaching pairs for a) SARM-76 5% HNO_3, b) SARM-76 10% HNO_3, and c) WPR-1 10% HNO_3, with the time of leaching increasing vertically within each figure. The bulk isotopic signature is shown with the black data point in each plot with the grey shaded area representing the analytical error.

A $\alpha^{198}Pt$ (Goldberg et al., 2009) was calculated to define the isotopic fractionation observed between the residue and the leachate (equation 4.2).

$$\alpha^{198}Pt = [1 + \delta^{198}Pt_{(residue)}/1000] / [1+ \delta^{198}Pt_{(leachate)}/1000] \qquad (4.2)$$

The $\alpha^{198}Pt$ of all samples is < 1, reflecting that the heavier isotopes in the system were partitioned into the product, in this instance the leachate, relative to the lighter isotopes, which preferentially remained in the residue (figure 4.3, table 4.2). The SARM-76 5 % HNO_3 samples show a decrease of $\alpha^{198}Pt$ with increasing time of leaching (i.e. the offset between the residue and leachate increased with time). The SARM-76 5% HNO_3 shows an increase of $\alpha^{198}Pt$ with increasing percent of platinum leached (i.e. the offset between the residue and leachate decreases with increasing proportion of platinum leached). The $\alpha^{198}Pt$ of SARM-76 10% HNO_3 series does not vary significantly with the percentage of platinum leached (figure 4.3). The WPR-1 samples had the lowest $\alpha^{198}Pt$ of 0.995, consistent with the largest offset between residue and leachate, 5.3 ‰.

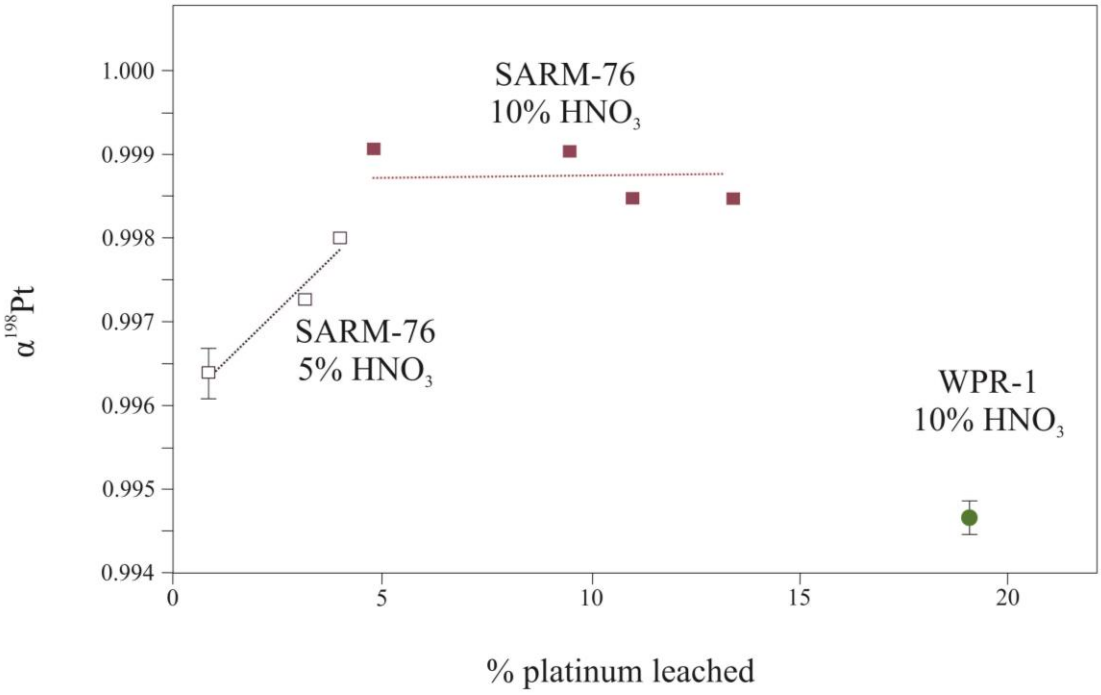

Figure 4.3 α^{198}Pt for SARM-76 5% HNO3, SARM-76 10% HNO3, and WPR-1 10% HNO_3 plotted against the isotope dilution calculated percent leached from each sample. The error bars are the 2se of the α^{198}Pt with only two being larger than the symbol.

4.5 Discussion

The leaching experiments proved most successful for the SARM-76 samples and to a lesser degree with the WPR-1 samples, however, very limited platinum was liberated from the PTA-1 samples. This most likely reflects the differing platinum mineralogy present in each material; platinum is associated with sulphides in SARM-76, primarily arsenides with likely sulphides in WPR-1, and Pt-Fe alloys in PTA-1. Thus, a first order observation appears to be that under the oxidizing environment mimicked by the experiments (acid attack with HNO_3), platinum associated with the sulphide phase is more readily mobilised than the platinum associated with Pt-Fe alloys i.e. S followed by As bound Pt are leached more readily that Fe bound Pt. This is consistent with previous work showing that sperrylite and Pt-Fe alloys are more resistant to oxidation than platinum associated with sulphide (Plimer and Williams, 1988).

However, it is worth noting that these digestion experiments were conducted on the bulk materials. A more in depth sequential leaching experiment would need to be undertaken on various mineral separates e.g. sulphides, arsenides etc. to fully assess the degree of mobility of varying platinum species in these materials as well as the corresponding degree of isotopic fractionation associated with the variously bound platinum.

On the basis of pH and Eh (Fuchs and Rose, 1974) considerations, platinum is most likely liberated as Pt^{2+} with $Pt(OH)_{2(aq)}$ being the dominant stable aqueous platinum species (figure 4.5 (a), equation 4.3), which coincides with the field of normal non-wet soils.

If chlorine were present in the system, $PtCl_4^{2-}$ may also be a dissolution product. Colombo et al. (2008) suggested that hydroxide species can transport platinum in oxidizing environments, including road-runoff, freshwater and soil solutions (figure 4.5 (b)) with chloride species being important in environments with a higher proportion of available chloride ion (e.g. seawater and snow melt). This suggests any isotopic fractionation is not related to a redox shift (c.f. chapter 3) but rather changes in bonding environment or in fractionation amongst the Pt-bearing minerals, with the most readily oxidisable minerals favouring the heavier isotopes of Pt (equation 4.3).

$$PtS_{(s)} + 2O_{(2)} = Pt^{2+} + SO_4^{2-}{}_{(aq)} \qquad (4.3)$$

The experiments are very consistent in showing that the heavier isotopes of Pt are preferentially leached into the solution with the light isotopes remaining in the solids with shifts of up to + 2 ‰ and + 3.5 ‰ for SARM-76, and + 5.3 ‰ for WPR-1 (figure 4.4). This level of isotopic shift is similar to that observed for other chalcophile metals. For example, an isotopic shift of up to + 2 ‰ for copper and + 0.2 ‰ for zinc is observed between leachate and sulfide phase in oxidative weathering of chalcopyrite and sphalerite, respectively (Fernandez and Borrok, 2009).

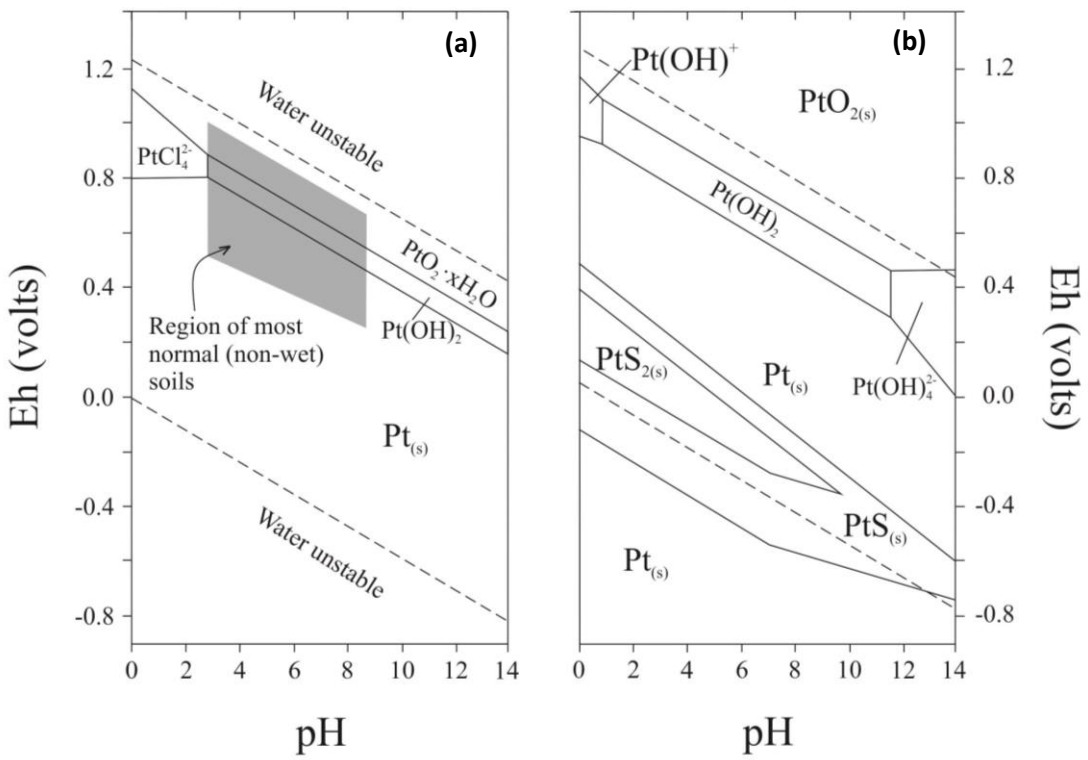

Figure 4.4 (a) Eh-pH diagram for the system Pt-H_2O-Cl at 25°C modified from Fuchs and Rose (1974). The dashed lines represent the Pt stability field of water, the grey shaded area represents the field of most normal (non-wet) soils as defined by Fuchs and Rose (1974). ΣPt = 10^{-12} M and ΣCl = 3 x 10^{-4} M. The region of most normal (non-wet) soils intersects the field of stability of $Pt(OH)_{2(aq)}$. (b) Eh-pH diagram for the Pt-S-H_2O system at 25°C modified from Colombo et al. (2008), data from Wood et al., (1994) and Wagman et al. (1982). ΣPt = 10^{-9} M and ΣS = 10^{-3} M

The SARM-76 5% HNO_3 shows a decrease in the offset with increasing fraction of platinum leached suggesting that the heavier platinum isotopes are the most mobile (figure 4.2). As more platinum is leached from the sample the heavier isotopes are then diluted by the lighter platinum isotope.

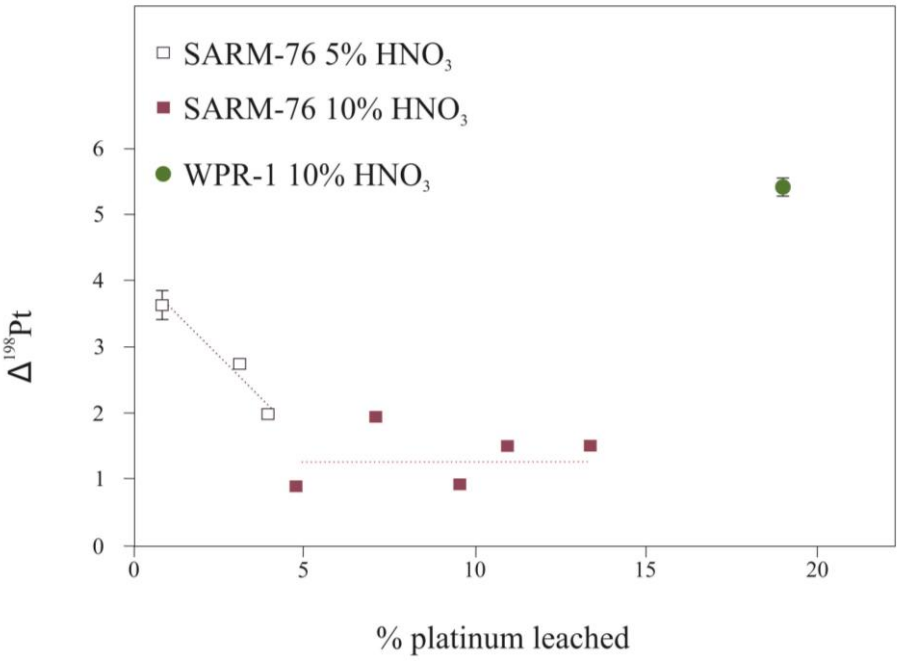

Figure 4.5 Δ^{198}Pt for SARM-76 5% HNO_3, SARM-76 10% HNO_3, and WPR-1 10% HNO_3 plotted against the isotope dilution calculated percent of platinum leached from the matrix.

4.5.1 Implications for riverine platinum input into seawater

Whilst the experiments are simplified, the consistent first order observation that heavier Pt isotopes are preferentially mobilised strongly suggests that the most readily oxidised Pt-bearing fractions in the surficial environments will result in the platinum leached to the riverine system being systematically heavier than the materials from which they leached.

To a first order then, riverine input is predicted to be isotopically heavier than continental crust, which is a similar pattern to that observed for other, more well studied, transition metal isotope systems. For example, Ni and Cu isotopes from leaching experiments (Fernandez and Borrok, 2009) and natural river waters (Cameron and Vance, 2014, Little et al., 2014, Vance et al., 2008) are substantially heavier than sulphide minerals or silicate rocks, respectively. The studies of natural samples have

suggested the heavier isotopic composition of dissolved metals in river waters results from isotopic partitioning between the dissolved species and particulates, either in the weathering environment (e.g. such as modelled by the leaching experiments here) or with particulates during transport i.e. isotopically light sinks (Cameron and Vance, 2014).

For both leaching experiments and adsorption experiments (chapter 3), δ^{198}Pt in the solution is heavier than that in the associated solid (figure 4.5), with a stronger fractionation shown by dissolution (pseudo weathering) than absorption. Taken together, this suggests that the platinum isotopic signature of seawater will be relatively heavy. The dominant source of platinum to the marine environment is riverine and the first order observations from this study suggests that oxidative weathering of terrestrial sources leads to isotopically heavier platinum being released into the riverine system and therefore into the marine environment. Further, the primary sink of Pt in the marine cycle is absorption onto FeMn minerals (an isotopically light sink), which will also, to a lesser degree, increase the proportion of heavy Pt in seawater due to the preferential adsorption of lighter Pt isotopes (chapter 3 and chapter 5). This would suggest that platinum behaves similarly to other transition metals in the marine environment such as Cu and Ni, which have an isotopically heavy riverine source relative to the continental crust with Cu also having an isotopically light sink in FeMn nodules and crusts (Cameron and Vance, 2014, Little et al., 2014).

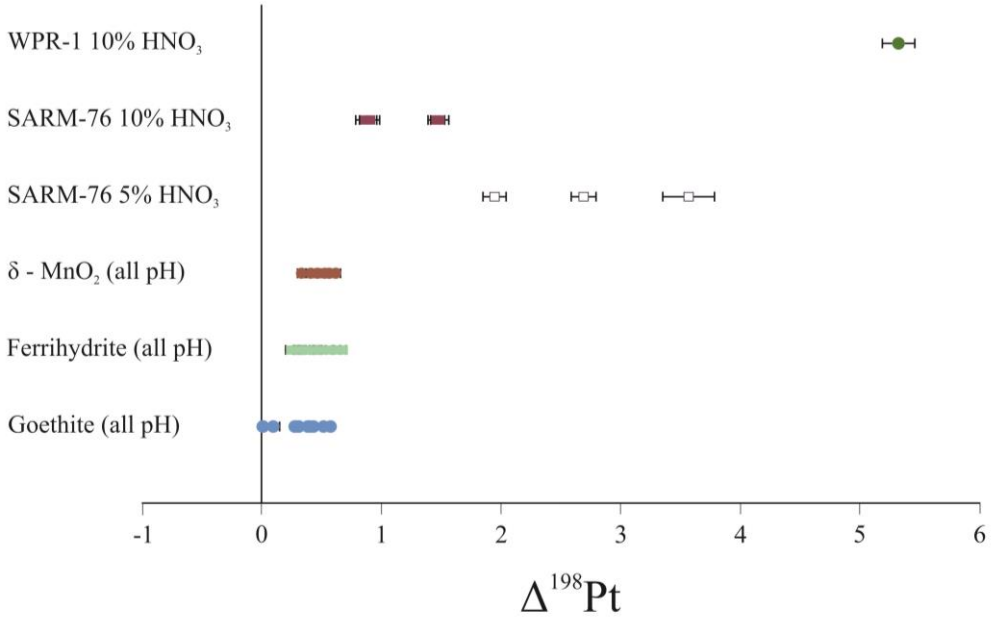

Figure 4.6 Δ^{198}Pt of the leachates and the platinum bearing solutions of the goethite, ferrihydrite and δ-MnO_2 adsorption experiments over all pH values from chapter 3. All leachates and platinum bearing solutions are isotopically heavy compared to the leaching residue and solids from the adsorption experiments.

4.5 Summary

The results of the leaching experiments indicate that the material with a higher proportion of platinum bound sulphides (SARM-76 and WPR-1) are more readily leached than materials with platinum associated with arsenides or Pt-Fe alloys with a maximum of 13.5 % platinum being leached after 336 hours. Irrespective of the material being leached, all leachates had a heavy platinum isotopic composition with up to + 5.3 ‰ δ^{198}Pt offset observed with respect to the residue. Using the experiments as a first order constraint on the platinum released to the rivers by terrestrial leaching, indicates that the Pt riverine input to the oceans is likely to be isotopically heavy.

Chapter 5

Stable platinum isotopic composition of modern ferromanganese crusts and nodules

Preface

This chapter addresses the second of the research questions posed in chapter 1:

"What variations are observed in platinum stable isotope chemistry in the modern oxic oceans?"

This chapter describes the natural ferromanganese crust and nodules samples examined in this study. These globally distributed natural ferromanganese crusts and nodules were analysed to investigate the spatial variation of both platinum concentration and platinum isotopic composition in the modern oxic marine environment, and provide further constraints on the marine Pt cycle.

5.1 Introduction

In the modern oxic oceans, slow growing hydrogenetic ferromanganese crust (FMC) and ferromanganese nodules (FMN) precipitate directly from seawater over geological time resulting in a record of changing seawater chemistry. As the primary sink of Pt in the marine environment, the Pt stable isotopic system recorded in these crusts and nodules is a potentially useful tracer to investigate ocean chemistry. Previous studies of FMN and FMC have investigated various metals to gain insight into a range of processes including the source of metals to the marine environment, the redox condition of the oceans through time, and changes in productivity (chapter 1). For example, variations observed in Fe stable isotope in FMC have been used to distinguish sources of Fe to the marine environment, identifying how glaciations increase the amount of detrital Fe delivered to the marine environment (Beard et al., 2003). Fe has also been used to identify changes in sources of Fe and oxygenation of the oceans through temporal variations of stable Fe isotope compositions within FMC and FMN (Severmann et al., 2008, Zhu et al., 2000). Molybdenum has been used to trace the spatial extent of oceanic redox conditions given the different isotope fractionations observed during adsorption of Mo onto authigenic sediments in oxic to anoxic environments (Goldberg et al., 2009). Thallium has also been shown to produce a distinct isotopic fractionation dependent on redox conditions during incorporation onto marine sediments (FMC, pelagic clays and biogenic oozes), and has been used to evaluate the volume of input fluxes of Tl to the marine system (Rehkämper et al., 2004).

Ferromanganese sediments host well-documented enrichments of Pt over other platinum-group elements, the platinum anomaly (Hodge et al., 1985). For example, the Pt/Pd ratio in seawater is 4.5, whereas crusts from the western Pacific Ocean have yielded Pt/Pd of up to 1300 (Hodge et al., 1985). This platinum anomaly makes it possible to measure both the concentration and stable isotopic composition of Pt in ferromanganese sediments. As the primary sink of Pt in the modern oxic oceans, FeMn deposits are also key to understanding the marine Pt cycle.

5.2 Ferromanganese crust and nodule samples

A suite of 15 well characterised FMN and FMC samples covering four of the five oceans; Atlantic, Pacific, Indian, and Southern Oceans were investigated in this study. Details of the individual samples are given in the ensuing sections, 5.2.1 and 5.2.2, respectively, with the locations of all samples shown in figure 5.1.

5.2.1 Ferromanganese nodules (FMN)

Three bulk FMN samples were analysed during this study; USGS Nod-A-1, USGS Nod-P-1, and GSJ JMn-1, which are commercially available manganese nodule standard reference materials (SRM) distributed by USGS and GSJ. These three nodule standard materials were chosen because they are well characterized and readily available, and were used extensively for analytical method development (Chapter 2).

The USGS Nod-A-1 and Nod-P-1 SRMs were processed from approximately 45 kg of FMN material collected from the Blake Plateau in the Atlantic Ocean at a depth of 788 m and from the northeast Pacific Ocean at a depth of 4340 m, respectively (Flanagan and Gottfried, 1980). The material from each site was processed through a roller crusher, dried overnight and further refined with a ball mill. Flanagan and Gottfried (1980) noted that the soluble sea salt and a thin coating of grey pelagic clay were not removed from either bulk FMN material prior to processing. The major and trace element chemistry of these two nodules is given in full in appendix A with the sample location sites shown in figure 5.1.

The GSJ JMn-1 sample was processed from ca. 130 kg of FMN material collected on the RV Hakurei-Maru 1982 cruise from the southern Central Pacific Basin at a depth of 5200 to 5225 mbsl (Terashima et al., 1995). The bulk FMN material was dried for ten years at atmosphere, crushed using a jaw crusher and refined in a ball mill. Similar to the USGS processing, the soluble sea salt portion was not removed prior to processing. The major and trace element chemistry of this bulk nodule sample is given in full in appendix A with the sample location site shown in figure 5.1.

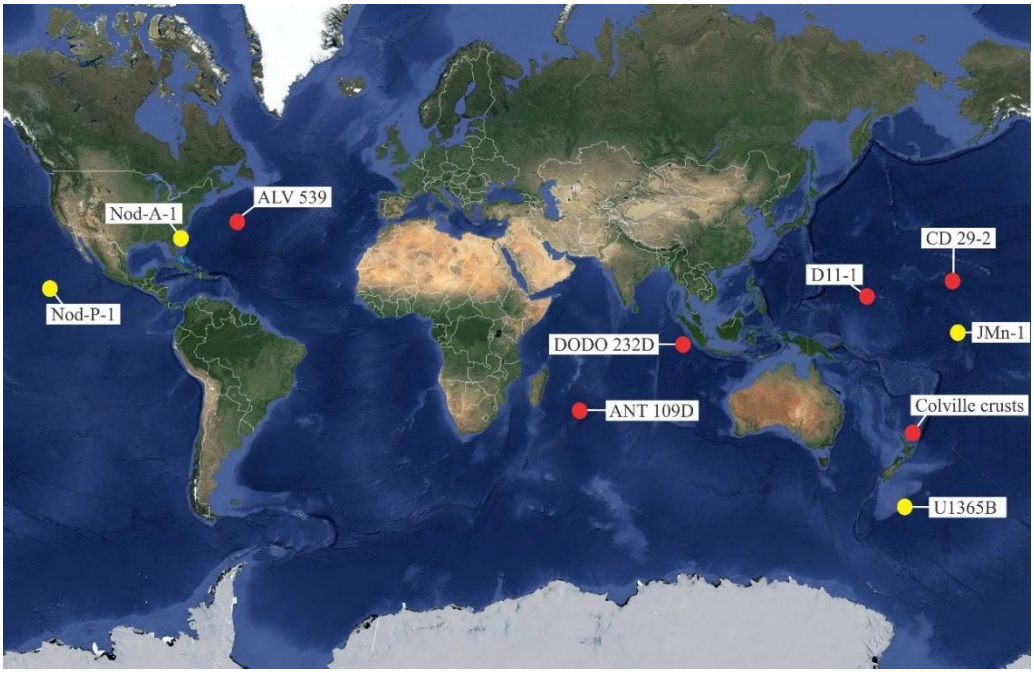

Sample	Section (mm)	Ocean	Latitude	Longitude	Depth (mbsl)	Growth rate (mm/Myr)
USGS Nod-A-1	Bulk	Atlantic	31.03	-78.37	788	--
USGS Nod-P-1	Bulk	Pacific	14.83	-124.47	4340	--
GSJ JMn-1	Bulk	Pacific	-0.79	-166.12	5213	--
U1365B	0-1	Southern	-52.99	174.95	4590	4.1 [(a)]
ALV 539	0 - 10	Atlantic	35.61	-58.79	2665	2.4 [(b)]
ANT 109D	0 - 10	Indian	-27.97	60.80	5438	1.6 [(b)]
CD 29-2	0 - 10	Pacific	16.71	-168.24	2280	2.1 [(c)]
D11-1	0 - 10	Pacific	11.65	161.68	1780	1.4 [(d)]
DODO 232D	0 - 10	Indian	-5.38	97.48	3839	4.3 [(e)]
Colville crusts	0 - 2	Pacific	-34.58	177.88	1670	--

Figure 5.1 Location map of FMN and FMC samples analysed in this study. The FMN are the yellow circles (n = 6) and the FMC are the red circles (n=4). The decimal latitude and longitude location and the mean depth of the dredge (mbsl) for each sample are given in the table. The growth rates are based on $^{10}Be/^{9}Be$ data from [(a)] Ditchburn and Graham, 2003, [(b)] O'Nions et al., 1998, [(c)] Christensen et al., 1997, [(d)] Ling et al., 1997, and [(e)] Rehkämper et al., 2004.

A single FMN, U1365B, was collected on the RV Tangaroa 1999 cruise from the eastern sector of the Campbell Nodule Field (CNF), Southern Ocean, at a depth of 4560-4619 mbsl (Chang et al., 2003). This nodule was sampled at a resolution of 1-2 mm using a Dremel® drill at the Institute of Geological and Nuclear Sciences (GNS) (Ditchburn and Graham, 2006b). The uppermost 1 mm layer from this sampling was analysed in this study. The major and trace element chemistry of this nodule is given in full in appendix A with the sample location site shown in figure 5.1.

FMN can form by hydrogenetic, diagenetic, hydrothermal, or mixed influences (Chapter 1). Nodule genesis can be differentiated based on geochemistry and mineralogy e.g. Mn/Fe ratio ≤ 2.5 and high concentrations of Ni and Cu typically indicate an early-diagenetic origin (Halbach et al., 1981, Hein et al., 2013). Based on Fe-Mn-(Co-Cu-Ni) x 10 discrimination plots (Figure 5.2), Nod-P-1 and JMn-1 plot in the early diagenetic field with Nod-A-1 and U1365B plotting in the hydrogenetic field (Bonatti et al., 1972, Elagami et al., 2000, Halbach et al., 1981, Toth, 1980). However, Nod-A-1 has previously been classed as a deep-water diagenetic nodule in a study conducted by Rehkämper et al. (2002) on the basis of a relatively high Mn/Fe ratio (1.7) and high Ni content. Nod-A-1 also has a high Ca concentration (< 10 wt%) which could indicate secondary diagenesis with carbonate fluorapatite (CFA) recrystallization or the inclusion of carbonate debris incorporated into the sample due to the bulk nature of the preparation (Cronan, 1975). For this study we have adopted the interpretation of Rehkämper et al. (2002) for the Nod-A-1 as well as Nod-P-1, and JMn-1 as deep-water diagenetic deposits for the bulk samples, although we note that as a bulk sample, Nod-A-1 could be of mixed hydrogenetic and diagenetic origin.

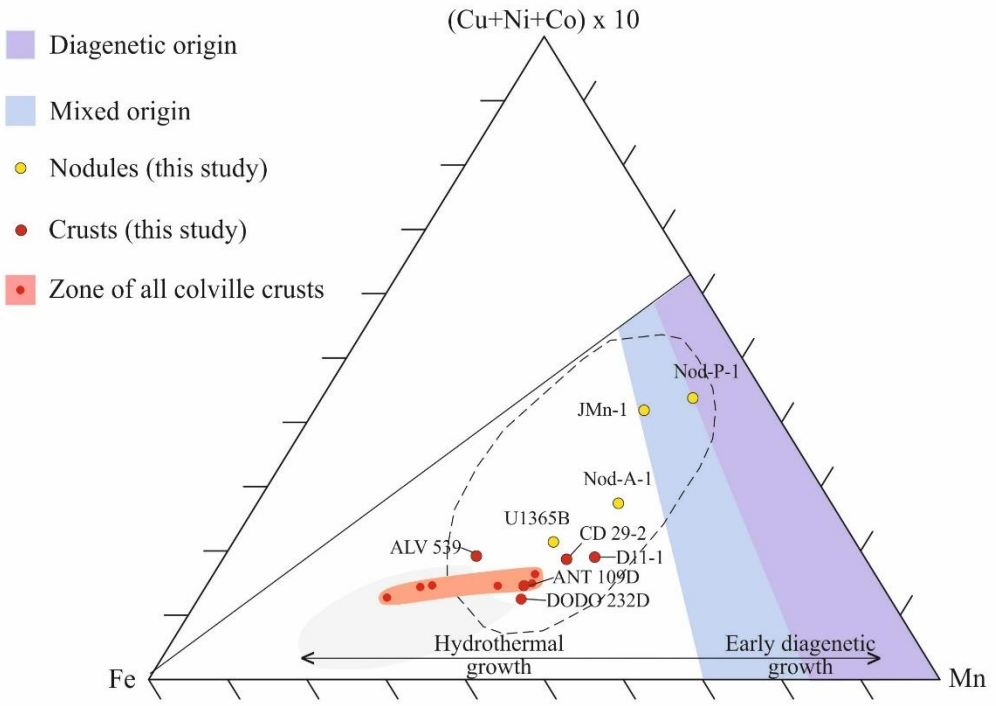

Figure 5.2 Fe-Mn nodule and crusts plotted on a discrimination plot with Fe, Mn, and Cu+Ni+Co (x 10) modified from Bonatti et al. (1972) and Halbach et al. (1981) to indicate the amount of hydrogenetic, hydrothermal, and diagenetic that occurred during the sediments deposition. The dashed line represents the field of hydrogenetic growth as described by Bonatti et al. (1972) and Toth (1980). The purple shaded area diagenetic growth with the blue shaded area being mixed diagenetic and hydrogenetic growth as defined by Halbach et al. (1981).

5.2.2 Ferromanganese Crusts (FMC)

Five FMC samples were supplied by J Hein, USGS; ANT 109D-E, ALVN 239-2-1, CD 29-2, D11-1, and DODO 232D-B (figure 5.3 and table 5.1) and an additional number of samples from the National Institute of Water and Atmospheric Research (NIWA) were collected from the Colville Ridge (figure 5.4 and table 5.1). The crust samples are well characterised for major and trace elements (Hein et al., 2013, Hein, unpublished, Levasseur, et al., 2004, Rehkämper et al., 2002, Rehkämper et al., 2004) and their locations given in figure 5.1.

ALV 539 (figure 5.3d) was recovered from the New England Seamounts in the NW Atlantic on the Alvin cruise ADA038115. The crust is approximately 12 cm thick, deposited on pillow and massive basaltic rocks. The dominant mineralogy is δ-MnO_2 (vernadite), 94 – 99 vol%, with < 1 vol% quartz and plagioclase. A mean growth rate of 2.4 mm/Myr has been determined from $^{10}Be/^{9}Be$ dating (Frank et al., 1999, O'Nions et al., 1998).

ANT 109D-E (figure 5.3e) was a dredge sample from the Melville Antipode cruise ANTP07MV (Mahoney et al., 1989). The crust is approximately 5 cm thick. The dominant mineralogy is δ-MnO_2, 92 – 97 vol%, with 2 - 8 vol% quartz and plagioclase. The mean growth rate is 1.6 mm/Myr, determined from $^{10}Be/^{9}Be$ dating (Frank et al., 1999, O'Nions et al., 1998).

CD 29-2 (figure 5.3b) was recovered from the Karin Ridge in the Johnston Island Economic Exclusion Zone (Line Islands) south of the Hawaiian Ridge on the Farnella cruise F7-86-HW. The crust is approximately 10 cm thick, and deposited on hyaloclastite. The crust has been partly phosphatised with CFA. The dominant mineralogy is δ-MnO_2, 89 – 96 vol%, with 1 – 4 vol% quartz and plagioclase. The CFA abundance increases with depth within the crust, below 50 mm it constitutes 7 – 10 vol% of the sample. The mean growth rate is 2.1 mm/Myr, as determined from $^{10}Be/^{9}Be$ dating (Christensen et al., 1997).

D11-1 (figure 5.3a) was collected form the Marshall Islands at a depth of 1.8 km on the Farnella cruise F10-89-CP. The 20 cm thick crust accumulated on a hyaloclastite substrate. The main phase present in this sample is δ-MnO_2, 71 – 100 % depending on the layer within the sample, minor amounts of quartz plus plagioclase (1 – 3 vol%) are also present. The CFA abundance increases with depth within the crust, below 50 mm it constitutes 14 – 29 vol% of the sample. The mean growth rate is 1.4 mm/Myr over the past 6 Myr, as determined from $^{10}Be/^{9}Be$ dating (Christensen et al., 1997).

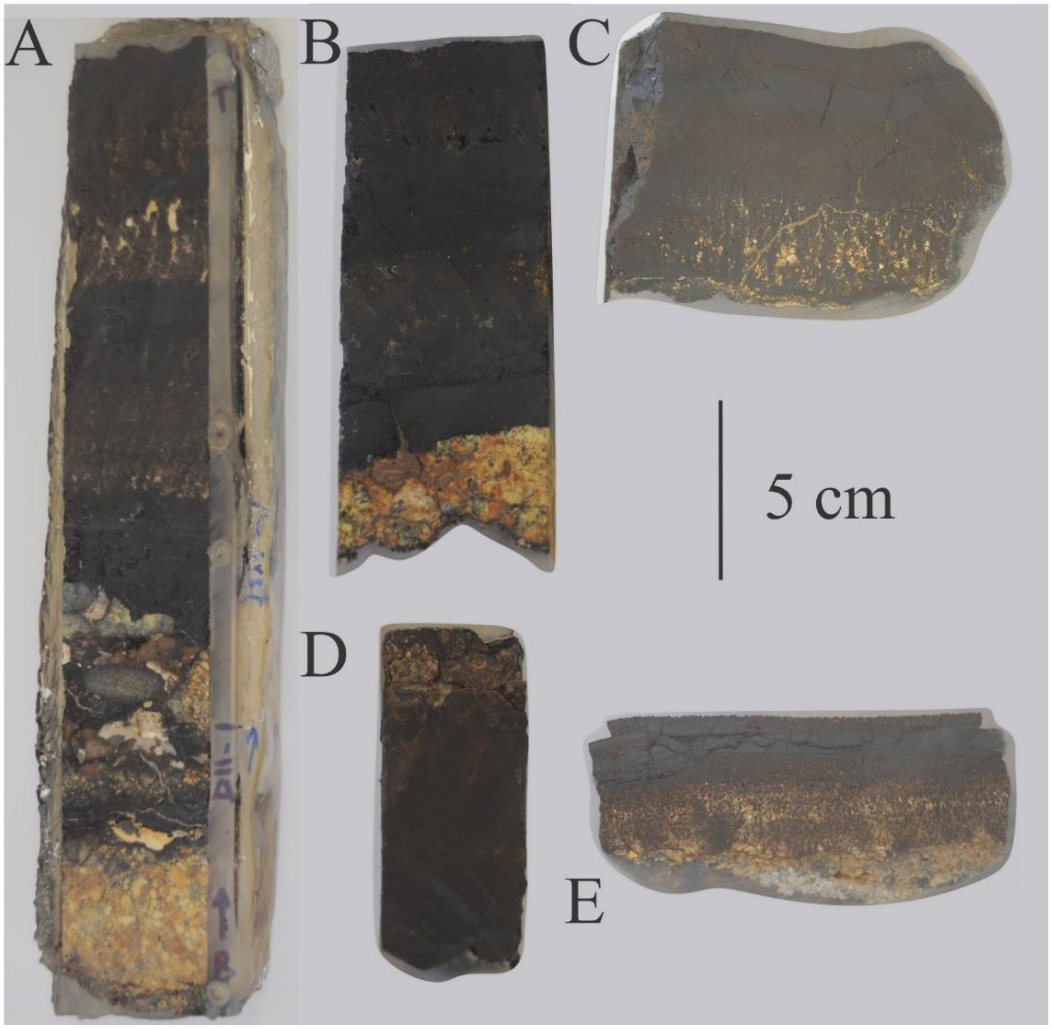

Figure 5.3 Photographs of the USGS suite ferromanganese crust samples; a) D 11-1, b) CD29-2, c) DODO 232D-B, d) ALV 539, and e) ANT 109D.

DODO 232D (figure 5.3c) was collected from the northern tip of the Investigator Ridge, adjacent to Sumatra and the Java Trench in the Wharton Basin on the Argo cruise DODO. The crust is approximately 7 cm thick with no substrate collected with the crust, however the dominant substrate in the area is basalt. The mean growth rate is 4.3 mm/Myr over the past 16.5 Myr, as determined from $^{10}Be/^{9}Be$ dating (Frank et al., 2006).

In addition to the above well characterised FMC a number of samples were collected at a depth of 1.7 km from the Colville Ridge, a remnant oceanic arc located between New Zealand and the Fiji archipelago, on the R.V. Tangaroa cruise TAN1007. The dominant substrate in the Colville Ridge region is volcanic (basalt to andesitic; Wright, 1997). In total six samples from this cruise were investigated in this study; CR 1007 19 B1/2, TAN 1007 19 B1/2, TAN 1007 19 B2/2 sample 1, 2, and 3, and TAN 1007 19 R (Fig 5.4). The crust thickness is not uniform across the samples, ranging from < 1 mm to approximately 5 mm. These crusts have not been previously described and major element and rare earth element (REE) concentration data were obtained by XRF (NIWA) and ICP-MS (Element2, VUW) here (appendix D and E).

Figure 5.4 Photographs of the Colville Ridge crusts; a) TAN 1007 19 B1/2, b) TAN 1007 19 B2/2 sample 1, c) TAN 1007 19 B2/2 sample2, d) CR1007 19 B1/2, e) TAN 1007 19 R, and f) TAN 1007 19 B2/2.

The five USGS crusts (ANT 109D-E, ALVN 239-2-1, CD 29-2, D11-1, and DODO 232D-B) all plot within the field of hydrogenetic growth as defined by Bonatti et al., 1972 (figure 5.2). By contrast, the six samples collected from the Colville Ridge show a range of hydrogenetic to hydrothermal influenced growth; TAN 1007 19 B 2/2 sample 1, 2, 3, plot within the hydrogenetic growth zone and CR 1007 19 B1/2, TAN 1007 19 B1/2, and TAN 1007 19 R toward hydrothermal (figure 5.5).

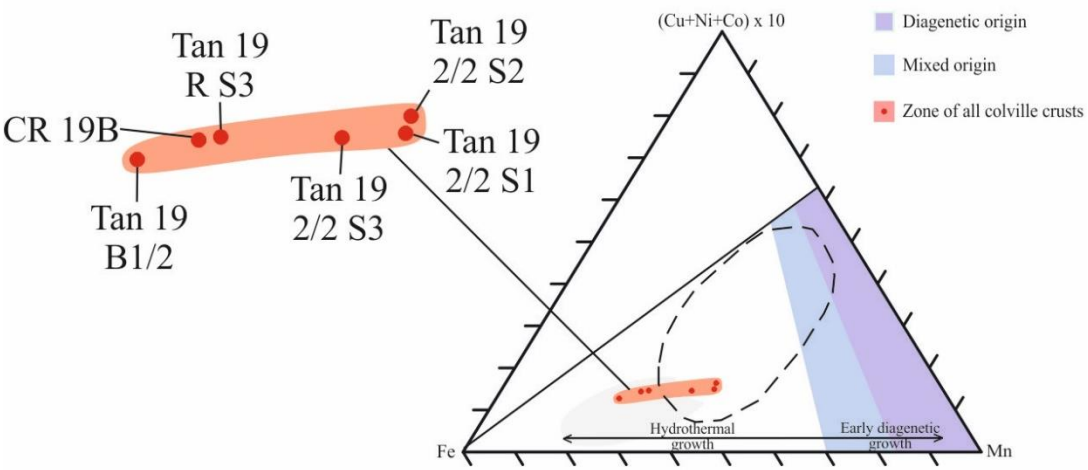

Figure 5.5 Colville ridge samples plotted on a Fe, Mn, and Cu+Ni+Co (x 10) discrimination plot with modified from Bonatti et al. (1972) and Halbach et al. (1981) enlarged from figure 5.2 with the dashed line representing the field of hydrogenetic growth.

Rare earth element patterns of FMC can also be used to distinguish between a hydrothermal and hydrogenetic source of trace metals. Hydrothermally sourced FMC typically have either a negative or no Ce anomaly whereas hydrogenetic sourced crusts display positive Ce anomalies, possibly due to the kinetic controls of Ce adsorption as hydrothermal crusts precipitate at faster rates than hydrogenetic crusts and a more reduced environment minimising the amount of Ce^{4+} available (Hein et al., 1997, Kuhn, 1998, Takahashi et al., 2007). Figure 5.6 shows the Post Archean Australian Shale (PAAS) normalised REE patterns for the six Colville Ridge samples and the average of the six hydrogenetic crusts (ANT 109D-E, ALVN 239-2-1, CD 29-2, D11-

1, and DODO 232D-B). Three of the Colville Ridge samples show negative to no Ce anomalies (TAN 1007 19 B 2/2 sample 1, 2, 3) whereas three show a slight positive Ce anomaly. By contrast, the average hydrogenetic crusts display a significantly more pronounced positive Ce anomaly. Interestingly, the three Colville crusts suggested to be hydrothermal in origin on the basis of major and minor elements (Fig 5.5) show a slight positive Ce anomaly (figure 5.6), which is the opposite of what would be expected. However, the REE abundances are low, which is consistent with a hydrothermal origin. Conversely, the Colville crust samples that show a hydrogenetic origin based on major and minor elements (figure 5.5) have a negative Ce anomaly and show intermediate abundances of REE (figure 5.6). Taken together, we interpret all the Colville Ridge crusts to be of mixed hydrothermal and hydrogenetic origin.

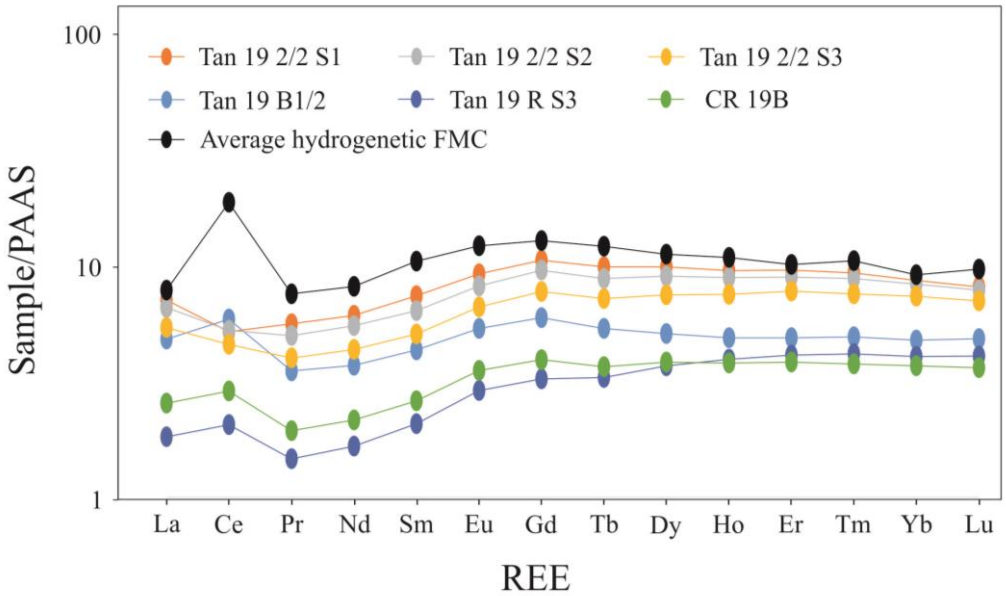

Figure 5.6 REE patterns for the six Colville Ridge crusts, normalised to Post Archean Australian Shale (PAAS; McLennan, 2001). The average REE pattern of the hydrogenetic crusts (n = 6; ANT 109D-E, ALVN 239-2-1, CD 29-2, D11-1, and DODO 232D-B) is shown for comparison.

The hydrothermal to hydrogenetic range observed in the Colville Ridge samples may result from the sample site proximity (< 200 km) to a currently hydrothermally active arc, the Kermadec Arc (de Ronde et al., 2011). The Colville Ridge marks the western

boundary of the rifting Havre Trough back-arc basin with the currently active Kermadec volcanic front to the east. The Kermadec Arc front is ~ 1,200 km long and ~ 40 km wide with > 33 volcanoes. The New Zealand American PLUme Mapping Expendition (NZAPLUME) surveyed 13 volcanoes in the southern portion of the Kermadec Arc in 1999 and found that 7 of the 13 volcanoes had active hydrothermal venting systems with one volcano, Brothers, having at least 100 dead and active sulphide chimneys (de Ronde et al., 2001, de Ronde et al., 2011). The hydrothermal system in this arc system has been active over a long period (~ 5 Ma) but individual circulations/chimneys may have very short lifetimes. Hence, in a hydrothermally active region, it is likely that over the longer time frame that the FMC are accumulating, hydrothermally sourced trace metals may be introduced from varying venting sources interspersed with periods of quiescence. The Colville Ridge is currently separated from the active volcanic front by up to 200 km, however the actively rifting back arc basin contains stratovolcanoes that were still active at least as recently as 800,000 ka (Ar-Ar dating of Gill Volcano, A Zohrab, unpublished data).

Further, it has been shown that hydrothermally sourced elements can travel great distances from their source, for example hydrothermally sourced Fe, ^{3}He, and Mn, have been reported as travelling > 2,000 km from source (De Flierdt, 2004, Resing et al., 2015, Sander and Koschinsky, 2011). To date, the transport of platinum in hydrothermal plumes has not been examined, however, elements with similar residence times to platinum (16 kyr – 1 Myr), such as Cu, Zn, and Ni, have been observed to travel > 200 km from their hydrothermal source (Barrett et al., 1987, Li, 1982, Li, 1991, Soyol-Erdene and Hui, 2012). Barrett et al. (1987) examined sediments located 200 km from hydrothermal activity on the ridge axis of the East Pacific Rise, where the concentrations of Cu, Zn, and Ni are orders of magnitude higher in these sediments relative to sediments from the abyssal seafloor away from hydrothermal influence (Barrett et al., 1987). Given the six Colville Ridge samples were all collected in close proximity to each other (a single dredge) and the geochemical evidence for mixed metal origins, it seems reasonable that all of the Colville Ridge crusts sampled will have grown with variable input from hydrothermal systems.

5.3 Ferromanganese crust and nodule sample preparation and analysis

The upper 10 mm of the FMC samples provided by the USGS (ANT 109D-E, ALV 239-2-1, CD 29-2, D11-1, and DODO 232D-B) were prepared for elemental and isotopic analysis. The surface of the sample was wiped with ethanol to remove any loosely held detrital sediment. The upper 0.5 cm^2 was removed using a Dremel® fitted with a cutting wheel and transferred to an agate pestle and mortar and fully powdered until the sample was homogeneous. The powdered sample was then transferred to a pre-cleaned Teflon beaker.

A surface-scraping sample was prepared from the FMC samples provided by NIWA (CR 1007 19 B1/2, TAN 1007 19 B1/2, TAN 1007 19 B2/2 sample 1, 2, and 3, and TAN 1007 19 R). The surface of the sample was initially cleaned with ethanol and a clean CeraStar ceramic knife was used to scrap the uppermost layer of the sample to a maximum depth of 2 mm (figure 5.7). The surface scrapings were collected on filter paper, transferred to a pestle and mortar and fully powdered until the sample was homogeneous. The powdered sample, approximately 1 g, was then transferred to a precleaned Teflon beaker.

Once all FMN and FMC samples were powdered they were prepared for concentration and isotopic analysis as described in detail in chapter 2 and outlined briefly here. An approximately 50 mg aliquot from each powdered sample was digested in aqua regia at 120 °C for 48 hours for Pt concentration analysis using the Element2 ICP-MS.

Figure 5.7 Sample photograph of the ferromanganese crust deposited on the volcanoclastic substrate (sample CR1007 19 B1/2) showing the typical thickness of the crust on the Colville samples.

Once the platinum concentration was determined, ca. 1 g aliquots of the samples were double spiked using the mixed ^{196}Pt-^{198}Pt spike. The double spike was added to produce a natural Pt to spike ratio of 0.55:0.45 (Creech et al., 2013). The samples were then digested and preconcentrated using nickel sulphide fire assay (NiS fire assay). The nickel sulphide beads were digested in aqua regia, then converted to chloride form for anion exchange column chemistry. Following column chemistry, the Pt cuts were dried, refluxed in aqua regia overnight, dried and refluxed in an HNO_3 and H_2O_2 mixture overnight to eliminate any organics that may have been stripped from the resin during anion exchange chemistry. Samples were prepared in 0.5 M HCl for analysis on the MC-ICP-MS (chapter 2).

5.4 Platinum concentration and isotopic composition of the natural samples

The platinum concentration and isotopic data for the nodules and crusts are summarised in Table 5.1, and figures 5.8 and 5.9.

To evaluate reproducibility of both exchange chemistry and the full analytical procedure, several digests of the three nodule SRMs were made and these split into two separate aliquots for Pt purification using the anion exchange column chemistry. Nod-P-1 and JMn-1 were reproducible between separate digests and samples splits for both concentration and δ^{198}Pt (Table 5.1). Platinum concentration was determined by isotope dilution (chapter 2) with Nod-P-1 having an average concentration of 126 ng/g ± 5 ng/g 2sd, n = 8, and JMn-1 of 137 ng/g ± 0.4 ng/g 2sd, n = 8, consistent with previously published values: Pt = 110 – 120 ng/g and 110 – 159 ng/g, respectively (Axelsson et al., 2002, Balaram et al., 2006, Terashima et al., 1995). The measured platinum concentrations for Nod-A-1 however, shows a wide range, 412 – 550 ng/g, although the average concentration of 487 ng/g (± 120 ng/g 2sd, n = 6), is also consistent with previously published values of 450 ng/g – 520 ng/g (Axelsson et al., 2002, Balaram et al., 2006). The concentrations in Nod-A-1 reproduce within splits of the same digest, but not between individual digests (table 5.1).

The average δ^{198}Pt for Nod-P-1 and JMn-1 is 0.158 ± 0.065 ‰ 2sd, n = 8, and 0.163 ± 0.089 ‰ 2sd, n = 9, respectively. The reproducibility of JMn-1 (± 0.089 ‰ 2sd) is comparable to the reproducibility reported by Creech et al., (2014) for silicate samples (± 0.088 ‰ 2sd), and is adopted here as representative of the external precision for the ferromanganese sample analyses. By contrast, the δ^{198}Pt of Nod-A-1 shows a large range, 0.048 – 0.706 ‰, n = 12 (figure 5.8). The Nod-A-1 concentration and isotopic composition heterogeneity will be discussed in the proceeding section.

Table 5.1 Platinum concentrations (ID) and δ^{198}Pt of the natural ferromanganese crust and nodules listed in order of sample type; diagenetic, hydrogenetic, and mixed hydrogenetic and hydrothermal. The digest # is labelled in a sequence of XX-X with splits labelled A or B for the SRMs. n indicates the number of MC-ICP-MS analyses conducted on each sample split.

Sample type	Ocean	Digest	Split	δ^{198}Pt (‰)	δ^{198}Pt ‰ (2se)	Pt ng/g	n
Diagenetic nodules							
USGS Nod-A-1	Atlantic	35-1		0.678	0.022	554	2
		35-2		0.500	0.022	550	2
		36-1	A	0.308	0.016	496	2
		36-1	B	0.312	0.017	496	2
		36-2	A	0.067	0.016	412	2
		36-2	B	0.067	0.018	412	2
USGS Nod-P-1	Pacific	36-1	A	0.145	0.035	123	2
		36-1	B	0.123	0.036	123	2
		36-2	A	0.187	0.041	128	2
		36-2	B	0.178	0.035	128	2
GSJ JMn-1	Pacific	35-1		0.234	0.042	133	1
		35-2		0.156	0.040	138	2
		36-1	A	0.196	0.043	138	2
		36-1	B	0.125	0.047	138	1
		36-2	A	0.121	0.039	138	1
		36-2	B	0.142	0.039	138	2
Hydrogenetic nodules							
U1365B	Southern	M-27855		0.126	0.026	284	1
Hydrogenetic crusts							
ALV 539	Atlantic			0.417	0.017	383	1
ANT 109D	Indian			0.082	0.045	93	1
DODO 232D	Indian			-0.075	0.031	71	1
CD 29-2	Pacific			0.081	0.027	120	1
D11-1	Pacific			0.879	0.026	191	1
Mixed (hydrogenetic and hydrothermal) crusts							
TAN 19-B1/2	Pacific			0.264	0.025	289	2
TAN 19-B2/2-S1	Pacific			1.281	0.035	181	2
TAN 19-B2/2-S2	Pacific			-0.274	0.027	251	2
TAN 19-B2/2-S3	Pacific			-0.446	0.040	260	1
TAN 19-R-S3	Pacific			0.336	0.026	90	1
CR 19 B	Pacific			-0.236	0.032	128	1

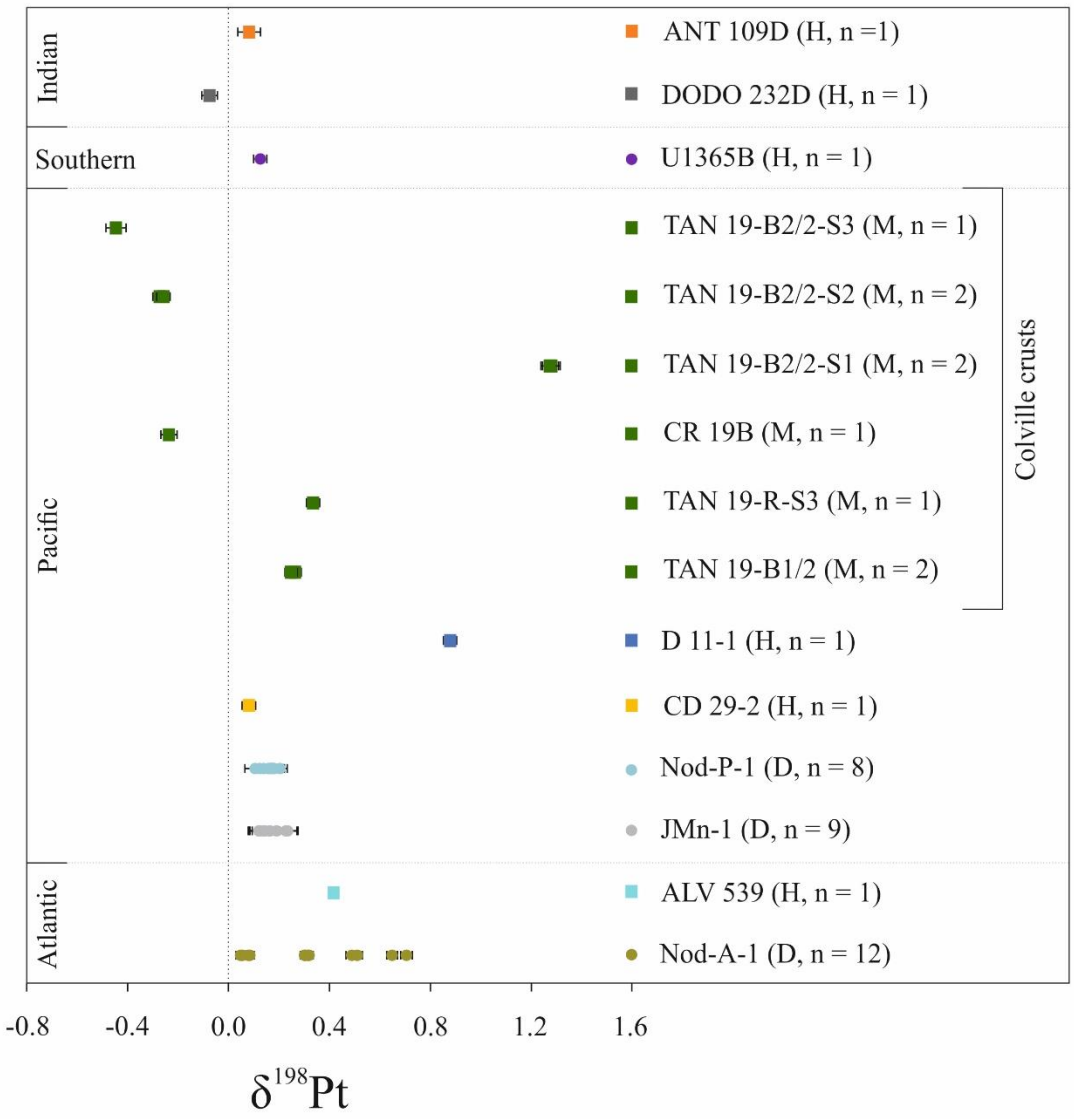

Figure 5.8 δ^{198}Pt of the FMN (circles) and FMC (squares) analysed in this study. The dashed vertical line represents the IRMM-010 standard. The type of sample is represented as H = hydrogenetic, D = diagenetic, and M = mixed hydrogenetic and hydrothermal. The number of individual analysis is given as n.

The FMS from the two Atlantic Ocean locations have a platinum concentration range of 383 – 487 ng/g, consistently higher than any of the other sampled locations (Pt < 290 ng/g). The samples from the five Pacific Ocean locations display the largest range, 90 – 289 ng/g Pt, however much of this range is from the mixed hydrothermal/hydrogenetic crusts from Colville Ridge, with the hydrogenetic and diagenetic samples only ranging from 120 – 190 ng/g Pt. The FMS from the two Indian Ocean locations have the lowest platinum concentrations, 71 – 93 ng/g Pt, and the sole sample from Southern Ocean has a platinum concentration of 284 ng/g (table 5.1, figure 5.1).

The two locations from the Atlantic Ocean have a δ^{198}Pt range of 0.067 – 0.678 ‰, however this range is defined by the multiple sampling of the bulk sample, Nod-A-1. The average isotopic composition for Nod-A-1 is 0.322 ‰, which is similar to the Atlantic Crust, ALV 539, value of 0.417 ‰. The hydrogenous and diagenetic Pacific Ocean samples range from 0.081 – 0.879 ‰, with all but one (D11-1) clustering between 0.081 and 0.196 ‰. The Colville Ridge crusts (mixed hydrothermal and hydrogenetic), in contrast, show the greatest variability, δ^{198}Pt ranging from – 0.446 to +1.281 ‰ (figure 5.9). The Pacific Ocean samples give a mean δ^{198}Pt of 0.192 ‰ for just the diagenetic and hydrogenetic samples combined, whereas if the mixed hydrothermal and hydrogenetic samples are included the mean δ^{198}Pt value decreases to 0.184 ‰. The two samples from the Indian Ocean basin have generally lighter isotopic compositions that range from -0.075 to +0.082 ‰, and the sole Southern Ocean crust has a δ^{198}Pt of 0.126 ‰.

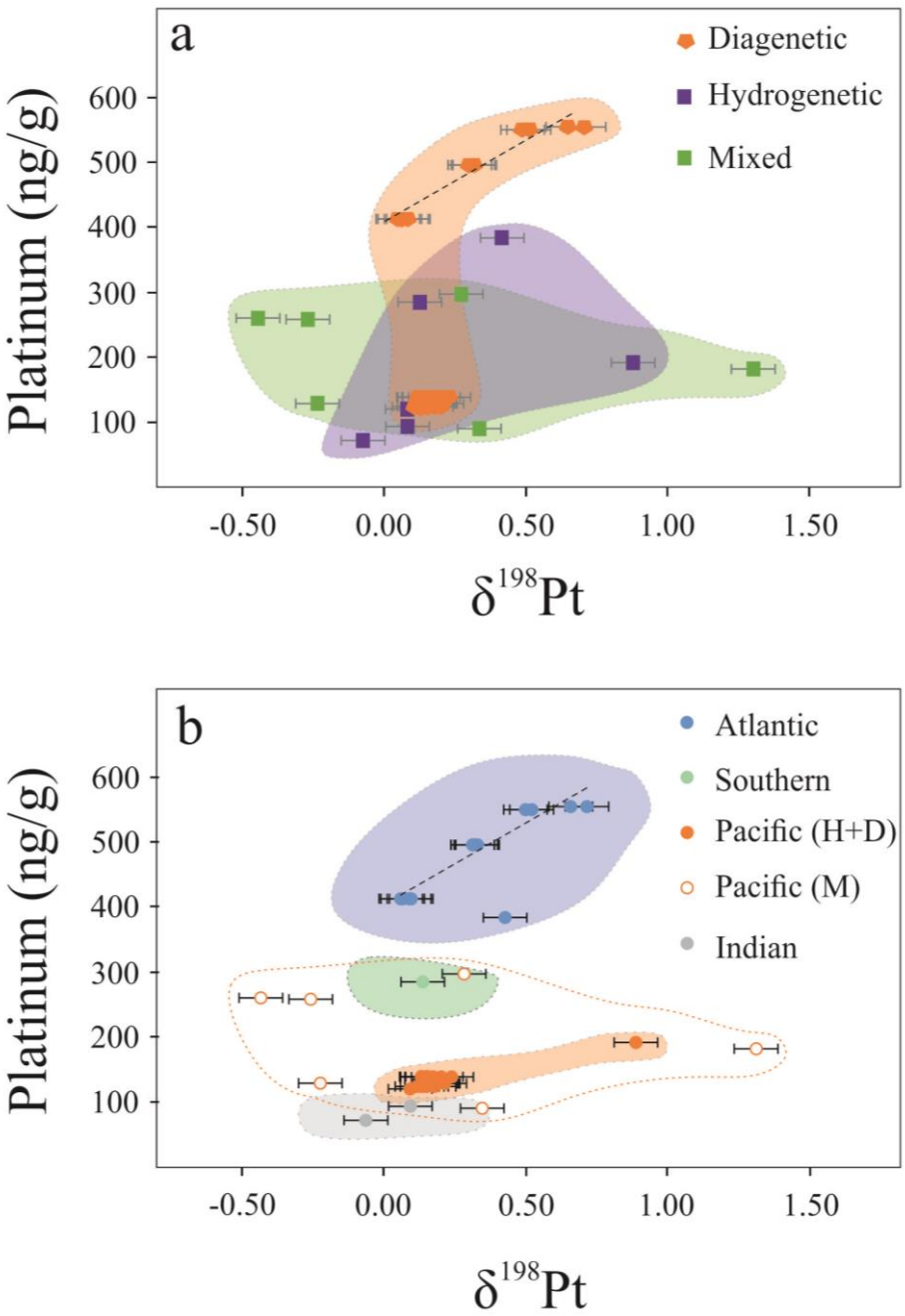

Figure 5.9 (a) Platinum concentration versus δ^{198}Pt with the samples distinguished by type of sediment (diagenetic, hydrogenetic, and mixed hydrogenetic and hydrothermal). The shaded areas represent the field of each type. **(b)** Platinum concentration versus δ^{198}Pt, distinguishing the sample locations; Atlantic, Southern, Pacific, and Indian. The Pacific basin samples are further divided into hydrogenetic and diagenetic (H+D) and mixed hydrothermal and hydrogenetic (M) sediments. All errors in both figures are based on the 2sd of JMn-1, 0.089‰.

5.5 Discussion

5.5.1 Platinum heterogeneity in Nod-A-1

A large range is observed for both Pt concentration and δ^{198}Pt for Nod-A-1, 412 to 554 ng/g Pt and δ^{198}Pt of 0.048 ‰ to 0.706 ‰, respectively (figure 5.10). This range either reflects real variation in the sample or an analytical artefact, and these possibilities are explored here. Individual sample digests that have been split and processed separately through the anion exchange chemistry reproduce both concentration and isotopic composition within uncertainties (table 5.2), indicating the variations in both concentration and isotopic composition are linked to the different sample digestions. δ^{198}Pt correlates strongly with platinum concentration, with a lighter δ^{198}Pt composition associated with lower platinum concentrations, consistent with a two component mixing process (figure 5.10).

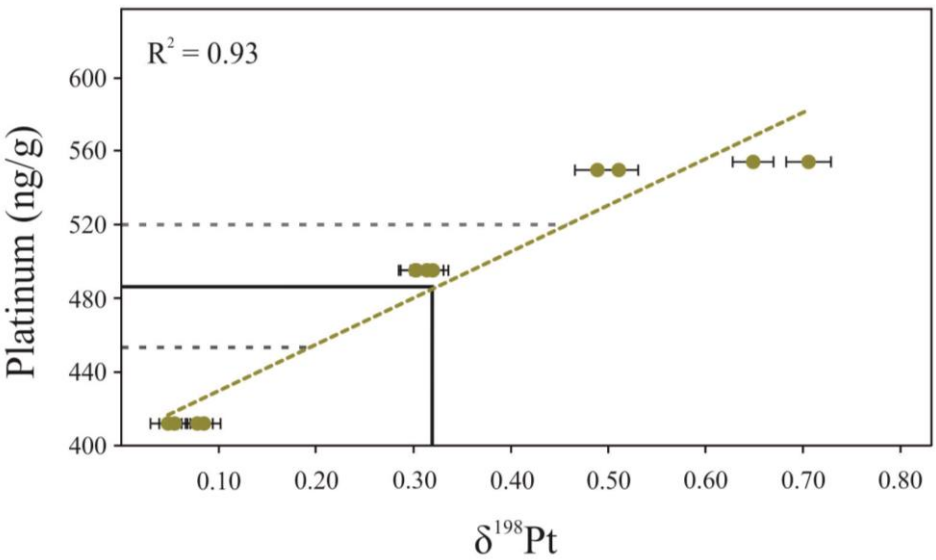

Figure 5.10 Platinum concentration versus δ^{198}Pt for Nod-A-1. The green dashed line represents the linear best fit line. The black solid lines are the average concentration and δ^{198}Pt, 487ng/g and δ^{198}Pt 0.322 ‰. The grey dashed lines represent concentration data from previous studies; 453 ng/g from Flanagan and Gottfried, (1980) and 520 ng/g from Axelsson et al. (2002).

Potential analytical artefacts could arise from contamination (e.g. blank – sample mixing), or matrix effects during analysis. It is unlikely that the observed variations stem from a mix between an analytical blank and the sample Pt for several reasons. First, the Pt concentrations for Nod-A-1 are significantly higher than for both Nod-P-1 and JMn-1, which both reproduced well with isotopic compositions heavier than the lightest composition measured for NOD-A-1. Second, full procedural blanks were conducted with each batch of digestions, with a platinum concentration of < 4 ng/g. This comprises ≤ 1 % of the Nod-A-1 platinum content. For the blank to be able to leverage the variations in measured isotopic composition it would need a δ^{198}Pt of -200 ‰, or lighter. This is significantly lower than any natural Pt measured to date (Creech et al., 2014). The higher overall concentrations of Pt could be consistent with contamination from a high concentration Pt source with an extremely heavy isotopic composition, however, the only material yet measured with a Pt isotopic composition as heavy or heavier than the end member (δ^{198}Pt = +0.678 ‰), including Pt ore samples, are a few of the FMC samples. The Nod-A-1 samples were all processed and analysed prior to any of these heavier FMC samples entering the laboratory environment. Thus, contamination during sample processing appears to be highly unlikely.

Another possibility is that the platinum purity in the final processed samples affected the measured isotopic composition, i.e. matrix effects during MC-ICPMS analysis. In this case, the lower Pt concentration samples would likely be the ones most strongly affected. Creech et al., (2013) showed that doping double spiked (^{196}Pt-^{198}Pt) IRMM-010 with up to 10 % the concentration of Pt with a number of elements (Mg, Al, Ca, Ti, Cr, Mn, Fe, N, Mo, W, Rh, Pd, Ir and Au) did not significantly affect the reliability and accuracy of the double spike method. Contamination with 5 % Mg resulted in the largest negative offset from the undoped IRMM-010 sample, δ^{198}Pt = -0.045 ‰ ± 0.023 ‰ 2sd, which still falls within the analytical uncertainty of the undoped IRMM 010 sample (0.0 ‰ ± 0.043 ‰ 2sd). This would also not explain the platinum concentration range among the different digests, given that the samples were spiked prior to NiS fire assay. Similarly, the double spike should account for any fractionation that may have occurred during column chemistry.

Ruling out analytical artefacts suggests that the platinum concentration is not homogenous at the sampling scale of this study (< 2g). Variations in the concentrations of PGE in geological samples have long been recognised as the so called 'nugget effect', reflecting the concentration of PGE in minor accessory phases that may be heterogeneously distributed even in a powdered sample (Davies and Tredoux, 1985, Enzweiler et al., 1995, Meisel and Moser, 2004, Rao and Reddi, 2000, Ravizza and Pyle, 1997). For example, Shinotsuke and Suzuki (2007) observed variations in Ru, Ir, Pt, and Os data within BHVO-2 and JA-2 SRMs, which they attributed to the heterogeneity of minor minerals. Platinum homogeneity for the Pt SRM SARM-76 is certified for 25 g aliquots or larger (c.f. base metals certified for only 0.2 g aliquots). A range of Pt concentrations (2535 – 3920 ng/g) was observed in the 1 g aliquots of SARM-76 measured in this study (chapter 4), however the average of these (still representing only ~ 7 g) was within error of the certified concentration (3059 ± 657 ng/g (1sd) and 3590 ng/g, respectively).

The sample size used for the determination of the Pt concentration in Nod-A-1, Nod-P-1 and JMn-1 given on GeoRem (Geological and Environmental Reference Materials) is not clearly defined with only some studies providing this information. For example, Axelsson et al. (2002) and Flanagan and Gottfried (1980) both analysed Nod-A-1 with Axelsson et al. (2002) using 50 mg of material and Flanagan and Gottfried (1980) simply stating that they used a portion of a bottle, with no indication to the actual size. The variation in the Pt concentration between these studies is ~ 13 % (453 – 520 ng/g). The average Pt concentration for Nod-A-1 here (487 ± 120 ng/g) is in good agreement with the reported Pt concentrations (Axelsson et al., 2002, Flanagan and Gottfried, 1980).

Several studies have indicated the importance of sample size in reducing this nugget effect (e.g. Enzweiler et al., 1995 and Meisel and Moser, 2004). Here, sample sizes of < 2 g were used for Nod-A-1, Nod-P-1 and JMn-1. For Nod-P-1 and JMn-1 this appears to be sufficient for platinum concentration and isotopic homogeneity, but not for Nod-A-1.

The range in platinum concentrations and isotopic compositions measured in Nod-A-1 are thus interpreted as reflecting mixture of two natural components within the bulk nodules sampled from Blake Ridge, ranging from a low concentration, isotopically light component to a higher concentration, isotopically heavy component. The formation of the nodules comprising the Nod-A-1 sample is also somewhat ambiguous compared to the Nod-P-1 and JMn-1 samples, with both diagenetic and hydrogenous interpretations having been made (see section 5.2). This may reflect the complex nature of the nodules collected for this bulk sampling, made more apparent in analyses of elements such as Pt, that are subject to nugget effects.

5.5.2 Platinum concentrations

Based on the limited dataset presented here, preliminary observations suggest a variation in platinum concentration between basins with Atlantic > Southern ≥ Pacific > Indian, even allowing for the wide range in concentrations exhibited by the Blake Ridge bulk sample (Nod-A-1). This is broadly consistent with the average Pt in FMS for the ocean basins compiled by Hein et al., (1997), Atlantic (0.57 ug/g) > Pacific (0.23 – 0.48 ug/g) > Indian (0.21 ug/g) (chapter 1.333).

Three previous studies have examined the concentration and depth profile of platinum in seawater and these also suggest an intra-basin variation, however with a different order to that observed in the FMS; Pacific > Indian ≥ Atlantic (Colodner, 1991, Goldberg et al., 1986, Jacinto and Van Den Berg, 1989) (chapter 1). The mean concentration in the Atlantic Ocean is ~ 0.3 pM, with a conservative profile (Colodner, 1991). The Indian Ocean also has a mean concentration of ~ 0.3 pM but it shows a scavenger profile with a concentration of 1.6 pM at the surface and decreases to 0.3 pM at the depths where the ferromanganese deposits analysed here have accumulated (Jacinto and Van Den Berg, 1989) (chapter 1.3.2). There is a decrease in the Pacific Ocean Pt concentrations from east to west, 1.0 – 0.3 pM. The eastern Pacific profiles show a nutrient profile with the platinum concentration increasing from 0.4 pM to 1.2 pM with depth (Goldberg et al., 1986). This pattern of higher concentrations in the east is the opposite of what is observed in the Pt concentrations of the Pacific hydrogenetic

FMC and FMN; the crusts decrease in Pt concentration from 191 ng/g (D-11) to 120 ng/g (CD-29), and the bulk nodules from 135 ng/g (JMn-1) to 125 ng/g (Nod-P-1). A wider dataset of Pt concentrations from the literature is also consistent with the trends in FMS Pt concentration data in this study, with mean Pt concentrations for FMS decreasing from the central Pacific, 420 - 480 ng/g, to the California margin, 70 ng/g (Hein et al., 1997; Halbach et al. 1984). Ravizza et al. (2001) and Colodner (1991) suggested that the variation between the seawater concentration and depth profiles between the east and west Pacific Ocean and the Indian Ocean profile may be due to analytical artefacts as all three studies used different analytical methodologies. This is further supported by the moderately long residence time of platinum in the marine environment, 16 kyr – 1 Myr, which would suggest a uniform oceanic platinum concentration, with the potential for localized perturbations from hydrothermal activity (Colodner, 1991, Soyol-Erdene, 2012). If the measured basinal variations in seawater Pt are real, this would suggest that there is not a simple relationship between seawater Pt concentration and the concentration of Pt sequestered in the Fe-Mn deposits, and would further require eastern Pacific FeMn deposits, particularly those close to the California margin, to be much less effective in scavenging Pt from the seawater than elsewhere in the Pacific.

In chapter 3 I showed that platinum preferentially adsorbs onto manganese oxide phases relative to iron oxyhdroxide phases in an oxic environment at the pH of the modern ocean, pH = 7 - 8, with 19 times more Pt adsorbed onto δMnO_2 than onto the iron oxyhydroxides. This suggests the Mn/Fe ratio should have a control on the platinum concentration. Other elements that preferentially adsorb onto the manganese oxide phase, such as Ba^{2+}, $Ni^{2+}$and Zn^{2+}, demonstrate a direct correlation ($R^2 \sim 0.8$) with the Mn/Fe ratio (figure 5.11 (b), Hein et al., 2013), and an earlier study of FMS from the central Pacific showed both Ni and Pt correlated with Mn concentrations (Halbach et al., 1984). However, the samples analysed in this study show no direct relationship between Mn/Fe (or Mn) and platinum concentration, suggesting that composition is not the sole factor that controls the observed platinum concentration in the crusts and nodules (figure 5.11 (a) and (c)).

Previous studies have suggested that platinum concentration decreases with the depth at which the sample forms due to the mobility of manganese in the oxygen minimum zone, ~ 200 – 1000 mbsl (Halbach et al., 1984, Halbach et al., 1989). An overall correlation between Pt concentration and the water depth is not readily apparent in this study for hydrogenetic or diagenetic FMS. However, the sample with the lowest platinum content is from the deepest location and the highest platinum content from the shallowest, ANT 109D at 5,438 mbsl and Nod-A-1 at 788 mbsl, respectively (figure 5.11 (d)). Within individual basins, the two Atlantic samples, and the two Pacific hydrogenetic samples show positive correlations with depth, however this is a very limited sampling and any within-basin relationship appears to break down at depths > 3000 m.

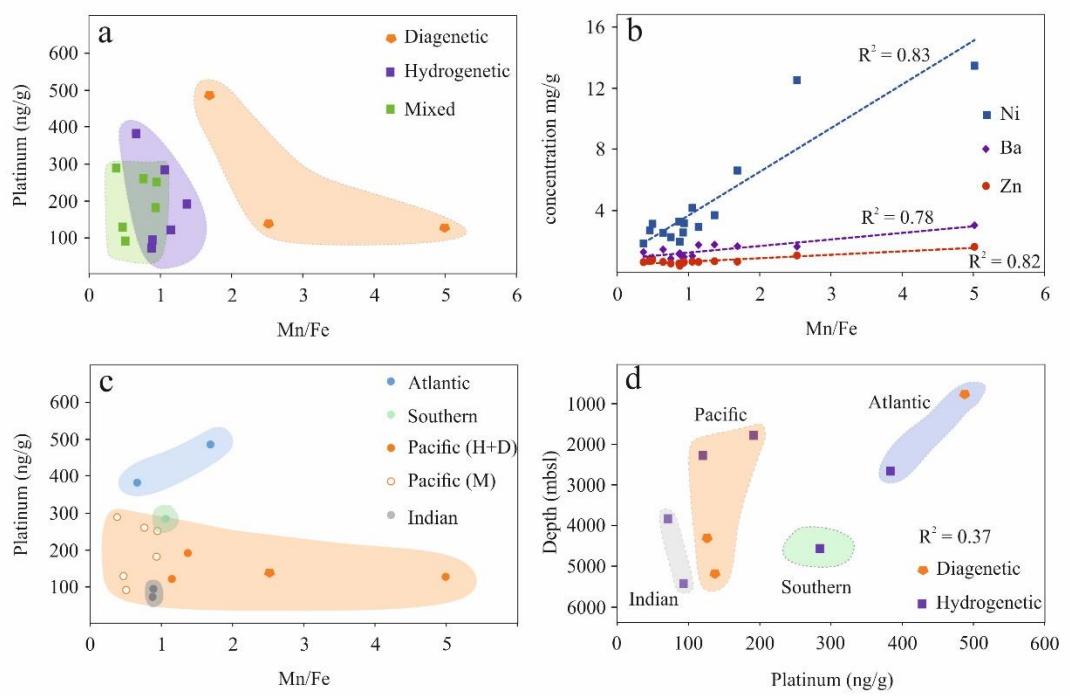

Figure 5.11 (a) Platinum concentration (ng/g) versus Mn/Fe ratio grouped by sample type (diagenetic, hydrogenetic, and mixed hydrogenetic and hydrothermal). **(b)** Ni, Ba, and Zn (mg/g) versus Mn/Fe **(c)** Platinum concentration (ng/g) versus Mn/Fe ratio grouped by ocean basin. **(d)** The platinum concentration of diagenetic and hydrogenetic samples with depth of sample with them grouped by ocean basins.

Adsorption of Pt is a chemisorptive redox mechanism (Chapter 3), suggesting that redox conditions may be a significant control on Pt concentrations. Two redox indices, V/(V+Ni) and U/Th, that have been used previously to indicate the palaeo-oxygen levels of sediments at the time of deposition, are shown in figure 5.12 (a) for all samples in this study (Riquier et al., 2006, Soua, 2011). All samples plot within the oxic field, dissolved oxygen content of 90 – 355 µmol/Kg, of both redox indices with the exception of the Colville Ridge sample TAN 19R S3, which plots in the dysoxic field, dissolved oxygen content of 9 – 90 µmol/Kg, for the U/Th index (Riquier et al., 2006, Soua, 2011). The Colville Ridge samples, which were all dredged from the same location, show a large range U/Th ratio, 0.33 – 1.03, which lends further support to the mixed hydrogenetic and hydrothermal source of trace metals i.e. variable addition of an anoxic signal from a hydrothermal source. As an estimate of the broad redox environment of the sample locations, the localities (within 500 km) are compared to the modern dissolved oxygen ocean profiles compiled by the National Oceanic and Atmospheric Administration (NOAA) World Ocean Circulation Experiments (WOCE) in figure 5.13. All of the sample locations are in the oxic zone (O_2 content > 90 µmol/Kg), with the exception of the approximate Colville Ridge sample location (O_2 concentration > 50 µmol/Kg; Schlitzer, 2000, Riquier et al., 2006). Although the location shown for the Colville Ridge sample in figure 5.13 is < 250 km to the west of the actual sample location, in combination with the U/Th redox indices this suggests that these samples were deposited in an oxic to dysoxic environment.

Ferromanganese sediments commonly display Ce anomalies, which appear to be primarily controlled by redox conditions (Hein et al., 2012, Hodge et al., 1985, Takahashi et al., 2000). The adsorption mechanism for Ce is similar to the chemisorptive redox mechanism suggested for platinum in chapter 3 (figure 5.12 (b)). The hydrogenetic FMS samples show a distinctive higher cerium anomaly relative to the diagenetic and mixed hydrothermal and hydrogenetic samples, which have overlapping cerium anomalies (figure 5.12 (b)). If the FMS cerium anomalies are grouped per ocean basin, the Pacific Ocean samples have distinctly lower cerium anomalies compared to the other three ocean basins (figure 5.12 (c)).

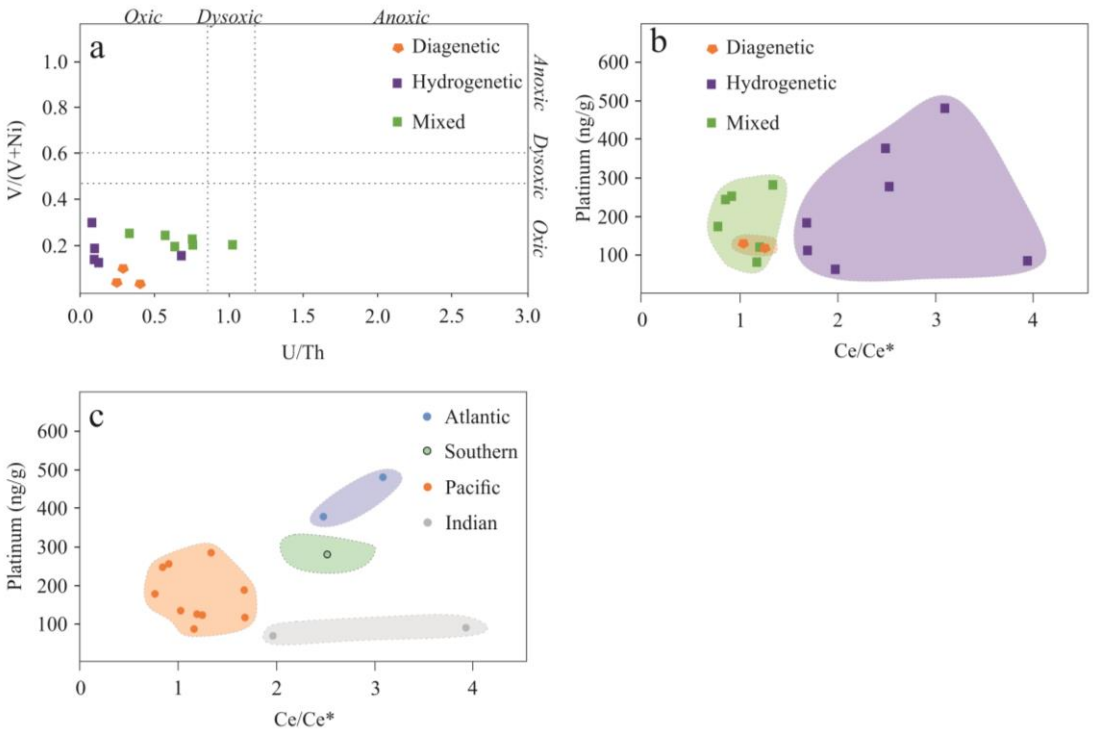

Figure 5.12 (a) Crossplot of redox indices V(V+Ni) versus U/Th, which is used to estimate the redox conditions of the samples, with the oxic, dysoxic, and anoxic zones having a range of ≈ 355 - 90, 90 – 9, and 0 µmol/Kg of dissolved oxygen, respectively (Riquier et al., 2006, Soua, 2011). **(b)** Cerium anomaly versus Pt concentration (ng/g) grouped by sample type. **(c)** Cerium anomaly versus Pt concentration (ng/g) grouped by sample location. $Ce/Ce^* = Ce_N / (La_N^{0.667} \times Nd_N^{0.333})$ with $_N$ = normalised to PAAS (McLennan, 2001).

Alternatively, Takahashi et al. (2007), proposed that the primary control of the adsorption of cerium is kinetic and they observed a decrease in cerium with increase of sediment growth rate i.e. cerium anomalies are predicted to range from hydrogenetic > diagenetic > hydrothermal. This general trend can be seen with the hydrogenetic samples having the highest cerium anomaly. The cerium anomalies in the diagenetic samples overlap with the mixed origin samples, which is consistent with the latter representing a mixture of fast growing hydrothermal and slow growing hydrogenetic sources.

There is no overall correlation between Pt concentrations and cerium anomalies (figure 5.12). However, the samples from the Pacific, Southern and Atlantic oceans show a broad positive correlation between Pt concentration and Ce anomaly, particularly when only the hydrogenetic and diagenetic samples are considered. There is no overall correlation of Pt concentration with growth rate for the samples where growth rate has been measured (Table 5.1), however for the Pacific samples, and for the Indian samples, Pt concentrations decrease with increasing growth rate, consistent with some kinetic influence. The Indian Ocean samples appear to have anomalously low Pt concentrations yet include the highest Ce anomaly, suggesting that the controls on Pt and Ce adsorption (be they redox or growth-rate related) are decoupled in the Indian Ocean samples. The reasons for this are unclear.

Figure 5.13 (overleaf) Five oxygen profiles located closest to the samples used in this study from NOAA World Ocean Circulation Experiments (WOCE), with the approximate sample depths marked (Schlitzer, 2000). **(a)** USGS Nod-A-1 and ALV 539 plotted on AO3 profile from the Atlantic Ocean at ~ 35 °N latitude. **(b)** DODO 232D plotted on IO2 profile from the Indian Ocean along the ~ 8 °S latitude. **(c)** ANT 109D plotted IO5 along the ~ 35 °S latitude. **(d)** D11-1, CD 29-2, and USGS Nod-P-1 are plotted on PO4 from the Pacific Ocean at the ~ 10°N latitude. **(e)** GSJ JMn-1 and the Colville Ridge samples are plotted on the P14 profile taken at the ~ 175 °W longitude. The longitudes of plots a – d are given on the x-axis and latitudes are given on the x-axis of plot e. The depth (mbsl) of the ocean on all plots is given on the y-axis and the colour bar legend indicates the oxygen concentration (µmol/Kg).

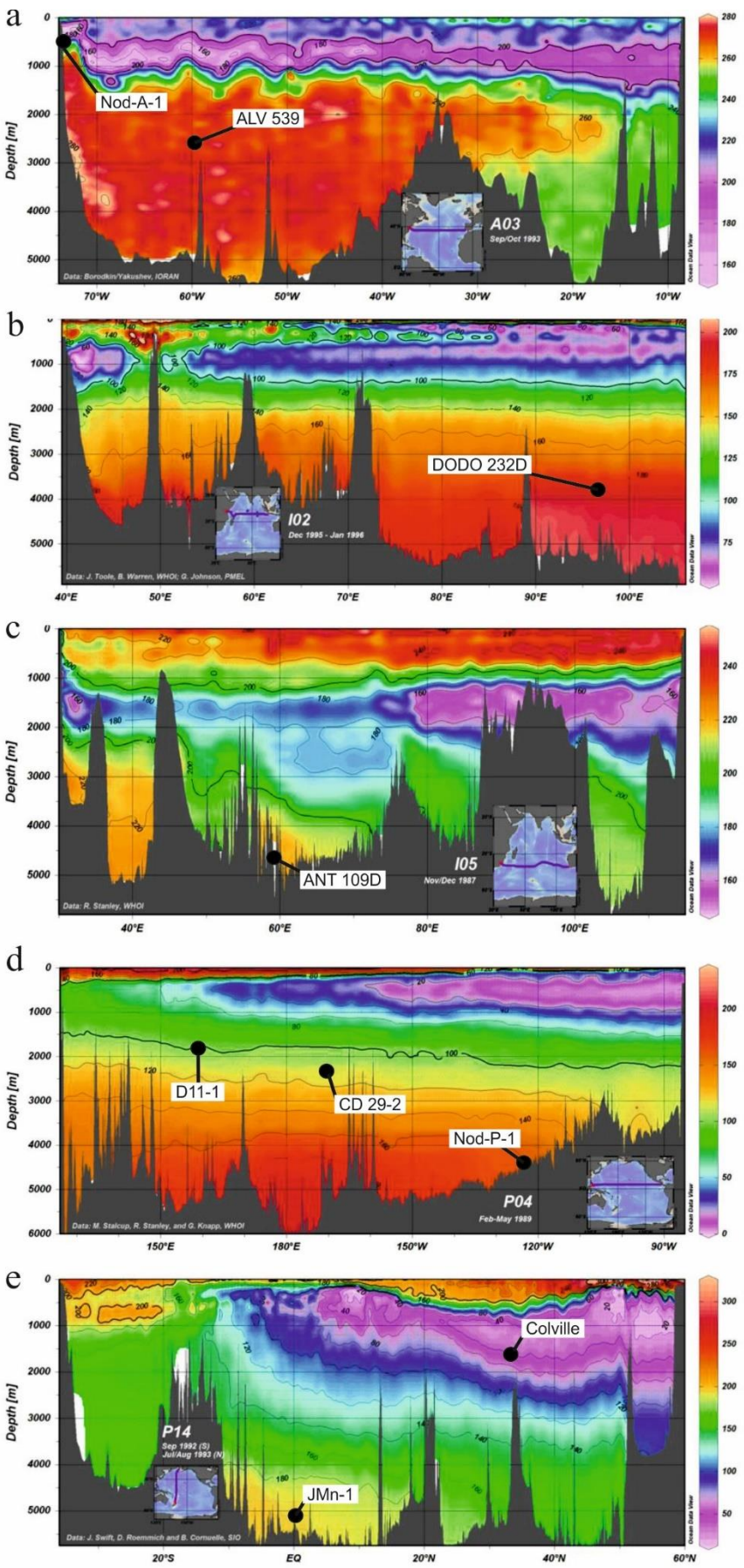
a
Nod-A-1
ALV 539
A03
Sep/Oct 1993
Depth [m]
70°W
60°W
50°W
40°W
30°W
20°W
10°W
b
DODO 232D
I02
Dec 1995 - Jan 1996
Data: J. Toole, B. Warren, WHOI; G. Johnson, PMEL
40°E
50°E
60°E
70°E
80°E
90°E
100°E
c
ANT 109D
I05
Nov/Dec 1987
Data: R. Stanley, WHOI
40°E
60°E
80°E
100°E
d
D11-1
CD 29-2
Nod-P-1
P04
Feb-May 1989
Data: M. Stalcup, R. Stanley, and G. Knapp, WHOI
150°E
180°E
150°W
120°W
90°W
e
Colville
P14
Sep 1992 (S)
Jul/Aug 1993 (N)
JMn-1
Data: J. Swift, D. Roemmich and B. Cornuelle, SIO
20°S
EQ
20°N
40°N
60°N

5.5.3 Platinum isotopic variations

The most striking observation from this study is the overall heavier composition of the natural ferromanangese crust and nodules relative to IRMM-010 and previously reported platinum isotope compositions measured on geological and meteorite samples (figure 5.14, Creech et al., 2014). The hydrogenetic and diagenetic sourced FMC and FMN have a platinum isotope range of δ^{198}Pt = -0.075 to 0.879 ‰, overlapping with the heaviest silicate samples but extending to compositions almost 1 ‰ heavier. The mixed origin samples from the Colville Ridge, which were collected from a relatively limited area, span an even wider range in Pt isotopic composition, δ^{198}Pt = -0.446 – 1.281 ‰, extending from lighter δ^{198}Pt compositions similar to that of the mantle and extra-terrestrial materials described by Creech et al. (2014) to more than 1.1 ‰ heavier. Unlike platinum concentration, there appears to be no systematic inter-basin variation with the platinum isotopic composition (figure 5.8 and 5.9).

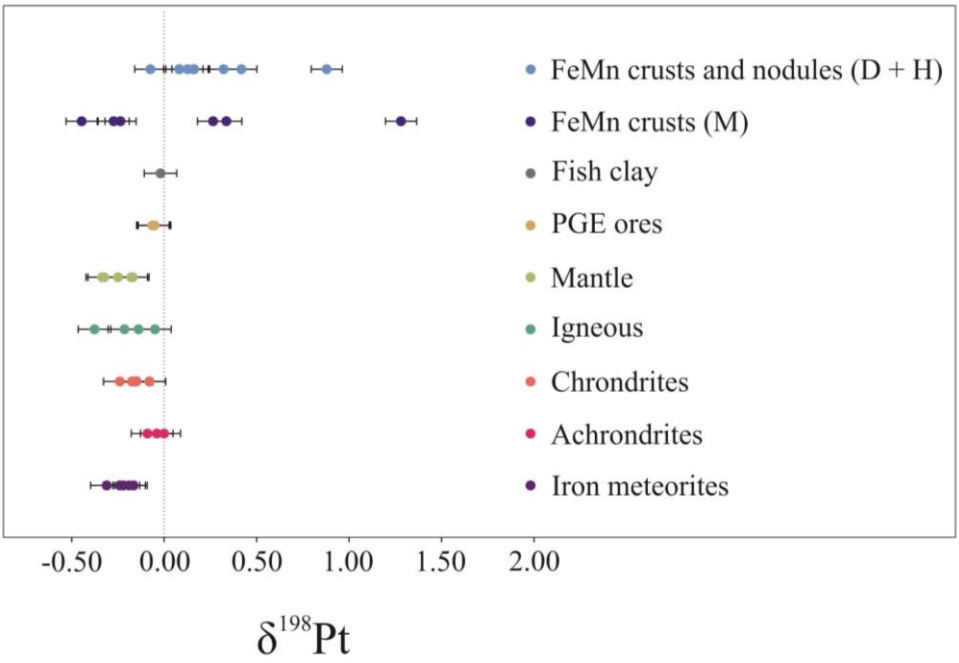

Figure 5.14 δ^{198}Pt of all extra-terrestrial and terrestrial samples measured by Creech et al., 2014 and terrestrial marine samples measured in this study. The vertical line represents the IRMM-010 composition. All errors for the mean 2sd for the individual studies, 0.088 ‰ for Creech et al., 2014 and 0.089 ‰ for this study.

The platinum isotopic compositions of the mixed Colville Ridge samples do not correlate with Pt concentration, however the diagenetic nodules show a direct relationship with the inverse Pt concentration, $R^2 = 0.99$, and the hydrogenetic crusts and nodules (n = 6) broadly follow the same trend but with significantly more scatter, $R^2 = 0.35$ (figure 5.15 (a)). Much of this scatter is defined by the Pacific Ocean D11-1 crust however, which is ~ 0.5 ‰ heavier than any of the other hydrogenetic crusts or nodules measured in this study. Excluding D11-1 the correlation between the inverse concentration and δ^{198}Pt improves to $R^2 = 0.71$. Interestingly, the heterogeneity in measurements of Nod-A-1, interpreted as representing mixing of two components within the bulk sample, also exhibits higher Pt concentrations associated with heavier isotopic compositions and lower Pt concentrations with lighter isotopic compositions, albeit with a much steeper slope in δ^{198}Pt vs 1/Pt space. If seawater Pt concentrations are fairly constant, as suggested by some of the seawater measurements and the estimated long residence times, then lower concentrations of adsorbed Pt imply a smaller proportion of Pt adsorbed and higher concentrations reflecting more efficient adsorption. Larger isotopic fractionation may occur initially at small proportions of adsorption. As the solid favours the lighter isotopes (chapter 3) this would lead to lighter Pt coupled with lower Pt concentrations. This would drive the dissolved Pt fraction to a heavier composition (at least locally), and as more of the aqueous Pt is adsorbed the composition adsorbed shifts toward heavier isotopes. Alternatively, isotopic fractionation dependent on differing aqueous species has been suggested for other trace metals, e.g. Tl and Fe (Anbar et al., 2000, Rehkämper et al., 2004). In chapter 3, the two dominant platinum species were evaluated ($PtCl_4^{2-}$ and $Pt(OH)_{2(aq)}$) with both showing similar fractionation (within uncertainties). However, other species that may potentially occur, such as organic bound platinum, have not been examined, and speciation effects therefore cannot be discounted.

Possible explanations for the large offset in the δ^{198}Pt of D11-1 include either hydrothermal or cosmic input to this sample. Other stable isotope systems reported for this crust sample, such as Ni, Hf, Nd, and Tl, do not display any notable offset, nor do major element or REE data support a hydrothermal contribution (e.g. figure 5.2), therefore, hydrothermal activity is unlikely to cause the offset (David et al., 2001. Gall

et al., 2013, Rehkämper et al., 2004). A cosmic component may affect Pt but not be observable in these other stable isotope systems. A cosmic Pt component would be expected to shift δ^{198}Pt to lighter values, rather than the observed heavier composition, as all extra-terrestrial material measured to date has δ^{198}Pt compositions lighter than the ferromanganese deposits, ~ -0.3 – 0.0 ‰ (figure 5.14; Creech et al., 2014). This sample is also one of the shallowest at 1780 mbsl, with previous studies suggesting that shallower crusts have a higher proportion of metals incorporated (e.g. 5.11; Halbach et al., 1989), however whilst this sample does have a higher Pt concentration than the other Pacific crust (190 ng/g vs 120 ng/g), this is not particularly high for the suite overall. It remains unclear why D11-1 has this heavy Pt composition.

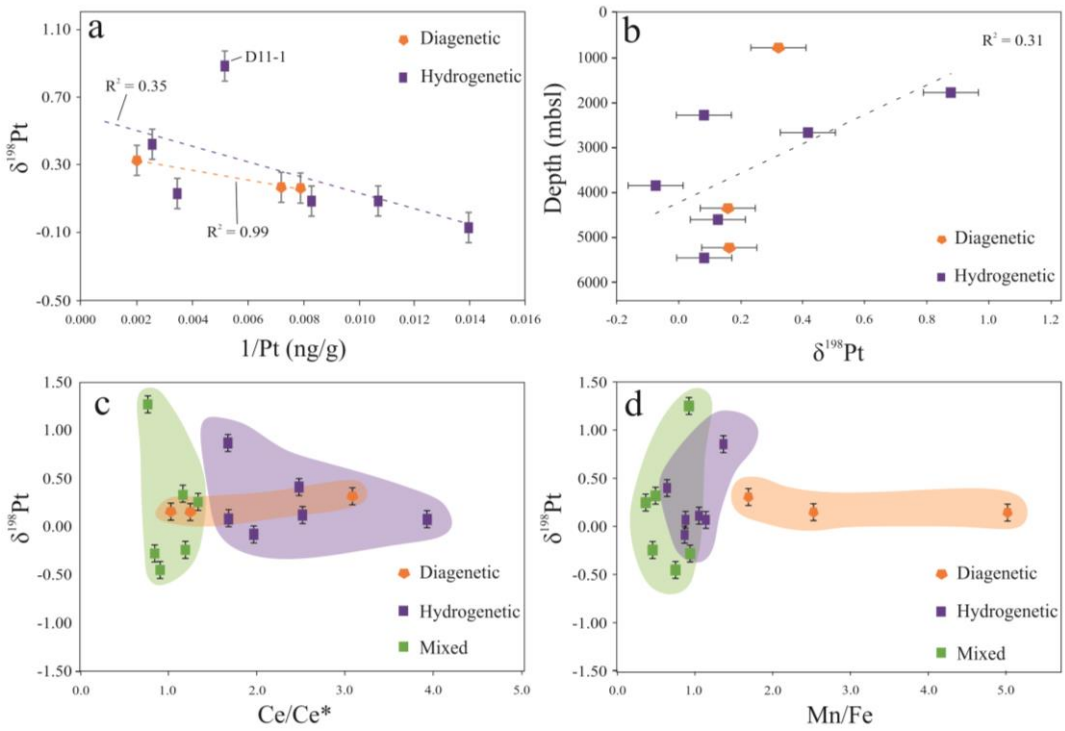

Figure 5.15 (a) δ^{198}Pt plotted against the inverse platinum concentration (ng/g) of all FMC and FMC, labelled according to sediment type. The orange dashed line is the best fit line for the diagenetic samples, which has a R^2 value of 0.99. The purple dashed line represents the best fit line for all the hydrogenetic samples with an R^2 value of 0.35. **(b)** δ^{198}Pt of diagenetic and hydrogenetic samples versus depth of sample All errors are given as the 2sd of GSJ JMn-1, 0.089‰. **(c)** δ^{198}Pt versus the cerium anomaly. **(d)** δ^{198}Pt versus the Mn/Fe ratio.

The bulk composition of the samples (e.g. Mn/Fe ratio) also does not appear to have a direct effect on the associated δ^{198}Pt fractionation as no correlation is identified between the Mn/Fe ratio and the platinum isotopic composition (figure 5.15 (d)).

The mixed hydrothermal and hydrogenetic samples show the greatest range in Pt isotopic composition. The samples with (muted) positive Ce anomalies have δ^{198}Pt values similar to the hydrogenetic crusts. However, the most extreme isotopic compositions, both light and heavy, are exhibited by the samples with the negative to no Ce anomaly (figure 5.16), which have been suggested to reflect greater influence of hydrothermal Pt sources. This large range of δ^{198}Pt in the Colville crusts may be due to different platinum species with variable platinum isotope composition. In particular, platinum sulphide and bisulphide, which may be of more importance than chloride or hydroxyl species close to hydrothermal vent systems (Gammon et al., 1992, Mountain and Wood, 1988). Additionally, both heavy and light isotopic fractionations have been observed in other metal stable isotope systems in hydrothermal systems, for example depending on kinetic versus equilibrium processes (e.g. Butler et al., 2005). The data here suggest that large and varied Pt isotopic fractionations may be induced via hydrothermal systems.

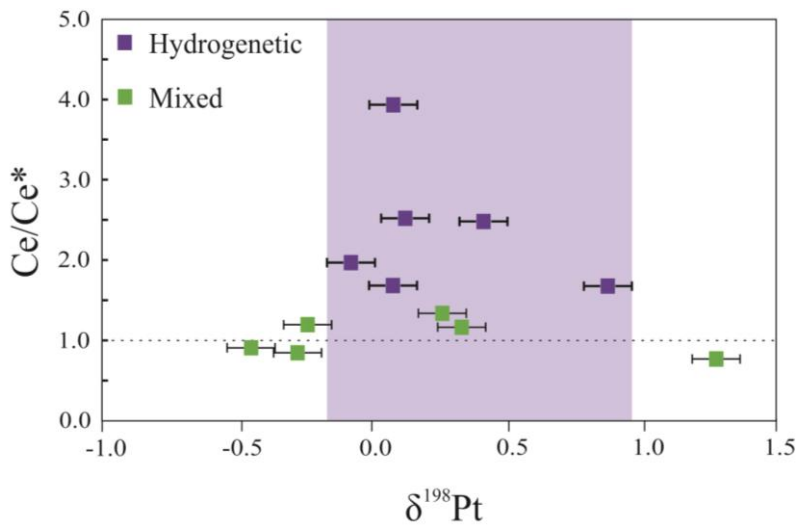

Figure 5.16 Ce anomaly and δ^{198}Pt for the Colville crust samples and the hydrogenetic samples. The purple shaded area represents the measured δ^{198}Pt of the hydrogenetic samples.

5.5.3 Implications for the marine Pt cycle

The marine platinum cycle involves an interplay between sources (dominantly riverine, but also hydrothermal and cosmic) and sinks (primarily ferromanganese deposits) controlling the Pt concentration, residence time and isotopic composition of seawater. A first order estimate of the platinum isotopic composition of seawater can be made using the δ^{198}Pt composition of the primary sink (as represented by ferromanganese samples examined in this study) and the fractionation factors (α^{198}Pt) for Pt adsorption determined experimentally in chapter 3. Platinum preferentially adsorbs onto δ-MnO_2 at the natural pH of the ocean (pH ~ 7.8 at depth), which is most closely approximated by the experiments conducted on δ-MnO_2 at pH = 8. By treating the seawater as the solution and the natural FMC and FMN samples analysed as the solid in the α^{198}Pt calculation (equation 5.1), the equation can be rearranged to solve for seawater (equation 5.2).

$$\alpha^{198}\text{Pt} = [1 + \delta^{198}\text{Pt}_{(\text{seawater})}/1000] / [1+ \delta^{198}\text{Pt}_{(\text{FMC,FMN})}/1000] \qquad (5.1)$$

$$\delta^{198}\text{Pt}_{(\text{seawater})} = [\alpha^{198}\text{Pt} * (\delta^{198}\text{Pt}_{(\text{FMC,FMN})}/1000)] - 1 \qquad (5.2)$$

Based on the δ^{198}Pt of the hydrogenetic and diagenetic samples the platinum isotopic composition of seawater is predicted to have a range of $\delta^{198}\text{Pt}_{(\text{seawater})}$ = 0.50 – 1.45 ‰ and 0.65 – 1.25 ‰, respectively (appendix d). A δ^{198}Pt range can also be calculated from the mixed hydrogenetic-hydrothermal Colville Ridge samples ($\delta^{198}\text{Pt}_{(\text{seawater})}$ = 0.12 to 1.85 ‰), representing a combination of global seawater and an unknown proportion from a localised hydrothermal source. This slightly extends the range calculated for the purely hydrogenetic crusts and nodules to both heavier and lighter compositions, reflecting the apparent complex nature of hydrothermally sourced Pt.

A first order estimate of the δ^{198}Pt of riverine input into the oceans was calculated based on leaching experiments, with a δ^{198}Pt range of 0.959 – 5.44 ‰ (chapter 4), which is heavier than silicate (crustal) samples and overlaps but extends to much heavier compositions than the estimates for seawater. This result is broadly similar to

that observed for some other transition metal isotope systems, such as Ni and Cu, where direct measurements of riverine waters have documented heavier isotopic compositions compared with silicate rocks (Cameron and Vance, 2014; Vance et al., 2008).

The cosmic input into the marine environment is estimated to be < 1 % of the annual platinum budget (chapter 1). The Pt isotopic composition of this component can be estimated from measurements of extra-terrestrial materials; δ^{198}Pt = -0.3 – 0.0 ‰ for iron, chondrite and achondrite meteorites (figure 5.17; Creech et al., 2014) and is lighter than both the riverine input and the estimated bulk seawater composition.

Hydrothermal inputs have the potential to introduce both heavy and light Pt to seawater, based on the wide range of isotopic compositions observed in the mixed hydrothermal – hydrogenetic Colville Ridge samples, although this will also be a minor and localised source (maximum 1.6 %, chapter 1).

The estimated ranges of δ^{198}Pt for the various sources, sinks, and seawater composition are summarised in figure 5.17. Rivers, the primary source to the marine environment, are isotopically heavy relative to crustal rocks and to the primary sink, ferromanganese deposits. Iron hydroxyoxides and δ-MnO_2 preferentially adsorb lighter isotopes (Chapter 3) and are isotopically lighter than seawater, so that scavenging of Pt onto ferromanganese deposits will result in heavier Pt remaining in the seawater. Given the dominance of the riverine source for Pt, this would suggest there is a missing light Pt source, or additional sink(s) of heavier Pt. However, the leaching experiments are an oversimplification of the riverine source, both with respect to the very limited range in materials leached and the dynamic weathering and riverine environment. For example, they do not take into account fractionation that may occur in river or estuarine environments, with interaction between particulates and dissolved Pt. The composition of the riverine input suggested here is considered to be only broadly indicative of Pt that is heavier than silicate rocks.

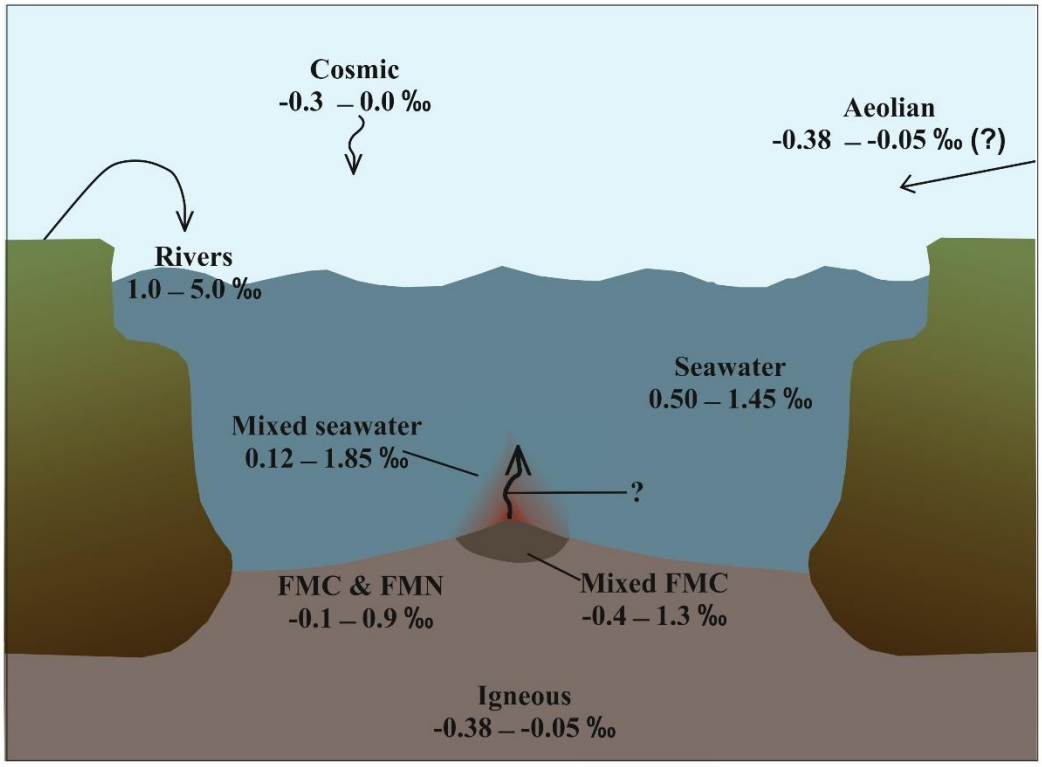

Figure 5.17 Range of δ^{198}Pt based on experimental and natural ferromanganese nodule and crusts measured in this study. The seawater δ^{198}Pt was calculated using the fractionation factor of δ-MnO_2 at pH = 8 determined in chapter 3 and the δ^{198}Pt of the natural ferromanganese nodule and crusts. The river input range is derived from the leaching experiments from chapter 4. The cosmic input and igneous δ^{198}Pt are based extra-terrestrial and igneous samples by Creech et al., 2014. The composition of the aeolian flux has been estimated as the δ^{198}Pt of the igneous samples. The composition of hydrothermal fluid is not known and is represented on the schematic with a question mark.

The δ^{198}Pt values presented in this discussion provide first order constraints on the platinum isotopic cycle in the marine environment, but clearly each of the pathways and reservoirs require further characterisation, in particular, the riverine and hydrothermal sources, which by analogy to other transition metal isotope systems are likely to involve complex fractionation processes, and additional sinks such as massive sulphide deposits.

5.6 Summary

A globally distributed suite of natural ferromanganese crust and nodules were analysed to constrain the spatial distribution of both platinum concentration and isotopic composition in the modern oxic marine environment. The ferromanganese crusts and nodules on average show heavier δ^{198}Pt compared to all other natural materials that have been measured to date; up to ~ 0.8 ‰ heavier than IRMM-010 and up to ~ 1.0 ‰ heavier than terrestrial mantle and extra-terrestrial samples.

The Atlantic Ocean diagenetic and hydrothermal crusts and nodules show both the highest platinum concentrations and the heaviest δ^{198}Pt compositions, with the exception of one sample from the Pacific Ocean (figure 5.8). The Southern, Pacific and Indian Ocean have similar δ^{198}Pt compositions whereas platinum concentration decreases, on average, from the Southern to the Pacific to the Indian Ocean (figure 5.9). Mixed hydrothermal and hydrogenetic crusts record a larger range of δ^{198}Pt relative to the diagenetic and hydrogenetic samples, which is interpreted as reflecting the mix of the platinum source material.

First order estimates of the Pt isotopic composition of sources, sinks and seawater have been compiled from the experimental and natural samples analysed throughout this study, resulting in an indicative composition of δ^{198}Pt = 1.0 – 5.0 ‰ for the river input, -0.3 – 0.0 ‰ for cosmic input, and a calculated seawater composition of ~ 0.5 – 1.5 ‰, with a range of δ^{198}Pt from -0.4 to 1.3 ‰ for ferromanganese deposits (diagenetic, hydrogenetic, and mixed hydrothermal and hydrogenetic).

Chapter 6

Conclusions and future directions

Preface

This chapter summarises the key findings of this study with particular attention paid to how these results address the research questions set forth in chapter 1. Some promising areas of future research are also suggested.

6.1 Summary and Conclusions

The primary aim of this study was to enhance our understanding of platinum in the marine environment by evaluating some key aspects of the platinum marine cycle, such as the adsorption mechanism and the associated platinum isotopic fractionation associated with incorporation onto ferromanganese crust and nodules, and to evaluate the platinum stable isotopic system as a potential tracer of changing marine chemistry.

To date, there have been limited studies evaluating the concentration of platinum in the surficial and marine environment (Cobel-Garcia et al., 2013, Colodner et al., 1993, Hein et al., 1988, Hein et al., 2005, Halbach et al., 1984, Hodge et al., 1985, Koschinsky et al., 2005, Soyol-Erdene and Huh, 2012). The only study to have examined the platinum isotopic composition of natural terrestrial samples focussed on analytical methodology and reported Pt isotopic compositions for a range of silicate and metallic materials (Creech et al., 2014). As this is the first study to examine the platinum isotopic composition of ferromanganese crusts and nodules, a series of tests were undertaken on the methodology established by Creech et al. (2013; 2014) to test its applicability to the different sample matrix of FeMn hydroxyoxides (chapter 2).

The method for analysis of ferromanganese sediments for platinum isotopic composition and concentration has been established, with an external reproducibility of ± 0.089 ‰. This external reproducibility is based on replicate analyses of two ferromanganese nodule standard reference materials, USGS Nod-P-1 and GSJ JMn-1, and is comparable to the external reproducibility previously reported for silicate SRMs (± 0.088 ‰, Creech et al., 2014). The very real issue of nugget effects for Pt reproducibility are highlighted by replicate analyses of the SRM USGS Nod-A-1. This effect has been well documented for Pt concentration, and the data here shows it can also affect Pt isotopic measurements, suggesting that external reproducibility of natural samples may be ultimately limited by sample heterogeneity rather than analytical limitations. As analytical precision improves, sample homogenisation will become increasingly important.

Following the calibration of the method, a series of experiments and analyses were undertaken to address the research questions posed in chapter 1.

6.1.1 How is platinum incorporated into the sediment record, and what effect has the incorporation mechanism on the platinum stable isotope composition?

Experiments on synthesized Mn oxide and Fe oxyhydroxides were undertaken to examine the adsorption mechanism of platinum on ferromanganese deposits (chapter 3). This represents one of the first studies to examine the adsorption of platinum onto the surface of Fe-Mn (oxyhydr)oxides using X-ray absorption spectroscopy (Maeno et al., 2015) and the first to quantify the associated isotopic fractionation.

Platinum is dominantly present in seawater as Pt^{2+} complexes with $[Cl]^-$ and $[OH]^-$ ($PtCl_4^{2-}$ and $Pt(OH)_{2(aq)}$, chapter 3). The oxidation state of the platinum adsorbed onto the surface of both Mn oxide and Fe oxhydroxide is Pt^{4+} and at a pH equivalent to that of the marine environment (pH ≈ 8), platinum is preferentially adsorbed onto the Mn oxide surface over the Fe oxyhydroxide by a factor of > 19. Experimental results over a range of pH suggest that the chloride bound platinum ($PtCl_4^{2-}$) is more strongly held than the platinum in $Pt(OH)_{2(aq)}$ as the proportion of platinum adsorbed increases at pH > 6, with $Pt(OH)_{2(aq)}$ becoming available in the marine environment at pH = 6.3. The platinum adsorbed onto the surface of the Fe oxyhydroxide shows both a 4- and 6-fold coordination depending on the pH at which the adsorption experiment was conducted, whereas a 6-fold coordination is associated with the MnO_2 phase, irrespective of pH.

Measureable platinum isotopic fractionation occurs during adsorption onto the surface of the minerals, with an $\alpha^{198}Pt_{lq\text{-}so} = 1.00058 \pm 0.00005$ determined experimentally for δ-MnO_2 at pH = 8. By analogy to the ocean, this adsorption experiment suggests that the platinum in seawater will be isotopically heavier than platinum in marine ferromanganese crusts and nodules.

Taken together, these results are consistent with the leading proposed mechanism for platinum adsorption in the literature i.e. the surface oxidation of Pt^{2+} to Pt^{4+} on the Mn oxide surface in crusts and nodules. This chemisorptive redox mechanism is also consistent with that suggested for Ce, which, like Pt, typically exhibits positive abundance anomalies in Fe-Mn sediments. Furthermore, in addition to a similar surface oxidation process proposed for Ce, the direction and scale of isotopic fractionation is also similar, $\alpha^{142}Ce_{lq\text{-}so}$ = 1.00041± 0.00008 reported for similar experiments on δ-MnO_2 (Nakada et al., 2013)

6.1.2 What variations are observed in platinum stable isotope chemistry in the modern oxic oceans?

A global suite of modern ferromanganese crusts and nodules were measured to investigate variations in platinum concentration and isotopic composition in the modern oxic marine environment. The most striking observation is that hydrogenetic and diagenetic crusts and nodules are isotopically heavier than any other natural materials measured to date; up to ca 0.8 ‰ heavier than mantle and extra-terrestrial samples (Creech et al., 2014).

The diagenetic and hydrogenetic crusts and nodules have platinum concentrations ranging from 70 to 490 ng/g, with a mean value of 210 ng/g, and $\delta^{198}Pt$ of -0.08 – 0.88 ‰, mean value of 0.24 ‰. With the limited dataset analysed, no systematic differences in the platinum isotopic composition of the ocean basins could be discerned, however, platinum concentration decreases on average from Atlantic > Southern, Pacific > Indian Oceans.

Mixed hydrothermal - hydrogenetic crusts from the western Pacific show a similar platinum concentration range to Pacific hydrogenetic and diagenetic samples, 90 – 260 ng/g and a mean value of 164 ng/g, but with a larger range of $\delta^{198}Pt$, -0.45 – 1.29 ‰, with a mean value of 0.15 ‰, than the hydrogenetic and diagenetic samples from all the oceans investigated. The lighter $\delta^{198}Pt$ composition is similar to that of the mantle derived materials reported by Creech et al. (2014), which would be consistent with

mantle-like isotopically light hydrothermal sources to the marine environment. However, the heavier δ^{198}Pt compositions suggest hydrothermal processes may also induce Pt isotopic fractionation, perhaps through precipitation of light-Pt bearing phases at or near the vent – seawater interface. As observed with other transition metal stable isotope systems, e.g. Fe, Pt isotopic fractionation processes in hydrothermal systems are likely to be complex.

Overall, the primary controls on platinum concentration in the natural ferromanganese sediments could not be constrained, however, platinum concentration does appear to influence δ^{198}Pt composition, with the higher concentrations generally associated with heavier isotopic signatures.

6.1.3 Do platinum stable isotopes have potential as a marine geochemical tracer?

To evaluate the potential of Pt stable isotopes to trace marine processes, a first order evaluation of the marine cycle of platinum was undertaken. In addition to determining the isotopic composition of adsorption and natural ferromanganese samples, leaching experiments on silicate rocks were undertaken as a simplified analogy for the platinum delivered by rivers to the marine environment from oxidative weathering of terrestrial sources. These experiments show that the isotopic composition of the leachate is heavier than the bulk silicate, likely due to the preferential leaching of sulphide bound platinum. This is similar to the fractionation observed for some other transition metal isotope systems, e.g. Cu, Ni, where riverine metals are isotopically heavier than crustal silicate rocks (Cameron and Vance, 2014).

By combining the results from this study and measurements on silicate and meteorite samples from Creech et al. (2014), a schematic representation of the marine Pt stable isotopic cycle and a prediction of the platinum isotopic composition of seawater are proposed (figure 6.1). The main features of the marine Pt stable isotopic system are a predicted heavy Pt isotopic composition for seawater, 0.5 – 1.5 ‰, reflecting the interplay between sources and sinks:

Sources – Riverine input (~ 97 %) is heavy, relative to silicate crust, with lesser (~ 1.6 %) complex contributions from hydrothermal sources, and minor (<1%) light Pt contributions from aeolian and cosmic sources comparable to silicate crustal compositions.

Sinks – Ferromanganese sediments incorporate light Pt stable isotopes relative to seawater, but overall, are heavier than mantle and igneous rocks.

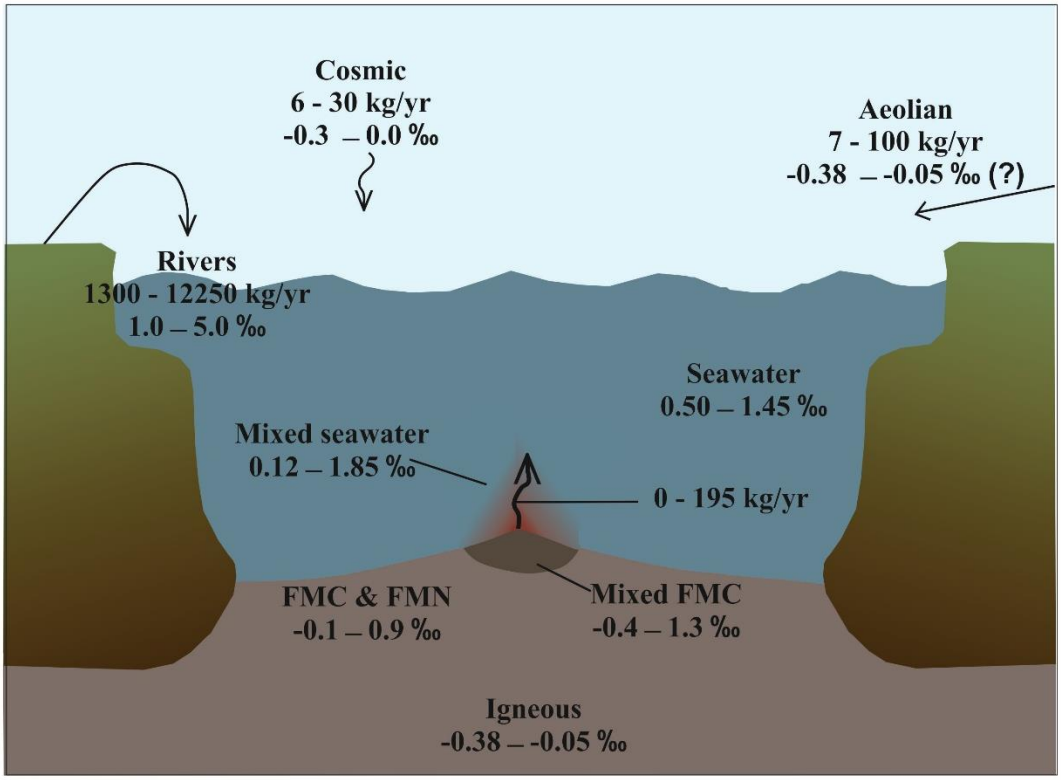

.

Figure 6.1 Range of δ^{198}Pt based on experimental and natural ferromanganese nodule and crusts measured in this study. Details described in chapter 5. The range in Pt source is described in chapter 1.

This study represents a first examination of the main components in the marine cycle, and has documented Pt isotopic fractionation during Pt adsorption to FMS involving surface oxidation together with measureable isotopic differences among the different components of the marine system. Together, this suggests that the Pt stable isotope

system does indeed show promise as a new tool to add to the growing arsenal of non-traditional stable isotope systems to unravel low-temperature marine processes and changes in marine chemistry through time.

6.2 Future Directions

As the first study to evaluate the platinum isotopic composition of the primary source and sinks of platinum to the marine environment, there are many areas that require more detailed investigation. Similar to other isotope systems that have been investigated over the past decade, for example, Mo, Ni, Cu, and Fe (Anbar, 2004, Beard et al., 2003, Gall et al., 2013, Goldberg et al., 2009, Little et al., 2014, Severmann et al., 2008). A number of studies could be conducted on the sources and sinks of platinum to better constrain the behaviour of Pt in the oxic marine environment.

A basic uncertainty in the Pt concentration profiles of the oceans remains, and Pt concentration profiles targeting dissolved Pt remains an important first order parameter to be constrained. Direct measurements of seawater from various locations around the globe including depth profiles, would confirm the type of profile platinum has in the water column. The residence time of Pt. Platinum stable isotopic measurements on seawater would be ideal, including at a range of depths to investigate potential effects of variations in pH. However, to determine the isotopic values of Pt significant volumes of seawater (> 1000 L) would likely be needed for analysis with current analytical limitations, requiring method development to handle the large sample sizes.

Direct measurement of the potential sources of platinum to the marine environment, such as, river samples, aeolian, groundwater, and hydrothermal flux and deposits, would need to be conducted to better characterise the concentration and isotopic compositions of these components. Analysis of a river samples from both upriver and estuary locations would aid in better defining the riverine Pt isotopic composition, as well as any isotopic fractionation due to estuarine processes. In addition to

concentration and isotopic composition it would also be beneficial to constrain the proportion of soluble platinum released to the ocean by these various source fluxes. At present, a direct measurement of Pt stable isotopes in riverine sources and seawater is not possible, pre-concentration of larger samples are needed.

Coupled with measuring Pt in rivers draining catchments with varying lithologies, more in-depth experiments targeting leaching of different mineral phases would better evaluate the isotopic fractionation associated with weathering various platinum species. Hydrothermal systems are likely to involve complex fractionation processes and concentration and isotopic analysis of vent fluids and sulphides from active hydrothermal systems would begin to place better constraints on this source of Pt to the oceans as well as on Pt behaviour within hydrothermal sulphide deposits.

Further evaluation of potential platinum sinks in the marine environment, such as pelagic clays and hydrothermal deposits, as well as further characterising ferromanganese sediments is needed. In addition, sediments from a variety of redox conditions, such as suboxic and euxinic waters, could be evaluated to extend the system to the wider marine environments. In less oxygenated environments, Pt may be concentrated in authigenic pyrite, for example.

6.21 Temporal variations in platinum concentration and δ^{198}Pt

Ferromanganese crusts and nodules produce long-lived records of marine chemistry and can be used to evaluate temporal variations though geological time. This has been explored for other non-traditional isotope systems, such as Mo, Ni, Cu, and Fe (Anbar, 2004, Beard et al., 2003, Gall et al., 2013, Goldberg et al., 2009, Little et al., 2014, Severmann et al., 2008). Given the observation that riverine sources to the marine environment appear to be isotopically heavy, variations in the river discharge to the marine environment during glaciation events for example, may impart a measureable isotopic shift in Pt recorded in FeMn deposits. Further characterisation of the modern marine environment may also show if Pt isotopes are affected by changes in pH or oxygenation levels, as may be expected from the adsorption experiment results here.

References

Addy, S. K. (1978). Distribution of Fe, Mn, Cu, Ni and Co in coexisting manganese nodules and micronodules. *Marine Geology*, *28*(1-2), M9–M17.

Albarede, F., and Beard, B. (2004). Analytical Methods for Non-Traditional Isotopes. In *Reviews in Mineralogy and Geochemistry* (Vol. 55, pp. 113–152).

Albarede, F., Telouk, P., Blichert-Toft, J., Boyet, M., Agranier, A., and Nelson, B. (2004). Precise and accurate isotopic measurements using multiple-collector ICPMS. *Geochimica et Cosmochimica Acta*, *68*(12), 2725–2744.

Algeo, T. J., and Lyons, T. W. (2006). Mo-total organic carbon covariation in modern anoxic marine environments: Implications for analysis of paleoredox and paleohydrographic conditions. *Paleoceanography*, *21*(1).

Alt, F., Bambauer, A., Hoppstock, K., Mergler, B., and Tölg, G. (1993). Platinum traces in airborne particulate matter. Determination of whole content, particle size distribution and soluble platinum. *Fresenius' Journal of Analytical Chemistry*, *346*(6-9).

Anbar, A. D., and Rouxel, O. (2007). Metal Stable Isotopes in Paleoceanography. *Annual Review of Earth and Planetary Sciences*, *35*(1), 717–746.

Anders, E., and Grevesse, N. (1989). Abundances of the elements - Meteoritic and solar. *Geochimica et Cosmochimica Acta*, *53*, 197–214.

Anthony, E. Y., and Williams, P. A. (1994). Thiosulfate complexing od f platinum-group elements-implications for supergene geochemistry. *Environmental Geochemistry of Sulfide Oxidation*, *550*, 551–560.

Axelsson, M. D., Rodushkin, I., Ingri, J., and Ohlander, B. (2002). Multielemental analysis of Mn-Fe nodules by ICP-MS: optimisation of analytical method. *The Analyst*, *127*(1).

Azaroual, M., Romand, B., Freyssinet, P., and Disnar, J. R. (2001). Solubility of platinum in aqueous solutions at 25 °C and pHs 4 to 10 under oxidizing conditions. *Geochimica et Cosmochimica Acta*, *65*(24), 4453–4466.

Baker, J.A., and Krogh Jensen, K. (2004). Coupled 186Os-187Os enrichments in the Earth's mantle - core-mantle interaction or recycling of ferromanganese crusts and nodules? *Earth and Planetary Science Letters*, *220*(3-4), 277–286.

Balaram, V., Mathur, R., Banakar, V. K., Hein, J. R., Rao, C. R. M., Gnaneswara Rao, T., and Dasaram, B. (2006). Determination of the platinum - Group elements (PGE) and gold (Au) in manganese nodule reference samples by nickel sulfide fire-assay and Te coprecipitation with ICP-MS. *Indian Journal of Marine Sciences*, *35*(1), 7–16.

Balcerzak, M. (2002). Sample digestion methods for the determination of traces of precious metals by spectrometric techniques. *Analytical Sciences : The International Journal of the Japan Society for Analytical Chemistry*, *18*(7).

Banakar, V. K., Hein, J. R., Rajani, R. P., and Chodankar, A. R. (2007). Platinum group elements and gold in ferromanganese crusts from Afanasiy-Nikitin seamount, equatorial Indian Ocean: Sources and fractionation. *Journal of Earth System Science*, *116*(1), 3–13.

Banerjee, R., and Iyer, S.D. (1991). Biogenic influence on the growth of ferromanganese micronodules in the Central Indian Basin. *Marine Geology*, *97*(3-4), 413–421.

Barbante, C., Veysseyre, A., Ferrari, C., Van De Velde, K., Morel, C., Capodaglio, G., and Boutron, C. (2001). Greenland snow evidence of large scale atmospheric contamination for platinum, palladium, and rhodium. *Environmental Science and Technology*, *35*(5), 835–839.

Barkov, A. N. Y. (2002). Platinum-group minerals from the Wellgreen Ni - Cu - PGE deposit, Yukon, Canada. *The Canadian Mineralogist*, *40*, 651–669.

Barling, J., and Anbar, A. D. (2004). Molybdenum isotope fractionation during adsorption by manganese oxides. *Earth and Planetary Science Letters*, *217*(3-4), 315–329.

Barling, J., Arnold, G. L., and Anbar, A. D. (2001). Natural mass-dependent variations in the isotopic composition of molybdenum. *Earth and Planetary Science Letters*, *193*(3-4), 447–457.

Barnes, S. J., and Maier, W. D. (2002). Platinum-Group Element Distributions in the Rustenburg Layered Suite of the Bushveld Complex , South Africa. *In: The Geology Geochemistry Mineralogy and Mineral Beneficiation of the Platinum-Group Elements. Canad Inst Min Metall Petro CIM Sp*, *54*(Special Volume), 431–458.

Barrett, T. J., Taylor, P. N., and Lugowski, J. (1987). Metalliferous sediments from DSDP Leg 92: The East Pacific Rise transect. *Geochimica et Cosmochimica Acta*, *51*, 2241–2253.

Bau, M., Schmidt, K., Koschinsky, A., Hein, J., Kuhn, T., and Usui, A. (2014). Discriminating between different genetic types of marine ferro-manganese crusts and nodules based on rare earth elements and yttrium. *Chemical Geology*, *381*, 1–9.

Bayon, G., German, C. R., Boella, R. M., Milton, J. A., Taylor, R. N., and Nesbitt, R. W. (2002). An improved method for extracting marine sediment fractions and its application to Sr and Nd isotopic analysis. *Chemical Geology*, *187*, 179–199.

Beard, B. L., Johnson, C. M., Von Damm, K. L., and Poulson, R. L. (2003). Iron isotope constraints on Fe cycling and mass balance in oxygenated Earth oceans. *Geology*, *31*(7), 629–632.

Becker, H., Horan, M. F., Walker, R. J., Gao, S., Lorand, J. P., and Rudnick, R. L. (2006). Highly siderophile element composition of the Earth's primitive upper mantle: Constraints from new data on peridotite massifs and xenoliths. *Geochimica et Cosmochimica Acta*, *70*(17), 4528–4550.

Bennet, S.A., Achterberg, E.P., Connelly, D. P., and German, C. R. (2008). *Earth and Planetary Science Letters*, 270(3), 157–167.

Bermin, J., Vance, D., Archer, C., and Statham, P. J. (2006). The determination of the isotopic composition of Cu and Zn in seawater. *Chemical Geology*, *226*(3-4), 280–297.

Bigeleisen, J. (1965). Chemistry of isotopes. *Science*, 147:463–71

Bonatti, E., Kraemer, T., and Rydell, H. (1972): Classification and genesis of submarine iron-manganese deposits. In *Papers from a Conference on Ferromanganese Deposits on the Ocean Floor: National Science Foundation/International Decade of Ocean Exploration Publication* (pp. 149–166).

Brenan, J. M. (2008). The platinum-group elements: "Admirably adapted" for science and industry. *Elements*, *4*(4), 227–232.

Brown, P. L., and Sylva, R. N. (1987). Unified theory of metal ion complex formation constants. OECD, NEA, Paris.

Brownlee, D. E., Bates, B. A., and Wheelock, M. M. (1984). Extraterrestrial platinum group nuggets in deep-sea sediments. *Nature*, *309*.

Bruland, K. W. (1980). Oceanographic distributions of cadmium, zinc, nickel, and copper in the North Pacific. *Earth and Planetary Science Letters*, *47*(2), 176–198.

Burns, R. G., and Mee Burns, V. (1975). Mechanism for nucleation and growth of manganese nodules. *Nature*, *255*, 130–131.

Butler, I. B., Archer, C., Vance, D., Oldroyd, A., and Rickard, D. (2005). Fe isotope fractionation on FeS formation in ambient aqueous solution. *Earth and Planetary Science Letters*, *236*(1-2), 430–442.

Cameron, V., and Vance, D. (2014). Heavy nickel isotope compositions in rivers and the oceans. *Geochimica et Cosmochimica Acta*, *128*, 195–211.

Cameron, V., Vance, D., Archer, C., and House, C. H. (2009). A biomarker based on the stable isotopes of nickel. *Proceedings of the National Academy of Sciences of the United States of America*, *106*(27),

Carroll, S. A, Roberts, S. K., Criscenti, L. J., and O'Day, P. A. (2008). Surface complexation model for strontium sorption to amorphous silica and goethite. *Geochemical Transactions*, *9*, 2.

Cave, R. R., Ravizza, G. E., German, C. R., Thomson, J., and Nesbitt, R. W. (2003). Deposition of osmium and other platinum-group elements beneath the ultramafic-hosted Rainbow hydrothermal plume. *Earth and Planetary Science Letters*, *210*(1-2), 65–79.

Chang, F. H., Zeldis, J., Gall, M., and Hall, J. (2003). Seasonal and spatial variation of phytoplankton assemblages, biomass and cell size from spring to summer across the north-eastern New Zealand continental shelf. *Journal of Plankton Research*, *25*(7), 737–758.

Chapman, J. B., Weiss, D. J., Shan, Y., and Lemburger, M. (2009). Iron isotope fractionation during leaching of granite and basalt by hydrochloric and oxalic acids. *Geochimica et Cosmochimica Acta*, *73*(5), 1312–1324.

Christensen, J. N. (1997). Climate and Ocean Dynamics and the Lead Isotopic Records in Pacific Ferromanganese Crusts. *Science*, *277*(5328), 913–918.

Chu, N. C., Johnson, C. M., Beard, B. L., German, C. R., Nesbitt, R. W., Frank, M., and Graham, I. (2006). Evidence for hydrothermal venting in Fe isotope compositions of the deep Pacific Ocean through time. *Earth and Planetary Science Letters*, *245*(1-2), 202–217.

Cobelo-García, A., López-Sánchez, D. E., Almécija, C., and Santos-Echeandía, J. (2013). Behavior of platinum during estuarine mixing (Pontevedra Ria, NW Iberian Peninsula). *Marine Chemistry*, *150*, 11–18.

Cobelo-García, A., López-Sánchez, D. E., Schäfer, J., Petit, J. C. J., Blanc, G., and Turner, A. (2014). Behavior and fluxes of Pt in the macrotidal Gironde Estuary (SW France). *Marine Chemistry*, *167*, 93–101.

Cobelo-Garcia, A., Turner, A., and Millward, G. E. (2008). Fractionation and reactivity of platinum group elements during estuarine mixing. *Environmental Science and Technology*, *42*(4).

Colodner, D. (1991). The Marine Geochemistry of Rhenium, Iridium and Platinum. *PhD thesis*, Massachusetts Institute of Technology.

Colodner, D. C., Boyle, E. A, and Edmond, J. M. (1993). Determination of rhenium and platinum in natural waters and sediments, and iridium in sediments by flow injection isotope dilution inductively coupled plasma mass spectrometry. *Analytical Chemistry*, *65*(10).

Colombo, C., Oates, C. J., Monhemius, A. J., and Plant, J. A. (2008). Complexation of platinum, palladium and rhodium with inorganic ligands in the environment. *Geochemistry: Exploration, Environment, Analysis*, *8*(1), 91–101.

Cook, S. J., and Fletcher, W. K. (1992). Distribution and behaviour of platinum in soils of the Tulameen ultramafic complex, southern British Columbia. Province of British Columbia, Geological Survey Branch. pp 94.

Cornell, R. M., and Schwertmann, U. (2003). *The Iron Oxides: Structure, Properties, Reactions, Occurrences and Uses*. John Wiley and Sons.

Creech, J. B. (2014). Stable Isotopes of Platinum : Measurement and Application to Constraining the Formation and Differentiation of Earth. *PhD thesis*, Victoria University of Wellington, New Zealand.

Creech, J. B., Baker, J. A, Handler, M. R., and Bizzarro, M. (2014). Platinum stable isotope analysis of geological standard reference materials by double-spike MC-ICPMS. *Chemical Geology*, *363*, 293–300.

Creech, J. B., and Paul, B. (2015). IsoSpike: Improved Double-Spike Inversion Software. *Geostandards and Geoanalytical Research*, *39*, 7–15.

Creech, J., Baker, J., and Handler, M. (2013). Platinum stable isotope ratio measurements by double-spike multiple collector ICPMS. *Journal of Analytical Atomic Spectrometry*, *28*, 853–865.

Cronan, D. S. (1975). Manganese nodules and other ferromanganese oxide deposits from the Atlantic Ocean. *Journal of Geophysical Research*, *80*(27), 3831–3837. .

David, K., Frank, M., O'Nions, R. K., Belshaw, N. S., and Arden, J. W. (2001). The Hf isotope composition of global seawater and the evolution of Hf isotopes in the deep Pacific Ocean from Fe-Mn crusts. *Chemical Geology*, *178*(1-4), 23–42.

Davies, G., and Tredoux, M. (1985). The platinum-group element and gold contents of the marginal rocks and sills of the Bushveld complex. *Economic Geology*, *80*(4), 838–848.

de Ronde, C. E., Hannington, M., Stoffers, P., Wright, I. C., Ditchburn, R. G., Reyes, A. G., and Lebon, G. T. (2005). Evolution of a Submarine Magmatic-Hydrothermal System : Brothers Volcano, Southern Kermadec Arc, New Zealand. *Economic Geology*, *100*, 1097–1133.

de Ronde, C. E., Baker, E. T., Massoth, G. J., Lupton, J. E., Wright, I. C., Feely, R. A., and Greene, R. R. (2001). Intra-oceanic subduction-related hydrothermal venting, Kermadec volcanic arc, New Zealand. *Earth and Planetary Science Letters*, *193*(3-4), 359–369.

de Ronde, C. E., Baker, E. T., Massoth, G. J., Lupton, J. E., Wright, I. C., Sparks, R. J., and Lebon, G. T. (2007). Submarine hydrothermal activity along the mid-Kermadec Arc, New Zealand: Large-scale effects on venting. *Geochemistry, Geophysics, Geosystems*, *8*(7).

de Ronde, C. E. J., Massoth, G. J., Butterfield, D. A., Christenson, B. W., Ishibashi, J., Ditchburn, R. G., and Takai, K. (2011). Submarine hydrothermal activity and gold-rich mineralization at Brothers Volcano, Kermadec Arc, New Zealand. *Mineralium Deposita*, *46*(5), 541–584.

Ditchburn, R. G., and Graham, I. J. (2003). Preparation Procedures for the ^{10}Be Analysis of Marine Deposits. *Institute of Geological and Nuclear Sciecnes: Science report*, *10*, 1-15.

Ditchburn, R. G., and Graham, I. J., (2006b). Re-dating of mego nodule U1365B-M along new sampling transect using 10Be/9Be dating methods. *Institute of Geological and Nuclean Sciences: Miscellaneous - Unpublished data, Issue Excel Workbook.*

Eckstrand, O. R., and Hulbert, L. J. (2007). Magmatic Nickel-Copper-Platinum Group Element Deposits. *Goodfellow, W.D., Ed., Mineral Deposits of Canada: A Synthesis of Major Deposit Types, District Metallogeny, the Evolution of Geological Provinces, and Exploration Methods: Geological Association of Canada,* (5), 205–222.

Economou-Eliopoulos, M. (2010). Platinum-group elements(PGE)in various geotectonic settings: Opportunities and risks. *Hellenic Journal of Geosciences, Vol. 45, 45,* 65–82.

Ek, K. H., Morrison, G. M., and Rauch, S. (2004). Environmental routes for platinum group elements to biological materials--a review. *The Science of the Total Environment, 334-335,* 21–38.

Elagami, N. L., Ibrahim, E. H., and Odah, H. H. (2000). Sedimentary origin of the Mn-Fe ore of Um Bogma, Southwest Sinai: Geochemical and paleomagnetic evidence. *Economic Geology, 95*(3), 607–620.

Elding, L. I. (1978). Stabilities of platinum(II) chloro and bromo complexes and kinetics for anation of the tetraaquaplatinum(II) ion by halides and thiocyanate. *Inorganica Chimica Acta, 28,* 255-262.

Ellis, A. S., Johnson, T. M., and Bullen, T. D. (2002). Chromium isotopes and the fate of hexavalent chromium in the environment. *Science, 295,* 2060–2062.

Enzweiler, J., and Potts, P. J. (1995). The separation of platinum, palladium and gold from silicate rocks by the anion exchange separation of chloro complexes after a sodium peroxide fusion: an investigation of low recoveries. *Talanta, 42*(10), 1411–1418.

Enzweiler, J., Potts, P. J., and Jarvis, K. E. (1995). Determination of platinum, palladium, ruthenium and iridium in geological samples by isotope dilution inductively coupled plasma mass spectrometry using a sodium peroxide fusion and tellurium coprecipitation. *The Analyst*, *120*(5), 1391.

Esser, B. K., and Turekian, K. K. (1988). Accretion rate of extraterrestrial particles determined from osmium isotope systematics of Pacific Pelagic clay and manganese nodules. *Geochimica et Cosmochimica Acta*, *52*(6), 1383–1388.

Fernandez, A., and Borrok, D. M. (2009). Fractionation of Cu, Fe, and Zn isotopes during the oxidative weathering of sulfide-rich rocks. *Chemical Geology*, *264*(1-4), 1-12).

Findlay, D. C. (1969). Origin of the Tulameen ultramafic-gabbro complex, southern British Columbia. *Canadian Journal of Earth Sciences*, *6*(3), 399–425.

Flanagan, F. J., and Gottfried, D. (1980). USGS rock standards; III, Manganese-nodule reference samples USGS-Nod-A-1 and USGS-Nod-P-1. *Professional Paper, USGS*.

Fletcher, W. K., Cook, S. J., Hall, G. E. M., Scagel, R. K., and Dunn, C. E. (1995). Enrichment of platinum and associated elements in organic seepage soils of the Tulameen ultramafic complex, southern British Columbia. *Journal of Geochemical Exploration*, *54*(95).

Foster, G. L., and Vance, D. (2006). Negligible glacial-interglacial variation in continental chemical weathering rates. *Nature*, *444*(December), 918–921.

Frank, M. (2002). North Atlantic Deep Water export to the Southern Ocean over the past 14 Myr: Evidence from Nd and Pb isotopes in ferromanganese crusts. *Paleoceanography*, *17*(2).

Frank, M., O'Nions, R. K., Hein, J. R., and Banakar, V. K. (1999). 60 Myr records of major elements and Pb-Nd isotopes from hydrogenous ferromanganese crusts: Reconstruction of seawater paleochemistry. *Geochimica et Cosmochimica Acta*, *63*(11-12), 1689–1708.

Frank, M., Whiteley, N., van de Flierdt, T., Reynolds, B. C., and O'Nions, K. (2006). Nd and Pb isotope evolution of deep water masses in the eastern Indian Ocean during the past 33 Myr. *Chemical Geology*, *226*(3-4), 264–279.

Fuchs, W. A., and Rose, A. W. (1974). The geochemical behavior of platinum and palladium in the weathering cycle in the Stillwater Complex, Montana. *Economic Geology*, *69*(3), 332–346.

Fujii, T., Moynier, F., Dauphas, N., and Abe, M. (2011). Theoretical and experimental investigation of nickel isotopic fractionation in species relevant to modern and ancient oceans. *Geochimica et Cosmochimica Acta*, *75*(2), 469–482.

Gall, L., Williams, H. M., Siebert, C., Halliday, a. N., Herrington, R. J., and Hein, J. R. (2013). Nickel isotopic compositions of ferromanganese crusts and the constancy of deep ocean inputs and continental weathering effects over the Cenozoic. *Earth and Planetary Science Letters*, *375*, 148–155.

Gammons, C., Bloom, M., and Yu, Y. (1992). Experimental investigation of the hydrothermal geochemistry of platinum and palladium: I. Solubility of platinum and palladium sulfide minerals in NaCl/H2SO4 solutions at 300°C. *Geochimica et Cosmochimica Acta*, *56*(11), 3881–3894.

Ghode, R., Muley, R., and Sarin, R. (1995). Operationally determined chemical speciation of barium and chromium in drilling fluid wastes by sequential extraction. *Chemical Speciation and Bioavailability*, *7*(4), 133–137.

Glasby, G. P. (1997). Fractionation of manganese from iron in Archaean and Proterozoic sedimentary ores. *Geological Society, London, Special Publications*, *119*(1), 29–42.

Glasby, G. P. (2006). Manganese: Predominant role of nodules and crusts. *Marine Geochemistry*, (Ii), 371–427.

Glasby, G. P., and Schulz, H. D. (1999). New Types of E H , pH Diagrams to the Study of Specific Problems in Marine Geochemistry. *Aquatic Geochemistry*, *5*(1988), 227–248.

Godel, B., Barnes, S. J., and Maier, W. D. (2006). 3-D distribution of sulphide minerals in the Merensky Reef (Bushveld Complex, South Africa) and the J-M Reef (Stillwater Complex, USA) and their relationship to microstructures using x-ray computed tomography. *Journal of Petrology*, *47*(9), 1853–1872.

Goldberg, E. D., Hodge, V., Kay, P., Stallard, M., and Koide, M. (1986). Some comparative marine chemistries of platinum and iridium. *Applied Geochemistry*, *1*(2), 227–232.

Goldberg, E. D., and Koide, M. (1990). Understanding the marine chemistries of the platinum group metals. *Marine Chemistry*, *30*, 249–257.

Goldberg, T., Archer, C., Vance, D., and Poulton, S. W. (2009). Mo isotope fractionation during adsorption to Fe (oxyhydr)oxides. *Geochimica et Cosmochimica Acta*, *73*(21), 6502–6516.

Gros, M., Lorand, J. P., and Luguet, A. (2002). Analysis of platinum group elements and gold in geological materials using NiS fire assay and Te coprecipitation; the NiS dissolution step revisited. *Chemical Geology*, *185*(3-4), 179–190.

Halbach, P., Hebisch, U., and Scherhag, C. (1981). Geochemical variations of ferromanganese nodules and crusts from different provinces of the Pacific Ocean and their genetic control. *Chemical Geology*, *34*(1-2), 3–17.

Halbach, P., Kriete, C., Prause, B., and Puteanus, D. (1989). Mechanisms to explain the platinum concentration in ferromanganese seamount crusts. *Chemical Geology*, *76*(1-2), 95–106.

Halbach, P., Puteanus, D., and Manheim, F. T. (1984). Platinum concentrations in ferromanganese seamount crusts from the Central Pacific. *Naturwissenschaften*, *71*(11), 577–579.

Halbach, P., Scherhag, C., Hebisch, U., and Marchig, V. (1981). Geochemical and mineralogical control of different genetic types of deep-sea nodules from the Pacific Ocean. *Mineralium Deposita*, *16*(1), 59–84.

Hein, J. R. (2014). Co-Rich Manganese Crusts. In *Encyclopedia of Marine Geosciences*. Springer Science Business Media Dordrecht.

Hein, J. R. (2014). Manganese Nodules. In *Encyclopedia of Marine Geosciences*. Springer Science Business Media Dordrecht.

Hein, J. R., and Koschinsky, A. (2013). *Deep-Ocean Ferromanganese Crusts and Nodules*. *Treatise on Geochemistry: Second Edition* (2nd ed., Vol. 13).

Hein, J. R., Koschinsky, A., and Halliday, A. N. (2003). Global occurrence of tellurium-rich ferromanganese crusts and a model for the enrichment of tellurium. *Geochimica et Cosmochimica Acta*, *67*(6), 1117–1127.

Hein, J. R., Koschinsky, A., and Mcintyre, B. (2005). The Global Enrichment of Platinum Group Elements in Marine Ferromanganese Crusts. In; *Extended Abstractsand Proceedings 10th International Platinum Symposium, Oulu, Finland*, 98–101.

Hein, J. R., Mizell, K., Koschinsky, A., and Conrad, T. A. (2013). Deep-ocean mineral deposits as a source of critical metals for high- and green-technology applications: Comparison with land-based resources. *Ore Geology Reviews, 51,* 1-14.

Hein, J. R., Schwab, W. C., and Davis, A. (1988). Cobalt- and platinum-rich ferromanganese crusts and associated substrate rocks from the Marshall Islands. *Marine Geology*, *78*(3-4), 255–283.

Hein, J. R., Schwab, W. C., Foot, D. G., Masuda, Y., Usui, A., Davis, A. S., and Gein, L. M. (1986). *Farnella Cruise F7-86-HW, Cobalt-rich Ferromanganese Crust Data (D11-1). USGS*.

Hill, R. F., and Mayer, W. J. (1977). Radiometric Determination of Platinum and Palladium Attrition from Automotive Catalysts. *IEEE Transactions on Nuclear Science*, *24*(6), 2549–2554.

Hodge, V. F., Stallard, M., Koide, M., and Goldberg, E. D. (1985). Platinum and the platinum anomaly in the marine environment. *Earth and Planetary Science Letters*, *72*(2-3), 158–162.

Hodge, V. F., and Stallard, M. O. (1986). Platinum and palladium in roadside dust. *Environmental Science and Technology*, *20*(10), 1058–1060.

Hodge, V., Stallard, M., Koide, M., and Goldberg, E. D. (1986). Determination of platinum and iridium in marine waters, sediments, and organisms. *Analytical Chemistry*, *58*(3), 616–620.

Hoefs, J. (2008). *Stable Isotope Geochemistry*. Springer Science and Business Media.

Horner, T. J., Schönbächler, M., Rehkämper, M., Nielsen, S. G., Williams, H., Halliday, A. N., and Hein, J. R. (2010). Ferromanganese crusts as archives of deep water Cd isotope compositions. *Geochemistry, Geophysics, Geosystems*, *11*(4), 1–10.

Hyde, T. I., Ash, P. W., Boyd, D. A., Randlshofer, G., Rothenbacher, K., and Sankar, G. (2011). X-Ray absorption spectroscopic studies of platinum speciation in fresh and road aged light-duty diesel vehicle emission control catalysts. *Platinum Metals Review*, *55*(4), 233–245. Springer-Verlag Berlin Heidelberg.

Hyde, T., and Sankar, G. (2015). Solid State Platinum Speciation from X-ray Absorption Spectroscopic Studies of Fresh and Road Aged Three Way and Diesel Vehicle Emission Control Catalysts. In F. Zereini and C. L. S. Wiseman (Eds.), *Platinum Metals in the Environment SE - 19* (pp. 289–308).

Jacinto, G. S., and van den Berg, C. M. G. (1989). Different behaviour of platinum in the Indian and Pacific Oceans. *Nature*, *388* 332-334.

Jaiswal, A., Banerjee, S., Mani, R., and Chattopadhyaya, M. C. (2013). Synthesis, characterization and application of goethite mineral as an adsorbent. *Journal of Environmental Chemical Engineering*, *1*(3), 281–289.

James, R. H., Green, D. R. H., Stock, M. J., Alker, B. J., Banerjee, N. R., Cole, C., and Connelly, D. P. (2014). Composition of hydrothermal fluids and mineralogy of associated chimney material on the East Scotia Ridge back-arc spreading centre. *Geochimica et Cosmochimica Acta*, *139*, 47–71.

Jickells, T. D., An, Z. S., Andersen, K. K., Baker, A, R., Bergametti, G., Brooks, N., and Torres, R. (2005). Global iron connections between desert dust, ocean biogeochemistry, and climate. *Science (New York, N.Y.)*, *308*(5718), 67–71.

Jin, X., and Zhu, H. (2000). Determination of platinum group elements and gold in geological samples with ICP-MS using a sodium peroxide fusion and tellurium co-precipitation. *Journal of Analytical Atomic Spectrometry*, *15*(6), 747–751.

Jochum, K. P., Nohl, U., Herwig, K., Lammel, E., Stoll, B., and Hofmann, A. W. (2005). GeoReM: a new geochemical database for reference materials and isotopic standards. *Geostandards and Geoanalytical Research*, *29*(3), 333–338.

Johnson, C. M., Beard, B. L., and Albarede, F. (2004). Geochemistry of Non-Traditional Stable Isotopes. *Reviews in Mineralogy and Geochemistry*, *55*.

Johnson, C. M., Beard, B. L., and Albarede, F. (2004). Overview and General Concepts. *Reviews in Mineralogy and Geochemistry*, *55*(1), 1–24.

Kashiwabara, T., Oishi, Y., Sakaguchi, A., Sugiyama, T., Usui, A., and Takahashi, Y. (2014). Chemical processes for the extreme enrichment of tellurium into marine ferromanganese oxides. *Geochimica et Cosmochimica Acta*, *131*, 150–163.

Kashiwabara, T., Takahashi, Y., Marcus, M. a., Uruga, T., Tanida, H., Terada, Y., and Usui, A. (2013). Tungsten species in natural ferromanganese oxides related to its different behavior from molybdenum in oxic ocean. *Geochimica et Cosmochimica Acta*, *106*, 364–378.

Kenison Falkner, K., and Edmond, J. M. (1990). Gold in seawater. *Earth and Planetary Science Letters*, *98*(2), 208–221.

Kersten, M., and Förstner, U. (1987). Effect of sample pretreatment on the reliability of solid speciation data of heavy metals—implications sesfor the study of early diagenetic processes. *Marine Chemistry*, *22*(2), 299–312.

Kohfeld, K. E., and Harrison, S. P. (2001). DIRTMAP: The geological record of dust. *Earth-Science Reviews*, *54*(1-3), 81–114.

Koschinsky, A, and Audroing, J. (2005). The Enrichment of Platinum and the Fractionation of Pt from Pd in Marine Ferromanganese Crusts. *Extended Abstractsand Proceedings 10th International Platinum Symposium, Oulu, Finland*, 429–432.

Koschinsky, A., and Halbach, P. (1995). Sequential leaching of marine ferromanganese precipitates: Genetic implications. *Geochimica et Cosmochimica Acta*, *59*(24), 5113–5132.

Koschinsky, A., and Hein, J. R. (2003). Uptake of elements from seawater by ferromanganese crusts: Solid-phase associations and seawater speciation. *Marine Geology*, *198*(3-4), 331–351.

Koschinsky, A., Stascheit, A., Bau, M., and Halbach, P. (1997). Effects of phosphatization on the geochemical and mineralogical composition of marine ferromanganese crusts. *Geochimica et Cosmochimica Acta*, *61*(19), 4079–4094.

Kosmulski, M. (2002). The pH-Dependent Surface Charging and the Points of Zero Charge. *Journal of Colloid and Interface Science*, *253*, 77–87.

Kuhn, T., Bau, M., Blum, N., and Halbach, P. (1998). Origin of negative Ce anomalies in mixed hydrothermal- hydrogenetic Fe-Mn crusts from the Central Indian Ridge. *Earth and Planetary Science Letters*, *163*(1-4), 207–220.

Lambert, F., Delmonte, B., Petit, J. R., Bigler, M., Kaufmann, P. R., Hutterli, M. A, and Maggi, V. (2008). Dust-climate couplings over the past 800,000 years from the EPICA Dome C ice core. *Nature*, *452*(7187), 616–619.

Levasseur, S., Frank, M., Hein, J. R., and Halliday, A. N. (2004). The global variation in the iron isotope composition of marine hydrogenetic ferromanganese deposits: Implications for seawater chemistry? *Earth and Planetary Science Letters*, *224*(1-2), 91–105.

Li, Y. H. (1982). A brief discussion on the mean oceanic residence time of elements. *Geochimica et Cosmochimica Acta*, *46*(12), 2671–2675.

Ling, H. F., Burton, K. W., O'Nions, R. K., Kamber, B. S., von Blanckenburg, F., Gibb, a. J., and Hein, J. R. (1997). Evolution of Nd and Pb isotopes in Central Pacific seawater from ferromanganese crusts. *Earth and Planetary Science Letters*, *146*(1-2), 1–12.

Little, S. H., Sherman, D. M., Vance, D., and Hein, J. R. (2014). Molecular controls on Cu and Zn isotopic fractionation in Fe-Mn crusts. *Earth and Planetary Science Letters*, *396*, 213–222.

Little, S. H., Vance, D., Walker-Brown, C., and Landing, W. M. (2014). The oceanic mass balance of copper and zinc isotopes, investigated by analysis of their inputs, and outputs to ferromanganese oxide sediments. *Geochimica et Cosmochimica Acta*, *125*, 673–693.

Lyle, M. (1978). The formation and growth of ferromanganese oxides on the Nazca Plate. *PhD thesis*, Oregan State University.

Maeno, M. Y., Ohashi, H., Yonezu, K., Miyazaki, A., Okaue, Y., Watanabe, K., and Yokoyama, T. (2015). Sorption behavior of the Pt(II) complex anion on manganese dioxide (δ-MnO2): a model reaction to elucidate the mechanism by which Pt is concentrated into a marine ferromanganese crust. *Mineralium Deposita*, (Ii).

Maier, W. D. (2005). Platinum-group element (PGE) deposits and occurrences: Mineralization styles, genetic concepts, and exploration criteria. *Journal of African Earth Sciences*, *41*(3), 165–191.

Mäkelä, M., Pöykiö, R., Watkins, G., Hannu, N., and Dahl, O. (2011). Approach to Investigate the Mobility and Availability of Trace Elements (As, Ba, Cd, Co, Cr, Cu, Mo, Ni, Pb, Zn, and Hg) from a Solid Residue Matrix Designed for Soil Ammendment. *World Academy of Science, Engineering and Technology*, *55*(7), 502–507.

Marcantonio, F., Reisberg, L., Zindler, A., Wyman, D., and Hulbert, L. (1994). An isotopic study of the Ni-Cu-PGE-rich Wellgreen intrusion of the Wrangellia Terrane: Evidence for hydrothermal mobilization of rhenium and osmium. *Geochimica et Cosmochimica Acta*, *58*(2), 1007–1018.

Maréchal, C. N., Nicolas, E., Douchet, C., and Albarède, F. (2000). Abundance of zinc isotopes as a marine biogeochemical tracer. *Geochemistry Geophysics Geosystems*, *1*(5), 1. 10.1029/1999GC000029

Mathew, R. J., and Russell, A. E. (n.d.). XAS of carbon supported platinum fuel cell electrocatalysts: advances towards real time investigations. *Topics in Catalysis*, *10*(3), 231–239.

Mathur, R., Ruiz, J., Titley, S., Liermann, L., Buss, H., and Brantley, S. (2005). Cu isotopic fractionation in the supergene environment with and without bacteria. *Geochimica et Cosmochimica Acta*, *69*(22), 5233–5246.

McDonough, W. F. (2003). Compositional model for the Earth's core. *Treatise on Geochemistry*, *2*, 568.

McKibben, M. a., Williams, A. E., and Hall, G. E. M. (1990). Solubility and transport of platinum-group elements and Au in saline hydrothermal fluids: Constraints from geothermal brine data. *Economic Geology*, *85*(8), 1926–1934.

McLennan, S. M. (2001). Relationships between the trace element composition of sedimentary rocks and upper continental crust. *Geochemistry, Geophysics, Geosystems*, *2*.(4). 10.1029/2000GC000109.

McManus, J., Berelson, W. M., Severmann, S., Poulson, R. L., Hammond, D. E., Klinkhammer, G. P., and Holm, C. (2006). Molybdenum and uranium geochemistry in continental margin sediments: Paleoproxy potential. *Geochimica et Cosmochimica Acta*, *70*(18), 4643–4662.

Meisel, T., and Moser, J. (2004). Platinum-Group Element and Rhenium Concentrations in Low Abundance Reference Materials. *Geostandards and Geoanalytical Research*, *28*(2), 233–250.

Meisel, T., Moser, J., Fellner, N., Wegscheider, W., and Schoenberg, R. (2001). Simplified method for the determination of Ru, Pd, Re, Os, Ir and Pt in chromitites and other geological materials by isotope dilution ICP-MS and acid digestion. *The Analyst*, *126*(3), 322–328.

Michel, F. M., and Ehm, L. (2007). The Structure of Ferrihydrite, a Nanocrystalline Material. *Science*, *316*(June), 1726–1729.

Millet, M.-A., Baker, J. A., and Payne, C. E. (2012). Ultra-precise stable Fe isotope measurements by high resolution multiple-collector inductively coupled plasma mass spectrometry with a ^{57}Fe–^{58}Fe double spike. *Chemical Geology*, *304-305*, 18–25.

Mondal, S. (2011). Platinum Group Element (PGE) Geochemistry to understand the chemical evolution of the earth's mantle. *Journal of the Geological Society of India*, *77*(April), 295–302.

Morcelli, C. P. R., Figueiredo, A. M. G., Enzweiler, J., Sarkis, J. E. S., Jorge, A. P. S., and Kakazu, M. (2004). Determination of Platinum-Group Elements in Geological Reference Materials by High Resolution-ICP-MS after Nickel Sulfide Fire-Assay Collection and Te Co-Precipitation. *Geostandards and Geoanalytical Research*, *28*(2), 305–310.

Mountain, B. W., and Wood, S. a. (1988). Chemical controls on the solubility, transport, and deposition of platinum and palladium in hydrothermal solutions: a thermodynamic approach. *Economic Geology*, *83*(3), 492–510.

Mukai, H., Ambe, Y., and Morita, M. (1990). Flow injection inductively coupled plasma mass spectrometry for the determination of platinum in airborne particulate matter. *Journal of Analytical Atomic Spectrometry*, *5*(1), 75.

Nakada, R., Takahashi, Y., and Tanimizu, M. (2013). Isotopic and speciation study on cerium during its solid-water distribution with implication for Ce stable isotope as a paleo-redox proxy. *Geochimica et Cosmochimica Acta*, *103*, 49–62.

Nakada, R., Takahashi, Y., and Tanimizu, M. (2016). Cerium stable isotope ratios in ferromanganese deposits and their potential as a paleo-redox proxy. *Geochimica et Cosmochimica Acta*, *181*, 89–100.

Naldrett, A. J., and Cabri, L. J. (1976). Ultramafic and related mafic rocks; their classification and genesis with special reference to the concentration of nickel sulfides and platinum-group elements. *Economic Geology*, *71*(7), 1131–1158.

Naldrett, A. J., Cameron, G., Von Gruenewaldt, G., and Sharpe, M. R. (1987). The formation of stratiform PGE deposits in layered intrusions. In *Origins of igneous layering* (pp. 313–397). Springer Netherlands.

Newville, M. (2001). IFEFFIT: Interactive XAFS analysis and FEFF fitting. *Journal of Synchrotron Radiation*, *8*, 322–324.

O'Nions, R., Frank, M., von Blanckenburg, F., and Ling, H.-F. (1998). Secular variation of Nd and Pb isotopes in ferromanganese crusts from the Atlantic, Indian and Pacific Oceans. *Earth and Planetary Science Letters*, *155*(1-2), 15–28.

Obata, H., Yoshida, T., and Ogawa, H. (2006). Determination of picomolar levels of platinum in estuarine waters: A comparison of cathodic stripping voltammetry and isotope dilution-inductively coupled plasma mass spectrometry. *Analytica Chimica Acta*, *580*(1), 32–38.

Ohta, A., and Kawabe, I. (2001). REE(III) adsorption onto Mn dioxide (δ-MnO2) and Fe oxyhydroxide: Ce(III) oxidation by δ-MnO2. *Geochimica*, *65*(5), 695–703.

Palmer, M. R. (1998). Reconstructing Past Ocean pH-Depth Profiles. *Science*, *282*(5393), 1468–1471.

Palmer, M. R., and Edmond, J. M. (1989). The strontium isotope budget of the modern ocean. *Earth and Planetary Science Letters*, *92*(1), 11–26.

Parida, K., Satapathy, P. K., and Das, N. (1996). Studies on Indian Ocean Manganese Nodules. *Journal of Colloid and Interface Science*, *181*, 456–462.

Pattan, J. N. (1993). Manganese micronodules: A possible indicator of sedimentary environments. *Marine Geology*, *113*(3-4), 331–344.

Peacock, C. L., and Sherman, D. M. (2004a). Copper (II) sorption onto goethite , hematite and lepidocrocite: A surface complexation model based on ab initio molecular geometries and EXAFS spectroscopy. *Geochimica et Cosmochimica Acta*, *68*(12), 2623–2637.

Peacock, C. L., and Sherman, D. M. (2004b). Vanadium (V) adsorption onto goethite (α-FeOOH) at pH 1.5 to 12: A surface complexation model based on ab initio molecular geometries and EXAFS spectroscopy. *Geochimica et Cosmochimica Acta*, *68*(8), 1723–1733.

Pearson, D. G., and Woodland, S. J. (2000). Solvent extraction/anion exchange separation and determination of PGEs (Os, Ir, Pt, Pd, Ru) and Re-Os isotopes in geological samples by isotope dilution ICP-MS. *Chemical Geology*, *165*(1-2), 87–107.

Pelejero, C., Calvo, E., and Hoegh-Guldberg, O. (2010). Paleo-perspectives on ocean acidification. *Trends in Ecology and Evolution*, *25*(6), 332–344.

Peng, J. feng, Song, Y. hui, Yuan, P., Cui, X. yu, and Qiu, G. lei. (2009). The remediation of heavy metals contaminated sediment. *Journal of Hazardous Materials*, *161*(2-3), 633–640.

Peucker-ehrenbrink, B. (2001). Rhenium-osmium isotope systematics and platinum group element concentrations: Loess and the upper continental crust. *Geochemistry, Geophysics, Geosystems*, *2*.(10). 10.1029/2001GC000172

Peucker-Ehrenbrink, B., and Ravizza, G. (2000). The effects of sampling artifacts on cosmic dust flux estimates: A reevaluation of nonvolatile tracers (Os, Ir). *Geochimica et Cosmochimica Acta*, *64*(11), 1965–1970.

Plant, A. A. (2015). Abyssal Archives: Unravelling the late Neogene evolution of the Pacific Deep Western Boundary Current from the New Zealand sector of the Southern Ocean. *Master thesis*, Victoria University of Wellington, New Zealand.

Plimer, I. R., and Williams, P. A. (1988). New mechanisms for the mobilization of the platinum-group elements in the supergene zone. In *Geo-Platinum 87* (pp. 83–92).

Pokrovsky, O. S., Pokrovski, G. S., Schott, J., and Galy, A. (2006). Experimental study of germanium adsorption on goethite and germanium coprecipitation with iron hydroxide: X-ray absorption fine structure and macroscopic characterization. *Geochimica et Cosmochimica Acta*, *70*(13), 3325–3341.

Ponthieu, M., Juillot, F., Hiemstra, T., van Riemsdijk, W., and Benedetti, M. F. (2006). Metal ion binding to iron oxides. *Geochimica et Cosmochimica Acta*, *70*, 2679–2698.

Rao, C. R. M., and Reddi, G. S. (2000). Platinum group metals (PGM); occurrence, use and recent trends in their determination. *Trends in Analytical Chemistry*, *19*(9), 565–586.

Rauret, G. (1998). Extraction procedures for the determination of heavy metals in contaminated soil and sediment. *Talanta*, *46*, 449–455.

Ravel, B., and Newville, M. (2005). Athena , Artemis , Hephaestus: data analysis for X-ray absorption spectroscopy using IFEFFIT. *Journal of Synchrotron Radiation*, *12*, 537–541.

Raven, K. P., Jain, A., and Loeppert, R. H. (1998). Arsenite and arsenate adsorption on ferrihydrite: kinetics, equilibrium, and adsorption envelopes. *Environmental Science and Technology*, *32*(3), 344–349.

Ravizza, G. E., and Hole, W. (2001). Platinum group elements and their isotopes in the ocean, In *Elements of Physical Oceanography: A derivative of the Encyclopedia of Ocean Sciences* (pp. 494–503).

Ravizza, G., and Pyle, D. (1997). PGE and Os isotopic analyses of single sample aliquots with NiS fire assay preconcentration. *Chemical Geology*, *141*(3-4), 251–268.

Rehkämper, M., Frank, M., Hein, J. R., and Halliday, A. (2004). Cenozoic marine geochemistry of thallium deduced from isotopic studies of ferromanganese crusts and pelagic sediments. *Earth and Planetary Science Letters*, *219*(1-2), 77–91.

Rehkämper, M., Frank, M., Hein, J. R., Porcelli, D., Halliday, A., Ingri, J., and Liebetrau, V. (2002). Thallium isotope variations in seawater and hydrogenetic, diagenetic, and hydrothermal ferromanganese deposits. *Earth and Planetary Science Letters*, *197*(1-2), 65–81.

Rehkämper, M., and Halliday, a N. (1997). Development and application of new iondashexchange techniques for the separation of the platinum group and other siderophile elements from geological samples. *Talanta*, *44*(4), 663–672.

Reith, F., Campbell, S. G., Ball, a. S., Pring, a., and Southam, G. (2014). Platinum in Earth surface environments. *Earth-Science Reviews*, *131*, 1–21.

Resing, J. A., Sedwick, P. N., German, C. R., Jenkins, W. J., Moffett, J. W., Sohst, B. M., and Tagliabue, A. (2015). Basin-scale transport of hydrothermal dissolved metals across the South Pacific Ocean. *Nature*, *523*(7559), 200–203.

Righter, K. (2003). Metal-Silicate partitioning of Siderophile elements and core formation inthe early earth. *Annual Review of Physical Chemistry*, *31*, 135.174.

Riquier, L., Tribovillard, N., Averbuch, O., Devleeschouwer, X., and Riboulleau, A. (2006). The Late Frasnian Kellwasser horizons of the Harz Mountains (Germany): Two oxygen-deficient periods resulting from different mechanisms. *Chemical Geology*, *233*(1-2), 137–155.

Rudge, J. F., Reynolds, B. C., and Bourdon, B. (2009). The double spike toolbox. *Chemical Geology*, *265*(3-4), 420–431. http://doi.org/10.1016/j.chemgeo.2009.05.010

Sander, S. G., and Koschinsky, A. (2011). Metal flux from hydrothermal vents increased by organic complexation. *Nature Geoscience*, *4*(3), 145–150.

Sakura, 2013. AS-VeRSI, ver. 0.2.1, Computer Program, Sakura: Data Explorer for X-ray Absorption Spectroscopy (XAS) Data. Developers: Kappen P. (Australian Synchrotron), Gary R., (VeRSI-Victorian eResearch Strategic Initiative), Victoria, Australia

Sanders, C. I., and Martin Jr, D. S. (1961). Acid Hydrolysis of $[PtCl_4]^{=}$ and $[PtCl_3(H2O)]^{-1}$. *Journal of the American Chemical Society*, *83*(4), 807–810.

Sassani, D. C., and Shock, E. L. (1998). Solubility and transport of platinum-group elements in supercritical fluids: Summary and estimates of thermodynamic properties for ruthenium, rhodium, palladium, and platinum solids, aqueous ions, and complexes to 1000??C and 5 kbar. *Geochimica et Cosmochimica Acta*, *62*(15), 2643–2671.

Schlitzer, R. (2000). Electronic Atlas of WOCE Hydrographic and Tracer Data. *Eos Trans, AGU*, *81*(5), 45.

Schutyser, P., Govaerts, A., Dams, R., and Hoste, J. (1977). Neutron activation analysis of platinum metals in airborne particulate matter. *Journal of Radioanalytical Chemistry*, *37*(2), 651-660.

Scoates, J. S., and Friedman, R. M. (2008). Precise age of the platiniferous Merensky Reef, Bushveld Complex, South Africa, by the U-Pb zircon chemical abrasion ID-TIMS technique. *Economic Geology*, *103*(3), 465–471.

Sen, I. S., and Peucker-Ehrenbrink, B. (2012). Anthropogenic disturbance of element cycles at the Earth's surface. *Environmental Science and Technology*, *46*(16), 8601–8609.

Severmann, S., Lyons, T. W., Anbar, A., McManus, J., and Gordon, G. (2008). Modern iron isotope perspective on the benthic iron shuttle and the redox evolution of ancient oceans. *Geology*, *36*(6), 487–490.

Shinotsuka, K., and Suzuki, K. (2007). Simultaneous determination of platinum group elements and rhenium in rock samples using isotope dilution inductively coupled plasma mass spectrometry after cation exchange separation followed by solvent extraction. *Analytica Chimica Acta*, *603*(2), 129–139.

Siebert, C., Kramers, J. D., Meisel, T., Morel, P., and Nägler, T. F. (2005). PGE, Re-Os, and Mo isotope systematics in Archean and early Proterozoic sedimentary systems as proxies for redox conditions of the early Earth. *Geochimica et Cosmochimica Acta*, *69*(7), 1787–1801.

Siebert, C., McManus, J., Bice, A., Poulson, R., and Berelson, W. M. (2006). Molybdenum isotope signatures in continental margin marine sediments. *Earth and Planetary Science Letters*, *241*(3-4), 723–733.

Siebert, C., Nägler, T. F., von Blanckenburg, F., and Kramers, J. D. (2003). Molybdenum isotope records as a potential new proxy for paleoceanography. *Earth and Planetary Science Letters*, *211*(1-2), 159–171.

Soua, M. (2011). Productivity and bottom water redox conditions at the Cenomanian-Turonian Oceanic Anoxic Event in the southern Tethyan margin, Tunisia. *Revue Méditerranéenne de L'environnement*, *4*, 653–664.

Soyol-Erdene, T. O., Han, Y., Lee, B., and Huh, Y. (2011). Sources and fluxes of Pt, Ir and REE in the Seoul metropolitan area through wet scavenging processes. *Atmospheric Environment*, *45*(11), 1970–1978.

Soyol-Erdene, T. O., and Huh, Y. (2012). Dissolved platinum in major rivers of East Asia: Implications for the oceanic budget. *Geochemistry, Geophysics, Geosystems*, *13*(6), 1–13.

Soyol-Erdene, T. O., Huh, Y., Hong, S., Hwang, H. J., and Hur, S. Do. (2011). Quantification of ultra-trace levels of Pt, Ir and Rh in polar snow and ice using ICP-SFMS coupled with a pre-concentration and desolvation nebulization system. *Bulletin of the Korean Chemical Society*, *32*(6), 2105–2108.

Soyol-Erdene, T.-O., Huh, Y., Hong, S., and Hur, S. Do. (2011). A 50-Year Record of Platinum , Iridium , and Rhodium in Antarctic Snow : Volcanic and Anthropogenic Sources. *Environmental Science and Technology*, (45), 5929–5935.

Stoffers, P., Glasby, G. P., and Frenzel, G. (1984). Comparison of the characteristics of manganese micronodules from the equatorial and South-West Pacific. *TMPM Tschermaks Mineralogische Und Petrographische Mitteilungen*, *33*(1), 1–23.

Strelow, F., and Toerien, F. V. S. (1966). Separation of Lead (II), from Bismuth (III), Thallium (III), Cadmium (II), Mercury (II), Gold (III), Platinum (IV), Palladium (II), and Other Elements by Anion Exchange Chromatography. *Analytical Chemistry*, *38*(4), 545–548.

Tagliabue, A., Bopp, L., Dutay, J. C., Bowie, A. R., Chever, F., Jean-Baptiste, P., Bucciarelli, E., Lannuzel, D., Remenyi, T., Sarthou, G., Aumont, O., Gehlen, M., and Jeandel, C. (2010). Hydrothermal contribution to the oceanic dissolved iron inventory. *Nature Geoscience*, 3, 252 - 256.

Takahashi, Y., Manceau, A., Geoffroy, N., Marcus, M. a., and Usui, A. (2007). Chemical and structural control of the partitioning of Co, Ce, and Pb in marine ferromanganese oxides. *Geochimica et Cosmochimica Acta*, *71*(4), 984–1008.

Takahashi, Y., Shimizu, H., Usui, A., Kagi, H., and Nomura, M. (2000). Direct observation of tetravalent cerium in ferromanganese nodules and crusts by X-ray-absorption near-edge structure (XANES). *Geochimica et Cosmochimica Acta*, *64*(17), 2929–2935.

Takahashi, Y., Uruga, T., Suzuki, K., Tanida, H., Terada, Y., and Hattori, K. H. (2007). An atomic level study of rhenium and radiogenic osmium in molybdenite. *Geochimica et Cosmochimica Acta*, *71*(21), 5180–5190.

Terashima, S., Usui, a, and Imai, N. (1995). 2 new GSJ geochemical reference samples - syenite JSY-1 and manganese-nodule JMN-1. *Geostandards Newsletter*, *19*(2), 221–229.

Tessier, A., Campbell, P. G. C., and Bisson, M. (1979). Sequential leaching procedure for the speciation of particulate trace metals. *Analytical Chemistry*, *51*, 7.

Toth, J. R. (1980). Deposition of submarine crusts rich in manganese and iron. *Geological Society of America Bulletin*, *91*(1 pt.I), 44–54.

Urey, H. C. (1947). The thermodynamic properties of isotopic substances. *Journal of Chemical Society*, 562–81

Usui, a., and Someya, M. (1997). Distribution and composition of marine hydrogenetic and hydrothermal manganese deposits in the northwest Pacific. *Geological Society, London, Special Publications*, *119*(1), 177–198.

van de Flierdt, T., Frank, M., Halliday, A. N., Hein, J. R., Hattendorf, B., Günther, D., and Kubik, P. W. (2004). Tracing the history of submarine hydrothermal inputs and the significance of hydrothermal hafnium for the seawater budget - A combined Pb-Hf-Nd isotope approach. *Earth and Planetary Science Letters*, *222*(1), 259–273.

Vance, D., Archer, C., Bermin, J., Perkins, J., Statham, P. J., Lohan, M. C., Mills, R. A. (2008). The copper isotope geochemistry of rivers and the oceans. *Earth and Planetary Science Letters*, *274*(1-2), 204–213.

Wagman, D. D., Evans, W. H., Halow, I., Bailey, S. M., Churney, K. L., and Nuttall, R. L. (1982). The NBS tables of chemical thermodynamic properties. *Journal of Physical and Chemical Reference Data*, *11*(Supplement No. 2).

Walker, R. J., Morgan, J. W., and Horan, M. F., 1995. Osmium-187 enrichment in some plumes: Evidence for core-mantle interaction? *Science*, *269*, 819–822.

Wedepohl, K. H. (1995). The composition of the continental crust. *Geochimica et Cosmochimica Acta*, *59*(7), 1217–1232.

Wilburn, D. R., and Bleiwas, D. I., (2004). Platinum-Group Metals -- World Supply and Demand. *U.S. Geological Survey Open-File Report*.

Wood Pan, P., Zhang, Y., Mucci, A., S. a. (1994). The solubility of Pt and Pd sulphides and Au in bisulphide solutions. I. Results at 25-90°C and 1 bar pressure. *Mineralium Deposita*, *29-4*, *309-*, 309–317.

Wood, S. A, Mountain, B. W., and Pan, P. (1992). The aqueous geochemistry of platinum, palladium and gold: recent experimental constraints and a re-evalutaion of the theoritical predictions. *Canadian Mineralogist*, *30*(4), 955–982.

Wood, S. A. (1991). Experimental determination of the hydrolysis constants of Pt2+ and Pd2+ at 25°C from the solubility of Pt and Pd in aqueous hydroxide solutions. *Geochimica et Cosmochimica Acta*, *55*(7), 1759–1767.

Wright, I. C. (1997). Morphology and evolution of the remnant Colville and active Kermadec arc ridges south of 33 30′ S. *Marine Geophysical Researches*, *19*(2), 177–193.

Yacoub, C., Pérez-Foguet, A., Valderrama, C., and Miralles, N. (2014). Impacts on effluent contaminants from mine sites: risk assessment, fate, and distribution of pollution at basin scale. *Environmental Science and Pollution Research*, *21*(9), 5960–5971.

Yamamoto, H., Tanaka, S., Nagai, T., and Takei, T. (1964). Electrochemistry of platinum group metals. II. *Reduction of PtCl*, *6*, 43–48.

Yoshida, H., Nonoyama, S., and Hattori, Y. Y. T. (2005). Quantitative Determination of Platinum Oxidation State by XANES Analysis. *Physica Scripta*, *T115*, 813-815.

Yuan-Hui, L. (1991). Distribution patterns of the elements in the ocean: A synthesis. *Geochimica et Cosmochimica Acta*, *55*(11), 3223–3240.

Zhu, X. (2000). Secular Variation of Iron Isotopes in North Atlantic Deep Water. *Science*, *287*(5460), 2000–2002.

Zhu, X. K., Guo, Y., Williams, R. J. P., O'Nions, R. K., Matthews, A., Belshaw, and N. S., Salvato, B. (2002). Mass fractionation processes of transition metal isotopes. *Earth and Planetary Science Letters*, *200*(1-2), 47–62.

Zhu, X. K., O'Nions, R. K., Guo, Y., Belshaw, N. S., and Rickard, D. (2000). Determination of natural Cu-isotope variation by plasma-source mass spectrometry: Implications for use as geochemical tracers. *Chemical Geology*, *163*(1-4), 139–149.